DISS. ETH NO. 26465

# POST-COMBUSTION CARBON CAPTURE – TOWARD THE INTEGRATION OF COOLING CRYSTALLIZATION INTO AMMONIA-BASED PROCESSES

A dissertation submitted to attain the degree of

DOCTOR OF SCIENCES of ETH ZURICH
(Dr. sc. ETH Zurich)

presented by

FEDERICO MILELLA
Laurea Magistrale in Ingegneria Chimica e di Processo, con lode
Alma Mater Studiorum Università di Bologna
born on February 22nd, 1987
citizen of Italy

accepted on the recommendation of

Prof. Dr. Marco Mazzotti (ETH Zurich), examiner
Prof. Dr. Matteo Gazzani (Utrecht University), co-examiner
Prof. Dr. Stefano Menegatti (North Carolina State University), co-examiner

2020

Federico Milella: *Post-Combustion Carbon Capture – Toward the Integration of Cooling Crystallization into Ammonia-Based Processes*, © 2020

DOI: 10.3929/ethz-b-000414786

To my parents, grandparents, my brother, and Giuseppe who
encouraged me to be myself
&
to those who will not have the benefit of two billion years' accumulated
energy reserves.

# ABSTRACT

The Chilled Ammonia Process (CAP) enables the separation of $CO_2$ from concentrated and stationary $CO_2$ emission sources. In particular, this process can be used to treat large-scale power plants' flue gas, thus reducing the carbon dioxide concentration of the stream sent to stack. More recently, the development of an advanced CAP configuration in which a fraction of the absorbed $CO_2$ is precipitated in the form of an inorganic salt via cooling crystallization, allowed for an increase of the $CO_2$ capture efficiency as well as for a reduction of the overall plant's energy consumption.

This novel process, referred as the controlled solid formation-Chilled Ammonia Process (CSF-CAP), produces solids in a closed-loop system described in the following and uses them as a carbon carrier. At first, the ammonium bicarbonate is crystallized from the $CO_2$-loaded solution exiting the absorption unit and partially separated from the mother liquor by means of hydro-cyclones, thus obtaining a concentrated slurry at a reduced mass flow-rate. Then, the slurry is sent to the regeneration section where the solid phase is completely dissolved before to entering the desorption unit where the solvent regeneration cycle is completed. Assessing the feasibility of integrating continuous crystallization into a $CO_2$ capture plant framework necessarily requires the analysis of thermodynamic and kinetics limitations of the system. This thesis seeks to serve as a template for the design and optimization of a continuous solid handling section integrated with the CSF-CAP and by doing so it tackles several engineering challenges related to the process. At first, the use of a *bottom-up* approach has allowed to achieve a solid understanding of the system thermodynamics as well as of the ammonium bicarbonate solid formation kinetics via a combined experimental and modeling strategy. Then, the knowledge gathered on these fundamental aspects of the system has been used in a rate-based mathematical model that accounts for heat and mass transfer limitations during continuous

crystallization.

Finally, this thesis shows that the *first principle* mathematical framework developed, combined with the experimental solid-liquid equilibria data of the $CO_2-NH_3-H_2O$ system, represents a powerful tool for the understanding of the system's behavior and for the optimization of the overall process performance.

# ZUSAMMENFASSUNG

Der Chilled Ammonia Process (CAP; *Verfahren mittels gekühltem Ammoniak*) ermöglicht die Trennung von $CO_2$ aus konzentrierten und stationären $CO_2$-Emissionsquellen. Insbesondere können mit diesem Verfahren die Abgase von Grosskraftwerken aufbereitet werden, wodurch deren Kohlendioxidkonzentration verringert wird.
Vor Kurzem wurde durch die Entwicklung einer fortschrittlichen CAP-Konfiguration, bei der ein Teil des absorbierten $CO_2$ durch Kühlkristallisation als anorganisches Salz gefällt wird, eine Steigerung der $CO_2$-Abscheidungseffizienz sowie eine Reduktion des Energieverbrauchs der Gesamtanlage ermöglicht.
Dieses neuartige Verfahren, das als "Controlled Solid Formation-Chilled Ammonia Process-(CSF-CAP) bezeichnet wird, erzeugt Feststoffe in einem im Folgenden beschriebenen geschlossenen Kreislauf und verwendet diese als Kohlenstoffträger. Zunächst wird das Ammoniumbicarbonat aus der die Absorptionseinheit verlassenden $CO_2$-haltigen Lösung kristallisiert und mittels Hydrozyklonen teilweise von der Mutterlauge abgetrennt, wodurch sich eine konzentrierte Aufschlämmung mit verringertem Massendurchsatz bildet. Dann wird die Aufschlämmung zum Regenerationsabschnitt geschickt, wo die feste Phase vollständig gelöst ist, bevor sie in die Desorptionseinheit eintritt, wo der Lösungsmittelregenerationszyklus geschlossen wird.
Um die Durchführbarkeit der Integration der kontinuierlichen Kristallisation in ein $CO_2$-Abscheideanlagengerüst zu beurteilen ist zwangsläufig die Analyse der thermodynamischen und kinetischen Beschränkungen des Systems erforderlich. Diese Dissertation soll als Vorlage für die Konzeption und die Optimierung eines in die CSF-CAP integrierten kontinuierlichen Solid Handling-Abschnitts dienen und auf diese Weise verschiedene verfahrenstechnische Probleme lösen. Die Verwendung eines Bottom-up-Ansatzes ermöglichte durch eine kombinierte experimentelle und modellbasierte Strategie zunächst ein solides

Verständnis der Thermodynamik des Systems sowie der Kinetik der Ammoniumbicarbonat-Feststoffbildung. Das gesammelte Wissen über diese grundlegenden Aspekte des Systems wurde in einem geschwindigkeitsbasierten mathematischen Modell verwendet, das die Einschränkungen des Wärme- und Stofftransfers während der kontinuierlichen Kristallisation berücksichtigt.

Schliesslich zeigt diese Arbeit, dass das erste entwickelte mathematische Grundgerüst in Kombination mit den experimentellen Daten zu Fest-Flüssig-Gleichgewichten des $CO_2-NH_3-H_2O$-Systems ein leistungsfähiges Instrument zur Analyse des Systemverhaltens und zur Optimierung des Gesamtprozesses darstellt.

# ACKNOWLEDGEMENTS

I would like to express my most sincere and profound gratitude to my supervisor Prof. Dr. Marco Mazzotti who has contributed to this work in many different ways and has diligently accompanied me on this journey.

I am also very grateful to Prof. Dr. Matteo Gazzani and Prof. Dr. Stefano Menegatti who generously agreed to co-supervise this thesis.

This work was conducted in the framework of the SCCER-EIP (Swiss Competence Center for Energy Research - Efficiency of Industrial Processes) and funded by the Swiss Commission for Technology and Innovation (KTI 1-002957-001). In this context, I would like to thank Prof. Philipp von Rohr for his interest in my research activity.

Additionally, I would like to thank Prof. Kaj Thomsen from the Department of Chemical Engineering and Biochemical Engineering at the Technical University of Denmark for making the thermodynamic model available and for having accepted me as a student of his course on electrolyte solutions, which constituted the foundation of my work.

Warm thanks to all my colleagues at the Separation Processes Laboratory with whom I shared the joy and the pitfalls of my days at ETH. Particularly, I want to thank the CAP team composed by Daniel, Paco, Matteo, and Johannes for the dedication and perseverance in producing original and high quality work, and for fruitful discussions.

I am very grateful to Daniel Trottman, Markus Huber, and Sarah Kienast for their expert management of the workshop and the laboratories. Their help has been crucial for the success of my research during these years. Furthermore, the students who supported my research, namely Davide Bernardo Preso, Selin Güngör, Kevin Ammann, and Lars Behle, deserve a warm thank you.

During the last years, my work has benefited greatly from discussions with Ashwin Rajagopalan, Fabio Salvatori, Stefano Zanco, Stefan Bötschi, Giovanni Maria Maggioni, Ramona Achermann, Pietro Binet,

Ahn Byeongho, Lisa Joss, and Subrahmaniam Hariharan.

A very special thanks goes to my (former and present) office mates, who have endured me during these years (I still do not know how they managed. . . ) and for whom I have profound respect.

I want to thank one last person that has been a great source of inspiration during these years and has always believed in me. "*Einen guten Smokerinen*", my friend.

Finally, I want to thank my family and Giuseppe, for their unconditional support throughout my studies and, above all, for their love that goes beyond words.

# CONTENTS

# LIST OF FIGURES

# LIST OF TABLES

# 1

# INTRODUCTION

## 1.1 CLIMATE CHANGE

Since the beginning of the industrial revolution, the imbalance between the anthropogenic emissions of $CO_2$ and the carbon dioxide removal by oceans and by the biosphere has led to a steady increase of the $CO_2$ concentration in the atmosphere over time. The current observed amount of $CO_2$ (i.e. the sudden spike in Figure 1.1) exceeds the geological record maxima ($\sim 300$ ppm) obtained from ice core data[3] and has been shown to be highly correlated with the raising of the average world temperature (cf. Figure 1.2), whose rate of increase has nearly tripled since 1970 reaching the value of 0.16 °C per decade.
As shown in Figure 1.3, even though carbon dioxide is not a green-

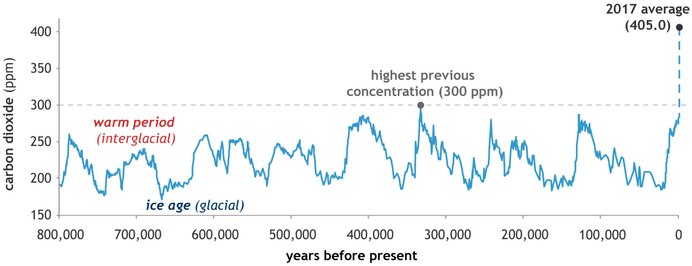

FIGURE 1.1: Evolution of the atmospheric carbon dioxide concentration in parts per million (ppm) in the past 800,000 years, based on EPICA (ice core) data. Adapted from NOAA Climate.gov, based on EPICA Dome C data from Lüthi et al.[1] The peaks and valleys in carbon dioxide levels track the coming and going of ice ages (low carbon dioxide) and warmer interglacials (higher levels). Throughout these cycles, atmospheric carbon dioxide was never higher than 300 ppm; in 2017, it reached 405.0 ppm (black dot).

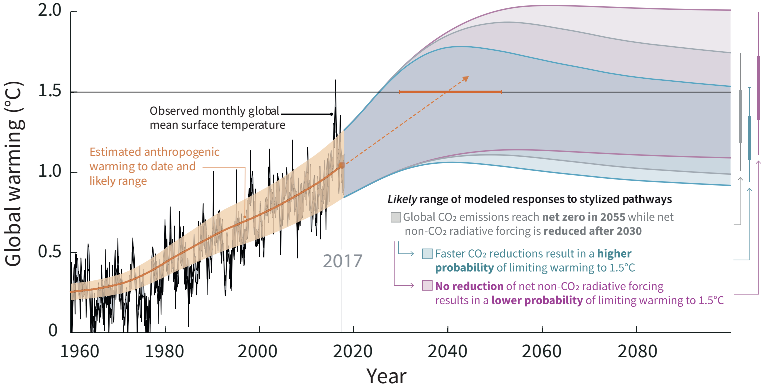

FIGURE 1.2: Observed monthly Global Mean Surface Temperature change (GMST, black line up to 2017, from the HadCRUT4, GISTEMP, Cowtan–Way, and NOAA datasets) and estimated anthropogenic global warming (solid orange line up to 2017, with orange shading indicating assessed *likely* range) adapted from Masson-Delmotte et al.[2] Orange dashed arrow shows the central estimate of the time at which 1.5 °C is reached if the current rate of warming continues. Blue, purple, and gray lines are model projections explained in the figure.

house gas as potent as water vapor, it absorbs energy in longer wavelengths (12–15 µm) compared to water, thus reducing the *infrared window* through which heat radiated by the surface would normally escape to space. Furthermore, $CO_2$ is the gas that is emitted in larger quantities and, together with other greenhouse gases such as methane, ozone, nitrous oxides and CFCs, it contributes to the heat imbalance of the planet (cf. Figure 1.4).

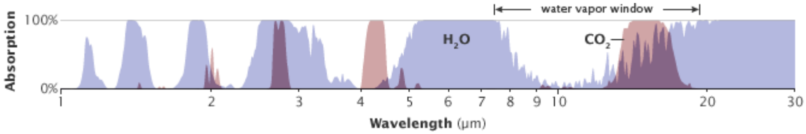

FIGURE 1.3: Infrared absorption patterns of water and carbon dioxide gases. The absorption patterns of water vapor (blue peaks) and carbon dioxide (pink peaks) overlap in some wavelengths. Carbon dioxide is not as a potent greenhouse gas as water vapor, but it absorbs energy in longer wavelengths (12–15 µm) compared to water, thus reducing the *infrared window* through which heat radiated by the surface would normally escape to space. Illustration adapted from NASA: Climate Forcings and Global Warming.

Currently, about 80 % of the global primary energy demand is covered by fossil fuels. These represent exceptionally low-cost, energy-dense fuels in the form of coal, oil, and gas that have been powering economic growth for decades and still play a pivotal role in several aspects of modern energy systems including electricity generation, transportation as well as residential sectors.[4] Projections of the global primary energy demand point towards the direction of more than a 40 % energy increase from 2011 to 2035.[5] At the same time, the concomitant increase in global temperatures caused by the release of greenhouse gases to the atmosphere is expected to produce significant humanitarian crises including famines, floods, and extreme climatic events.[6]

The call for a substantial and prompt reduction in $CO_2$ emissions to mitigate such severe scenarios represents therefore a necessity rather than a choice.

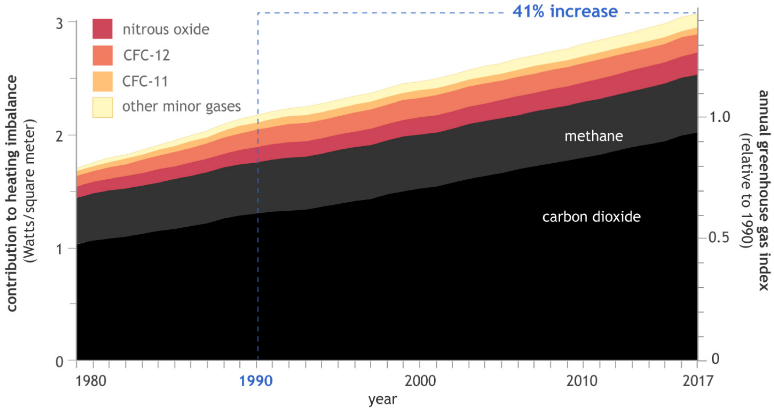

FIGURE 1.4: (left vertical axis) The heating imbalance in watts per square meter relative to the year 1750 caused by all major human-produced greenhouse gases: carbon dioxide, methane, nitrous oxide, chlorofluorocarbons, and a group of 15 other minor contributors. Today's atmosphere absorbs about 3 extra watts of incoming solar energy over each square meter of Earth's surface. According to NOAA's Annual Greenhouse Gas Index (right axis) the combined heating influence of all major greenhouse gases has increased by 41 % relative to 1990. NOAA Climate.gov graph, based on data from NOAA ESRL.

## 1.2 THE CCS VALUE CHAIN AND THE $CO_2$ CAPTURE TECHNOLOGIES

The need for stabilizing or even reducing the concentration of atmospheric greenhouse gases has prompted researchers to develop a variety of mitigation measurements aimed at preventing dangerous anthropogenic interference with the climate system.[7]
Carbon dioxide Capture and Storage (CCS) is one of the bridging technologies that aims at reducing the global $CO_2$ emissions while ensuring a flexible supply of energy from fossil fuels that, as a matter of fact, will continue to be a substantial part of the energy mix for decades to

come.[8]

The CCS value chain is comprised of four main elements:

1. **$CO_2$ point source**
   CCS can be applied to stationary, large-scale sources of $CO_2$ emissions at relatively high concentration (12-24 % vol). Such point sources account for more that 50 % of the global emissions. Among them, coal and natural gas-fired power plants as well as industrial plants, with iron and steel, cement, and chemicals being the most relevant industries.[9]

2. **$CO_2$ capture**
   In this step, an almost pure $CO_2$ stream is obtained. Different types of capture technologies can be exploited to reach the stream specifications.
   In a post-combustion capture process, the carbon dioxide is captured from the treated exhaust gas of a standard combustion process.
   In pre-combustion capture, the fuel is transformed into syngas and the $CO_2$ obtained from the *water-gas shift reaction* is captured before the combustion of the $H_2$ stream.
   The oxy-combustion capture technique burns fuel in pure oxygen (hence, it requires an air distillation step), such that the flue gas consists mainly of concentrated $CO_2$ and water vapor; the latter can be simply condensed and separated.

3. **$CO_2$ transport**
   The $CO_2$ captured at the point source has to be transported to a dedicated storage site by means of pipelines in the supercritical state ($\geq 100$ bar) or as a liquid in cryogenic ships.

4. **$CO_2$ storage**
   In order to prevent the captured $CO_2$ from entering in contact with the atmosphere, suitable geological formations are used for storage. At a suitable depth, the geological pressure gradient ensures a safe and permanent storage of carbon dioxide: a caprock located above the reservoir prevents the ascent of $CO_2$ (which has

> a positive buoyancy) thanks to its extremely low permeability (*stratigraphic trapping*). Due to the capillarity of the rock, the pores of the reservoir immobilizes supercritical $CO_2$ in the form of droplets (*residual trapping*), which eventually stratifies as the $CO_2$ dissolves in the brine originally present in the reservoir (*dissolution trapping*). Over the course of millenia, the $CO_2$ mineralizes as it reacts with the host rock minerals to form solid carbonates (*mineral trapping*).

The most energy and cost intensive step in the CCS value chain is the capture of $CO_2$ (including the compression step). Absorption-based processes, discussed in the next section, offer the opportunity to retrofit CCS to existing large $CO_2$ point source, thus fulfilling the required reduction of emission intensity at a fast rate. Against this background, the International Energy Agency, IEA, predicts that to achieve stabilization of global warming, 114 GW of coal-fired capacity (roughly 17 % of the actual total coal-fired capacity) will need to be retrofitted with carbon capture technologies.[10] It must be noted however that the carbon capture targets are still far from being reached: so far, just 2 Mt tonnes of $CO_2$ is being removed a year. That compares with the 10 Gt $CO_2$ emitted by coal-fired power plants last year, according to the IEA.

## 1.3 ABSORPTION-BASED $CO_2$ CAPTURE PROCESSES

Reactive absorption processes with aqueous amine solutions represent the state-of-the-art for $CO_2$ capture from flue gas, mainly due to the large number of existing plants for acid gas treatment and the proven maturity of the technology.[11] Since the first patent in 1930 by R. R. Bottoms,[12] significant optimization of the process has occurred, particularly in the directions of increasing the durability of the solvent and of reducing the energy penalty of the capture process. More recently, researchers have tested a variety of new amine sorbents, amine blends, and mixtures with carbonate salts to replace the traditional monoethanolamine (MEA) sorbent.[13–15] Furthermore, the use of liquid biphasic solvents, which allow splitting the solution into a $CO_2$-rich phase and a $CO_2$-lean phase, are likely to significantly enhance the performance of $CO_2$ capture by absorption over the coming years.[16] As extensively discussed later in this chapter, on the one hand, the $CO_2$-lean stream obtained after the phase-splitting process can be exploited to boost the $CO_2$ uptake capacity of the solvent. On the other hand, the $CO_2$-rich stream, which represents only a fraction of the total solvent, is thermally regenerated with a significant reduction of the specific energy requirement.

### 1.3.1 *The Chilled Ammonia Process*

When first introduced, absorption-based technologies that exploit an aqueous solution of ammonia as a sorbant showed several advantages over the existing amine processes. Among them, the high $CO_2$ absorption rates and capacity combined to a lower energy need for solvent regeneration.[17–21] Furthremore, the possibility of regenerating the sorbant at a higher pressure compare to the amine process allows for a reduction of the specific $CO_2$ compression duty.[18] It has to be mentioned that, drawbacks such as the high auxiliary loads for chilling and for the ammonia emission control partially offset the benefits resulting from lower steam consumption in the regeneration section.[21,22] Due to the ionic equilibria established in the system, extensively discussed in Section 1.4, solid formation can occur within the absorber, thus limiting substantially the operability of the equipment.[23] In response to this issue, Alstom Power developed an efficient solid-free capture process called Chilled Ammonia Process (CAP) and characterized by a lower aqueous ammonia concentration of the solvent[24] that prevents solid formation.

### 1.3.2 *The Controlled Solid Formation-CAP*

Recently, Sutter et al.[25] investigated the potential of solid formation applied to the CAP in a more energetically favourable process called the Controlled Solid Formation-CAP (CSF-CAP). In this novel process

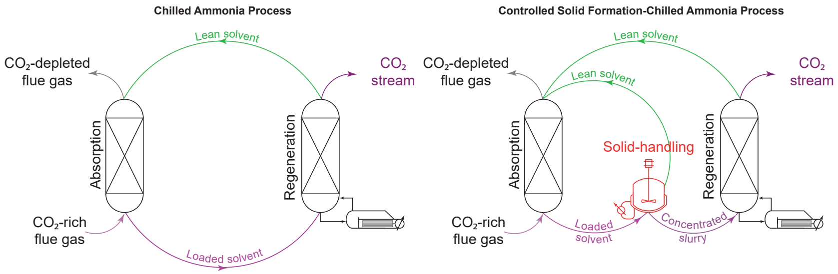

(a) (b)

Figure 1.5: Schematic representation of the Chilled Ammonia Process that uses an aqueous ammonia solution for capturing $CO_2$. (a) the Chilled Ammonia Process (CAP); (b) the Controlled Solid Formation-Chilled Ammonia Process (CSF-CAP). The formation of ammonium bicarbonate in the process is carried out, strictly outside the absorption unit, in a dedicated solid handling section (highlighted in red), which comprises a series of continuous crystallizers and a continuous solid-liquid unit operation (that uses hydrocyclones for example) to separate the solid phase from the mother liquor recycled to the absorption section.

the $CO_2$-loaded solvent forms a slurry comprising solid ammonium bicarbonate particles, which are generated only after absorption, thus preventing fouling of the equipment.

From the comparison of the two processes shown in Figures 1.5a-b it can be seen that the major difference between the CAP and CSF-CAP is a crystallization section (schematically indicated as a crystallizer highlighted in red) which serves the purposes of (1) generating a slurry at increased $CO_2$ concentration (with a consequent reduction of the mass flow-rate sent to regeneration), and of (2) producing a $CO_2$-lean stream recycled to the absorption section and used to increase the $CO_2$ uptake of the solvent (cf. Figure 1.5b).

It is worth mentioning that, alongside with a reduction of the operating costs compared to the standard CAP an increase of the capital costs is to be expected due to the presence of a new plant section dedicated to solid handling.[25]

## 1.4 THERMODYNAMICS OF THE $CO_2-NH_3-H_2O$ SYSTEM

The $CO_2-NH_3-H_2O$ system is a highly volatile system characterized by the following vapor-liquid-solid equilibria.[26–29]

*Vapor-Liquid Equilibria*:

$$CO_2(g) \rightleftharpoons CO_2(aq) \tag{1.1}$$

$$NH_3(g) \rightleftharpoons NH_3(aq) \tag{1.2}$$

$$H_2O(g) \rightleftharpoons H_2O \tag{1.3}$$

*Liquid Speciation*:

$$NH_3(aq) + H_2O \rightleftharpoons {NH_4}^{+} + OH^{-} \tag{1.4}$$

$$CO_2(aq) + H_2O \rightleftharpoons H^{+} + {HCO_3}^{-} \tag{1.5}$$

$${HCO_3}^{-} \rightleftharpoons H^{+} + {CO_3}^{2-} \tag{1.6}$$

$$H_2O \rightleftharpoons H^{+} + OH^{-} \tag{1.7}$$

$$NH_3(aq) + {HCO_3}^{-} \rightleftharpoons NH_2COO^{-} + H_2O \tag{1.8}$$

*Solid-Liquid Equilibria*:

$${NH_4}^{+} + {HCO_3}^{-} \rightleftharpoons NH_4HCO_3(s) \tag{1.9}$$

$${NH_4}^{+} + NH_2COO^{-} \rightleftharpoons NH_2COONH_4(s) \tag{1.10}$$

$$2\,{NH_4}^{+} + {CO_3}^{2-} + H_2O \rightleftharpoons (NH_4)_2CO_3 \cdot H_2O(s) \tag{1.11}$$

$$4\,{NH_4}^{+} + {CO_3}^{2-} + 2\,{HCO_3}^{-} \rightleftharpoons (NH_4)_2CO_3 \cdot 2\,NH_4HCO_3(s) \tag{1.12}$$

Due to the operating conditions investigated in this thesis, the formation of $H_2O(s)$ (ice) has not been included in the set of solid-liquid equilibria considered.

## *Modeling*

Each of the equilibrium reactions represented by eqs 1.1–1.12 can be expressed as an equation of the form:

$$-\frac{\Delta G_j^\circ(T)}{RT} = \sum_i \nu_{i,j} \ln a_i \quad \forall j \tag{1.13}$$

where $\Delta G_j^\circ(T)$ is the change in standard Gibbs free energy for the $j$-th reaction at the temperature $T$, $a_i$ is the activity of the $i$-th component, and $\nu_{i,j}$ is the stoichiometric coefficient of the $i$-th component in the $j$-th reaction. In this work, the non-idealities of the liquid and gas phases are accounted for using the extended-UNIQUAC activity coefficient model and the Soave–Redlich–Kwong cubic equation of state, respectively.

In order to compute the equilibrium phase composition of a mixture containing $CO_2$, $NH_3$, and $H_2O$, eqs 1.1-1.8 must be brought in a form like eq 1.13 and solved simultaneously. Extent of reactions can be used as iteration variables instead of the amounts of individual components to fulfill automatically the electroneutrality condition:

$$m_{\mathrm{NH_4}^+} + m_{\mathrm{H}^+} - m_{\mathrm{OH}^-} - m_{\mathrm{HCO_3}^-} - 2m_{\mathrm{CO_3}^{2-}} - m_{\mathrm{NH_2COO}^-} = 0 \tag{1.14}$$

This work uses molality as solute concentration (mole of component per unit mass of water), where the solvent itself is a reactive species, therefore $m_i$ in eq. 1.14 is the molality of the $i$-th component in the liquid phase.

The presence of a vapor phase at a given temperature $T$ is assessed by checking that the value of the bubble point pressure of the mixture is greater or equal to the total pressure of the system, $P$. The calculation is performed by first guessing a bubble pressure and a vapor composition, then solving eqs 1.4-1.8 simultaneously. Then, the calculated fugacities of the vapor-phase components in eq 1.13 (expressed as $y_i \Phi_i P$; where $y_i$ and $\Phi_i$ are the mole fraction and the fugacity coefficient of the $i$-th component) are used to obtain the mole fractions of the vapor phase. If their summation is different from one, a new bubble pressure is guessed till convergence is reached.

After the equilibrium composition is found, eqs 1.9-1.12 are consulted to verify the presence of any solid phase. If one or more solid phases are formed, the corresponding equation(s) must be solved together with eqs 1.1-1.8 and the process has to be reiterated accounting for the presence of solids.

Despite the fact that water and ammonia are completely miscible in the range of operating conditions explored, ammonia has been considered a solute rather than a solvent. This choice allows for the application of the traditional tabulated standard chemical potentials (NIST Tables) to ions and non-dissociated molecules for the equilibria calculations in water-ammonia-salt mixtures performed with the extended-UNIQUAC model as well as for the computation of the activity of $NH_3$(aq) in solution.

Furthermore, the concentrations of the components must satisfy the following overall mass balances, in addition to the charge balance of eq 1.14.

$$m_{\mathrm{C}}^{\circ} - m_{\mathrm{CO_2}} - m_{\mathrm{HCO_3^-}} - m_{\mathrm{CO_3^{2-}}} - m_{\mathrm{NH_2COO^-}} - \sum_k \nu_{k,\mathrm{C}} m_k^{(\mathrm{s})} = 0 \tag{1.15a}$$

$$m_{\mathrm{N}}^{\circ} - m_{\mathrm{NH_3}} - m_{\mathrm{NH_4^+}} - m_{\mathrm{NH_2COO^-}} - \sum_k \nu_{k,\mathrm{N}} m_k^{(\mathrm{s})} = 0 \tag{1.15b}$$

In eq 1.15, $m_{\mathrm{C}}^{\circ}$ and $m_{\mathrm{N}}^{\circ}$ are the overall concentration of carbon and nitrogen in the system (computed on a molality basis using the information of the initial mass of solvent, $M_{\mathrm{s}}^{\circ}$, added to the system), $m_k^{(\mathrm{s})}$, $\nu_{k,\mathrm{C}}$ and $\nu_{k,\mathrm{N}}$ are respectively the concentration of the $k$-th solid compound in the system (eqs 1.9-1.12) and its carbon and nitrogen stoichiometric coefficients.

Finally, a ternary phase diagram is a convenient way of representing the number of thermodynamic stable phases in the system, at a given temperature, pressure, and overall carbon dioxide, ammonia, and water compositions (note that those are only *apparent* composition of the system that do not consider the speciation. The diagram shown in Figure 1.6 is an exemplary case of the equilibrium phases present in the $CO_2-NH_3-H_2O$ system at 15 °C and 1 bar computed using the thermodynamic model proposed by Darde et al.[30]

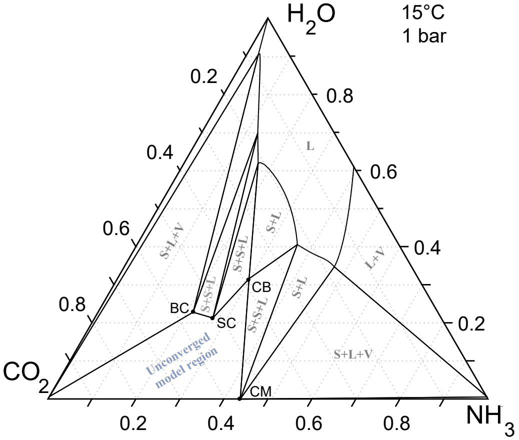

FIGURE 1.6: Ternary phase diagram for the $CO_2-NH_3-H_2O$ system at 15 °C and 1 bar obtained using the thermodynamic model proposed by Darde et al.[30] The compositions are expressed in weight fractions and its construction and use have been described in detail elsewhere.[31] The black dots (•) indicate the composition of the stable solid phases, namely ammonium bicarbonate (BC), ammonium carbonate monohydrate (CB), ammonium sesquicarbonate (SC), and ammonium carbamate (CM). The type of phase, e.g. liquid (L), solid (S), or vapor (V), is indicated with a gray letter. Please note that the text *Unconverged model region* indicates, the region of the ternary phase diagram in which the model fails to converge.

## 1.5 SUPERSATURATION OF ELECTROLYTE SOLUTIONS

An important thermodynamic property involved in the description of solid-liquid equilibria is the supersaturation of a $k$-th solid compound in solution, $S_k$. This thermodynamic quantity is defined in a dimensionless form by the following ratio:[32,33]

$$S_k = \frac{\Delta\mu_k}{RT} = \frac{1}{RT}(\mu_k - \mu_k^*) \tag{1.16}$$

In eq 1.16, the superscript * indicates quantities at solubility, $\mu_k$ is the chemical potential of the dissolved salt, $T$ is the temperature of the system, and $R$ is the ideal gas law constant.

Note that for an electrolyte solution the chemical potential of a $k$-th dissolved salt is the summation of the chemical potentials of the $i$-th dissociated electrolyte species constituting the salt:

$$\mu_k = \sum_i \nu_{i,k}\mu_i^\circ + \nu_{i,k}RT\ln(m_i\gamma_i) \tag{1.17}$$

where $\nu_{i,k}$ is the stoichiometric coefficient of the $i$-th electrolyte in the $k$-th salt, and $\gamma_i$ and $\mu_i^\circ$ are the activity coefficient and the reference chemical potential of the $i$-th species, respectively.

By applying the definition in eq 1.17 to eq 1.16 the following expression for the supersaturation is obtained:

$$S_k = \ln\left[\frac{\prod_i (m_i\gamma_i)^{\nu_{i,k}}}{K_{\mathrm{SP},k}(T)}\right] \tag{1.18}$$

Usually, the numerator in eq 1.18 is referred to as the ionic product of the $k$-th salt, $K_{\mathrm{IP},k}$, function of the temperature and composition of the system. Analogously, the denumerator in eq 1.18 is the solubility product of the $k$-salt in solution defined as:

$$K_{\mathrm{SP},k}(T) = \exp\left[-\frac{\Delta G_k(T)}{RT}\right] \tag{1.19}$$

where the term $\Delta G_k(T)$ is the increment in standard Gibbs free energy of formation of the $k$-th salt in aqueous solution taken from Darde et al.[30] Its dependence on pressure is typically weak and for this reason it has been neglected here.

Based on eq 1.18, the estimation of the driving force for crystallization requires the knowledge of the solubility of the salt, of the speciation of the system, and of the activity coefficients of the species in solution.

## 1.6 MODELING OF CRYSTALLIZATION/DISSOLUTION PROCESSES

In each and every industrial crystallization or dissolution process an ensemble of particles of characteristic size $L$ (in a three-dimensional domain) undergoes a transformation dictated by the thermodynamics as well as the kinetics of the phenomena involved.
The population of particles is usually described using the distribution $n(t, L)$ of an extensive property of the ensemble of particles. This can be the number of particles, but the mass or the volume are possible alternatives. In this thesis, a one-dimensional number distribution is referred to as the crystal size distribution (CSD) and it is defined as:

$$n(t, L) = \frac{\mathrm{d}N(t, L + \mathrm{d}L)}{\mathrm{d}L} \tag{1.20}$$

where, $N$ is the number of particle in the size interval $L + \mathrm{d}L$ at time $t$. In this thesis, $n(L, t)$, has been also rescaled based on the mass of solvent (or on the volume of solution in Chapter 5). Furthermore, the technique adopted to sample the CSD of a given population of crystals is described, in detail, in Section 1.7.

### *Population Balance Modeling*

In order to describe a crystallization or dissolution process a population balance equation (PBE) is employed. It accounts for both the thermodynamics and kinetics of the process through the supersaturation (i.e. the driving force of the system in the current state compared to equilibrium, cf. Section 1.5), and the nucleation, growth, or dissolution rates, which are in turn function of supersaturation. Formation of new particles, referred to as the *birth* of particles, can occur due to primary or secondary nucleation (the latter occurs only in presence of suspended crystals in solution[33]), aggregation, agglomeration, and breakage. On the contrary, the disappearance of particles is referred to as the *death* of particles that can occur due to dissolution or due to the former mentioned phenomena. Hence, the general formulation of the one-dimensional PBE for a batch (well-mixed) system is given as:

$$\frac{\partial n(t,L)}{\partial t} = \frac{\partial}{\partial L}[v(t,L,S)n(t,L)] = B(t,L,S) - F(t,L,S) \qquad (1.21)$$

where $v$ is the advection velocity of the particles in the internal size $L$ at time $t$ and supersaturation $S$ of the continuous phase; $B$ and $F$ are the *birth* and *death* terms, respectively. The convective velocity $v$ may either be the growth rate, $G$, or the dissolution rate, $D$, depending on the phenomenon considered. It is worth noting that eq 1.21 must be coupled to a continuity equation for the solute, which describes the evolution of the concentration of the solute, $m$, during the process:

$$\frac{\mathrm{d}m}{\mathrm{d}t} = \rho_\mathrm{s} \frac{\mathrm{d}}{\mathrm{d}t} \int_\Omega V_\mathrm{s}(L)n(t,L) \qquad (1.22)$$

where $\rho_\mathrm{s}$ is the crystal density, $\Omega$ is the size domain, and $V_\mathrm{s}$ is the volume of the crystals with size $L$.

As discussed in detail in Chapters 3-5, a *high resolution* finite volume method has been used to compute the numerical solution of the PBE.[34,35] Contrary to other numerical schemes such as the method of moments that gives information only on the moments of the distribution, a finite volume method has the advantage of proving a CSD fully resolved in the space and time domains.[36] The drawback of this method is the higher computational cost required.

## 1.7 OVERVIEW OF THE EXPERIMENTAL METHODS

The experimental study of the solid-liquid equilibria in aqueous ammonia solutions as well as the estimation of the kinetics of crystallization and dissolution of a solid phase require the characterization of the liquid phase composition and of the properties of the suspended phase.

### 1.7.1 *Experimental Setup*

In the context of this thesis, the crystallization and the dissolution processes studied have been carried out in well-mixed batch reactor. Furthermore, the study of the $NH_3-CO_2-H_2O$ system required the mitigation of the the evaporation of the solutes (mostly $CO_2$ and $NH_3$) during the experiments. This has been achieved by performing experimental campaigns in a sealed and pressurized reactor illustrated in Figure 1.7. The vessel of a volume of 1.4 L is equipped with a magnetically driven stirrer and online monitoring tools described in the following. The probes are connected to the reactor by means of custom-made pressure connectors installed in the lid of the vessel. Further technical details of the reactor can be found in reference [37] as well as in Chapters 2-3.

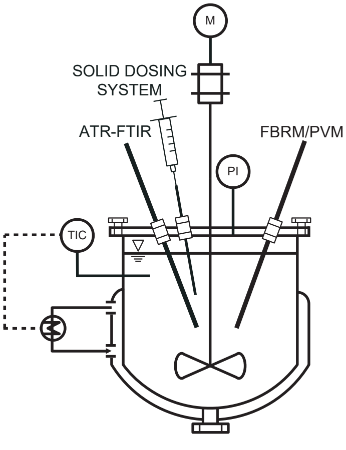

Figure 1.7: Graphical representation of the experimental setup. The reactor is equipped with a thermostate jacket, a magnetically driven stirrer, monitoring probes (e.g. ATR-FTIR, FBRM or PVM), a digital pressure indicator, and a custom made solid dosing system.

### 1.7.2 *Liquid Phase Characterization*

#### *Infrared Spectroscopic Measurements*

Infrared spectroscopy has been used to monitor the concentration of the species in solution. As schematically shown in Figure 1.8, the Beer–Lambert law is the fundamental equation describing the incident ($I_0$) and transmitted ($I$) infrared radiation intensities in vibrational spectroscopy. The light absorbance, $A_i(\bar{\nu})$, at a specific wavenumber $\bar{\nu}$ can be expressed as:

$$A_i(\bar{\nu}) = q_i(\bar{\nu}) m_i \mathscr{L} = \log_{10}\left(\frac{I_0}{I}\right) \tag{1.23}$$

where $q_i(\bar{\nu})$ is the absorption coefficient of the $i$-th component, and $\mathscr{L}$ the effective path length of light in the sampled medium.

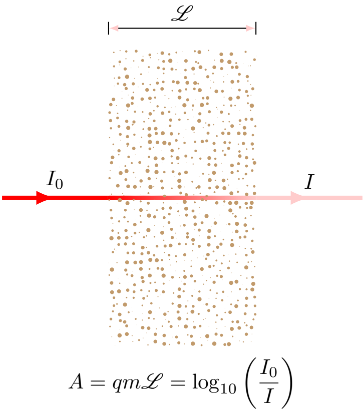

FIGURE 1.8: Graphical representation of the Beer–Lamber law. The beam radiant power becomes weaker as it passes through the solution.

### 1.7.3 *Solid Phase Characterization*

#### *FBRM Measurements*

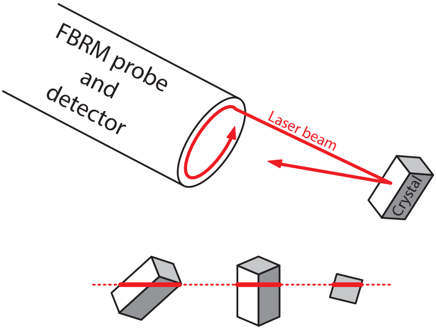

Figure 1.9: Graphical representation of the FBRM measurements. Computations on the laser beam reflection time allow to compute the chord-length distribution of the population of crystals measured. A value of the average mean-size can be also computed for monitoring and control purposes.

A laboratory-scale device (Lasentec, WA) has been used to perform focused beam reflectance measurements (FBRM) in which a rotating laser beam strikes suspended particles at any random place as shown schematically in Figure 1.9. The laser light is then reflected by each crystals and absorbed by a detector in the probe. Then, a chord length can be computed from the information on the rotation speed of the laser beam and on the duration of the reflection. These type of measurements have been used to detect the onset of particle formation, to monitor particle dissolution, and to assess statistically the steady-state of the crystallization process.
In this work, a 1 min measurement duration has been set for all the FBRM measurements at a laser speed of $2\,\mathrm{m\,s^{-1}}$.

### *PVM Measurements*

A probe-based microscope (Mettler-Toledo, Switzerland) has been used for particle vision and measurements (PVM) during cooling crystallization experiments.

### *μ-DISCO Measurements*

An opto-mechanical stereoscopic device known as the μ-DISCO described elsewhere[38] has been used to perform an off-line characterization of the crystal size distribution (CSD) of the seeds as well as of the product of the crystallization. The μ-DISCO can be either operated in an online mode (cf. Figure 1.10) to characterize the dispersed phase during a crystallization process, or in an off-line mode. In the online mode, an external sampling loop allows for a continuous withdrawal of the suspension using a peristaltic pump. Then, the sample is sent to the stereoscopic device (flow channel) for the online analysis prior to being conveyed back to the vessel. The temperature variation within the loop can be neglected because of the small hold-up of the tubing ($\approx$100 mL) compared to the volume of the reactor and of the recirculation flow rate used (150 mL min$^{-1}$). The main limitation of such an operational mode is set by the maximum allowed pressure of the device (ca 0.5 barg) and the maximum suspension density (ca. 1 % wt) which must not be exceeded during the measurement.[38]

In the off-line mode, the CSD of a population of crystals can be characterized by a batch analysis of a suspension circulated through the μ-DISCO.

It is worth mentioning that, besides the ATR-FTIR probe, only one additional monitoring device (among FBRM, μ-DISCO, and PVM) could be used during each experiment due to space restriction in the reactor's lid.

## 1.8 OBJECTIVES AND OUTLINE OF THE THESIS

This work builds up on the previous knowledge acquired on the optimization of the CAP by controlling solid formation.[39] The overarching

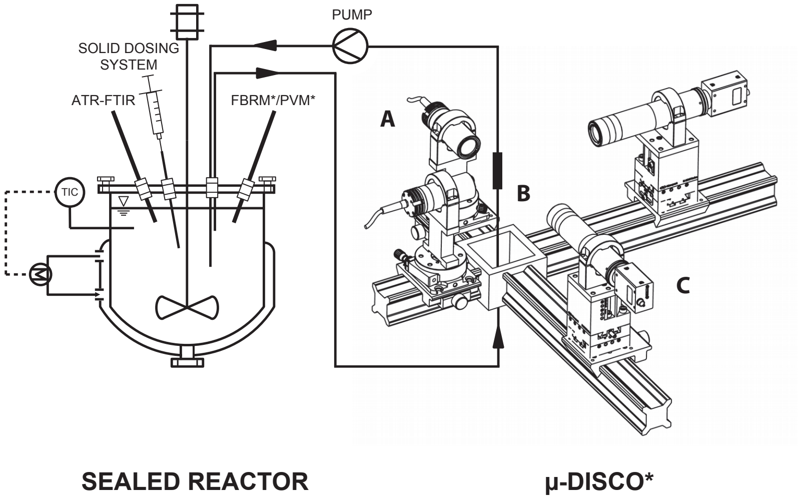

FIGURE 1.10: Illustration of the experimental setup and the μ-DISCO sampling loop for online suspension monitoring. The suspension flowing from the reactor through the flow channel (B) is back-light illuminated using two telecentric illuminators (A) and photographed using two digital cameras (C) with telecentric optics. The camera and the lens, and the illumination system are mounted orthogonally on an optical rail construction. Due to spatial restrictions, the reactor allowed for the use of only one monitoring tool (marked with an asterisk) at a time during the measurement.

goal of this thesis is to integrate a continuous crystallization section for ammonium bicarbonate in the CSF-CAP accounting for the thermodynamic and kinetics constraints of the process.

The first part of the thesis is strongly experimental and focuses on the estimation of the crystallization and the dissolution kinetics of ammonium bicarbonate from aqueous ammonia solutions. The second part of the thesis is more computational and exploits process modeling and optimization for the synthesis of a novel crystallization section

for the CSF-CAP. Both the thermodynamic framework established in the previous chapters and the mathematical model developed for the simulations are key for the analysis of the overall process performance in terms of specific energy consumption and productivity.
Quite a number of challenges, both experimental and computational, have been addressed in this thesis and few of the most relevant ones have been listed below:

- estimation of the species concentration for a highly volatile system for which the application of standard IR spectroscopic techniques is infeasible;
- characterization of the shape and the properties of ammonium bicarbonate crystals;
- development and experimental validation of kinetic models for the estimation of crystal growth and dissolution rates of ammonium bicarbonate;
- derivation of a first-principle dimensionless model that captures the main features of a continuous crystallization section with heat integration.

**Chapter 2** of the thesis focuses on the $CO_2-NH_3-H_2O$ system and characterizes it in terms of the liquid phase reactions and of the solid-liquid equilibria that can be established at the relevant operating conditions.
**Chapter 3** introduces the thermodynamic framework used to estimate growth and dissolution kinetics of ammonium bicarbonate crystals in a complex electrolyte system.
**Chapter 4** investigates the effect of the presence of impurities on the crystallization kinetics of ammonium bicarbonate with the attempt of providing a more realistic description of the solvent used in the CAP-CSF. In detail, the effect of sulfates ions, a side-product of the combustion reactions of coal for power plants, has been investigated in terms of the inhibition induced on the ammonium bicarbonate crystal growth kinetics.

**Chapter 5** provides a conceptual design of the crystallization section as well as a selection of the most suitable industrial crystallization equipment. In this chapter, a mathematical model of the solid-handling section has been derived and used to perform a rigorous process optimization of the overall $CO_2$ capture process. In particular, the analysis focused on the study of the optimal process parameters (*decision variables*) that affect the productivity and the specific energy penalty of the process the most.

**Chapter 6** summarizes the main conclusions of this thesis and provides an industry perspective on the potential applications of the CSF-CAP.

Please note that this is a thesis by published work and, as such, the contents of the different chapters has been adapted from articles published in a number of peer-reviewed journals. Each chapter can be considered as a standalone piece of work, for which all the necessary terminology and definitions are provided within the corresponding section.

## NOMENCLATURE

### *Acronyms*

| | |
|---|---|
| (aq) | Aqueous state |
| ATR-FTIR | Attenuated total reflection-infrared spectroscopy |
| CAP | Chilled ammonia process |
| CCS | Carbon dioxide capture and storage |
| CFCs | Chlorofluorocarbons |
| CSD | Crystal size distribution |
| CSF-CAP | Controlled solid formation-Chilled ammonia process |
| DISCO | Dual imaging system for crystallization observation |
| EPICA | European project for ice coring in antarctica |
| FBRM | Focused beam reflectance measurement |
| (g) | Gaseous state |
| GMST | Global mean surface temperature |
| IEA | International Energy Agency |
| (l) | Liquid state |
| MEA | Monoethnolamine |
| NIST | National Institute of Standards and Technology |
| NOAA | National oceanic and atmospheric administration |
| PBE | Population balance equation |
| PVM | Particle vision measurement |
| (s) | Solid state |

### *Greek Symbols*

| | |
|---|---|
| $\Delta\mu$ | Change in chemical potential $[\mathrm{J\,mol^{-1}}]$ |
| $\Delta G_r^\circ$ | Change in standard Gibbs free energy of the $r$-th reaction $[\mathrm{J\,mol^{-1}}]$ |
| $\gamma$ | Activity coefficient (molality-based) [-] |
| $\mu$ | Chemical potential $[\mathrm{J\,mol^{-1}}]$ |
| $\nu$ | Stoichiometric coefficient |
| $\tilde{\nu}$ | IR Wavenumber $[\mathrm{cm^{-1}}]$ |
| $\Delta G_k$ | Standard Gibbs free energy of formation of the $k$-th salt $[\mathrm{J\,mol^{-1}}]$ |
| $\Omega$ | Size domain of the crystals [m] |

### *Roman Symbols*

| | |
|---|---|
| $\mathscr{L}$ | Effective path length of light in the medium [m] |
| $\rho_\mathrm{s}$ | Density of the solid phase $[\mathrm{kg/m^3}]$ |

| | |
|---|---|
| $A_i$ | Light absorbance [A.U.] |
| $a_i$ | Activity of the *i*-th species (molality-based) [mol/kg$_\mathrm{w}$] |
| $B$ | Birth term |
| $D$ | Crystal dissolution rate [m s$^{-1}$] |
| $F$ | Death term |
| $G$ | Crystal growth rate [m s$^{-1}$] |
| $I$ | Transmitted light [lx] |
| $I_0$ | Incident light [lx] |
| $K_\mathrm{IP}$ | Ionic product (mole frac. based) [-] |
| $K_\mathrm{SP}$ | Solubility product (mole frac. based) [-] |
| $L$ | Internal space coordinate of the crystals [m] |
| $m_i$ | Molality of the *i*-th component [mol/kg$_\mathrm{w}$] |
| $N$ | Number of particles [-] |
| $n$ | Crystal size distribution (number-based) [m$^{-1}$ kg$^{-1}$] |
| $q_i$ | Absorption coefficient for the *i*-th component [A.U. kg mol$^{-1}$ m$^{-1}$] |
| $R$ | Ideal gas law constant [J mol$^{-1}$ °C$^{-1}$] |
| $S$ | Salt supersaturation [-] |
| $T$ | Temperature [°C] |
| $t$ | Time [s] |
| $v$ | Advection velocity of the particles [m s$^{-1}$] |
| $V_\mathrm{s}$ | Volume of the solid phase [m$^3$] |

*Subscripts and Superscripts*

| | |
|---|---|
| $\circ$ | Superscript pertaining to a nominal quantity |
| $i$ | Subscript pertaining to the *i*-th species in solution |
| $j$ | Subscript pertaining to the *j*-th reaction |
| $k$ | Subscript pertaining to the *k*-th salt in the system |
| $*$ | Superscript pertaining to quantity at solubility |

# 2

# CHEMICAL EQUILIBRIA AND SPECIATION

## 2.1 INTRODUCTION

The characterization of the $CO_2-NH_3-H_2O$ system in terms of the liquid phase reactions and of the solid-liquid equilibria that can be established at the relevant operating conditions is based on extensive experimental work carried out almost one hundred years ago.[26,27,40,41] Furthermore, thermodynamic models capable of computing such equilibria have been developed with the aim of designing and optimizing relevant industrial processes such as wastewater and flue gas treatment, and enhanced oil recovery.[28,30] As an example, the Chilled Ammonia Process (CAP) developed by Alstom Power captures greenhouse gases from large $CO_2$ point sources such as power plants by means of aqueous ammonia solutions.[25] Several variants of the process exist; among them the so-called Controlled Solid Formation-Chilled Ammonia Process (CSF-CAP) allows for the precipitation of ammonium bicarbonate ($NH_4HCO_3$, in the following also "BC") to lower the specific energy demand of the process by increasing the $CO_2$ uptake capacity of the solvent system.[25] In this process, the information about the phase equilibria and the kinetic effects of chemical reactions and mass transfer are key for the design and optimization of a continuous crystallization section fully integrated with the rest of the capture plant.[42] Retrieving crystallization kinetics of BC for this system is complicated by the high volatility of the solutes,[37] i.e. $NH_3$ and $CO_2$, and requires the information on the speciation of the solution for the computation of the driving force of the crystallization process, i.e. the supersaturation. In this regard, the use of available thermodynamic models,[28,30] usually

---

The work presented in this chapter has been reproduced from Milella, F.; Mazzotti, M. Estimating speciation of aqueous ammonia solutions of ammonium bicarbonate: application of least squares methods to infrared spectra. *React. Chem. Eng.*, **2019**, 4, 1284–1302 . DOI: 10.1039/C9RE00137A. Copyright 2019 Royal Society of Chemistry.)

fitted on vapor-liquid equilibrium data and only on a limited amount of liquid speciation data,[43,44] leads to inaccurate estimates of the BC solubility.

The call for an improved accuracy in the description of the solid-liquid equilibrium of BC in aqueous ammonia solutions motivated this work in which a methodology for the measurement of the speciation of aqueous ammonia solutions of ammonium bicarbonate is developed. Attenuated Total Reflection-Fourier-Transform Infrared spectroscopy (ATR-FTIR)[45,46] has been used to measure the overall carbon concentration, as well as the equilibrium speciation in solution. The advantage of such a technique over Raman spectroscopy, also used to study properties of this system[29,47–49] is that it allows for liquid-phase concentration monitoring exclusively, in spite of the presence of a solid phase suspended. The analysis of the IR spectrum of the mixtures reveals complex overlaps of the bands of the individual components that have been resolved by means of a simple but effective Classical Least Squares (CLS) method. Then, the information retrieved has been used to estimate the solutes concentration while fulfilling the mass and charge balances in solution.

The BC solubility and the concentration estimates of the species in saturated aqueous ammonia solutions of BC at different nominal ammonia concentrations in the solvent (between 0 and 3 % wt) have been, at first, compared to the literature data in the temperature range 8-23 °C. Then, they have been used to improve the accuracy of the description of the liquid-solid equilibrium of ammonium bicarbonate by using a thermodynamic model.

The chapter is organized as follows. In section 2, the experimental setup, the analytical methods and the characterization techniques used are discussed with particular emphasis on the preparation of the standard analytes for the ATR-FTIR calibration measurements. Section 3 provides a description of the mathematical model used to resolve complex overlapping spectra and the estimation of the concentration of the individual species. Finally, in Section 4 the methodology is applied to the case of real mixtures containing $CO_2$, $NH_3$, and $H_2O$ and a rigorous thermodynamic framework for the estimation of the supersaturation of aqueous ammonia solutions of ammonium bicarbonate is established. In our experimental setup (cf. Section 1.7.1), the presence of a gas phase, consisting mainly of inert air, leads to the evaporation of $CO_2$, $NH_3$, and $H_2O$. This phenomenon can be minimized by reducing the dead gas volume of the reactor, thus allowing to neglect the presence of a gas phase in the mass balances.

In this work, mixtures containing $CO_2$, $NH_3$, and $H_2O$ have been obtained by dissolving BC in aqueous ammonia solutions at different nominal ammonia concentrations in the solvent (up to 3 % wt). While ammonium bicarbonate in water dissociates by forming equimolar mixtures of $CO_2$ and $NH_3$ (before speciation), the presence of an excess of ammonia shifts the ratio between the total nitrogen and carbon content, $\zeta$, to values greater than one, and significantly affects the speciation in solution.

The overall composition of such systems can be identified in the ternary diagram shown in Figure 2.1; each point in the diagram corresponds to the overall mass fraction of equivalent $CO_2$, $NH_3$, and $H_2O$ (regardless of the liquid speciation and of the number of phases present at a given temperature and pressure). Additionally, the composition of the solid compounds are shown as black points. Mixtures characterized by a molar ratio $\zeta$ of one are represented by the isopleth (dashed black line) that connects the composition of the BC salt to the pure water vertex, while the other two isopleths drawn represent systems that are characterized by a molar ratio $\zeta$ of 1.3 and 2.0.

As a consequence of the equilibria of eqs 1.1-1.8 discussed in Chapter 1, when comparable amounts of nitrogen and carbon are present in the system ($\zeta \approx 1$), the equilibria of eqs 1.4-1.5 leads to mildly alkaline solutions in which the ammonium and bicarbonate ions are the main species present (cf. Section 2.4.6). As the value of $\zeta$ becomes larger than one, the mixture becomes more and more alkaline (cf. the pH of the liquid phase shown in Figure 2.1 using a color code) shifting the carbon speciation towards the carbonate and carbamate species.

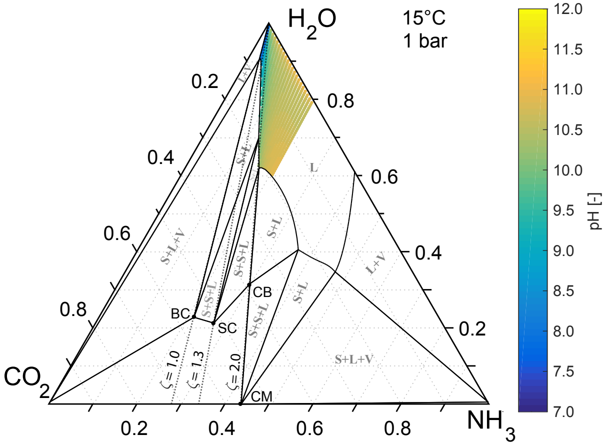

FIGURE 2.1: Ternary phase diagram for the $CO_2-NH_3-H_2O$ system at 15 °C and 1 bar obtained using the thermodynamic model proposed by Darde et al.[30] The compositions are expressed in weight fractions and its construction and use have been described in detail elsewhere.[31] The black dots (●) indicate the composition of the stable solid phases, namely ammonium bicarbonate (BC), ammonium carbonate monohydrate (CB), ammonium sesquicarbonate (SC), and ammonium carbamate (CM). The type of phase, e.g. liquid (L), solid (S), or vapor (V), is indicated with a gray letter. The dashed isopleths (black lines) refer to $CO_2$, $NH_3$, and $H_2O$ mixtures characterized by a constant ratio, $\zeta$, between the nitrogen and carbon species, while a colorcode is used to indicate the pH of the liquid phase calculated using the thermodynamic model proposed by Darde et al.[30]

## 2.2 EXPERIMENTAL SECTION

### 2.2.1 *Materials*

Electrolyte solutions have been prepared using analytical grade chemicals purchased from Sigma-Aldrich (Buchs, Switzerland) and Milli-Q water (18.2 MΩ cm at 25 °C). Ammonium bicarbonate ($NH_4HCO_3$, BioUltra, $\geq$ 99.5 % pure), ammonium chloride ($NH_4Cl$, BioUltra, $\geq$ 99.5 %

pure), potassium bicarbonate ($KHCO_3$, BioUltra, $\geq$ 99.5 % pure), and potassium carbonate ($K_2CO_3$, BioUltra, $\geq$ 99 % pure) have been used without further purification.
The formation of potassium carbonate hydrates has been minimized by exploiting a drying step of the raw material at 100 °C under vacuum for a period of about 5 hours.
Ammonia solutions have been prepared by diluting commercial ammonium hydroxide solutions (Sigma-Aldrich, puriss. p.a., reag. ISO, reag. Ph. Eur. 25 % wt).

### 2.2.2 *Experimental Setup and Analytical Methods*

#### *Experimental Setup*

The equilibrium $CO_2$ partial pressure of aqueous solutions of ammonium bicarbonate and potassium bicarbonate exceeds by far the atmospheric pressure in the range of salt conditions explored in this work, eventually leading to a substantial material loss due to solute evaporation. The problem has been overcome by using a jacketed sealed vessel described in detail elsewhere[37] that allows to maintain samples under their own vapor pressure, thus minimizing $CO_2$ or $NH_3$ losses from the liquid phase. In our experimental setup, the evaporation of $CO_2$, $NH_3$, and $H_2O$ to the vapour phase, consisting mainly of inert air, has been minimized by almost completely filling the reactor with the liquid during operation. The vessel's maximum operating pressure has been set to 5 bar and an impeller speed of 400 RPM has ensured adequate mixing. The process temperature control has been performed by means of a CC230 thermostat (Huber, Germany) connected to a Pt-100 probe immersed in the liquid phase of the reactor acquiring data at a frequency of 30 $s^{-1}$.
The immersion probes of the monitoring tools such as the ATR-FTIR and FBRM have been connected to the reactor by means of custom-made pressure connectors installed in the lid of the vessel (the interested reader is referred to Appendix A for an illustration of the experimental setup).

### *Analytical Methods*

The preparation of electrolyte solutions of inorganic salts used in this work has been carried out with a PG8001 analytical balance (Mettler-Toledo, Switzerland). The balance readability and maximum capacity are 0.1 g and 8.1 kg, respectively; and the estimated accuracy of the static measurements is ± 0.23 g.
The concentration of commercial ammonium hydroxide solutions has been measured by acid-base titration using a 702 SM Titrino (METROHOM, Switzerland) and a 1M HCl solution as titrant.

### *Preparation of Aqueous Ammonia Solutions of Ammonium Bicarbonate*

Aqueous ammonia solutions of BC have been prepared by dissolving specific amounts of ammonium bicarbonate in aqueous solution containing ammonia at the nominal concentration of 0, 2, and 3 % wt, respectively. Since ammonium bicarbonate represents the only source of carbon in the system, the overall carbon and nitrogen balances for the liquid phase can be written as follows:

$$m^{(1)}_{\mathrm{C,OL}} = m^{(1)}_{\mathrm{BC}} = m_{\mathrm{CO_2}} + m_{\mathrm{HCO_3{}^-}} + m_{\mathrm{CO_3{}^{2-}}} + m_{\mathrm{NH_2COO^-}} \tag{2.1}$$

$$m^{(1)}_{\mathrm{N,OL}} = m^{(1)}_{\mathrm{BC}} + m^{\circ}_{\mathrm{NH_3}} = m_{\mathrm{NH_3}} + m_{\mathrm{NH_4{}^+}} + m_{\mathrm{NH_2COO^-}} \tag{2.2}$$

where $m^{(1)}_{\mathrm{C,OL}}$ and $m^{(1)}_{\mathrm{N,OL}}$ are the overall carbon and nitrogen concentration in the liquid phase, $m^{\circ}_{\mathrm{NH_3}}$ is the nominal concentration of ammonia in the initial solution (that plays the role of solvent for BC), and $m^{(1)}_{\mathrm{BC}}$ is the overall concentration of ammonium bicarbonate in the liquid phase.

## 2.2.3 *In Situ Characterization Techniques*

### *ATR-FTIR Spectroscopy*

ATR-FTIR spectroscopy has been applied to monitor the liquid phase concentration. Due to its low penetration depth, typically $2 - 3$ μm, the ATR probe allows exclusively for liquid-phase monitoring also in the presence of a suspended solid phase. Samples have been collected using a ReactIR 45m system (Mettler-Toledo, Switzerland), equipped with a 1.6 cm DiComp immersion probe and a 6 internal reflections diamond ATR crystal. The number of Spectra have been collected in the 800-3000 $\mathrm{cm}^{-1}$ region with a wavenumber resolution of 4 $\mathrm{cm}^{-1}$ and averaged over 256 scans using an exposure time of 1 min. The ATR-FTIR background signal has been collected in air, at ambient conditions, before every experiment.

*Focused Beam Reflectance Measurements*

The device used for focused beam reflectance measurements (FBRM) allows for in-situ determination of the chord length distribution (CLD) of suspended particles. In this work, a laboratory-scale FBRM device (Lasentec, Redmond, WA) has been used to detect the onset of particle formation during the ATR-FTIR calibration measurements and to monitor the complete dissolution of particles during BC solubility measurements in aqueous ammonia solutions.[50] A 1 min measurement duration has been used for all FBRM measurement at a laser speed of $2\,\mathrm{m\,s^{-1}}$.

### 2.2.4 *IR Peaks Indentification*

ATR-FTIR spectroscopic analyses of aqueous solutions are challenging due to the strong water absorption over the entire mid-infrared spectral region. Nevertheless, characteristic and well distinct IR-active bending modes of the species investigated in this work, i.e. $NH_4{}^+$, $NH_3$(aq), $CO_2$(aq), $HCO_3{}^-$, $CO_3{}^{2-}$, and $NH_2COO^-$ are observable in the spectrum of aqueous solutions containing $CO_2$ and $NH_3$[43,44,56] (cf. Table 2.1). The first step towards the resolution of such mixtures is represented by the isolation of the characteristic IR modes of each individual component. Then, a set of ATR-FTIR standards of the solute of interest can be prepared for calibration purposes.

Binary subsystems consisting of an inorganic salt and water in which the ionic species of interest dissociate completely with negligible spe-

| **Species** | **Band Position** [$cm^{-1}$] | **Assignment** |
|---|---|---|
| $H_2O$ | 1640 | $\delta(H_2O)$[51] |
| $CO_2(aq)$ | 2343 | $\nu_a(CO_2)$[51] |
| $NH_3(aq)$ | 1111 | $\delta(NH_3)$[51] |
| $NH_4^+$ | 1458 | $\delta$(-NH)[51] |
| $CO_3^{2-}$ | 1395 | $\nu_a$(-CO)[52] |
| $NH_2COO^-$ | 1120 | $\nu$(-CN)[44,53,54] |
|  | 1413 | $\nu$(-CN)[44,55] |
|  | 1545 | $\delta$(-N−H)[44,53] |
| $HCO_3^-$ | 1005 | $\nu_a$(-C−OH)[52] |
|  | 1300 | $\delta$(-C−OH)[52] |
|  | 1365 | $\nu$(-C−O)[52] |
|  | 1650 | $\nu_a$(-C−O)[52] |

Table 2.1: Main infrared band assignments of the species present in the $CO_2-NH_3-H_2O$ system. The symbols $\nu$, $\nu_a$ and $\delta$ indicate the stretching mode, the asymmetric stretching mode, and the bending mode of the relevant molecules, respectively.

ciation have therefore been selected. It has to be acknowledged that, due to the electrolytic nature of the solutes, the measurement of the IR spectrum necessarily embeds the absorbance of the solvent that can be removed during post-processing.[57] In this work the subsystems $NH_4Cl(aq)$, $KHCO_3(aq)$, $K_2CO_3(aq)$, and $NH_3(aq)$ have been used to isolate the characteristic peaks of the ammonium, bicarbonate, carbonate ions, and ammonia respectively.[44] This was possible thanks to the negligible extent of speciation of the single components within each subsystem. The presence of spectator ions such as $K^+$ and $Cl^-$ is accounted for in the electroneutrality condition and does not affect the relevant dissociation equilibria. Moreover, their effect on the absorbance of the solute of interest has not been significant in the range of concentrations investigated.[58]

| **Compound** | **Concentration** [mol/kg$_w$] | | | | **Temperature** [°C] | | | |
|---|---|---|---|---|---|---|---|---|
| *Sample No.* | 1 | 2 | 3 | 4 | 1 | 2 | 3 | 4 |
| $NH_4HCO_3$(aq) ($m^\circ_{NH_3}$ = 0 m) | 1.76 | 2.02 | 2.31 | 2.64 | 5- 25 | $10^\dagger$ - 25 | $10^\dagger$ - 25 | $16^\dagger$ - 25 |
| $NH_4HCO_3$(aq) ($m^\circ_{NH_3}$ = 1.2 m) | 2.64 | 2.89 | 3.05 | 3.17 | 5 - 25 | $8^\dagger$ - 25 | $12^\dagger$ - 25 | $14^\dagger$ - 25 |
| $NH_4HCO_3$(aq) ($m^\circ_{NH_3}$ = 1.8 m) | 3.06 | 3.27 | 3.42 | 3.53 | 5 - 25 | $6^\dagger$ - 25 | $8^\dagger$ - 25 | $13^\dagger$ - 25 |
| $KHCO_3$(aq) | 1.79 | 2.14 | 2.48 | 2.83 | 5 - 25 | | | |
| $K_2CO_3$(aq) | 0.25 | 0.35 | 0.45 | 0.55 | 5 - 25 | | | |
| $NH_4Cl$(aq) | 1.71 | 2.14 | 2.48 | 2.83 | 5 - 25 | | | |
| $NH_3$(aq) | 0.61* | 1.25 | 1.93 | n/a | 5 - 25 | | | |

Table 2.2: Set of standard solute concentrations and temperatures used for the species-wise ATR-FTIR calibration models. (*) ATR-FTIR detection limit for the $NH_3$(aq), (†) temperature value corresponding to the onset of primary nucleation (cf. Appendix A for further information).

ATR-FTIR polythermal measurements[45] have been performed using the aforementioned subsystems in the thermostated, stirred and sealed vessel described in Section 2.2.2. The range of temperatures and concentrations selected for the different subsystems is representative of the range of equivalent $CO_2$ and $NH_3$ concentrations investigated in this study and it is reported in Table 2.2. Samples of pure water, in the same temperature range, have also been collected for background subtraction.

The dissolution of $KHCO_3$ in aqueous solution leads to a slightly alkaline environment in a wide range of salt concentrations.[59] The formation of ${CO_3}^{2-}$ and $CO_2$(aq) according to the equilibria of eqs 1.5-1.7 occurs as well, and a spontaneous depletion of ${HCO_3}^{-}$ in the liquid phase, albeit minimal, is expected until the vapor pressure of $CO_2$ in the sealed reactor reaches the equilibrium partial pressure of $CO_2$(aq). Because of these phenomena, the analytical concentration of the $KHCO_3$(aq) standards has been corrected accounting for the presence of ${CO_3}^{2-}$ and $CO_2$(aq) in solution using the geochemical equilibrium software package EQ3/6 v. 8.0.[60] The extent of speciation of the ${HCO_3}^{-}$ ion has been found anyhow to be less than 5 % wt. Similarly, the speciation of ${CO_3}^{2-}$ in the standard samples of $K_2CO_3$(aq) has not been observed given the detection limit of the ATR-FTIR spectrometer.

Due to the acidic nature of $NH_4Cl$(aq) solutions, the speciation of the $NH_4^+$ into $NH_3$(aq) is virtually absent, thus facilitating the isolation of the characteristic $NH_4^+$ peak. Conversely, the alkaline environment of aqueous ammonia solutions inhibits the hydrolysis of $NH_3$(aq) into $NH_4^+$, thus allowing the extraction of the $NH_3$(aq) peak from the infrared spectrum.

The asymmetric C=O stretching band of the $CO_2$ located at 2343 $\text{cm}^{-1}$ in the infrared spectrum does not overlap with the spectrum of any other species in solution and has good analytical potential for the determination of the carbon dioxide concentration in water[61] (cf. Appendix A for further information). However the extent of $CO_2$(aq) formation has been found negligible in the range of operating conditions explored (cf. Section 2.4.6), and its concentration has been determined by using a mass balance on the liquid phase instead of developing a dedicated calibration model.

The formation of carbamate ions ($NH_2COO^-$) due to the reaction of eq 1.8 yields several characteristic peaks associated to this species located respectively at 1545 $\text{cm}^{-1}$, at $\sim$ 1400 $\text{cm}^{-1}$, and at 1120 $\text{cm}^{-1}$ in the infrared spectrum[43,44,54] (cf. Figure 2.2b). The segregation of these peaks is complicated by the pronounced overlap with the spectrum of the other species; the extent of speciation, in general, does not allow for a direct measurement of the actual concentration of the carbamate ion. In light of these considerations, two of the three characteristic peaks of the carbamate ion have been modeled, after subtraction of the spectrum of the solvent, using Gaussian functions such as:

$$a(\tilde{\nu}) = \exp\left[-\frac{(\tilde{\nu}-\mu)}{\sigma}\right]^2 \tag{2.3}$$

in which the location of each peak, $\mu$, has been set based on the available literature data[43,44] and its broadness, $\sigma$, has been chosen by appling an optimization procedure discussed in Section 2.4.6. In eq 2.3, $a$ is the infrared absorbance function of the wavenumber $\tilde{\nu}$, and the values of $\mu$ and $\sigma$ are respectively equal to 1545 $\text{cm}^{-1}$ and 1413 $\text{cm}^{-1}$, and 43.1

cm$^{-1}$ and 19.2 cm$^{-1}$ for the two modeled peaks of the carbamate ion. The carbamate band located at 1120 cm$^{-1}$, characterized by a much lower absorptivity compared to the other characteristic peaks,[43,44] has been neglected from the modeling procedure without significantly affecting the representation of the system.

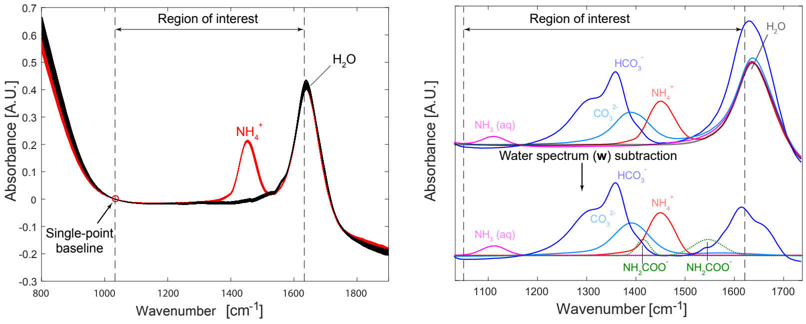

(a) (b)

FIGURE 2.2: Exemplary cases of the IR spectrum single-point baseline correction (a) and background subtraction (b) applied to all the IR spectra collected in this study (cf. Section 2.2.5). The examples refer to the IR spectrum of the $NH_4^+$ ion (red curves) and to the spectrum of $H_2O$ (black curves), respectively. The region of interest of the infrared spectrum of this study is indicated by dashed lines. (b) Examples of solvent (water) background subtraction from the measured spectrum of different ionic species in aqueous solution, i.e. $NH_3$(aq), $NH_4^+$, $HCO_3^-$, and $CO_3^{2-}$. Note that the characteristic bands of the $NH_2COO^-$ (green spectra) have been modeled, net of the spectrum of the solvent, as Gaussian functions using eq 2.3 (cf. Section 2.2.4 for further details).

### 2.2.5 *Preprocessing Techniques*

As illustrated in Figure 2.2a, the ATR-FTIR pre-processing technique for all the raw IR spectra collected consisted of a *single-point* baseline correction applied at 1033 cm$^{-1}$ of the spectrum (red circle), The technique has been developed in our laboratory and implemented in MATLAB. The use of this constant baseline correction is effective in removing the background signal of the solvent (water) that appears almost as an off-set over the range of wavenumbers of interest, i.e. $1033 - 1610\ \mathrm{cm}^{-1}$. Figure 2.2b shows how the IR spectrum of each pure component has been isolated from the background signal of the solvent by subtracting the baseline-corrected spectrum of water from the measured spectrum of the electrolytes in aqueous solution at the relevant temperature.

## 2.3 MODELING

### 2.3.1 *Model Equations*

From a mathematical point of view the infrared absorbance of a multicomponent liquid mixture of given composition is a continuous function $a(\tilde{\nu}, T)$ defined on the wavenumber, $\tilde{\nu}$, and temperature, $T$, domains. However, from a practical point of view, due to the instrument finite resolution, the measured spectrum can be described as a vector of data points recorded at $m$ discrete wavenumber values, i.e. $\mathbf{a}(\tilde{\boldsymbol{\nu}}, T) = [a(\tilde{\nu}_1, T), \ldots, a(\tilde{\nu}_\mathrm{m}, T)]^\mathrm{T}$, at a given temperature.

This work uses a multivariate Classical Least Squares method[57,62] to model the multicomponent spectrum of mixtures of $CO_2$, $NH_3$, and $H_2O$. It assumes the Beer-Lambert law (cf. Section 1.7.2) for each pure component to be valid and the effect of intermolecular interactions on the IR spectrum to be negligible.

Additionally, the method requires a calibration step that relates the spectra of a given set of standards to their known concentration.

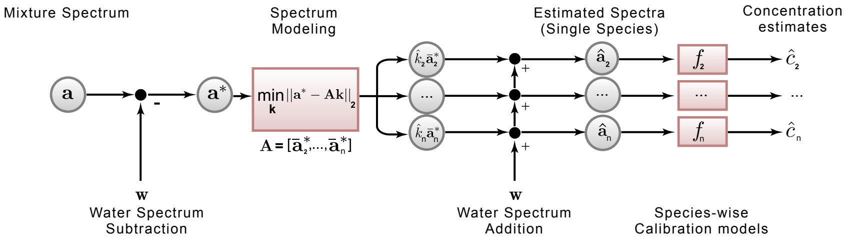

Figure 2.3: Graphical representation of the algorithm used to resolve overlapping ATR-FTIR bands of aqueous species in solution. The algorithm includes a modeling step of the spectrum of the mixture represented by a Classical Least Squares (CLS) method, and uses calibration functions (eq 2.9) for the computation of the concentration estimates.

### 2.3.2 *Classical Least Squares Method*

The linear model of an ATR-FTIR spectrum discretized over $m$ wavenumbers, the vector $\mathbf{a}$, which embeds $n$ overlapping components is, at a given temperature $T$:

$$\mathbf{a} = \mathbf{a}^* + \mathbf{w} = \sum_{i=2}^{n} k_i \bar{\mathbf{a}}_i^* + \mathbf{w} + \epsilon \tag{2.4}$$

where the index $i$ associated with the solvent (water) is 1; the vector $\mathbf{a}^*(T)$ is the spectrum of the mixture after subtracting the contribution of the solvent, i.e. the vector $\mathbf{w}(T)$; $k_i$ is the CLS weight parameter relative to the $i$-th component; the vector $\bar{\mathbf{a}}_i^*$ is the IR reference spectrum of the $i$-th component used by the CLS method; and the vector $\epsilon$ is the residual error of the model. The CLS reference spectra are defined as the spectra of the standards at the lowest concentration value of the calibration set reported in Table 2.2. Since $m \gg n$, the optimal set of parameters, $\hat{\mathbf{k}} = [\hat{k}_2, \ldots, \hat{k}_n]^\mathrm{T}$, that minimizes the residual error $\epsilon$ of eq 2.4 can be computed by solving the following optimization problem:

$$\underset{\mathbf{k}}{\text{minimize}} \; ||\mathbf{a}^* - \mathbf{A}\mathbf{k}||_2 \tag{2.5}$$

where the IR reference spectra of the pure components (solutes) used by the CLS method are collected column-wise into the matrix $\mathbf{A}$. The set of reference spectra also accounts for the temperature dependence of the spectrum of each species in solution:

$$\mathbf{A}(T) = [\bar{\mathbf{a}}_2^*(T), \ldots, \bar{\mathbf{a}}_n^*(T)] \tag{2.6}$$

Therefore, the vector estimator $\hat{\mathbf{k}}$ (with $[n-1]$ elements) of the unknown parameters is calculated as:[63]

$$\hat{\mathbf{k}} = (\mathbf{A}^{\mathrm{T}}\mathbf{A})^{-1}\mathbf{A}^{\mathrm{T}}\mathbf{a}^* \tag{2.7}$$

Then, the set of optimal parameters allows to estimate the spectrum of the mixture, $\hat{\mathbf{a}}$, as:

$$\hat{\mathbf{a}} = \mathbf{A}\hat{\mathbf{k}} + \mathbf{w} \tag{2.8}$$

Eventually, the concentration estimate of the $i$-th solute, $\hat{c}_i$, can be calculated using a calibration model $f_i$ that relates its estimated IR spectrum, the vector $\hat{\mathbf{a}}_i = \hat{k}_i\bar{\mathbf{a}}_i^* + \mathbf{w}$, to its concentration.

$$\hat{c}_i = f_i(\hat{\mathbf{a}}_i) \quad i = 2, \ldots, n \tag{2.9}$$

The CLS algorithm is illustrated in Figure 2.3, while the derivation of the calibration models is discussed, in detail, in Section 2.4.3.

## 2.4 RESULTS AND DISCUSSION

The following sections address important aspects related to the application of the CLS method to real mixtures containing $CO_2$, $NH_3$, and $H_2O$. At first, the validity of the Beer-Lambert law and the capability of the CLS model to resolve complex overlapping spectra are investigated. Then, different calibration approaches are compared in terms of accuracy and reliability of the concentration estimates. Against this background, the speciation of aqueous ammonia solutions of BC have been assessed, investigating, in particular, the effect of a stoichiometric excess of ammonia, on the equilibria established in solution. Additionally, the solid-liquid equilibrium of ammonium bicarbonate has been characterized and modeled, thus establishing a rigorous thermodynamic framework for the estimation of the solution supersaturation.

### 2.4.1 *Validity of the Beer-Lambert Law*

The validity of the Beer-Lambert law for the pure components, in the range of concentrations explored in this work, is a prerequisite for the application of the CLS method to the spectrum of a mixture of unknown composition. In this regard, Figure 2.4 shows the sets of normalized (and overlapping) spectra of the pure species in aqueous solution corresponding to the different concentrations used for calibration (cf. Table 2.2). The overlapping of spectra is indicative of systems for which the Beer-Lambert law applies, i.e. a linear relationship between the absorbance and the concentration. However, in this system deviations from the linear behavior can be noticed especially for the $NH_4^+$ and the $HCO_3^-$ ions. More in detail, Figure 2.4a shows a slight shift of the absorption bands of $NH_4^+$, while in Figure 2.4b a certain absorbance variability is noticeable in the proximity of the lower shoulder of the $HCO_3^-$ peak; deviations in the wavenumber range between 1350-1450 $cm^{-1}$ may be attributed to the concomitant presence of $CO_3^{2-}$ in solution, while no significant deviations could be reported in the case of $CO_3^{2-}$ and of $NH_3(aq)$.

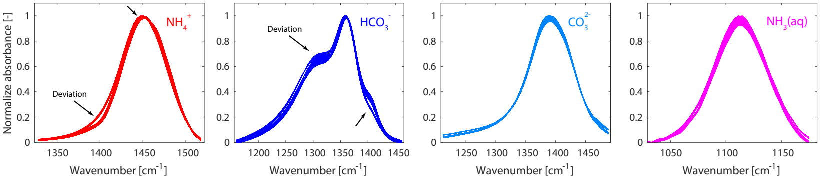

(a) (b) (c) (d)

Figure 2.4: Set of normalized and overlapped spectra of pure electrolyte species in aqueous solution in the concentration and temperature ranges investigated in this work (cf. Table 2.2). The main deviations are indicated by arrows. (a-d) IR spectra relative to the $NH_4^+$, $HCO_3^-$, $CO_3^{2-}$, and $NH_3(aq)$ species respectively.

### 2.4.2 *Effect of Temperature on Pure Solutes' Spectrum*

As described in Section 2.3, the proposed modeling approach accounts also for the temperature dependence of the spectrum of the unknown mixture, in order to improve the accuracy of the concentration estimates. To prove the relevance of this effect, Figure 2.5 shows a cursory analysis on the temperature behavior of the maximum peak height and position of the characteristic IR bands of the pure species. As a general trend, the maximum peak heights decrease linearly with increasing values of temperature, for all the species, at fixed concentration values. This phenomenon is probably due to the weakening of the H-bonds between water and solutes with increasing temperature;[48] it is distinct in the case of the $CO_3^{2-}$ spectrum, while the decreasing trend is negligible for the remaining species. The peak position of the $NH_4^+$ ion slightly shifts to lower values with increasing temperature as shown in Figure 2.5a.

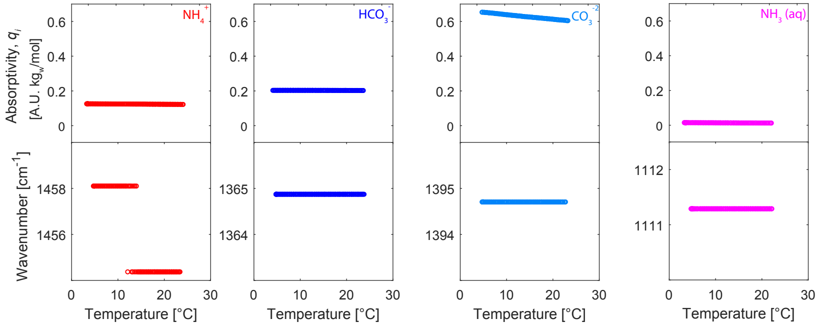

(a) (b) (c) (d)

FIGURE 2.5: Measured absorptivities and positions of the maximum IR peaks of the solutes as a function of temperature, at constant solute concentration. The analyses are relative to the IR bands corresponding to the minimum value of the standard concentrations of $NH_4Cl$(aq), $KHCO_3$(aq), $K_2CO_3$(aq), and $NH_3$(aq) reported in Table 2.2). The discontinuity in the maximum IR peak position of the $NH_4^+$ ion is due to the finite resolution of the IR spectrum recorded.

### 2.4.3 *ATR-FTIR Calibration Methods*

Several functional forms for the general calibration model presented in eq 2.9 have been suggested and analyzed in order to identify the most accurate method for the estimation of the solute concentrations. The screening carried out in this study considered calibration models based on the maximum absorbance peak height (model I), on the maximum absorbance peak area (model II), and on a partial least squares regression (PLSR) of spectral data (model III). The root mean squared error of prediction, RMSE, has been used to compare the performance of the different calibration models of each component as follows:

$$\mathrm{RMSE}_i = \sqrt{E[(\hat{\mathbf{c}}_i^\circ - \mathbf{c}_i^\circ)^2]} \quad i = 2, \ldots, n \tag{2.10}$$

where $E$ is the mean operator; $\hat{\mathbf{c}}_i^\circ$ and $\mathbf{c}_i^\circ$ are respectively the vector of concentration estimates of the standards of the $i$-th component, and the vector of the relative standard concentrations.

Before discussing the details of each method, it is useful to introduce the operator $S$ that extracts the specific features of a generic IR spectrum, $\mathbf{s}$, used by the different calibration methods:

$$S(\mathbf{s}, T) = \begin{cases} \max \mathbf{s}(T) & \text{Peak Height Method} \\ \sum\limits_{j=a}^{b} s(\tilde{\nu}_j, T)\Delta\tilde{\nu} & \text{Peak Area Method} \\ [s(\tilde{\nu}_a, T), \ldots, s(\tilde{\nu}_b, T)]^\mathrm{T} & \text{PLSR Method} \end{cases} \tag{2.11}$$

where $s(\tilde{\nu}_j, T)$ is the absorbance at a specific wavenumber $\tilde{\nu}_j$ and temperature $T$; $\Delta\tilde{\nu}$ is the fixed interval between two discretized wavenumbers; and $[a, b]$ is a generic range of wavenumbers. Details on the maximum peak positions and wavenumber ranges adopted for each component are reported in Table 2.3.

#### *ATR-FTIR Calibration Methods Based on Peak Properties*

For each pure component, a set of $(N_i \cdot M)$ reference spectra of the pure electrolytes has been used for the regression of a linear calibration model based on two independent variables: either the maximum peak height or the maximum peak area, and the temperature (cf. Figure 2.6). We name such reference spectra $\mathbf{a}^{\circ}_{i,n,m'}$, where $n = 1, \ldots, N_i$ and $m' = 1, \ldots, M$ are the reference concentration and the reference temperature indices, respectively. The estimate of the model parameters vector, $\hat{\mathbf{p}}_i$, is obtained by solving the multiple linear regression (MLR) problem defined by:

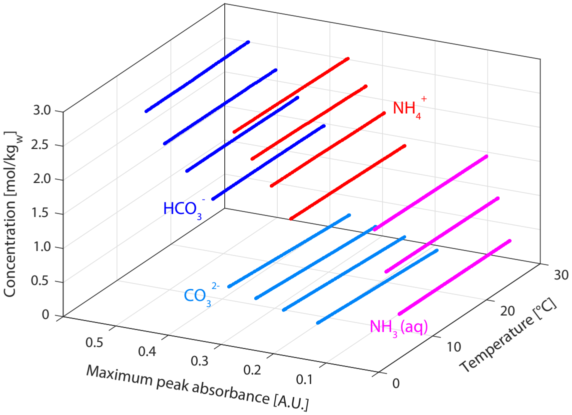

FIGURE 2.6: ATR-FTIR calibrations based on the maximum peak height and temperature for the concentration estimate of the $HCO_3{}^-$, $CO_3{}^{2-}$, $NH_4{}^+$, and $NH_3$(aq) respectively.

$$\underset{\mathbf{p}_i}{\text{minimize}} \ ||\mathbf{c}^{\circ}_i - \mathbf{X}_i \mathbf{p}_i||_2 \quad i = 2, \ldots, n \tag{2.12}$$

where the vector $\mathbf{p}_i = [p_{0,i}, p_{1,i}, p_{2,i}]^{\mathrm{T}}$ is the parameters vector, the matrix $\mathbf{X}_i$ contains a first column vector of ones to account for the intercept term $p_{0,i}$, a second column vector that stores the features of the reference spectra extracted by the operator $S$ according to the calibration method considered ($[S(\mathbf{a}^{\circ}_{i,1,1}, T_{i,1,1}), \ldots, S(\mathbf{a}^{\circ}_{i,N_i,M}, T_{i,N_i,M})]^{\mathrm{T}}$), and a third column vector of measured temperatures, $\mathbf{T}_i$. For the sake of completeness, the sets of optimal parameters are reported in Appendix A.

The good quality of the fitting is confirmed by the values of the coefficient of determination, $R^2$ (cf. Table 2.3). This is also indicative of the validity of the Beer-Lambert law in the range of operating conditions explored in this work.
Ultimately, the regressed models can be used to estimate the concentration of the $i$-th component as:

$$\hat{c}_i = \hat{p}_{0,i} + \hat{p}_{1,i} S(\hat{\mathbf{a}}_i, T) + \hat{p}_{2,i} T \quad i = 2, \ldots, n \tag{2.13}$$

*ATR-FTIR Calibration Based on PLS Analysis*

Contrary to the univariate calibration methods that correlate the solute concentration to specific peak heights or peak areas, a multivariate PLS model exploits a range of absorption bands characteristic of the solute to estimate its concentration. In this regard, the operator $S$ applied to a generic reference spectrum $\mathbf{a}^{\circ}_{i,n,m}$, yields a (row) vector of $k$ elements that represent the spectral absorbances in the range of wavenumbers considered (cf. Table 2.3). The matrix $\mathbf{S}_i = [S(\mathbf{a}^{\circ}_{i,1,1}, T_{i,1,1})^{\mathrm{T}}, \ldots, S(\mathbf{a}^{\circ}_{i,N_i,M}, T_{i,N_i,M})^{\mathrm{T}}]^{\mathrm{T}}$ that contains the processed reference spectra of the $i$-th component is projected onto a score matrix $\mathbf{K}_i$ (eq 2.14) by using a matrix of weights, $\mathbf{W}_i$, computed in such a way that the covariance between the colum vectors $\mathbf{k}_{i,j}$ ($j$-th column of $\mathbf{K}_i$) and the vector of reference concentrations $\mathbf{c}^{\circ}_i$ is maximized:[45]

$$\mathbf{K}_i = \mathbf{S}_i \mathbf{W}_i \tag{2.14}$$

The method allows to reduce the collinearity of the raw spectral data and leads to a score matrix $\mathbf{K}_i$ that contains a set of linearly independent combinations of the original $k$ wavenumbers that still carry the relevant information about the spectra. Similarly to eq 2.12, the PLS regressor vector $\mathbf{b}_i$ is estimated by solving the following minimization problem:

$$\underset{\mathbf{b}_i}{\text{minimize}} \; ||\mathbf{c}^{\circ}_i - \mathbf{K}_i \mathbf{b}_i||_2 \quad i = 2, \ldots, n \tag{2.15}$$

for which the least-square estimator of $\mathbf{b}_i$ is:

$$\hat{\mathbf{b}}_i = (\mathbf{K}_i^{\mathrm{T}} \mathbf{K}_i)^{-1} \mathbf{K}_i^{\mathrm{T}} \mathbf{c}^{\circ}_i \tag{2.16}$$

Finally, the PLSR model can be used to estimate the concentration of the $i$-th component as:

$$\hat{c}_i = S(\hat{\mathbf{a}}_i, T)^{\mathrm{T}} \mathbf{W}_i \hat{\mathbf{b}}_i \tag{2.17}$$

The optimal number of linearly independent combinations of the original $k$ wavenumbers (latent variables of the PLS model), $r$, has been chosen so as the root mean squared error of 10-fold cross-validation, $\mathrm{RMSECV}_{10}$, of the PLS model is minimized[45] (cf. Table 2.3).

*Comparison of the ATR-FTIR Calibration Methods*

Figure 2.7 shows the comparison of the different calibration models in terms of RMSE. As expected, the most accurate and robust concentration estimates are those based on a multivariate PLS regression that has the ability of weighing absorbances that are highly predictive of the concentration of the different species.[46] Among the PLSR models, the least accurate ones are those for the concentration prediction of the $HCO_3^-$ and the $NH_4^+$ ions. In fact, the ATR-FTIR bands of these species, as discussed in Section 2.4.1, exhibit the largest deviations from linearity over the range of wavenumbers considered for the calibration.
In light of these considerations, this work adopts a set of multivariate PLS calibration models $f_i$ (eq 2.9) to estimate solute concentrations, unless explicitly stated otherwise.

### 2.4.4 *Model Validation*

First, the predictive capability of the proposed CLS methodology has been assessed for the case of binary mixtures of known composition, namely $NH_4Cl$(aq) and $KHCO_3$(aq). In detail, the validation exploits a set of *in silico* generated IR spectra of $NH_4Cl$(aq) and $KHCO_3$(aq) obtained by combining the spectra of the pure standards, as well as a set of real spectra of aqueous mixtures of $NH_4Cl$(aq) and $KHCO_3$(aq), and of aqueous solutions of $NH_4HCO_3$ (BC). For the real mixtures $^{13}$C-NMR spectroscopic analyses[64,65] (reported in Appendix A) have been used to select the solutions that exhibit a low degree of speciation (e.g.

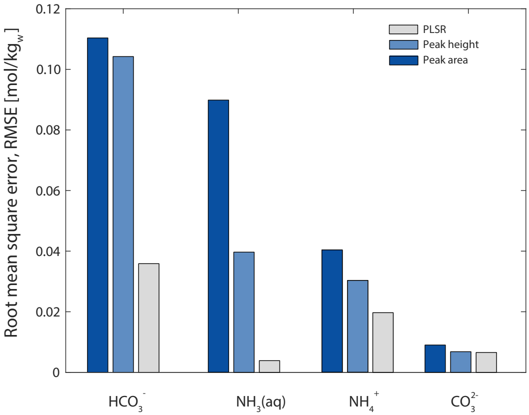

Figure 2.7: Comparison of the root mean square errors (RMSEs) of prediction of the concentration of solutes obtained using the different ATR-FTIR calibration methods discussed in Section 2.4.3.

absence of carbamate ion formation) to be included in the validation set. Then, the spectral data, both the simulated and experimental, has been processed using the CLS method proposed in Section 2.3, and the resulting concentration estimates have been compared with the reference values. Figure 2.9 shows that the absolute error of prediction for the $NH_4^+$ and $HCO_3^-$ ions in virtual binary mixtures (red and blue dots, respectively) is below 5 %. Similar results are obtained for real mixtures of $NH_4Cl$(aq) and $KHCO_3$(aq) indicated by stars, and for aqueous solutions of BC indicated by triangles. The underprediction of the $HCO_3^-$ concentrations for the case of real mixtures may be attributed to the formation of $CO_2$(aq) and $CO_3^{2-}$ in solution.

An analysis on the accuracy of the concentration estimates for the case of mixtures of $CO_2$, $NH_3$, and $H_2O$ characterized by the formation of more than 2 main species cannot be directly performed due to the lack of information on the actual concentration of the species in solution. However, meaningful insights can be provided about the robustness of the CLS algorithm and on its capability of resolving the spectrum

| **Species** | **Method** | **Wavenumber** [$\mathrm{cm^{-1}}$] | $r$ [-] | **RMSE** [$\mathrm{mol/kg_w}$] | $R^2$ [-] |
|---|---|---|---|---|---|
| $NH_4^+$ | Peak Area | $1324 \leq \tilde{\nu} \leq 1522$ | n/a | 0.0404 | 0.9985 |
| | Maximum Peak Height | $\tilde{\nu} = 1458$ | n/a | 0.030 | 0.9918 |
| | PLSR | $1324 \leq \tilde{\nu} \leq 1522$ | 2 | 0.0207 | n/a |
| $HCO_3^-$ | Peak Area | $1156 \leq \tilde{\nu} \leq 1466$ | n/a | 0.1104 | 0.9990 |
| | Maximum Peak Height | $\tilde{\nu} = 1365$ | n/a | 0.1042 | 0.9937 |
| | PLSR | $1156 \leq \tilde{\nu} \leq 1466$ | 5 | 0.0317 | n/a |
| $CO_3^{2-}$ | Peak Area | $1208 \leq \tilde{\nu} \leq 1492$ | n/a | 0.0090 | 0.9974 |
| | Maximum Peak Height | $\tilde{\nu} = 1395$ | n/a | 0.0068 | 0.9943 |
| | PLSR | $1208 \leq \tilde{\nu} \leq 1492$ | 3 | 0.0060 | n/a |
| $NH_3$ | Peak Area | $1033 \leq \tilde{\nu} \leq 1178$ | n/a | 0.0898 | 0.9988 |
| | Maximum Peak Height | $\tilde{\nu} = 1111$ | n/a | 0.0397 | 0.9976 |
| | PLSR | $1033 \leq \tilde{\nu} \leq 1178$ | 6 | 0.0022 | n/a |
| **BC** (aq) | PLSR | $980 \leq \tilde{\nu} \leq 1036$ | 7 | $7.97 \cdot 10^{-5}$(*) | 0.9999 |
| **BC** ($m^{\circ}_{NH_3} = 1.2$ m) | PLSR | $980 \leq \tilde{\nu} \leq 1036$ | 10 | 0.0070(*) | 0.9982 |
| **BC** ($m^{\circ}_{NH_3} = 1.8$ m) | PLSR | $980 \leq \tilde{\nu} \leq 1036$ | 10 | 0.0062(*) | 0.9978 |

Table 2.3: Statistics of the different calibration models for the concentration estimates of species in solution. An asterisk (*) denotes that the value refers to a 10-fold cross validation RMSE for the BC concentration.[45]

of mixtures containing more than 2 overlapping components. In this regard, fictitious quaternary spectra containing the overlapping peaks of $NH_4^+$, $HCO_3^-$, $CO_3^{2-}$, and $NH_3$(aq) have been simulated by combining the experimental spectral data of the pure standards. Then, the CLS methodology has been applied to the *in silico* generated spectral data.

Based on the outcome of the model, provided in the parity plots of Figure 2.9, the CLS algorithm is capable of resolving effectively overlap-

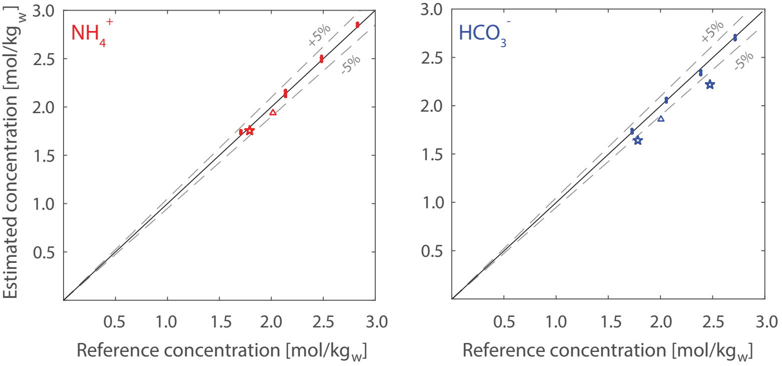

(a) (b)

FIGURE 2.8: Parity plots of the reference vs. estimated solute concentrations in the temperature range 6-23 °C. (a) Concentration estimates of the $NH_4^+$ ion, (b) Concentration estimates of the $HCO_3^-$ ion. Dots (•) refer to the *in silico* generated solutions, triangles (△) refer to the aqueous solution of BC (2 mol/kg$_W$), stars (⋆) refer to the real mixtures of binary salts, i.e. $NH_4Cl$ and $KHCO_3$, at the concentrations of 1.75 mol$_{NH_4Cl}$/kg$_W$ and 1.75 mol$_{KHCO_3}$/kg$_W$, and of 1.75 mol$_{NH_4Cl}$/kg$_W$and 2.50 mol$_{KHCO_3}$/kg$_W$, respectively.

ping bands in the IR spectrum of the mixture with a maximum error in the concentration estimates of ±10 %. These errors stem primarily from the difference that exists between the set of reference spectra $\bar{\mathbf{a}}$ used by the algorithm and the fitted spectra of the standards, $\mathbf{a}^\circ$. Based on the choice of reference spectra, the quality of the estimates may also decrease for mixtures whose species' concentrations significantly differ from those selected as a reference in the CLS method.

The highest absolute error related to the prediction of the $NH_3$(aq) concentration can be justified by the low signal-to-noise ratio that characterizes the peak of this species (cf. Figure 2.6) and that therefore renders its concentration estimates less accurate compared to that of the other components.

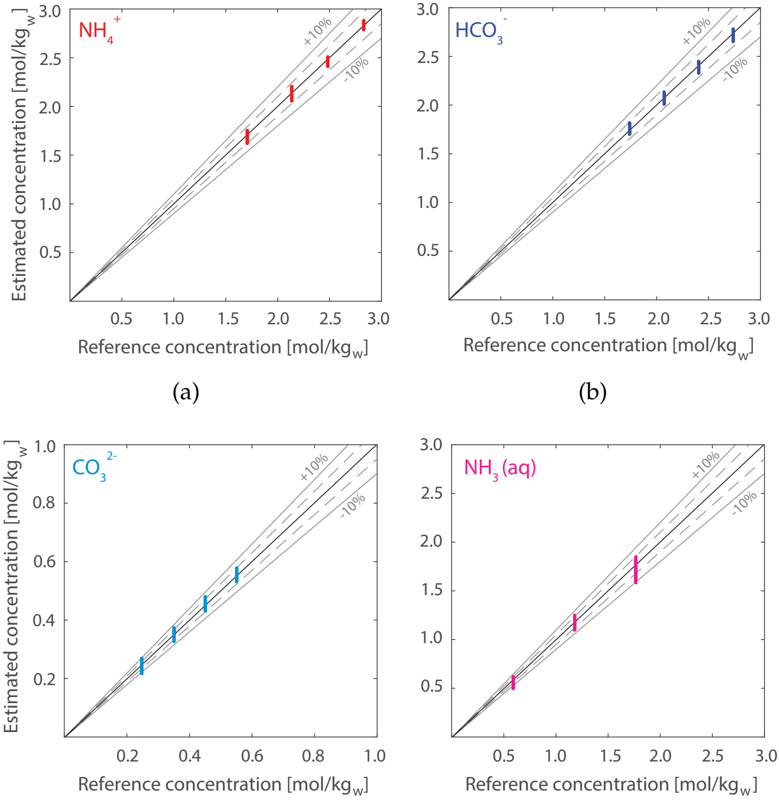

(a) (b)

(c) (d)

FIGURE 2.9: Parity plots of the reference vs. estimated concentrations for multicomponent virtual mixtures: (a-d) concentration estimates of the $NH_4^+$, $HCO_3^-$, $CO_3^{2-}$, and $NH_3$(aq) species, respectively.

### 2.4.5 *Concentration Estimation*

In aqueous ammonia solutions of ammonium bicarbonate (i.e. solutions whose representative point is on a isopleth line with $\zeta \geq 1$ in Figure 2.1)

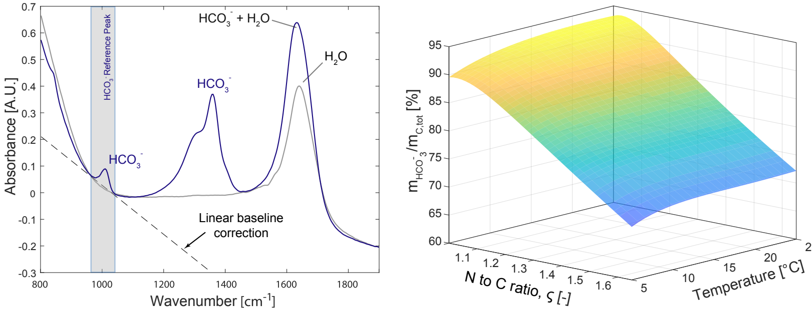

(a) (b)

Figure 2.10: (a) IR reference peak of the $HCO_3^-$ ion (blue spectrum) used for the estimation of the overall ammonium bicarbonate concentration in aqueous ammonia solutions. The peak has good analytical potential for the estimation of the $HCO_3^-$ ion concentration in solution. The spectrum of the solvent (gray spectrum) is reported for reference. (b) Percent distribution of the $HCO_3^-$ species as a function of temperature and total nitrogen to carbon ratio $\zeta$ at a fixed total carbon concentration ($2\,\text{mol/kg}_\text{w}$) in solution. Calculations have been performed using the thermodynamic model proposed by Darde et al.[30]

the distribution of carbon species changes significantly according to the overall nitrogen to carbon ratio of the system.[64] This phenomenon leads to spectral data that cannot be easily correlated to the overall BC concentration in the liquid phase, $m_{\text{BC}}^{(\text{l})}$, using a single PLS calibration model. Such challenge has therefore been overcome by building dedicated PLS calibrations for different nominal ammonia concentration $m_{\text{NH}_3}^{\circ}$ in the solvent (i.e. different values of $\zeta$). These models implictly account for the liquid speciation and correlate the overall BC concentration to the baseline corrected C$-$OH stretching band of the $HCO_3^-$ ion located at $1005\ \text{cm}^{-1}$ in the infrared spectrum[61] (cf. Figure 2.10a). In fact, this peak overlaps with the solvent band only, thus minimizing the interference with any other ionic species in solution. As shown in

Figure 2.10b, the ratio between the concentration of the $HCO_3^-$ ion and of the total carbon species steadily decreases with increasing overall nitrogen content, thus reducing accordigly the intensity of the $HCO_3^-$ peak. Nevertheless, the method can potentially be used to estimate reliably the BC concentration in a wide range of nominal ammonia concentrations in the solvent. It must be acknowledged that the proposed calibration models are inherently dependent on the solvent composition, the information on the nominal ammonia concentration in the solvent must be known in order to properly exploit the model.

In this work, a total of three PLS regression models have been computed at values of nominal ammonia concentration in the solvent equal to 0, 2, and 3 % wt, respectively. The training sets of the PLS calibrations are represented by the spectra of BC in aqueous ammonia solutions in a temperature range that covers both the undersaturated and the supersaturated conditions (cf. Tables 2.2 and 2.3). The models have been regressed including the information of the spectra of pure water, as well as the dependence of the IR spectra on temperature. During each experiment, a known amount of ammonium bicarbonate has been dissolved in the solution and spectral acquisition has been started shortly after reaching equilibrium. Then, a cooling rate of 10 $^\circ\mathrm{C\,h^{-1}}$ has been applied to the system, while measuring ATR-FTIR spectra every minute. The onset of primary nucleation has been monitored using FBRM measurements so that spectra measured after nucleation could be rejected from the training set of the PLSR models. For the sake of completeness the whole training data set is reported in Appendix A.

The prediction capability of the ATR-FTIR calibration models has been assessed using independent BC solubility measurements. A first type of experiment consists in heating saturated aqueous ammonia solutions in presence of suspended BC at a rate of $2^\circ\mathrm{C\,h^{-1}}$ while collecting spectral data. A second type of experiment is based on the measurement of the temperature at which the solid phase disappears.[50] In this case, the FBRM signal has been used to detect complete dissolution of particles while slowly heating the suspension at a rate of $1^\circ\mathrm{C\,h^{-1}}$.

Figure 2.11a shows the ATR-FTIR-based solubility measurements (circles) carried out at a nominal ammonia content in the solvent equal to 0 % wt, 2 % wt, and 3 % wt (indicated with a colorcode), while the measurements based on the temperature at which the solid phase disappears are shown as filled dots. The effect of an ammonia enrichment of the solution results in a remarkable increase of the ammonium bicarbonate solubility.

The good agreement of the solubility measurements obtained with independent methods supports the applicability of the ATR-FTIR calibration for the estimation of the overall BC concentration in solution. Figure 2.11b provides a different representation of the BC solubility data in the $CO_2-NH_3-H_2O$ ternary diagram as function of temperature and gives an indication of the operating region investigated experimentally.

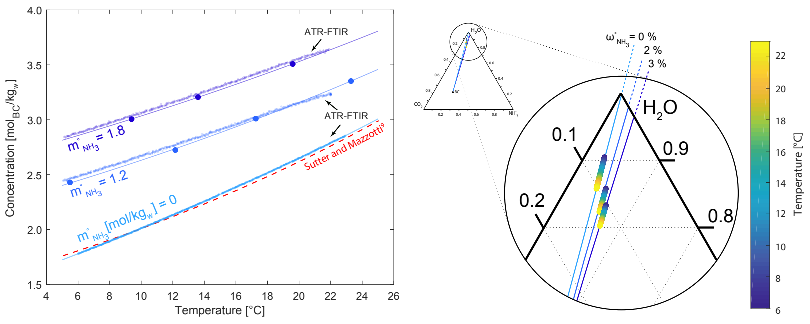

(a)　(b)

FIGURE 2.11: Ammonium bicarbonate solubility in aqueous ammonia solutions as a function of temperature and nominal ammonia concentration in the solvent, $m^{\circ}_{NH_3}$, (cf. blue colorcode). The solubility is based on a pure water mass basis. (a) ATR-FTIR-based solubility measurements (cf. arrows) and FBRM measurements of complete solid disappearance (filled dots). Solid curves are the interpolated solubility data, while the dotted red curve refers to the BC solubility in aqueous solution of Sutter and Mazzotti[37] (b) Representation of the BC solubility data of Figure 2.11a in the ternary diagram for the $CO_2-NH_3-H_2O$ system as a function of temperature. The blue lines are the operating lines that connect the composition of ammonium bicarbonate (BC) to aqueous ammonia solutions at different nominal ammonia concentration (cf. dashed lines).

### 2.4.6 *Solution Speciation*

The speciation of saturated aqueous ammonia solutions of ammonium bicarbonate has been measured by applying the proposed CLS methodology for a nominal ammonia concentration in the solvent in the range $0-3\,\%$ wt. For these mixtures the ratio between nitrogen to carbon species roughly spans values from 1 to 1.5.

Systems in which the $\zeta$ ratio is less than unity (cf. Figure 2.1) are characterized by a higher $CO_2$(aq) concentration in the liquid phase (compared to systems in which $\zeta$ is greater or equal to one) that leads to an increase of the value of $CO_2$ partial pressure. The investigation of such systems, not addressed in this work, is therefore limited by the maximum pressure of the vessel.

#### *Model Implementation*

Prior to the application of the CLS method to aqueous ammonia solutions of ammonium bicarbonate, the optimal set of adjustable parameters used to describe the IR bands of the carbamate ion (for which no prior knowledge is currently available from literature, cf. Section 2.2.4) has been estimated by solving the following minimization problem:

$$\underset{\sigma}{\text{minimize}} \sum_{i}^{N_s} ||\epsilon_i||_2 \tag{2.18}$$

where $\sigma$ is the vector of the broadnesses of the modeled carbamate bands, and $N_s$ is the total number of measured spectra of the aqueous ammonia solutions of BC investigated. Then, the vector of optimal broadnesses $\hat{\sigma}$ has been integrated in the CLS model and used for the concentration estimates of the relevant species in solution.

In principle, the proposed CLS methodology can be applied to any aqueous solution containing unknown amounts of $CO_2$ and $NH_3$ as long as the validity of the Beer-Lambert law is preserved for each component's spectrum and the interactions among the individual spectra are negligible. In practice, the CLS approach is not applicable in a fully predictive mode since the overall nitrogen and carbon concentrations in solution are unknown.

In the specific case of aqueous ammonia solutions of ammonium bicarbonate the total carbon concentration, $m_{\mathrm{C,OL}}$ has been estimated from ATR-FTIR measurements exploiting the calibration method discussed in Section 2.4.5, whereas the total nitrogen concentration $m_{\mathrm{N,OL}}$ has been computed using the information on the nominal ammonia concentration in the solvent, which is assumed to be known. Then, the overall carbon and nitrogen concentrations have been used together with the concentration estimates of the ammonium and bicarbonate ions, $\hat{c}_{\mathrm{NH_4}^+}$ and $\hat{c}_{\mathrm{HCO_3}^-}$, (retrieved by applying the CSL methodology proposed in Section 2.3 to the spectrum of the unknown mixture) to solve the charge and mass balances in the liquid phase, eq 1.14 and eqs 1.15a-b, thus retrieving the concentration of the unknown species. Although the solution of the latter system of equations allows to obtain the complete speciation of the system, the values of the remaining degrees of freedom have been specified by introducing the following simplifications. For the case of aqueous solutions of BC the presence of $NH_3$(aq) has been neglected due to mild alkalinity of the system[59,66] (cf. Figure 2.1). Analogously, for the case of aqueous ammonia solutions of BC the contribution of the $CO_2$(aq) has been neglected in the material balance due to the basicity of these mixtures. Finally, the presence of $H^+$ and $OH^-$ ions has been omitted in the charge balance due to their low concentration in solution, typically in the order of $10^{-7}$ mol/kg$_{\mathrm{w}}$.

Note that the choice of using the ammonium and bicarbonate concentration estimates as an input for the material and charge balances stems from the fact that the CLS concentration estimates of these species are the most reliable ones due the spectroscopic properties of their characteristic IR peaks, i.e. the high absorptivity and the high signal-to-noise ratio in the region of wavenumbers of interest.

An alternative method to estimate the concentration of the bicarbonate ion relies on a PLS calibration based on the $HCO_3^-$ peak located at 1005 cm$^{-1}$ that, compared to the CLS methodology, does not require any intermediate modeling step of the spectrum of the mixture. Nevertheless, the estimation of the $NH_4^+$ ion concentration, due to the high degree of overlap of the IR peak of this species with the spectra of the other solutes in solution, requires a modeling step of the spectrum of the unknown mixture.

*Speciation of Aqueous Solutions of Ammonium Bicarbonate*

As shown in Figure 2.12, the spectral data of *saturated* aqueous ammonia solutions of BC (blue curves) is fitted consistently (red curves) in the entire range of operating conditions investigated. This is indicative of the absence of relevant interactions among the spectrum of the pure components and confirms the applicability of the proposed CLS method. The corresponding species concentrations have been estimated in the temperature range 6-23 °C and compared to the predictions of the thermodynamic models proposed by Thomsen and Rasmussen[28] and Darde et al.,[30] respectively. Such mixtures have been obtained by slowly heating ($0.5\,°\mathrm{C\,h^{-1}}$) aqueous ammonia suspensions of BC in the temperature range investigated.
Aqueous solutions of BC are equimolar mixtures of $CO_2$ and $NH_3$ whose overall composition in the ternary diagram of Figure 2.1 and Figure 2.11b lies on the operating line that connects the composition of the BC salt to the vertex of pure water (0 % wt ammonia in the solvent or $\zeta = 1$). The measured speciation, indicated as dots in Figure 2.13, reveals that the dominant species present in solution are the ${NH_4}^+$ and ${HCO_3}^-$ ions, thus confirming the *congruent* solubility of ammonium bicarbonate in aqueous solution reported by Jänecke[26] The ratio $\hat{c}_{{HCO_3}^-}/\hat{c}_{{NH_4}^+}$ is 0.95 at 6 °C; it decreases for increasing values of temperature reaching a value of 0.92 at 23 °C due to the concomitant increment of the concentration of $CO_2$(aq) and $NH_2COO^-$ whose presence slightly shifts the carbon and nitrogen distributions towards these species. Evidence of dissolved $CO_2$ is confirmed by the presence of a marked antisymmetric stretching fundamental peak of $CO_2$(aq) located at 2343 $\mathrm{cm^{-1}}$ in the infrared spectrum (the interested reader is referred to Appendix A for further details). Finally, the trend followed by the estimated speciation is in agreement with the predictions of the thermodynamic models (indicated as dashed lines) in both qualitative and quantitative ways. Note that the concentrations of the $NH_3$(aq) and

the $CO_3^{2-}$ ion have not been represented due to their negligible level in all these cases.

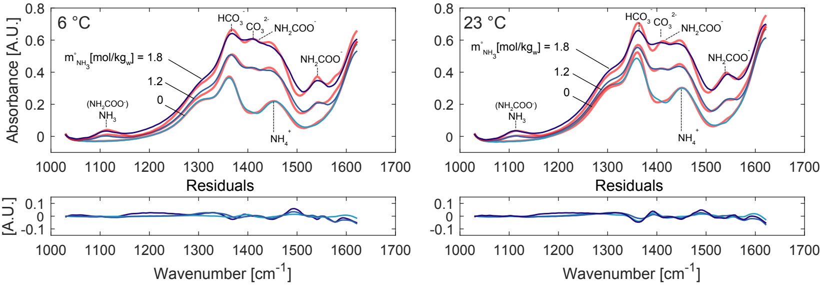

(a)

(b)

Figure 2.12: Quality of fitting of the ATR-FTIR spectra of saturated aqueous ammonia solutions of BC at different temperatures. The range of ammonia concentration in the solvent varies between 0-1.8 mol/kg$_W$. The red curves are the spectra resulting from the CLS fitting, while the blue curves are the experimental spectra of the mixtures (the colorcode refers to the nominal ammonia concentration of the solvent). (a) Fitting at 6 °C, (b) fitting at 23 °C. The plots underneath the fitted spectra show the residuals between the best fit and the experimental data.

### *Speciation of Aqueous Ammonia Solutions of Ammonium Bicarbonate*

In aqueous ammonia solutions of BC the shift of the carbon species distribution towards $CO_3^{2-}$ and $NH_2COO^-$ is due to the presence of a stoichiometric excess of ammonia. Due to the kinetically controlled reaction of carbamate formation (eq 1.8), these mixtures require longer equilibration times when compared to equimolar aqueous solutions of $CO_2$ and $NH_3$;[64,67] this aspect must be taken into account while performing experiments not to underestimate the equilibrium carbamate concentration.

Figure 2.13 shows (moving from left to right) how the carbon distribution in *saturated* aqueous ammonia solutions of BC changes from essentially bicarbonate only to an equilibrium mixture of bicarbonate, carbonate and carbamate ions[43,44,64] as the concentration of non-stoichiometric ammonia increases. The concentration estimates of the different species (indicated as dots) are relative to a nominal ammonia concentration in the solvent of 1.2 mol/$kg_w$ and 1.8 mol/$kg_w$ respectively, in the temperature range 6−23 °C. Note that in these two cases, the experimental values of the $NH_4{}^+$ concentration exceed slightly the range of concentrations used to build the model calibration for this species. However, literature data confirm the validity of the Beer-Lambert law for this species up to 5 mol/$kg_w$.[43,44]

Compared to the case of a pure aqueous solutions of BC ($m^\circ_{NH_3} = 0$ mol/$kg_w$), the presence of additional species such as $CO_3{}^{2-}$, $NH_2COO^-$, and $NH_3$(aq) can also be noticed by analyzing the IR spectra shown in Figure 2.12. The carbonate ion peak appears as highly convoluted, while the appearance of a visible carbamate peak (located at 1545 $cm^{-1}$), which is pronounced even at low concentrations, indicates a high absorptivity of this band.[44] Aqueous ammonia is present at a much lower concentration compared to its nominal value in the solvent, thus indicating that speciation into $NH_4{}^+$ and $NH_2COO^-$ occurred. Despite the low absorptivity of the aqueous ammonia band (cf. Figure 2.5) and its overlap with one of the weakest $NH_2COO^-$ peaks, the discrepancy between the reconciled concentration of aqueous ammonia and its CLS estimate has been found to be between ±5%. For the case of $CO_3{}^{2-}$ the difference lies between ±15%.

In general, both thermodynamic models from the literature describe the experimental trends quite well with the best quantitative agreement offered by the Thomsen model. Instead, Darde model slightly overestimates the carbamate concentration in the entire range of experimental conditions investigated, thus leading to a different distribution of the remaining nitrogen and carbon species in solution.

### 2.4.7 *Solid-Liquid Equilibrium of Ammonium Bicarbonate*

The speciation process occurring in the $CO_2-NH_3-H_2O$ system affects the several solid-liquid equilibria that can be established at the relevant conditions of temperature, pressure and composition of the system. In this study, the most stable solid that could form is ammonium bicarbonate.[26,27,40] As stated in Section 1.4, the strong non-ideality of the liquid phase requires an activity-based approach for the description of all the phase equilibria.

Figure 2.14 shows a comparison between the experimental solubility of ammonium bicarbonate[40] at 20 °C (black boxes and circles) and those computed using the Thomsen model (green curve), the Darde model (blue curve), and a re-fitted version of the Thomsen model (red curve) built in this work and discussed in the following. The solid-liquid envelopes of the $CO_2-NH_3-H_2O$ system have been obtained by performing solid-liquid flash calculations using the abovementioned models (cf. Appendix A for further details).

As it can be noted in Figure 2.14, both Thomsen and Darde models slightly underpredict the measured ammonium bicarbonate solubility (cf. magnification of the ternary diagram region). Such local inaccuracies, although negligible in the context of overall process simulations,[25,68] must be minimized for the monitoring and the kinetic investigation of BC crystallization processes for which an accurate computation of the supersaturation is required. To achieve this, we performed a re-estimation of the parameters of the Thomsen model (that provides the best representation of the speciation data measured in this work) with the aim of increasing the accuracy of the description of the solid-liquid equilibrium of BC in aqueous ammonia solutions. In detail, a subset of extended-UNIQUAC interaction parameters, represented by the matrices $\mathbf{u}^0$ and $\mathbf{u}^T$ of the Thomsen model reported in Table 2.4 and Table 2.5, has been optimized while keeping unaltered the remaining parameters and thermodynamic properties of the model.

Experimental data of aqueous ammonia solutions of BC at *saturated* conditions have been used in the following optimization problem:

$$
\begin{aligned}
\underset{\mathbf{u}^0,\mathbf{u}^\mathrm{T}}{\text{minimize}} \sum_{j=1}^{N_\mathrm{e}} \sum_{i=2}^{n-1} \sum_{k=1}^{N_\mathrm{obv}} \left( \frac{c^\mathrm{calc} - c^{*,\mathrm{exp}}}{c^{*,\mathrm{exp}}} \Big|_{j,i,k} \right)^2 + \\
+ \sum_{j=1}^{N_\mathrm{e}} \sum_{k=1}^{N_\mathrm{obv}} \left[ \ln \frac{K_\mathrm{IP}(T,\mathbf{c}^*)}{K_\mathrm{SP}(T)} \Big|_{j,k} \right]^2
\end{aligned}
\qquad (2.19)
$$

where $c_i^\mathrm{calc}$ and $c_i^\mathrm{exp}$ are the model predictions of the concentration of the $i$-th species and the one measured, respectively. The vector $\mathbf{c}$ indicates the composition of the system. The variables $n$, $N_\mathrm{e}$, and $N_\mathrm{obv}$ are the number of species, the number of experimental conditions investigated (i.e. the different nominal concentrations of ammonia in the solvent), and the number of observations of each species at the relevant experimental conditions, respectively. The data set to be fitted consisted of 13 concentration data points ($N_\mathrm{obv}$) for each species collected in the temperature range 6−20 °C at three different nominal ammonia concentration in the solvent, i.e. 0, 2, and 3 % wt.

The first term of the objective function in eq 2.19 accounts for the speciation data to be regressed, while the second term is used to impose the values of the BC solubility product to be fitted during the optimization. The speciation has been computed by solving the liquid speciation equilibria (eqs 1.4-1.8) while neglecting all the solid-liquid equilibria (eqs 1.9-1.12). The unconstrained optimization has been performed using the optimizer *fmincon* in the Matlab Optimization Toolbox[69] with an initial guess provided by the extended-UNIQUAC parameter set of the Thomsen model.

As shown in Figure 2.15, the optimal set of regressed parameters allowed for a good fitting of the experimental speciation data as well as of the solubility product of BC in the entire range of operating conditions investigated.

It is worth noting that since the optimization procedure does not include any solubility data of the additional solids that might form, the re-fitted Thomsen model proposed in this work is unable to describe accurately the solubilities of the different salts outside the ammonium bicarbonate region. Although being able to capture the experimental BC solubility[40] (black boxes and circles) significantly well (cf. Figure 2.14), it progressively underestimates the salts' solubilities as the equivalent ammonia content in the system increases. Not surprisingly, Darde model, by being fitted on a much larger set of experimental data,[30] is capable of describing effectively the entire set of solid-liquid equilibria.

## 2.5 CONCLUSIONS

In this study, a methodology that allows to determine the speciation of aqueous ammonia solutions of ammonium bicarbonate using in-situ ATR-FTIR spectroscopy measurements has been presented. The determination of the liquid composition of such systems, regardless of the type of analytical technique exploited to measure it, poses several challenges. Among them, the high volatility of the solutes, i.e. $CO_2$ and $NH_3$, requires to operate in a sealed reactor to minimize the material loss to the vapor phase, and the extent of the speciation in the liquid phase results, in general, in a complex overlap of the IR bands of the solutes in the infrared spectrum. A CLS methodology has therefore been used to segregate the contribution of each species to the IR signal of the mixture, and to estimate the concentration of the individual components in solution. This modeling approach, although simplified, is grounded on a physical description of the system and requires the estimation of fewer model parameters when compared to more complex modeling techniques such as the ones proposed by Lichtfers and Rumpf[43,44] and Kriesten et al.[70,71] As a matter of fact, the model's accuracy is expected to decrease as the absorbance of the individual species deviates from the values used as an internal reference of the CLS model (cf. Eq 2.4), thus making it difficult to extend the use of the proposed methodology to a wide range of compositions in the $CO_2-NH_3-H_2O$ system.
For the purposes of our experimental investigation, the quality of the CLS fitting of the spectra has been used as the main criterion to assess the reliability of the concentration estimates, and the agreement between the ATR-FTIR measurements and the results of the speciation models available in the literature[28,30] confirms the validity of the proposed

methodology that could be applied for reaction kinetics monitoring purposes, for instance.

The solubility and speciation data measured for saturated aqueous ammonia solutions of BC have been used to improve the accuracy of the available thermodynamic models in the description of the BC solid-liquid equilibrium in aqueous ammonia solutions, thus allowing for a precise estimation of the BC supersaturation during crystallization processes. Ultimately, this work paves the way for the estimation of the crystallization kinetics of ammonium bicarbonate in aqueous ammonia solutions essential for the design and control of solid formation in ammonia-based $CO_2$ capture processes.[25,42]

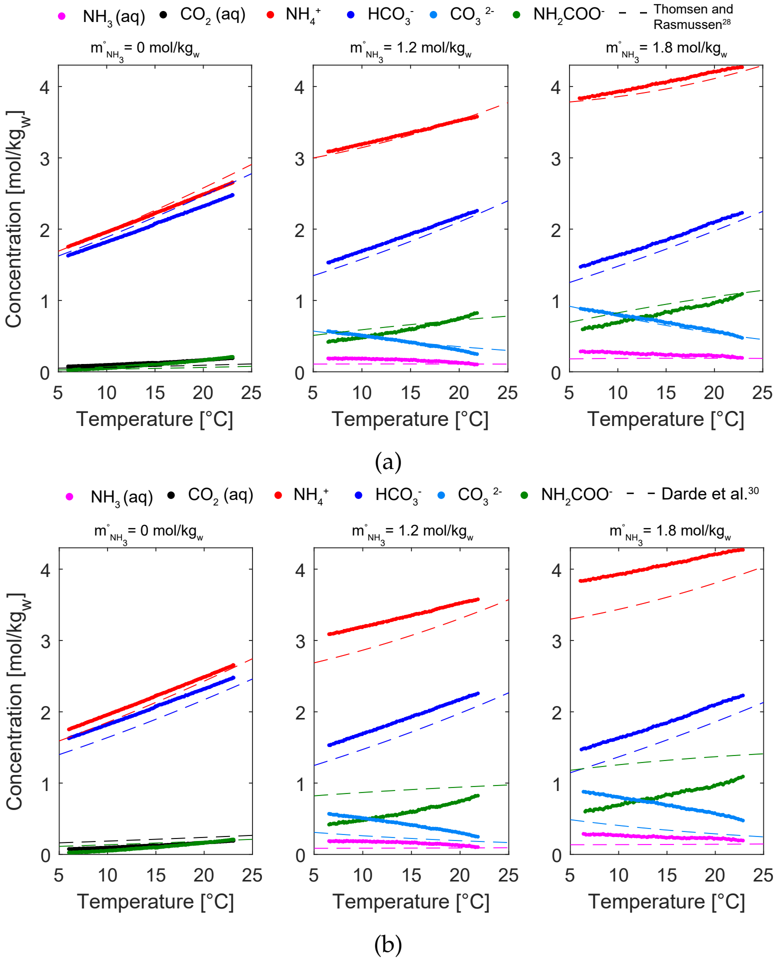

FIGURE 2.13: Comparison of the ATR-FTIR speciation data (dots) of saturated aqueous ammonia solutions of ammonium bicarbonate and the predictions of thermodynamic models (dashed lines) in the temperature range 5-23 °C. (a) Comparison to the Thomsen model.[28] (b) Comparison to the Darde model.[30] The range of investigated ammonia concentration in the solvent varies between 0-1.8 $\text{mol/kg}_{\text{W}}$.

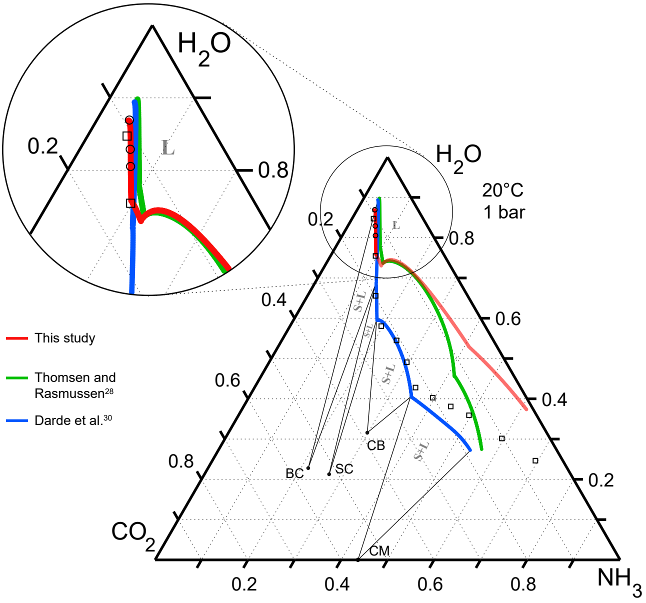

Figure 2.14: Solubility curves of the different salts in the $CO_2-NH_3-H_2O$ system at 20 °C and 1 bar computed with the Darde model[30] (blue curve), the Thomsen model[28] (green curve), and the re-fitted Thomsen model (red curve) respectively. Black boxes (□) indicate the solid-liquid equilibrium data by Jänecke,[40] while black circles (○) indicate the ammonium bicarbonate solubility measured in this work.

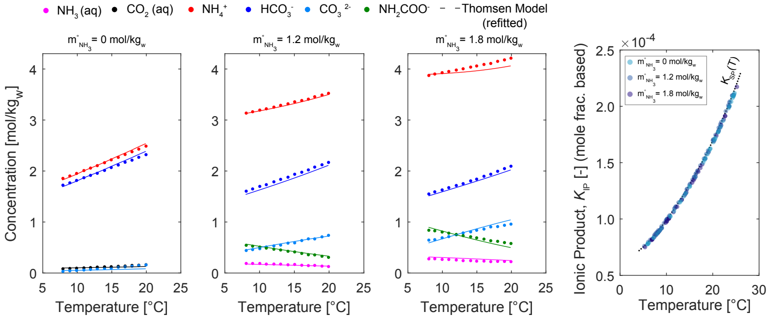

FIGURE 2.15: Quality of fit of the speciation and solubility product of ammonium bicarbonate using the thermodynamic model presented in this work (cf. Section 2.4.7). Measurements from saturated aqueous ammonia solutions of ammonium bicarbonate have been used for the fitting. The ammonia concentration in the solvent, indicated with a color code, has been varied from 0 to 1.8 mol/kg$_W$. The dots and the solid lines represent the experimental data and the model predictions, respectively. The ionic product of ammonium bicarbonate, at saturation, overlaps nicely with the values of the solubility product, $K_{SP}$, (dashed curve) in the temperature range 6-20 °C, thus indicating the good capability of the model to describe the solid-liquid equilibrium of ammonium bicarbonate in aqueous ammonia solutions.

| $u_{ij}^0$ | $H_2O$ | $NH_3$(aq) | $CO_2$(aq) | $NH_4{}^+$ | $H^+$ | $OH^-$ | $CO_3{}^{2-}$ | $HCO_3{}^-$ | $NH_2COO^-$ |
|---|---|---|---|---|---|---|---|---|---|
| $H_2O$ | 0 | | | | | | | | |
| $NH_3$(aq) | ***774.41*** | 1140.20 | | | | | | | |
| $CO_2$(aq) | ***205.32*** | 2500.00 | 40.52 | | | | | | |
| $NH_4{}^+$ | ***142.58*** | ***1010.60*** | ***-5.05*** | 0 | | | | | |
| $H^+$ | $10^5$ | $10^{10}$ | $10^{10}$ | $10^{10}$ | 0 | | | | |
| $OH^-$ | 600.50 | 2046.80 | 2500.00 | 1877.90 | $10^{10}$ | 1562.90 | | | |
| $CO_3{}^{2-}$ | ***232.71*** | 1662.40 | 2500.00 | 226.60 | $10^{10}$ | 1588.00 | 1458.30 | | |
| $HCO_3{}^-$ | ***625.93*** | ***3641.90*** | ***767.81*** | ***643.24*** | $10^{10}$ | 2500.00 | 800.01 | 771.04 | |
| $NH_2COO^-$ | ***1.27*** | 1006.40 | 2500.00 | 85.21 | $10^{10}$ | 2500.00 | 2500.00 | 612.95 | 1405.20 |

Table 2.4: Extended-UNIQUAC interaction energy parameters $\mathbf{u}_{ij}^0$ ($\mathbf{u}_{ij} = \mathbf{u}_{ij}^0 + \mathbf{u}_{ij}^T(T - 298.15)$ and $\mathbf{u}_{ij}^0 = \mathbf{u}_{ji}^0$). The values of parameters in bold-italics have been changed from the original version on the model.[28]

| $u_{ij}^T$ | $H_2O$ | $NH_3$(aq) | $CO_2$(aq) | $NH_4{}^+$ | $H^+$ | $OH^-$ | $CO_3{}^{2-}$ | $HCO_3{}^-$ | $NH_2COO^-$ |
|---|---|---|---|---|---|---|---|---|---|
| $H_2O$ | 0 | | | | | | | | |
| $NH_3$(aq) | ***0.0996*** | 4.0165 | | | | | | | |
| $CO_2$(aq) | ***11.8880*** | 0 | 13.6290 | | | | | | |
| $NH_4{}^+$ | ***0.0052*** | ***19.6218*** | ***14.8936*** | 0 | | | | | |
| $H^+$ | 0 | 0 | 0 | 0 | 0 | | | | |
| $OH^-$ | 8.5455 | 0.0904 | 0 | 0.3492 | 0 | 5.6169 | | | |
| $CO_3{}^{2-}$ | ***2.6495*** | -0.1314 | 0 | 4.0556 | 0 | 2.5176 | -1.3448 | | |
| $HCO_3{}^-$ | ***-1.9399*** | ***0.2249*** | ***0.0437*** | ***-0.0002*** | 0 | 0 | 1.7241 | -0.0198 | |
| $NH_2COO^-$ | ***6.8968*** | 6.1568 | 0 | 5.6035 | 0 | 0 | 0 | 3.4233 | 0 |

Table 2.5: Extended-UNIQUAC interaction energy parameters $\mathbf{u}_{ij}^T$ ($\mathbf{u}_{ij} = \mathbf{u}_{ij}^0 + \mathbf{u}_{ij}^T(T - 298.15)$ and $\mathbf{u}_{ij}^T = \mathbf{u}_{ji}^T$). The values of parameters in bold-italics have been changed from the original version on the model.[28]

## NOMENCLATURE

### *Acronyms*

| | |
|---|---|
| ATR-FTIR | Attenuated total reflection-infrared spectroscopy |
| BC | Ammonium bicarbonate |
| CAP | Chilled ammonia process |
| CB | Ammonium carbonate monohydrate |
| CLD | Chord length distribution |
| CLS | Classical least squares |
| CM | Ammonium carbamate |
| CSF-CAP | Controlled solid formation-chilled ammonia process |
| FBRM | Focused beam reflectance measurement |
| L | Liquid phase |
| MLR | Multiple linear regression |
| PLS | Partial least squares |
| RMSECV | Root mean squared error of cross validation [$\mathrm{mol\,kg^{-1}}$] |
| S | Solid phase |
| SC | Ammonium sesquicarbonate |
| UNIQUAC | Universal quasi-chemical |
| V | Vapor phase |

### *Greek Symbols*

| | |
|---|---|
| $\epsilon$ | Residual error of the fitting of the IR spectra [A.U.] |
| $\delta$ | IR bending mode |
| $\Delta\tilde{\nu}$ | Interval between two IR spectrum wavenumbers |
| $\mu$ | Mean of the IR spectrum distribution [$\mathrm{cm^{-1}}$] |
| $\nu$ | IR stretching mode |
| $\nu_\mathrm{a}$ | IR asymmetric stretching mode |
| $\sigma$ | Broadness of the IR spectrum distribution [$\mathrm{cm^{-1}}$] |
| $\tilde{\nu}$ | IR wavenumber [$\mathrm{cm^{-1}}$] |
| $\zeta$ | Ratio between the total nitrogen and carbon content in the system [-] |

### *Roman Symbols*

| | |
|---|---|
| $a$ | Infrared absorbance [A.U.] |
| $\bar{\mathbf{a}}_i^*$ | IR reference spectrum of the *i*-th component used by the CLS method [A.U.] |
| $\mathbf{A}$ | IR reference spectra of the pure components (solutes) [A.U.] |
| $\mathbf{a}$ | Vector of absorbance data point [A.U.] |

| | |
|---|---|
| $\mathbf{a}^*$ | IR spectrum of the mixture after water spectrum subtraction [A.U.] |
| $\mathbf{b}_i$ | PLS concentration regressor vector relative to the $i$-th component |
| $c_i$ | $i$-th component concentration [mol/kg$_\mathrm{w}$] |
| $E(\cdot)$ | Mean operator |
| $f_i$ | Calibration model relative to the $i$-th component |
| $\mathbf{K}_i$ | Score matrix of the PLS method relative to the $i$-th component |
| $K_\mathrm{IP}$ | Ammonium bicarbonate ionic product (mole frac. based) [-] |
| $K_\mathrm{SP}$ | Ammonium Bicarbonate solubility product (mole frac. based) [-] |
| $k_i$ | CLS weight parameter relative to the $i$-th component in solution [-] |
| $M$ | Total number of reference temperatures |
| $m$ | Number of discrete wavenumbers |
| $m_i$ | Molality of the $i$-th component [mol/kg$_\mathrm{w}$] |
| $n$ | Number of component in the system |
| $N_\mathrm{e}$ | Number of experimental conditions investigated |
| $N_\mathrm{obv}$ | Number of observations (cf. Eq 2.19) |
| $N_i$ | Total number of reference concentrations of the $i$-th component |
| $\mathbf{p}_i$ | Parameter vector of the MLR method relative to the $i$-th component |
| $r$ | PLSR latent variable |
| $R^2$ | Coefficient of determination [-] |
| $S(\cdot)$ | IR spectrum features-extractor operator |
| $\mathbf{s}$ | Generic IR spectrum [A.U.] |
| $\mathbf{S}_i$ | Matrix of processed IR reference spectra of the $i$-th component |
| $T$ | Temperature [°C] |
| $\mathbf{T}_i$ | Temperature vector of the MLR method relative to the $i$-th component |
| $\mathbf{u}^0$ | Extended-UNIQUAC energy interaction parameter vector [J mol$^{-1}$] |
| $\mathbf{u}^\mathrm{T}$ | Extended-UNIQUAC energy interaction parameter vector [J mol$^{-1}$] |
| $\mathbf{w}$ | IR spectrum of water [A.U.] |
| $\mathbf{W}_i$ | Weight matrix of the PLS method relative to the $i$-th component |
| $\mathbf{X}_i$ | Multiple linear regressors matrix relative to the $i$-th component |

*Subscripts and Superscripts*

| | |
|---|---|
| $\circ$ | Superscript pertaining to a nominal concentration |
| $j$ | Subscript pertaining to the $j$-th IR wavenumber |
| * | Superscript pertaining to quantity at solubility |
| ˆ | Superscript pertaining to an estimator |
| calc | Subscript pertaining to a calculated quantity |
| exp | Subscript pertaining to a measured quantity |

# 3

# GROWTH KINETICS OF AMMONIUM BICARBONATE

*God made the bulk; surfaces were invented by the devil*

— Wolfgang Pauli

## 3.1 INTRODUCTION

The investigation of the thermodynamic and kinetic properties of the $CO_2-NH_3-H_2O$ system is of fundamental interest across different areas of the physical sciences as well as in a variety of industrial fields such as waste water and flue gas treatment. Over the past decades, the extensive characterization of the vapor-liquid-solid equilibria[26,27,40,41,72–74] (VLSE) of this system allowed for the development of thermodynamic models capable of describing accurately the phase equilibria in a wide range of operating conditions.[28,30,75] Within the framework of absorption-based post-combustion $CO_2$ capture processes, these models have been extensively used for the synthesis and the optimization of the chilled ammonia process (CAP) which captures $CO_2$ from flue gas streams of large $CO_2$ point sources such as coal and natural gas power plants and cement plants.[31,68] Recently, the potential associated with the formation of solid ammonium bicarbonate within the $CO_2$ capture plant has also been investigated to mitigate the overall energy penalty of the process, thus resulting in a novel controlled solid formation-CAP (CSF-CAP).[25,76] In this context, the estimation of the crystallization and dissolution kinetics of ammonium bicarbonate in aqueous ammonia solutions is of paramount importance for the design of the crystalliza-

---

The work presented in this chapter has been reproduced with permission from Milella, F.; Mazzotti, M. Estimation of the Growth and the Dissolution Kinetics of Ammonium Bicarbonate in Aqueous Ammonia Solutions from Batch Crystallization Experiments. *Cryst. Growth Des.* **2019**, 57, 34, 11712-11727. DOI: 10.1021/acs.cgd.9b00941. Copyright 2019 American Chemical Society) tion units, while on a more fundamental level it deepens the scientific knowledge of the crystal growth mechanism in such a system, which is rather complex in terms of speciation in solution.

The experimental investigation of the $CO_2-NH_3-H_2O$ system poses several challenges due to the high volatility of $CO_2$ and $NH_3$ in solution as well as the fast decomposition rates of the solid compounds at ambient conditions.[40,77,78] This calls for the design of an experimental setup capable of operating the system under its own vapor pressure and for specific solid handling procedures that prevent the alteration of the product harvested after crystallization.[37]

The objective of this work is to extend the estimation of the growth kinetics of ammonium bicarbonate, which to our knowledge has only been measured in aqueous solution,[37] to the case of aqueous ammonia solutions (i.e. in presence of non stoichiometric ammonia), thus not only broadening the range of experimental conditions of industrial relevance, but also investigating the effects of the speciation and of the crystallization conditions on the crystal growth rates and on the crystal habit of ammonium bicarbonate.

The *in situ* liquid concentration has been measured by using a tailored attenuated total reflection Fourier-transform infrared (ATR-FTIR) spectroscopic methodology that allows retrieval of the overall concentration of ammonium bicarbonate despite the complex speciation of the mixture.[76] Furthermore, the electrolytic nature of the investigated mixtures requires the use of an activity coefficient model to compute the thermodynamic driving force of crystallization while accounting for the speciation in the system. Finally, the work focuses on the regression of the dissolution rates of ammonium bicarbonate estimated under operating conditions similar to the ones used for the growth experiments.

The chapter is organized as follows. In Section 3.2, the experimental setup, the analytical methods and the characterization techniques used are discussed. Section 3.3 provides a description of the population balance model used to simulate the growth and dissolution processes as well as of the parameter estimation procedure and numerical methods used. Finally, results and comparison to the existing literature are given in Section 3.4.

In the temperature, pressure, and composition ranges explored in this work (indicated by the green shaded area in the ternary diagram of Figure 3.1), the number of phases that can potentially form are a liquid phase, and a solid phase constituted by ammonium bicarbonate (also indicated as BC in the following) which is the most stable salt at these operating conditions. It is worth noting that, under the experimental conditions adopted, the evaporation of highly volatile species such as $CO_2$ and $NH_3$ in the gas phase of the reactor (that consists mainly of inert air) still occurs and has to be minimized in order to prevent solute loss from the liquid phase.

## 3.2 EXPERIMENTAL SECTION

### 3.2.1 *Materials*

#### *Ammonium Bicarbonate*

Ammonium bicarbonate salt has been used in this work. The compound has been purchased as a solid $\geq 99.5\,\%$ pure (Sigma-Aldrich, Switzerland) and it has been used without further purification.

Ammonium bicarbonate crystallizes in the orthorhombic space group *Pccn*, and at ambient conditions it appears as a transparent, crystalline and brittle material with the prismatic shape shown in Figure 3.2. The habit of the crystals ranges from needle-like (with a high prominence of the {110} and {010} faces) to more compact and prismatic (cf. Section 3.4.1). At room temperature it slowly decomposes into $NH_3$(g), $CO_2$(g), and $H_2O$(l), with a decomposition rate strongly influenced by temperature. Its dissociation pressure at 25 °C is 7.85 kPa and it rapidly increases to a value close to the atmospheric pressure at a temperature of ca. 60 °C.[81]

#### *Aqueous Ammonia Solutions*

Diluted aqueous ammonia solutions in the concentration range $0-3\,\%$ wt have been prepared using commercial ammonium hydroxide solutions (Sigma-Aldrich, puriss. p.a., reag. ISO, reag. Ph. Eur. 25 % wt) and

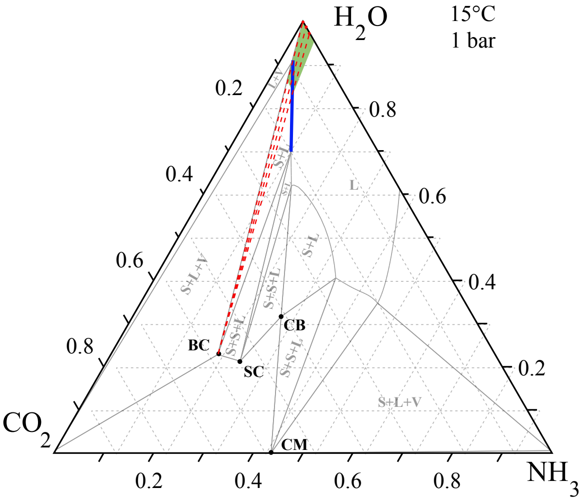

Figure 3.1: Ternary phase diagram for the $CO_2-NH_3-H_2O$ system at 15 °C and 1 bar obtained using the thermodynamic model proposed by Darde et al..[30] The compositions are expressed in weight fractions and the construction and use have been described in detail elsewhere.[31] The black circular markers (●) indicate the composition of the stable solid phases, namely ammonium bicarbonate (BC), ammonium carbonate monohydrate (CB), ammonium sesquicarbonate (SC), and ammonium carbamate (CM). The dashed isopleths (red lines) refer to $CO_2$, $NH_3$, and $H_2O$ mixtures characterized by an ammonia content (on a carbon free basis) of 0 % wt, 2 % wt, and 3 % wt, respectively. The region of the ternary phase diagram investigated in this study, highlighted in green, includes the formation of the ammonium bicarbonate salt, while the composition of the liquid phase in equilibrium with the solid phase is indicated by the BC solubility curve highlighted in blue.

Milli-Q water (18.2 MΩ cm at 25 °C). Acid-base titrations performed with a 702 SM Titrino (METROHM, Switzerland) and a 1M HCl titrant solution have been used to determine the ammonia concentration of the purchased solutions prior to dilution. The preparation of the solutions has been carried out with a PG8001 analytical balance (Mettler-Toledo,

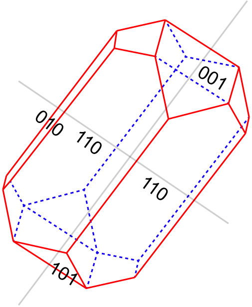

FIGURE 3.2: Crystal morphology of ammonium bicarbonate. The dimensions of the unit cell are: $a = 7.220$ Å, $b = 10.672$ Å, $c = 8.719$ Å, and $d = 671.927$ Å.[79,80]

Switzerland) with a readability and maximum capacity of 0.1 g and 8.1 kg, respectively. The estimated accuracy of the static measurement is ± 0.23 g.

### 3.2.2 *Methods*

Initially, the nominal amounts of aqueous ammonia, cooled at a temperature of 5 °C, and of BC have been fed into the reactor by almost filling it completely, thus minimizing the head space volume of air in the vessel. Then, the reactor has been sealed to prevent material loss due to the evaporation of $CO_2$(aq) and $NH_3$(aq) to the atmosphere (cf. Eqs 1.1-1.2). The maximum operating pressure of the vessel has been set to 5 barg, and a speed of 400 RPM of the 4-bladed stirrer with 45° pitched paddles has ensured adequate mixing of the liquid while minimizing attrition and breakage of the dispersed phase. The process temperature has been controlled by means of a CC230 thermostat (Huber, Germany) connected to a Pt-100 probe immersed in the liquid phase of the reactor acquiring data at a frequency of 30 $s^{-1}$.

Online monitoring tools have been connected to the reactor by means of custom-made pressure connectors installed in the lid of the vessel. A solid dosing system has been used for the injection of seed crystals directly into the liquid phase via an immersed fixed stainless-steel pipe. The system consists of a 20 mL male Luer lock syringe that can be screwed into a Luer lock female connector attached to a port on the lid of the vessel. The connection extends into the liquid phase of the reactor through a 6.4 mm stainless-steel pipe. The seeding procedure requires a partial filling of the syringe using the solution present in the reactor, followed by the injection of the suspended seed crystals by means of a series of repeated syringe flushes.

### *Measurement of the Overall Ammonium Bicarbonate Concentration*

Attenuated total reflection-Fourier transform infrared (ATR-FTIR) spectroscopy has been used to measure the overall BC concentration in solution, regardless of the presence of a suspended solid phase, and of the speciation reactions. Measurements have been performed with a ReactIR 45m (Mettler-Toledo, Switzerland) equipped with a 1.6 cm DiComp immersion probe and a diamond ATR crystal. Spectra have been collected in the 800-3000 $\mathrm{cm}^{-1}$ region with a wavenumber resolution of 4 $\mathrm{cm}^{-1}$ and averaged over 256 scans using an exposure time of 1 min for monitoring the growth process and 30 s for the case of dissolution. The ATR-FTIR background signal has been collected in air, at ambient conditions, before every experiment.

### *Characterization of the Suspended Phase*

In this work, the 1-D crystal size distribution (CSD) of the suspended phase has been sampled using the μ-DISCO, as discussed in Section 1.7.3. A measuring time of 20 min allowed to sample, on average, a total of ca. $5 \cdot 10^4$ particles. Furthermore, micrographs of the suspension have been recorded by means of a PVM probe at different phases of the crystallization process. The device allows for measurements in a pressurized environment (up to 10 bar) with an image resolution of 2 μm and a $10.1 \times 8.3$ mm field of view.

#### *Preparation of the Seed Crystals*

In a first step of preparing the seed crystals, the purchased material has been dry-sieved in order to obtain two different sized fractions in the size ranges 60−150 µm and 120−250 µm, respectively. Subsequently, the seeds have been stored under nitrogen atmosphere to prevent contact with moisture in the air. Henceforth, the two fractions of seeds obtained from the same purchased batch will be referred to as seeds A and seeds B. Figure 3.3 shows the normalized volume-weighted CSD of the populations of seeds together with their corresponding micrographs. The population of seed crystals, suspended in the stirred reactor in an ethanol solution saturated with respect to BC, has been measured using the µ-DISCO by circulating the suspension in a closed loop with the monitoring device as shown in Figure 1.10.

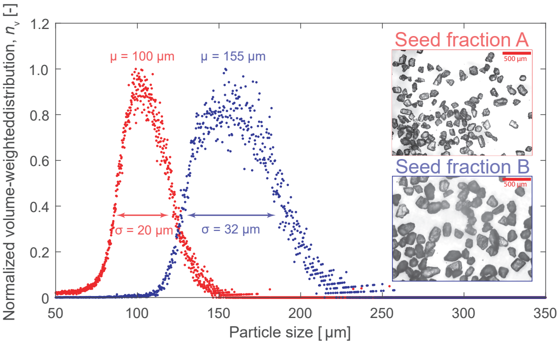

Figure 3.3: Normalized volume-weighted CSD of the seed particles used in the desupersaturation experiments and corresponding micrographs. The CSD of seeds A and of seeds B has been calculated based on 120,000 and 40,000 particles, respectively.

### 3.2.3 *Protocol for the Experiments*

The crystallization and dissolution experiments have been carried out in the temperature range between 9 °C and 23 °C by varying the initial

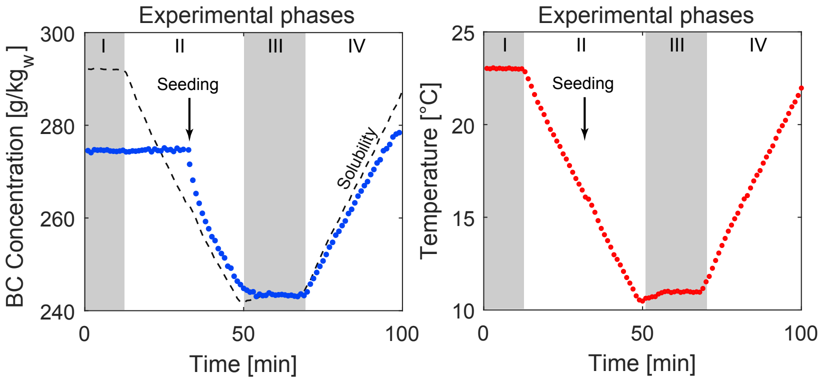

(a) (b)

Figure 3.4: Graphical representation of the experimental protocol for the polythermal growth and dissolution experiments. (a) Ammonium bicarbonate concentration profile followed during an exemplary experiment. The black dashed line indicates the BC solubility at the relative temperature. (b) Temperature profile followed during the experiment. The different experimental phases are indicated with roman numbers: I and III are the equilibration phases, while II and IV are the growth and dissolution phases, respectively; refer to Section 3.2.3 for further details.

supersaturation, the ammonia concentration in the solvent, and the seed fraction (i.e. seeds A or B).

The method followed in this work to estimate the rate constant of the growth and the dissolution processes relies on the measurement of the evolution of the solute concentration during crystallization. Based on this approach, the rate of acquisition of the BC concentration data has to be compatible with the characteristic time scale of crystallization or dissolution. Furthermore, in the case of growth, the supersaturation level (the driving force for crystallization) obtained by cooling the solution has to be generated at a faster rate compared to its consumption due to crystal growth to avoid a crystallization process that evolves virtually along the solubility curve (i.e. in a saturated solution). For this purpose, a *relaxation method* that consists of rapidly cooling the suspension during crystallization has been adopted instead of performing the desupersaturation experiments at isothermal conditions. This methodology, also applied to monitor dissolution, is often used to measure fast reaction kinetics by extracting the relevant information from the dynamic equilibration of the system after a sudden perturbation.[82] It is worth noting that the thermal inertia of the system (i.e. the thermal inertia of the suspension and of the steel reactor) makes it impossible to change instantaneously the temperature of the suspension; linear cooling and heating ramps have been used instead.

As shown in Figure 3.4, the experimental procedure has been divided into a maximum of four phases. During phase I, a clear undersaturated solution is prepared by heating a suspension of BC in an aqueous ammonia solution well above its saturation temperature. In phase II, a linear cooling ramp of $-20\,^{\circ}\mathrm{C\,h^{-1}}$ has been applied to induce supersaturation. Then, seeding has been performed by injecting either seeds A or seeds B in the supersaturated solution, thus preventing the dissolution of particles upon contact with the liquid. Finally, the evolution of the solute concentration and of the particle count has been monitored by means of ATR-FTIR and FBRM measurements, respectively, until reaching equilibrium during phase III where the temperature has been kept constant.

The slurry obtained after the growth experiment can be either filtered to recover the solid product used in a further CSD characterization, or it can be used to perform a dissolution experiment during phase IV. This is achieved by heating the suspension using a linear heating ramp (of $20\,^{\circ}\mathrm{C\,h^{-1}}$) until the solid phase disappears completely.

For all the experiments, performed using a total mass of solution of 1340 g, a seed loading equivalent to $8-12\,\%$ wt of the final solid yield has been used to minimize the extent of secondary nucleation.[83] The maximum supersaturation explored has been carefully kept below the primary nucleation threshold, as identified in the course of ad hoc experiments.

After harvesting the solid phase during phase III, the presence of interstitial mother liquor has been minimized by washing the solids with

| **Solute** | **Method** | **IR Wavenumber range**<br>$[\mathrm{cm}^{-1}]$ | **LV**<br>[-] | **RMSE-CV$_{10}$**<br>$[\mathrm{mol/kg_W}]$ |
|---|---|---|---|---|
| BC ($\omega^{\circ}_{NH_3} = 0\,\%$ wt) | PLSR | $980 \leq \tilde{\nu} \leq 1036$ | 7 | $7.97 \cdot 10^{-5}$ |
| BC ($\omega^{\circ}_{NH_3} = 2\,\%$ wt) | PLSR | $980 \leq \tilde{\nu} \leq 1036$ | 10 | $7.00 \cdot 10^{-3}$ |
| BC ($\omega^{\circ}_{NH_3} = 3\,\%$ wt) | PLSR | $980 \leq \tilde{\nu} \leq 1036$ | 10 | $6.20 \cdot 10^{-5}$ |

Table 3.1: Overview of PLS models used for the estimation of the BC concentration using ATR-FTIR measurements. The models are applied on a specific wavenumber range, using a number of latent variables (LV) between 7 and 10. The prediction capability of the models has been tested using a root mean square error of 10-fold cross validation (RMSE-CV$_{10}$).[45]

ice-cooled acetone solution saturated with BC. This procedure prevented a rapid decomposition of the BC in the presence of moisture, thus preserving the characteristics and properties of the crystals. While the choice of acetone is particularly convenient due to its drying effect, the possible occurrence of slow side reactions at room temperature in an aqueous solution of BC containing acetone has to be acknowledged. These reactions lead to the aging of the solution that turns slowly brownish due to the formation of amminic and pyrimidinic compounds.[84] The surface of the solids is usually affected by the same phenomenon, which can be minimized by performing a mild drying step of the crystals aimed at removing residual traces of acetone.

## 3.3 MODELING OF THE CRYSTALLIZATION PROCESS

### 3.3.1 *Concentration Estimation*

As ammonium bicarbonate dissociates completely in solution, the reactions occurring in the liquid phase (eqs 1.4-1.8) lead to a complex distribution of ionic species that complicates the estimation of the overall salt concentration. This work uses the ATR-FTIR methodology discussed in Chapter 2, which allows for the estimation of the BC concentration based on a partial least-squares (PLS) analysis of the spectral data of the mixture. As a prerequisite, the application of the model requires the value of the nominal ammonia concentration of the solvent $\omega^{\circ}_{NH_3}$ to be known. In this regard, three PLS models have been built (cf. Table 3.1) for the estimation of the BC concentration in aqueous ammonia solutions at a nominal ammonia concentration of 0 %, 2 %, and 3 % wt, respectively. The interested reader is referred to Appendix B for further details on the set of calibration standards used to build the PLS models.

Figure 3.5a shows that the measured solubility of BC increases with an increase of the nominal ammonia concentration in the solvent (indicated with a color code). If an activity-based approach is adopted to describe the solubility of ammonium bicarbonate in terms of the ionic product $K_{IP}$ of ammonium and bicarbonate ions in solution, the different solubility curves shown in Figure 3.5a collapse onto a single curve as shown in Figure 3.5b, where the circular markers are the experimental BC solubility data points, and the solid line is the solubility product of ammonium bicarbonate, $K_{SP}$, function of temperature only.

In this work, the temperature dependence of the BC solubility product reported by Darde et al.[30] has been used, while the speciation model proposed by Milella and Mazzotti[76] has been applied for the computation of the activity of the species in solution due to its accuracy in describing the solid-liquid equilibrium of BC in the range of operating conditions investigated in this work.

### 3.3.2 Population Balance Equation

This work uses a modeling framework based on a population balance equation (PBE) for the description of the evolution of a population of seed crystals during batch crystallization or dissolution. The population of crystals has been assumed consisting of geometrically similar particles modeled as cubes with the characteristic length of the cube side $L$. Moreover, neglecting agglomeration and breakage leads to the following PBE:

$$\frac{\partial n}{\partial t} + a\frac{\partial n}{\partial L} = 0 \tag{3.1}$$

where $t$ is the time, $n(t, L)$ is the distribution of the crystal population about a particle-size coordinate $L$ defined in the range (0,∞), as the number of particles per unit length, per unit mass of solvent ($M_s$); $a$ indicates generically an advection velocity along the particles' internal coordinate $L$, which is either the overall growth rate $G$ ($> 0$), or the overall dissolution rate $D$ ($< 0$), depending on the sign of the driving force given by eq 1.18 in Chapter 1.

Different initial and boundary conditions apply according to the phe-

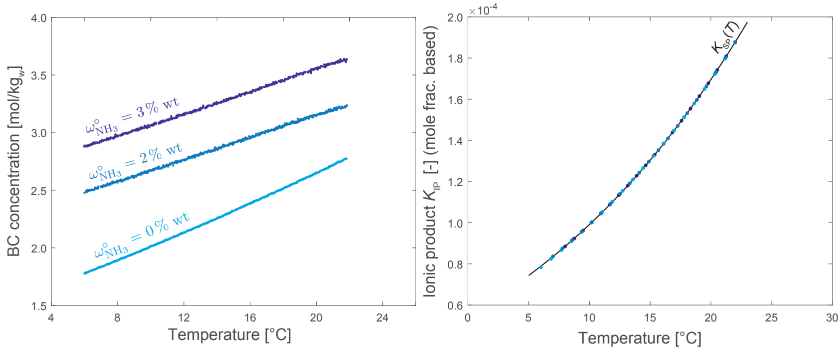

(a) (b)

FIGURE 3.5: (a) ATR-FTIR-based solubility of ammonium bicarbonate in aqueous ammonia solutions as a function of temperature and nominal ammonia concentration $\omega^\circ_{NH_3}$ in the solvent (cf. blue color code). The solubility is based on a pure water mass basis. (b) Ammonium bicarbonate ionic product $K_{IP}$ at saturated conditions as a function of temperature. The solid line is the solubility product of ammonium bicarbonate, $K_{SP}$, taken from Darde et al.,[30] while the circular markers are points corresponding to the BC solubility curves shown in Figure 3.5a, the color code indicates the nominal ammonia concentration in the solvent.

nomenon investigated. They are defined as follows, respectively for the growth and the dissolution cases:

**Growth**

$$n(0, L) = \varphi n_{0,\mathrm{s}}(L) \tag{3.2a}$$

$$n(t, 0) = 0 \tag{3.2b}$$

**Dissolution**

$$n(0, L) = \varphi n_{0,\mathrm{s}}(L) \tag{3.2c}$$

where $n_{0,\mathrm{s}}(L)$ is the number-based CSD of the population of seeds used in the sets of growth and dissolution experiments, respectively. Furthermore, the boundary condition of eq 3.2b implies the absence of nucleation in the system. For both the cases of growth and dissolution, the *regularity* condition[85] imposes that $a(t, \infty)n(t, \infty) = 0$. This implies that, if the growth or dissolution rate does not vanish for larger sizes, the number density must vanish for a particle size that tends to infinity. Note that, in this work, the mass of the seed population, sampled using the μ-DISCO, has been rescaled to the actual mass of seeds, $m_\mathrm{s}$, used during the growth or dissolution experiments by means of the scaling factor, $\varphi$, defined as:

$$\varphi = \frac{m_\mathrm{s}}{\rho_\mathrm{s} V_\mathrm{s}} \tag{3.3}$$

In eq 3.3, $\rho_\mathrm{s}$ is the density of the crystalline phase, and $V_\mathrm{s}$ is the total volume of the seed population sampled with the μ-DISCO. The $p$-th moment of a distribution, $n(L)$, is defined as:

$$\mu_p = \int_0^\infty n(t, L) L^p dL \tag{3.4}$$

eq 3.1 must be coupled to the continuous phase equation which accounts for the depletion or accumulation of solute in the continuous phase by growth or dissolution, thus:[36]

$$\frac{\mathrm{d}c}{\mathrm{d}t} = -3\rho_\mathrm{s} k_\mathrm{v} \mu_2 a \tag{3.5}$$

where $c$ is the molality of ammonium bicarbonate in solution, and $k_\mathrm{v}$ is the volumetric shape factor of a cubic crystal (equal to 1).
The initial condition of eq 3.5 is

$$c(0) = c_0 \tag{3.6}$$

where $c_0$ is the initial concentration (molality-based) of ammonium bicarbonate.

### 3.3.3 *Constitutive Equations for Growth and Dissolution*

Crystal growth and dissolution rates generally have a complex dependence on the temperature $T$, the solution supersaturation $S$ (cf. Chapter 1), the fluid dynamics of the system, and the crystal size. The effect of diffusional mass transfer on the overall growth rate, whose investigation is outside the scope of this work, has been minimized by ensuring a sufficiently high relative velocity between the solution and the crystal surface through adequate mixing. Therefore, an empirical growth rate expression has been assumed, while a diffusion-controlled rate has been adopted for dissolution given the almost entirely diffusional nature of the latter process.[36,86] Furthermore, both the growth rate $G$ and the dissolution rate $D$ have been assumed to be size-independent:

$$G = k_{\mathrm{g},1} S^{k_{\mathrm{g},2}} \tag{3.7a}$$

$$D = k_{\mathrm{d},1} S \tag{3.7b}$$

An Arrhenius type of equation has been postulated to account for the temperature dependence of the $k_{\mathrm{g},1}$ and $k_{\mathrm{d},1}$ parameters:

$$k_{\mathrm{g},1} = k_{\mathrm{g},0} \exp\left(-\frac{E_{\mathrm{a,g}}}{RT}\right) \tag{3.8}$$

In eq 3.8, the parameter $k_{\mathrm{g},0}$ is a pre-exponential factor, $E_{\mathrm{a,g}}$ is the apparent activation energy of the overall growth process, and $R$ is the ideal gas constant. Similarly, $k_{\mathrm{d},0}$ and $E_{\mathrm{a,d}}$ are the pre-exponential factor and apparent activation energy of the dissolution process, respectively.

### 3.3.4 *Fitting Procedure*

The parameter vectors associated to the growth and dissolution models, $\mathbf{k}_\mathrm{g} = [k_{\mathrm{g},0}, k_{\mathrm{g},2}, E_{\mathrm{a,g}}]^\mathrm{T}$ and $\mathbf{k}_\mathrm{d} = [k_{\mathrm{d},0}, E_{\mathrm{a,d}}]^\mathrm{T}$, can be estimated following the maximum likelihood estimation (MLE) approach. Under the assumptions of this method discussed in detail elsewhere,[63] the optimal values of the parameter vectors are such that the probability of observing the experimental data set, i.e. the measured BC concentration data points $c_i$, is maximized through the minimization of the following objective function:

$$\Psi(\mathbf{k}) = \frac{N_\mathrm{t}}{2} \ln \left[ \sum_{i=1}^{N_\mathrm{t}} \left( \frac{c_i - \hat{c}_i(\mathbf{k})}{c_\mathrm{ref}} \right)^2 \right] \tag{3.9}$$

In eq 3.9, the parameter vector $\mathbf{k}$ refers to either growth or dissolution, $N_\mathrm{t}$ is the number of experimental data points in the time series, the index $i$ refers to the $i$-th data point of the series, and $\hat{c}_i$ is the model prediction of the $i$-th data point (function of the parameter vector $\mathbf{k}$). In order to make the objective function dimensionless, the solute concentration has been normalized based on a reference concentration $c_\mathrm{ref}$ equal to 1 mol/kg$_\mathrm{W}$.

#### *Selection of the Experimental Data Points for Parameter Estimation*

A number of precautions need to be taken when attempting to measure reliable crystal growth or dissolution rates in systems that evolve rapidly towards equilibrium. The most important among them is certainly the quality of the experimental data set used for the regression of the model parameters. For example, solute concentration data points virtually lying on the solubility curve do not embed any kinetic information about the system, therefore they must be filtered from the experimental data set used for the optimization. The criterion adopted for the data selection is the following:[87]

$$|c_i - c^*(T_i)| \geq 4\bar{\sigma} \tag{3.10}$$

where $c^*(T_i)$ is the BC solubility at the $i$-th measured temperature, and $\bar{\sigma}$ is the standard deviation of the ATR-FTIR measurements estimated to be 0.35 g/kg$_\mathrm{w}$ (cf. Supplementary Information for further details).

*Identifiability of the Parameter Sets*

In this section, the practical identifiability[88] of the kinetic parameter sets relative to growth and dissolution is discussed. The analysis serves the purpose of detecting nonidentifiable parameters, i.e. model parameters that are statistically correlated. For the sake of brevity, only the case of crystal growth has been discussed, but its outcome can be extended easily to the case of dissolution. The sets of model parameters examined are two, the first being $k_{\mathrm{g},0}$ and $E_{\mathrm{a,g}}$, and the second being $k_{\mathrm{g},1}$ and $k_{\mathrm{g},2}$. The behavior of the objective function $\Psi$, computed using the experimental concentration data points relative to the growth experiments reported in Table 3.2 and the model response parametrized with respect to the kinetic rate constants, has been therefore analyzed. The isocontour curves of the objective function $\Psi$ are shown in Figures 3.6a and b, respectively. For both the cases, the presence of a locus of points in which the function is minized rather than a single, unique point is representative of the statistical correlation among the parameters, thus allowing to determine *only* relative values of the model parameters. For the first case shown in Figure 3.6a, the reason of the incapability of the growth model to capture the temperature dependence thoroughly might stem from the narrow temperature range explored experimentally (9 °C to 18 °C). For the second case shown in Figure 3.6b, the reason of the statistical correlation among the parameters might be more deeply rooted in the mathematical form of the growth rate equation (eq 3.7a) exploited in the model.

In light of these considerations, the recognized non-identifiabilities have been removed by fitting the parameter $k_{\mathrm{g},1}$ instead of $k_{\mathrm{g},0}$ and $E_{\mathrm{a,g}}$, and by arbitrarily setting the value of $k_{\mathrm{g},2}$ to 1. Thus, only two parameters need to be estimated, i.e. $k_{\mathrm{g},1}$ and $k_{\mathrm{d},1}$, for growth and dissolution, respectively.

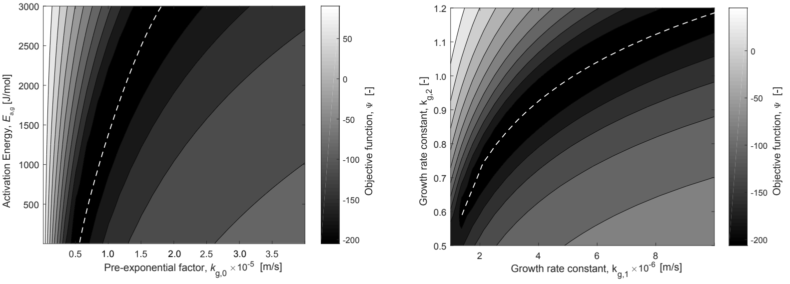

(a) (b)

FIGURE 3.6: Isocontour plots of the objective function Ψ (eq 3.9) parametrized with respect to the different growth rate constants of eq 3.7a and eq 3.8. Dashed white lines indicate the minimum values of the objective function Ψ.

### 3.3.5 *Numerical Methods*

*Population Balance Equation*

In this work, a *high resolution* method (HRM) has been chosen to solve the PBE (eq 3.1). This numerical scheme is derived on the basis of the integral form of the conservation law and it is *conservative* in a way that mimics the true solution of the balance equation.[34,35] Eq 3.1 has to be numerically integrated in the particle-size coordinate $L$ and in time. Hence, the particle-size domain has been discretized into $N_b$ (250) uniformly distributed grid points, and the time-resolved solution of the PBE has been computed through the following second-order accurate scheme for each $j$-th grid point.[89] Note that the initial distribution $n(0, L)$ for growth or dissolution has been discretized accordingly.

**Growth**

$$\begin{aligned} n_j^{t+1} &= n_j^t - \nu(n_j^t - n_{j-1}^t) + \\ &\quad - \frac{1}{2}\nu(1-\nu)[\kappa(\theta_{j+\frac{1}{2}}^t)(n_{j+1}^t - n_j^t) - \kappa(\theta_{j-\frac{1}{2}}^t)(n_j^t - n_{j-1}^t)] \end{aligned} \tag{3.11a}$$

**Dissolution**

$$n_j^{t+1} = n_j^t - \nu(n_{j+1}^t - n_j^t) + \\ + \frac{1}{2}\nu(1+\nu)[\kappa(\theta_{j+\frac{1}{2}}^t)(n_{j+1}^t - n_j^t) - \kappa(\theta_{j-\frac{1}{2}}^t)(n_j^t - n_{j-1}^t)] \tag{3.11b}$$

In eq 3.11, $\nu$ is the Courant number defined as:

$$\nu = \left| \frac{a\Delta t}{\Delta L} \right| \tag{3.12}$$

$\kappa(\theta)$ is a flux limiter function used to control the fluxes at the grid edges.
The stability of the numerical solution has been guaranteed by adapting the time step $\Delta t$ such that the Courant Friedrichs Lewy (CLF) condition, i.e. $\nu \leq 1$, is satisfied.
Among the wide variety of limiters proposed in the literature, the one proposed by Van-Leer[90] has been adopted:

$$\kappa^{\mathrm{VL}}(\theta) = \frac{\theta + |\theta|}{1 + |\theta|} \tag{3.13}$$

where the value of $\theta$ at the grid interface $j - 1/2$ is defined as:

$$\theta_{j-1/2} = \frac{n_I - n_{I-1}}{n_j - n_{j-1}} \tag{3.14}$$

in eq 3.14 the index $I$ varies according to the sign of the advection velocity $a$:

$$I = \begin{cases} i-1, & a > 0 \\ i+1, & a < 0 \end{cases} \tag{3.15}$$

*Parameter Estimation*

In this work, the local minimizer $\hat{\mathbf{k}}$ of eq 3.9 has been computed using the gradient-based optimizer LSQNONLIN (in which a trust-region-reflective algorithm is implemented) available in the MATLAB optimization toolbox.[69] A total of 30 different starting points, automatically selected by MATLAB's *MultiStart* has been used to screen multiple basins of attraction in order to increase the chance of finding a global minimum.

After performing the optimization, the confidence regions of the minimizer $\hat{\mathbf{k}}$ have been calculated. As explained in detail elsewhere,[63,91] the methodology requires the computation of the measurement error covariance matrix (or an approximation of it) and of the sensitivities of the model predictions with respect to the $N_k$ parameters, $\partial \hat{c}_i / \partial p_k$. After that, an estimate of the positive semidefinite parameter covariance matrix $\mathbf{V}_k$ can be obtained. Finally, setting a probability value of $\alpha$ allows to compute the hyperellipsoidal confidence region in the parameter space as:

$$\{\mathbf{k} \in \mathbb{R}^{N_k} | (\mathbf{k} - \hat{\mathbf{k}})^{\mathrm{T}} \mathbf{V}_k^{-1} (\mathbf{k} - \hat{\mathbf{k}}) \leq F_{\chi^2}^{-1}(\alpha | N_k)\} \tag{3.16}$$

where $F_{\chi^2}^{-1}(\alpha | N_k)$ is the inverse chi-square cumulative distribution function for a given probability $\alpha$ and $N_k$ degrees of freedom.

Finally, conservative estimates of confidence intervals can be obtained by finding the box that circumscribes the hyperellipsoidal confidence region of eq 3.16.

## 3.4 RESULTS AND DISCUSSION

In this section the growth kinetics and the dissolution kinetics of ammonium bicarbonate crystals are estimated by parameter regression of a monodimensional population balance model (eq 3.1) using the information on the evolution of the solution concentration during corresponding experiments. As discussed in Section 3.4.1, the BC crystal habit can be strongly influenced by the process conditions adopted such as the cooling rate used to generate supersaturation and/or the solvent composition. This requires the identification of a suitable supersaturation range in which ammonium bicarbonate crystals grow preferentially as cuboids, so that a constant value of the volumetric shape factor can be assumed in the continuous phase equation (eq 3.5) during the modeling phase of the growth and the dissolution experiments.

### 3.4.1 *Crystal Habit of Ammonium Bicarbonate*

Several literature studies carried out in the past decades address the remarkable effect of the solvent composition and of the presence of impurities on the crystallization rates and on the crystal habit of several compounds.[33,77,78,92,93] A few examples are the crystal habit modification of sodium chloride,[92] succinic acid,[94] gypsum,[95] or potassium dihydrogen phosphate (KDP)[96] induced by the presence of additives in solution or by a change in cooling profile during crystallization.

In this study it has been found that variations of the supersaturation level and/or of the composition of the solvent can influence significantly the habit of ammonium bicarbonate crystals grown from aqueous ammonia solutions. In the following, PVM micrographs of exemplary BC growth experiments are shown to qualitatively assess the effect of the solution composition as well as of different cooling rates on the crystal habit of ammonium bicarbonate crystals. Figures 3.7a-b show micrographs of seeds A grown from a 0 % and a 3 % wt aqueous ammonia solution respectively. Upon seeding the clear solution has been maintained slightly supersaturated with respect to BC, while a cooling rate of $-3\,^{\circ}\mathrm{C\,h^{-1}}$ has been applied during the growth process. Under these process conditions, the seeds grew predominantly as needles, regardless of the solvent composition. The same batch of seeds, grown from a 0 % and a 2 % wt aqueous ammonia solution by applying a faster cooling rate, i.e. $-20\,^{\circ}\mathrm{C\,h^{-1}}$, exhibited a different growth behavior as shown in Figures 3.7c-d. The ammonium bicarbonate crystals obtained from the pure aqueous solution grew mainly as cuboids (Figure 3.7c), while those crystallized in the presence of free ammonia (Figure 3.7d) appeared to be compact hexagonal prisms. Similar prismatic shapes have been obtained by exploiting a cooling rate of $-20\,^{\circ}\mathrm{C\,h^{-1}}$ at even higher nominal ammonia concentration in the solvent, i.e. 3 % or 9 % wt ammonia, as shown in Figures 3.7e-f, respectively.

Finally, the solid products collected after crystallization have been analyzed using solid Raman spectroscopy to rule out the formation of BC polymorphs, or of solid solutions as well as the precipitation of ammonium carbonate monohydrate[26,40,97] whose acicular habit resembles that of the ammonium bicarbonate crystals shown in Figure 3.7a (cf. Supplementary Information for the Raman characterization of the solid phase).

In order to confirm the reproducibility of the phenomena described above, the evolution of the shape of an entire population of BC crystals has been analyzed using online µ-DISCO measurements (cf. Section 1.7). Each particle detected by the device during the crystallization process has therefore been classified into one of the following five classes, i.e. cuboid, needle, agglomerate, platelet, and sphere using a supervised machine learning algorithm whose overall performance (over all five particle shape classes) has been estimated to be 69 %.[38]

In detail, the growth of seeds A from a 2 % wt supersaturated aqueous ammonia solution of BC with initial seed loading of ca. 0.5 % wt has been monitored using the µ-DISCO. Figure 3.8 shows the time-resolved evolution of the fractions of classes, the supersaturation level (red circular markers) as well as the temperature profile (black circular markers) of the experiment. As shown in Figure 3.8, a constant temperature profile (14 °C) and a rather low supersaturation (equivalent to roughly 0.5 °C of undercooling with respect to the solubility temperature) have been applied during the first two hours of the experiment. Under these conditions, the initial seed population consisting mainly of cuboidal particles has grown preferentially as needle-like particles (note the stationary decline of the fraction of cuboids during this phase). The growth process has occurred without a detectable depletion of the solute concentration in the liquid phase (constant supersaturation profile in Figure 3.8) due to the low suspension density and to the low growth rates observed. Moreover, the shape modification of ammonium bicarbonate crystals that occurred at low supersaturation levels ($S \leq 0.05$) can be primarily attributed to a change of relative growth rates of the crystal facets, which eventually led to elongated ammonium bicarbonate crystals.[36] In a second phase, the suspension has been rapidly cooled (cooling rate of ca. $-9\,°\mathrm{C\,h^{-1}}$) to 12 °C, thus inducing a higher supersaturation ($S \approx 0.07$). This temperature change triggered an inversion of the trend of the crystal habit modification that partially restored the distribution of classes to the initial one. In the last phase

of the experiment, no further changes in the BC crystal habit have been noticed due to the negligible amount of mass deposited on the grown crystals (the interested reader is referred to Appendix B for the μ-DISCO camera images of the different phases of the experiment).
The shape change of the BC crystals documented in this work only partially unfolds the complexity of the interactions that take place at the solid-liquid interface of the crystals. As discussed in Section 3.4.2, the causes of this phenomenon could be manifold: the adsorption of foreign species, i.e. primarily the carbamate and the carbonate ions (eq 1.6 and eq 1.8) resulting from the speciation of $CO_2$(aq) and $NH_3$(aq), on the active sites of the growing BC crystals could trigger growth inhibition processes well-known in the literature[77,78,98–100] and/or the chemical composition of the solvent could affect the BC crystal morphology as for the case of urea crystallized from different solvents.[93]

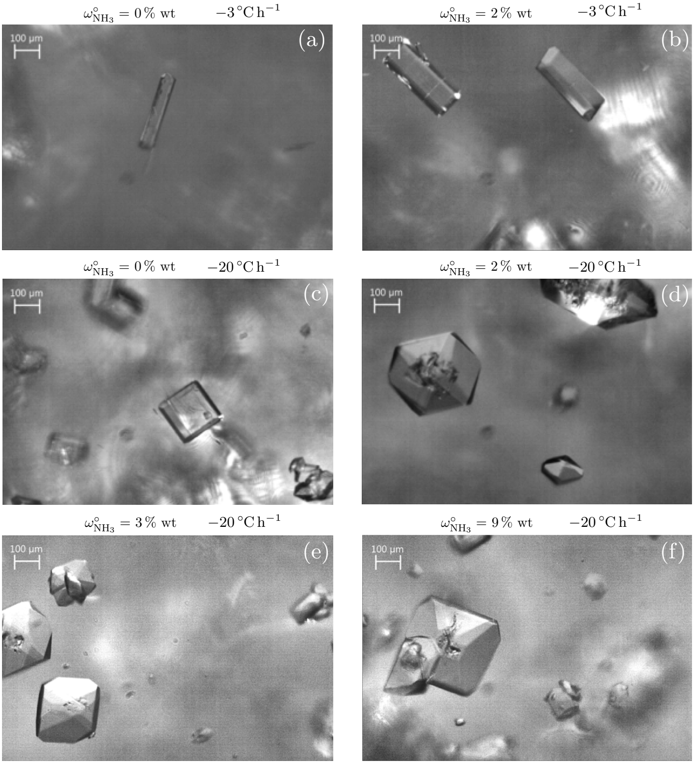

FIGURE 3.7: PVM micrographs of ammonium bicarbonate crystals grown from different aqueous ammonia solutions of BC. The experiments started from saturated aqueous ammonia solutions of BC; the same quantity and the seed fraction (seeds B) have been used in all the experiments while keeping constant the amount of mass deposited on the solid phase. The applied operating conditions are: (a)-(b) cooling rate of $-3\,°C\,h^{-1}$ in an aqueous ammonia solution of 0 % wt and 2 % wt ammonia, respectively; (c-d) cooling rate of $-20\,°C\,h^{-1}$ in an aqueous ammonia solution of 0 % wt and 2 % wt ammonia, respectively; (e)-(f) cooling rate of $-20\,°C\,h^{-1}$ in an aqueous ammonia solution of 3 % wt and 9 % wt ammonia, respectively.

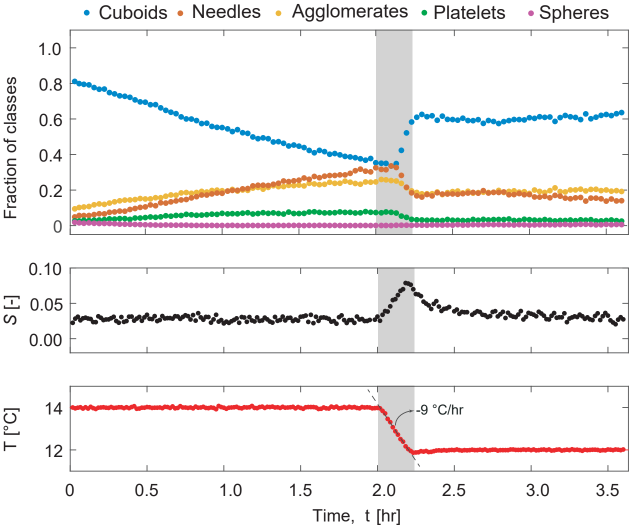

Figure 3.8: Time-resolved shape change of ammonium bicarbonate crystals during the growth experiment described in Section 3.4.1. Measurements have been performed every 2 min using the μ-DISCO acquiring 800 images per measurement. The number of sampled particles per measurement is roughly 25,000. The particle shape classification has been performed using an algorithm described elsewhere.[38]

| **Ammonia Content** | **Run** | $T_{\text{initial}}$ | $T_{\text{final}}$ | $S_0$ | $m_{\text{s}}$ | **Seeds** |
|---|---|---|---|---|---|---|
| | | [°C] | [°C] | [-] | [g] | |
| $\omega^{\circ}_{\text{NH}_3} = 0\,\%$ wt | G1 | 19.1 | 16.1 | 0.05 | 3.82 | A |
| | G2* | 14.5 | 13.0 | 0.07 | 3.56 | A |
| | G3 | 14.9 | 11.3 | 0.04 | 7.40 | B |
| $\omega^{\circ}_{\text{NH}_3} = 2\,\%$ wt | G4 | 18.1 | 15.7 | 0.06 | 3.78 | A |
| | G5* | 17.4 | 14.3 | 0.07 | 3.44 | A |
| | G6 | 15.5 | 10.1 | 0.06 | 7.64 | B |
| $\omega^{\circ}_{\text{NH}_3} = 3\,\%$ wt | G7 | 16.1 | 13.4 | 0.09 | 3.61 | A |
| | G8* | 16.5 | 14.0 | 0.10 | 3.61 | A |
| | G9 | 16.5 | 14.4 | 0.15 | 7.03 | B |
| $\omega^{\circ}_{\text{NH}_3} = 0\,\%$ wt | D1 (G1) | 14.2 | 23.0 | 0.00 | 42.6 | A |
| | D2 (G2) | 9.9 | 19.0 | 0.00 | 38.6 | A |
| $\omega^{\circ}_{\text{NH}_3} = 2\,\%$ wt | D3 (G4) | 14.4 | 22.3 | 0.00 | 24.0 | A |
| | D4 (G5) | 9.0 | 19.6 | 0.00 | 34.9 | B |
| $\omega^{\circ}_{\text{NH}_3} = 3\,\%$ wt | D5 (G7) | 11.2 | 22.0 | 0.00 | 32.7 | A |
| | D6 (G8) | 10.5 | 18.9 | 0.00 | 25.3 | B |

TABLE 3.2: Overview of the growth and the dissolution experiments presented in Figure 3.9 and Figure 3.14. The letters G and D are used to indicate the growth and the dissolution experiments, respectively. The experiments in brackets refer to the growth experiments used to perform the corresponding dissolution experiments. The asterisk indicates experiments used in the validation set of the growth model. $T_{\text{initial}}$ and $T_{\text{final}}$ are the initial and final temperature of the experiment, $S_0$ is the initial level of supersaturation exploited, $m_{\text{s}}$ and $m_{\text{solids}}$ refer to the initial mass of seeds of the growth experiments and the total BC mass dissolved during the experiment, respectively. The set of growth experiments for which the final product CSD has been characterized using μ-DISCO measurements is highlighted in red. All crystallization runs have been carried out using a cooling rate of $-20\,°\text{C}\,\text{h}^{-1}$, while the dissolution experiments have been performed using a heating rate of $20\,°\text{C}\,\text{h}^{-1}$.

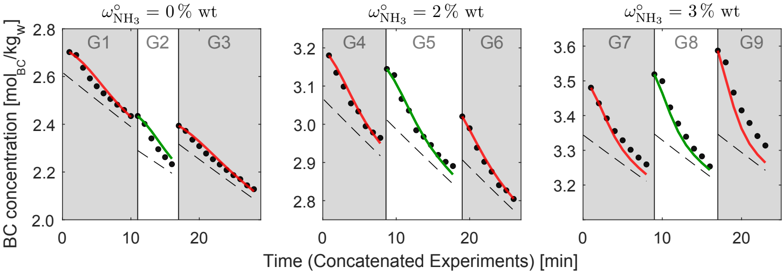

FIGURE 3.9: Concatenated seeded polythermal desupersaturation experiments in aqueous ammonia solutions of BC at 0 % wt, 2 % wt, and 3 % wt ammonia, respectively (cf. Table 3.2). The circular markers are the experimental BC concentration data points, the red curves are the fitted model's output. The green curves are the model's validation based on growth experiments not included in the fitting procedure (cf. Section 3.4.2), while the dashed lines indicate the BC solubility at the relevant temperature.

### 3.4.2 *Estimation of the Growth Rate Constant*

| **Kinetic Parameter** | **Value** |
|---|---|
| $\hat{k}_{g,1}$ [$\mathrm{m\,s^{-1}}$] | $(4.99 \pm 0.06) \cdot 10^{-6}$ |
| $\hat{k}_{d,1}$ [$\mathrm{m\,s^{-1}}$] | $(4.26 \pm 0.05) \cdot 10^{-6}$ |

Table 3.3: Optimal growth and dissolution kinetic parameters estimated using the procedure discussed in Section 3.3.5. Confidence intervals have been estimated with a probability $\alpha = 98\%$ assuming the model inputs to be error-free.

The growth rate constant $\hat{k}_{g,1}$ has been estimated using the set of growth experiments and corresponding operating conditions reported in Table 3.2. As illustrated in Figure 3.9, the parameter regression has been carried out by fitting the solute concentration profiles of six growth experiments performed in the temperature range 9 °C to 18 °C using a 0 %, 2 %, and a 3 % wt aqueous ammonia solution as solvent. In Figure 3.9 the red curves are the output of the model, the circular markers are the experimental BC concentration data points, and the green curves are the model predictions relative to a subset of growth experiments (intentionally excluded from the fitting data set) that serve the purpose of validating the growth model.

The range of initial supersaturation explored in the experiments ($0.05 \leq S \leq 0.15$) allowed for the growth of cuboidal crystals while minimizing the formation of needle-like particles (cf. Section 3.4.1). As shown in Figure 3.10, a particle shape classification performed on the CSDs of the final crystallization products confirmed the cuboidal shape of the majority of the particles sampled, thus validating the model assumption of constant volumetric shape factor (cf. Section 3.3). The resulting optimal value of the parameter $k_{g,1}$ (together with its confidence intervals) is reported in Table 3.3.

The repeatability of the growth experiments has been assessed by comparing the final normalized volume-weighted CSD, $n_v$, (rescaled based on its maximum value) of two crystallization experiments performed under similar experimental conditions. As shown in Figure 3.11, the data overlap nicely, thus indicating a good level of reproducibility. Despite the satisfactory quality of the overall fit shown in Figure 3.9, the solute concentration profiles relative to the sets of growth experiments performed in a 0 % and in a 2 % wt aqueous ammonia solution are slightly underestimated by the model, while the profiles relative to the experiments carried out using a 3 % wt aqueous ammonia solution are systematically overestimated. Additionally, Figure 3.12a shows a comparison between the optimal values of the model parameter $k_{g,1}$ (black circular markers) obtained by performing three independent parameter estimations, i.e. one for each solvent composition, and that resulting from the fitting of all the growth experiments together (dashed line); for the sake of completeness the fitting outcome of the individual sub sets of growth experiments is discussed in Appendix B.

As it can be noted from Figure 3.12a, the optimal values of the growth rate constant decrease with an increase of nominal ammonia concentration in the solvent. In particular, the decrease of the $\hat{k}_{g,1}$ value between the cases at 2 % and at 3 % wt aqueous ammonia solutions, for which no appreciable changes of the BC crystal habit has been noticed, may be due to crystal growth inhibition. Several mechanisms either based on the adsorption of foreign species on the active sites of the crystal surface, which blocks kink nucleation, or based on the formation of ion complexes in the solution, which decreases the number of growth units available for attachment on the surface of the crystals, have been proposed in the literature.[33,77,78,86,100] For the case of aqueous ammonia solutions of BC the concentration of carbonate and carbamate species increases as the nominal ammonia concentration in the solvent increases, thus resulting in significant concentration levels of foreign species in solution. This can be seen in Figure 3.12b where the speciation of the $CO_2-NH_3-H_2O$ system is shown as a function of the overall nitrogen to carbon species ratio, $\zeta$:

$$\zeta = \frac{c_{NH_4^+} + c_{NH_2COO^-} + c_{NH_3(aq)}}{c_{HCO_3^-} + c_{CO_3^{2-}} + c_{NH_2COO^-} + c_{CO_2(aq)}} \tag{3.17}$$

Within the range of $\zeta$ values explored in this study (cf. gray area highlighted in Figure 3.12b), i.e. between 1.0 (representative of aqueous solutions of BC) and 1.5, the carbon distribution in the liquid phase shifts from essentially bicarbonate ions to an equilibrium mixture of bicarbonate, carbonate, and carbamate ions as the value of $\zeta$ increases beyond one.

Finally, the capacity of the growth model to account for the effect of speciation on the BC supersaturation by means of a sound activity-based model renders the trend of the kinetic parameter $k_{g,1}$ shown in Figure 3.12a quite robust and reliable, thus further supporting the speculation on the role of impurities on the crystallization kinetics of ammonium bicarbonate.

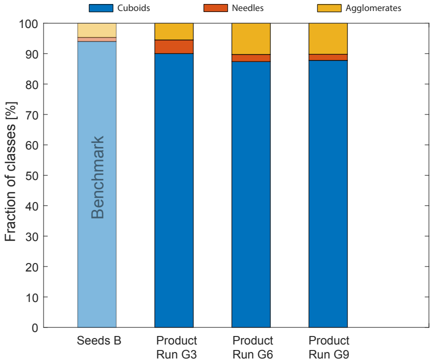

Figure 3.10: Fraction of classes in the final crystallization product relative to runs G3, G6, and G9 for which seeds B have been used. Additionally, the fraction of classes relative to the initial seed population (Seeds B) is reported as a benchmark.

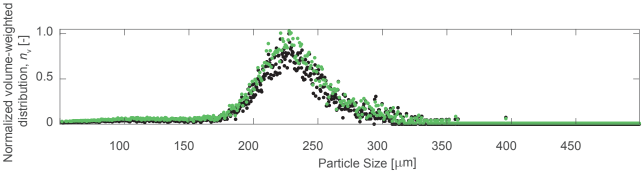

Figure 3.11: Reproducibility of the growth experiments. Black circular markers refer to the normalized volume-weighted CSD of the final crystallization product of run G3 (cf. Table 3.2), while the green circular markers represent a repetition of the experiment.

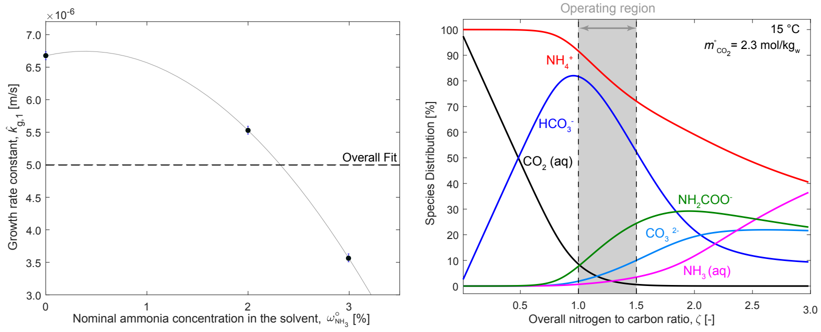

(a) (b)

Figure 3.12: (a) Optimal values of the growth rate constant $k_{g,1}$ (black circular markers) as a function of nominal ammonia concentration in the solvent $\omega^{\circ}_{NH_3}$. The optimal parameter values have been regressed from independent optimizations based on growth experiments performed in 0 % wt, 2 % wt, and 3 % wt aqueous ammonia solutions of BC, respectively. The dashed line indicates the value of the optimal parameter $k_{g,1}$ resulting from an overall optimization (performed using the whole set of growth experiments at different nominal ammonia concentration in the solvent); the solid black line is a guide for the eyes. (b) Modeled species distribution (in percentage) in an exemplary $CO_2-NH_3-H_2O$ system as a function of the ratio between nitrogen to carbon species $\zeta$; calculations have been performed with the thermodynamic model proposed by Darde et al.[30] The gray shaded area indicates the range of $\zeta$ values explored in this study. Due to the stoichiometry of the BC salt, aqueous solutions of BC are characterized by a $\zeta = 1$, while aqueous ammonia solutions of BC are characterized by $\zeta$ values greater than one depending on the nonstoichiometric ammonia content.

### 3.4.3 *Prediction of the CSD of a Crystallization Process*

After the estimation of the growth rate constant $\hat{k}_{g,1}$, the capability of the growth model to predict the final CSD of a crystallization process has been verified. For this purpose, off-line measurements of the CSD of final products resulting from a set of exemplary growth experiments have been compared to the output of the growth model. Furthermore, by evaluating the mismatch between the measured and modeled CSDs, the extent of phenomena such as agglomeration of particles or secondary nucleation has been analyzed.

In detail, off-line μ-DISCO measurements have been used to characterize the crystallization product of three different growth experiments in which seeds B have been grown from an aqueous solution at 0 %, 2 %, and 3 % wt ammonia, respectively (the set of experiments is highlighted in Table 3.2). Each product, collected at the end of phase III of the growth experiment according to the procedure discussed in Section 3.2.3, was dried at atmospheric conditions and then characterized. Each CSD measurement consisted, on average, of $5 \cdot 10^4$ sampled particles classified according to the algorithm described in Section 3.4.1. Contrary to other monitoring tools such as the Coulter-Counter,[101] the information on the crystal shape obtained using the μ-DISCO has been used to separate the contribution of the particles of similar aspect, e.g. cuboids, needles or agglomerates, to the overall CSD.

This work considers cubic and needle-like particles as primary particles, while agglomerates (cf. yellow bars in Figure 3.10) are treated as secondary particles; the CSDs accounting for primary particles only are referred to as primary distributions, while the ones also including agglomerates are secondary distributions. In all cases, the computation of the volume-weighted CSD, $n_V$, considers the equivalent volume of a cube of length $L$, regardless of the real shape of the particle.

Figure 3.13 shows a comparison between the measured and modeled normalized volume-weighted CSDs of the crystallization experiments mentioned earlier. The CSD of the seeds used for the experiments (i.e. seeds B) is shown as reference, while the primary and secondary CSDs are indicated using light blue and yellow circular markers, respectively.

The modeled CSDs of the seeds and of the final products are shown as solid red lines.

The secondary CSDs appear systematically skewed towards the larger crystal sizes compared to the model's simulations. Moreover, the fact that the primary CSDs also exhibit a marked positive skewness might indicated the presence of size-dependent growth that has not been investigated in this work.

Despite the deviations discussed, the agreement between the measurements and the model's simulations is satisfactory. The growth model is capable of predicting the mean size of the final primary CSDs with an underestimation of roughly 10 %. The trend of increasing values of the mean size of the CSDs of the experiments G3, G6, and G9 is also captured well by the model as shown in Figure 3.13, where the black and the red dashed lines indicate the value of the mean size of the measured and modeled CSDs, respectively.

### 3.4.4 *Estimation of the Dissolution Rate Constant*

A similar mathematical approach has been applied for the estimation of the parameter $k_{\mathrm{d},1}$ in eq 3.7b (cf. Section 3.3). The parameter regression is based on the simultaneous fitting of a set of six dissolution experiments performed in the temperature range 9 °C to 23 °C and in the nominal ammonia concentration range 0 % to 3 % wt. It must be noted that all dissolution experiments have been performed according to the experimental protocol described in Section 3.2.3 by heating a saturated suspension ($S = 0$) while monitoring the concentration evolution till complete dissolution. Of all the data points collected, only those that satisfy the criterion of eq 3.10 have been used for the parameter regression. The undersaturation levels explored were in a narrower range, i.e. $-0.05 \leq S \leq -0.02$, compared to those of growth experiments.

Determining the dissolution rate of ammonium bicarbonate using the setup described in Section 3.2.2 requires operation of the crystallizer at a minimum suspension density of 2−3 % wt to be able to detect changes in the solute concentration using ATR-FTIR measurements while dissolving crystals. As a consequence, the mass of solids required in each

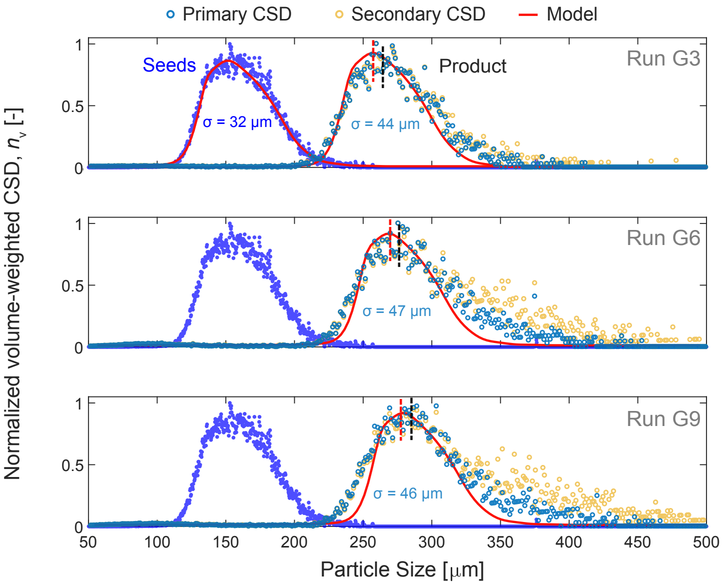

Figure 3.13: Normalized volume-weighted CSD of the final crystallization product of runs G3, G6, and G9 for which seeds B have been used (cf. Table 3.2). The initial seed distribution (seeds B) is indicated by blue markers, the hollow light blue and yellow markers indicate the primary and the secondary CSDs, respectively (cf. Section 3.4.3). The red solid curves are the initial seed distribution used in the growth model and the predicted final CSD of the growth process. The black and the red dashed lines indicate the values of the mean size of the measured and modeled CSDs, respectively. The parameter $\sigma$ refers to the standard deviation of each individual distribution of crystals.

dissolution experiment has to be at least 1 order of magnitude larger than the seed mass used during the growth experiments. Handling such an amount of solid material during the dissolution experiments would require a time-consuming characterization of the seeds, and most importantly, it would need a substantial upgrade of the seeds injection system to dose a greater amount of solids into a closed and pressurized system (while avoiding the evaporation of $NH_3$ and $CO_2$ to the atmosphere). Furthermore, the pressure built-up in the reactor and the suspension density level reached during operation do not always allow one to perform *in situ* μ-DISCO measurements.

To overcome this inconvenience, the real sampling of the population of crystals at the beginning of the dissolution experiment has been substituted with a prediction of the initial CSD computed using the growth model proposed in this work. The initial population of crystals used in a dissolution experiment has been obtained by growing seeds according to the procedure explained in Section 3.2.3 until reaching the equilibration step at the end of phase III. Then, the growth process has been simulated under the same experimental conditions, thus obtaining an estimate of the CSD of the population of crystals used in the aforementioned dissolution experiment.

It has to be noted that replacing the measurement of the real initial CSD with the prediction of the fitted growth model results in the underestimation of the dissolution kinetics of ammonium bicarbonate due to the model overestimation of the available crystal surface. This inaccuracy has been quantified by computing the ratio Γ between the second moments of the modeled and measured CSDs of a set of exemplary growth experiments shown in Figure 3.13:

$$\Gamma = \frac{\mu_{2,\mathrm{M}}}{\mu_{2,\mathrm{E}}} \tag{3.18}$$

where $\mu_{2,\mathrm{M}}$ and $\mu_{2,\mathrm{E}}$ are the second moment of the simulated and measured number-based CSD, respectively.

Prior to the computation of the ratio Γ, all the distributions have been rescaled so as their third moments (total crystal volume) would match, thus allowing for a fair comparison. The values of the ratio Γ reported in Table 3.4 show a systematic model overprediction of the crystal surface compared to the measured value. For the case of the primary CSDs, the overprediction has been quantified to an average value of approximately 4 %, while for the case of the secondary CSDs the error increases to approximately 8 %. This latter value can therefore be assumed as a conservative underestimation error of the overall dissolution rates.

The resulting optimal value of the dissolution rate constant $k_{d,1}$ (together with its confidence intervals) and the details on the experimental conditions adopted for the dissolution experiments are reported in Table 3.2 and Table 3.3, respectively.

The purely diffusional nature of the dissolution process, contrary to the case of crystal growth, does not involve any competition for active sites on the surface of the dissolving crystals. Therefore, the formation of species different from the ammonium and bicarbonate ions in the $CO_2-NH_3-H_2O$ system should, in principle, only influence the level of undersaturation of the solution. This may be the reason of the good overall fit of the solute concentration profiles shown in Figure 3.14, regardless of the speciation of the system. In Figure 3.14, the red curves are the dissolution model output, while the circular markers are the experimental BC concentration data points.

| **Run** | $\Gamma$ [%]<br>Primary CSD | $\Gamma$ [%]<br>Secondary CSD |
|---|---|---|
| G3 | 103.1 | 107.4 |
| G6 | 104.2 | 108.2 |
| G9 | 104.9 | 109.2 |

Table 3.4: Overview of the calculated ratios between the second moment of the modeled and of the measured number-based CSDs relative to the growth experiments G3, G6, and G9 shown in Figure 3.13.

### 3.4.5 *Comparison to Literature*

To the best of our knowledge the growth rates of ammonium bicarbonate have been previously investigated only by Sutter and Mazzotti,[37] while no published data is available on the dissolution rates of ammonium bicarbonate in aqueous ammonia solutions. When simply adopting the growth model proposed by Sutter and Mazzotti[37] and comparing the simulation results to our experiments, it is found that

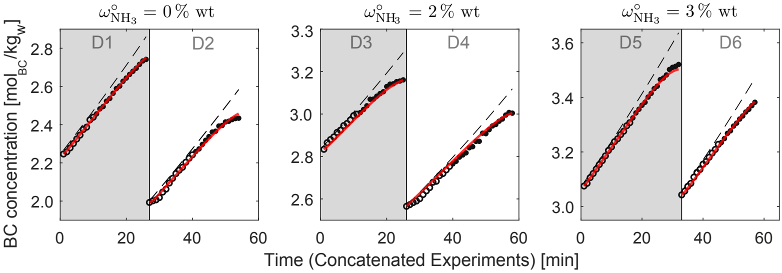

Figure 3.14: Concatenated polythermal dissolution experiments for 0 %, 2 %, and 3 % wt aqueous ammonia solutions of BC (cf. Table 3.2). The filled markers are the experimental BC concentration data points used for the parameter regression, while the hollow circular markers have been excluded from the fitting data set, according to eq 3.10. The red curves are the fitted model output. The dashed lines indicate the BC solubility value at the relevant temperature.

the predicted solute concentration depletion is vastly overestimated. The source of the deviation has been found to be a conversion error in the computation of the initial population of seeds measured experimentally by Sutter and Mazzotti[37] that led to an overestimation of the crystal growth rates. Therefore, in order to enable a comparison of the growth rates, we have newly estimated the value of the kinetic parameter $k_{g,1}$ of the growth model proposed in this work (cf. Section 3.3) based solely on the fitting of the experimental data provided by Sutter and Mazzotti.[37] We have thus obtained a value of the kinetic parameter of $4.15 \times 10^{-6}\,\mathrm{m\,s^{-1}}$, i.e. roughly 20 % lower than the value estimated in this work (cf. Table 3.3). It must be acknowledged that most of the experimental data provided by Sutter and Mazzotti[37] lies in a lower temperature range compared to the one investigated in this work, thus possibly explaining a lower value of the kinetic constant. We therefore refrain from doing any further comparison and only state that the modeled growth rates of ammonium bicarbonate in this work and in Sutter and Mazzotti's work[37] are very similar, though not identical, as shown in Figure 3.15, where the two growth rates are plotted as black

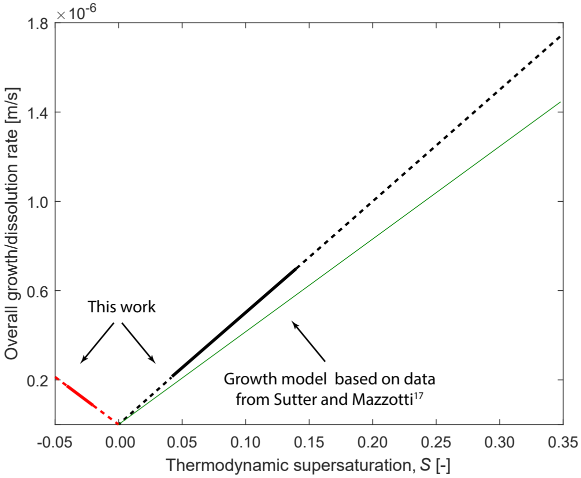

Figure 3.15: Overall growth and dissolution rates as a function of supersaturation, $S$. The growth and the dissolution rates of this study have been estimated in the temperature interval 10−19 °C and 10−23 °C, respectively (cf. Table 3.2). Solid lines indicate the growth/dissolution rates in the range of supersaturation investigated in this work. The dashed lines indicate the extrapolated values of the growth and the dissolution rates. The green line, shown for comparison, indicates the growth rates of the ammonium bicarbonate crystals in aqueous solution estimated based on the data from Sutter and Mazzotti.[37]

and green lines respectively, while the dissolution rate of ammonium bicarbonate is indicated as a red line.

## 3.5 CONCLUSIONS

In this work, the growth kinetics and the dissolution kinetics of ammonium bicarbonate have been estimated using a monodimensional population balance model (eq 3.1). The parameters of the model have been regressed using the information on the evolution of the solution concentration during batch polythermal experiments in which seed crystals of known distribution have been grown or dissolved depending on the process under consideration.

In the range of operating conditions adopted, aqueous ammonia solutions of ammonium bicarbonate can withstand a relatively low degree of subcooling before nucleating spontaneously ($\approx$ 4-5 °C). This limits considerably the maximum supersaturation level that can be explored experimentally (e.i. roughly $S \leq 0.15$). Furthermore, the range of supersaturation explored in this study has been carefully chosen so as ammonium bicarbonate crystals could grow preferentially as cuboids, thus allowing assumption of a constant shape factor (i.e. that of a cube) for all the simulations.

As discussed in Section 3.4.2 and Section 3.4.4, the models presented in this work capture accurately the evolution of the solute concentration measured during the experiments, thus allowing for a robust and reliable estimation of the kinetic parameters. It is worth noting that the main limitation of the growth model concerns the predictability of the final CSD after growth. The model is capable of describing quantitatively the properties of the CSD such as its mean size, and underpredicts systematically the skweness of the distribution. This is probably due to the effect of a size-dependent growth mechanism (and partially due to the effect of agglomeration) not included in the model because it is considered to be a negligible phenomenon under the operating conditions explored. Similarly, the limitation of the dissolution model lies in the methodology adopted to regress the kinetic parameter, $k_{\mathrm{d},1}$. This procedure, dictated by the experimental limitations discussed in Section 3.4.4, causes, on average, an overestimation of the available crystal surface that leads to an underestimation of the dissolution rates by approximately 4 % to 8 %.

In principle, the rigorous thermodynamic framework adopted in this work allows to extend the use of the models for growth and for dissolution to a wider range of nominal ammonia concentration in the solvent, provided that the supersaturation/undersaturation level lies in a similar range as reported in this study. However, particular care must be taken while extrapolating these models due to the sensitivity of the shape of the BC crystals to changes in the process conditions, i.e.

solvent composition and supersaturation (cf. Section 3.4.1).
Moreover, operating the μ-DISCO in an online mode by measuring the properties of slurries of BC crystals in aqueous ammonia solutions has posed several challenges due to the high volatility of the solutes and the pressure limitations of the monitoring device. In this respect, an improved design would allow for real-time measurements of the evolution of the BC crystal size and shape during crystallization and dissolution, thus enabling the implementation of a more complex and possibly accurate kinetic models.[89]
Despite the limitations mentioned above, the rate-based models developed in this work can be particularly useful for the design of crystallization and dissolution equipment in processes such as the CSF-CAP[25,42] in which solid formation is exploited for $CO_2$ capture purposes.

# NOMENCLATURE

## *Acronyms*

| | |
|---|---|
| ATR-FTIR | Attenuated total reflection-infrared spectroscopy |
| BC | Ammonium bicarbonate |
| CAP | Chilled ammonia process |
| CLF | Courant Friedrichs Lewy condition |
| CSD | Crystal size distribution |
| CSF-CAP | Controlled solid formation-chilled ammonia process |
| DISCO | Dual imaging system for crystallization observation |
| FBRM | Focused beam reflectance measurement |
| HRM | High resolution method |
| LV | PLSR latent variable |
| MLE | Maximum likelihood estimation |
| PBE | Population balance equation |
| PLS | Partial least squares |
| PVM | Particle view measurement |
| RMSE-CV$_{10}$ | Root mean squared error of 10-fold cross validation [$\mathrm{mol\,kg^{-1}}$] |
| SLE | Solid liquid equilibrium |
| UNIQUAC | Universal quasi-chemical |
| VLSE | Vapor liquid solid equilibrium |
| XRD | X-ray diffraction |

## *Greek Symbols*

| | |
|---|---|
| $\alpha$ | Probability [%] |
| $\bar{\sigma}$ | Standard deviation of the ATR-FTIR concentration measurements |
| $\Delta\mu$ | Chemical potential difference |
| $\Gamma$ | Ratio of the second moments of the CSDs [-] (eq 3.18) |
| $\gamma$ | Activity coefficient for an electrolyte species |
| $\mu$ | Chemical potential [$\mathrm{J\,mol^{-1}}$] |
| $\mu_p$ | $p$-th moment of the CSD [$\mathrm{m^p/kg}$] |
| $\nu$ | Courant number (eq 3.12) |
| $\omega^{\circ}_{\mathrm{NH_3}}$ | Nominal ammonia concentration in aqueous solution (% wt) [-] |
| $\Psi$ | MLE objective function |
| $\rho_\mathrm{s}$ | Density of the crystalline phase [$\mathrm{kg/m^3}$] |
| $\tilde{\nu}$ | IR spectrum wavenumber [$\mathrm{cm^{-1}}$] |
| $\varphi$ | CSD scaling factor [-] |
| $\zeta$ | overall nitrogen to carbon ratio [-] |

*Roman Symbols*

| | |
|---|---|
| $a$ | Advection velocity [$\mathrm{m\,s^{-1}}$] |
| $c$ | Solute concentration (molality-based) [$\mathrm{mol\,kg^{-1}}$] |
| $D$ | Overall crystal dissolution rate [$\mathrm{m\,s^{-1}}$] |
| $E_{\mathrm{a,g}}$ | Apparent activation energy of the growth process [$\mathrm{J\,mol^{-1}}$] |
| $F_{\chi^2}^{-1}$ | Inverse $\chi^2$ cumulative distribution function |
| $G$ | Overall crystal growth rate [$\mathrm{m\,s^{-1}}$] |
| $\mathbf{k}_{\mathrm{d}}$ | Parameter vector for the dissolution model |
| $k_{\mathrm{d},1}$ | Dissolution rate constant [$\mathrm{m\,s^{-1}}$] |
| $\mathbf{k}_{\mathrm{g}}$ | Parameter vector for the growth model |
| $k_{\mathrm{g},0}$ | Pre-exponential growth factor [$\mathrm{m\,s^{-1}}$] |
| $k_{\mathrm{g},1}$ | Growth rate constant [$\mathrm{m\,s^{-1}}$] |
| $K_{\mathrm{IP}}$ | Ammonium Bicarbonate ionic product (mole frac. based) [-] |
| $K_{\mathrm{SP}}$ | Ammonium Bicarbonate solubility product (mole frac. based) [-] |
| $k_{\mathrm{v}}$ | Volumetric shape factor [-] |
| $L$ | Particle-size coordinate [m] |
| $M_{\mathrm{s}}$ | Mass of the solvent (water) [kg] |
| $m_{\mathrm{s}}$ | Mass of seed crystals used in each growth/dissolution experiment [kg] |
| $n$ | Crystal size distribution (number-based) [$\mathrm{m^{-1}\,kg^{-1}}$] |
| $N_{\mathrm{b}}$ | Number of discretization grid points of the particle-size domain |
| $N_{\mathrm{t}}$ | Number of data points in the experimental time series |
| $n_{\mathrm{v}}$ | Crystal size distribution (volume-based) [$\mathrm{m^2kg^{-1}}$] |
| $N_k$ | Number of degrees of freedom |
| $R$ | Ideal gas law constant [$\mathrm{J\,mol^{-1}\,{}^{\circ}C^{-1}}$] |
| $S$ | Thermodynamic supersaturation [-] |
| $T$ | Temperature [°C] |
| $t$ | Time [s] |
| $V_{\mathrm{s}}$ | Volume of seed crystals sampled using the μ-DISCO [$\mathrm{m^3}$] |
| $\mathbf{V}_k$ | Parameter covariance matrix |

*Subscripts and Superscripts*

| | |
|---|---|
| $\circ$ | Superscript pertaining to a nominal concentration |
| 0 | Subscript pertaining to an initial condition |
| A | Subscript pertaining to the seed crystals of fraction A |
| B | Subscript pertaining to the seed crystals of fraction B |
| E | Subscript pertaining to measured quantities |

| | |
|---|---|
| $i$ | Subscript pertaining to the $i$-th experimental data point in the time series |
| $j$ | Subscript pertaining to the $j$-th grid point in the particle-size domain |
| $k$ | Subscript pertaining to the $k$-th model parameter |
| $l$ | Subscript pertaining to the $l$-th chemical species in solution |
| $\mathrm{M}$ | Subscript pertaining to modeled quantities |
| $p$ | Subscript pertaining to the $p$-th moment of the CSD |
| $*$ | Superscript pertaining to quantity at thermodynamic equilibrium |
| $\hat{\ }$ | Superscript pertaining to an estimator |

# 4

# EFFECT OF SULFATE IMPURITY ON THE GROWTH KINETICS

## 4.1 INTRODUCTION

Despite the urge to reduce the hydrocarbons consumption and eventually to replace it with sustainable energy sources, fossil fuels will continue to be an important part of the energy mix for decades to come.[8] In this context, carbon capture and storage (CCS) is an essential part of the portfolio of technologies that aim at mitigating the emissions

---

The work presented in this chapter has been reproduced with permission from Milella, F.; Mazzotti, M. Estimation of the Growth and the Dissolution Kinetics of Ammonium Bicarbonate in Aqueous Ammonia Solutions from Batch Crystallization Experiments. Part II. The Effect of Sulfate Impurity. *Cryst. Growth Des.* **2020**, 20, 2, 948-963. DOI: 10.1021/acs.cgd.9b01315. Copyright 2020 American Chemical Society)

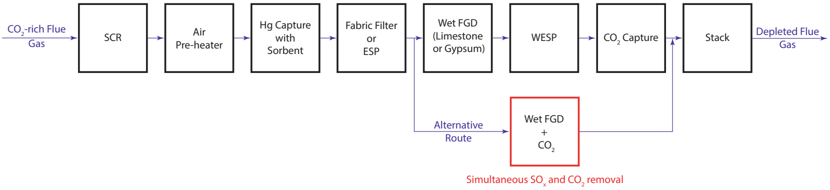

FIGURE 4.1: Arrangement of the emission-control equipment after a reference pulverized coal (PC) boiler.[102] The equipment arrangement for capturing $NO_x$, $SO_x$, particulate matter (PM), mercury, and carbon dioxide includes a selective catalytic reactor (SCR) for $NO_x$ removal, sorbents for Hg capture, electrostatic precipitators (ESPs) or fabric filters (FFs), a flue gas desulfurization unit (FGD) for $SO_x$ removal, wet electrostatic precipitators (WESP) for $SO_3$ removal, and eventually a $CO_2$ capture unit. The alternative route, highlighted with a red box, includes the flue gas desulfurization and the $CO_2$ capture in the same equipment, i.e. an absorption column.

of greenhouse gases and, ultimately, climate change.

Within the framework of post-combustion $CO_2$ capture processes, the so-called Chilled Ammonia Process (CAP) developed by Alstom[102] is an ammonia-based absorption process that may capture $CO_2$ from highly concentrated point sources such as cement, steel, and power plants. Contrary to amine-based processes the CAP uses a solvent, i.e. aqueous ammonia, that does not degrade and that can be regenerated at high pressure ($10-20\,\mathrm{bar}$), thus reducing $CO_2$ compression costs. More recently, it has been shown that a significant enhancement of the capture efficiency of the CAP can be obtained through a controlled solid formation-CAP (CSF-CAP) that exploits the precipitation of ammonium bicarbonate in a dedicated section of the plant.[25] With this novel process comes the call for the integration and optimization of a continuous solid-handling section in the capture plant[42] as well as for the estimation of the crystallization kinetics of ammonium bicarbonate[37,103] required for sizing the relevant crystallization equipment. Furthermore, the alkaline nature of the solvent used in the CSF-CAP allows not only for the abatement of $CO_2$, but also for the removal of sulfur-based compounds resulting from the combustion of coal or gas such as $SO_2$ and $SO_3$ (collectively referred to as $SO_x$), which speciate mainly into ${SO_4}^{2-}$ upon absorption.[102] Hence, the simultaneous capture of $CO_2$ and $SO_x$ in the absorption unit of the CSF-CAP, represented schematically in Figure 4.1 as an alternative to the standard process configuration, would in principle allow to avoid the capital cost of some of the equipment of the emission control system, i.e. the flue gas desulfurization unit (FGD). On the contrary, the presence of impurities in the solvent, such as sulfur compounds or heavy metals, might influence the thermodynamic and kinetic properties of the crystallizing system, thus significantly modifying the ammonium bicarbonate crystallization kinetics.[33,86]

Against this background, detailed thermodynamic models describing the liquid-vapor equilibria of aqueous systems containing ammonia, carbon dioxide, and sulfur (in the form of sulfate ions) can be found in the liturature,[74,104] while no information is currently available on the effect of sulfate ions on the solid-liquid equilibrium of ammonium bicarbonate and on its crystallization kinetics in solution.

The aim of this work is therefore to investigate the role of sulfate ions, on the growth kinetics of ammonium bicarbonate in aqueous ammonia solutions by means of a detailed thermodynamic and kinetic modeling approach. The proposed methodology is used to compute the activity-based solution supersaturation, thus allowing to estimate reliably the growth rates of ammonium bicarbonate in presence of sulfate ions.

The Chapter is organized as follows: Section 4.2 introduces the thermodynamics and the modeling of the $CO_2-NH_3-H_2O-SO_x$ system and, in particular, discusses the electrolyte species that form in solution. In Section 4.3, the experimental setup, the analytical methods and the characterization techniques used for the continuous and for the suspended phases are discussed. Section 4.4 provides a description of the mathematical framework used to simulate the crystal growth process as well as of the parameter estimation procedure adopted. Finally, the results are discussed comprehensively in Section 4.5.

## 4.2 THERMODYNAMICS OF THE $CO_2-NH_3-H_2O-SO_x$ SYSTEM

The quantity of sulfur present in fossil-fuels burnt in power plants varies widely and may range from 0.5 % to 5 % by weight.[102] Moreover, as the fossil-fuel burns in a power plant's furnace, more than the 90 % of the sulfur is oxidized to gaseous $SO_2$. The further conversion of $SO_2$ to $SO_3$ is a complex kinetically limited process, mostly controlled by the $SO_2$ oxidation due to the presence of molecular oxygen in the furnace.[102] Furthermore, the equilibrium conversion of the reaction

$$SO_2(g) + \frac{1}{2}O_2(g) \rightleftharpoons SO_3(g) \tag{4.1}$$

increases with decreasing temperature and approaches unity for temperatures below 250 °C. As a result, the concentration of sulfur oxides in the products of combustion ranges typically between 0.05 to 0.30 % by volume.

In the context of ammonia-based absorption processes for $CO_2$ capture, the presence of $SO_x$ in the flue gas to be treated makes it necessary to consider the quaternary $CO_2-NH_3-H_2O-SO_x$ system, which is the complex volatile electrolytic system shown schematically in Figure 4.2. Several chemical equilibria can be established according to the relevant operating conditions. In detail, eqs 4.2-4.6 describe the vapor-liquid equilibria of the system including the dissolved oxigen ($O_2$(aq)) from air, while the chemical reactions of eqs 4.7-4.12 describe the speciation of $NH_3$, $CO_2$ and $SO_x$ into nonvolatile electrolytic species in the liquid phase. The speciation reactions include, the dissociation of $CO_2$, $NH_3$, and $HCO_3^-$, the formation of the carbamate ion (eq 4.11), the autoprotolysis of water, and the reactions of $SO_x$ to $SO_4^{-2}$. In the alkaline environment of the aqueous ammonia solutions (pH $\geq$ 9), the formation of $HSO_4^-$ ions is thermodynamically unfavourable[105] and it has therefore been neglected in this study. Solid compounds such as $NH_4HCO_3$, $(NH_4)_2SO_4$, $(NH_4)_2CO_3 \cdot H_2O$, $(NH_4)_2CO_3 \cdot 2\,NH_4HCO_3$, $H_2O(s)$, and $NH_2COONH_4$ can form in the system, under the relevant process conditions.[28] However, ammonium bicarbonate (also referred to as BC in the following) is the only stable salt that could precipitate by being the least soluble compound among the inorganic salts mentioned above under the process conditions investigated.

*Vapor-Liquid Equilibria*:

$$CO_2(g) \rightleftharpoons CO_2(aq) \tag{4.2}$$

$$O_2(g) \rightleftharpoons O_2(aq) \tag{4.3}$$

$$NH_3(g) \rightleftharpoons NH_3(aq) \tag{4.4}$$

$$H_2O(g) \rightleftharpoons H_2O \tag{4.5}$$

$$SO_x(g) \rightleftharpoons SO_x(aq) \tag{4.6}$$

*Equilibrium Speciation (Liquid Phase)*:

$$NH_3(aq) + H_2O \rightleftharpoons NH_4^+ + OH^- \tag{4.7}$$

$$CO_2(aq) + H_2O \rightleftharpoons H^+ + HCO_3^- \tag{4.8}$$

$$HCO_3^- \rightleftharpoons H^+ + CO_3^{2-} \tag{4.9}$$

$$H_2O \rightleftharpoons H^+ + OH^- \tag{4.10}$$

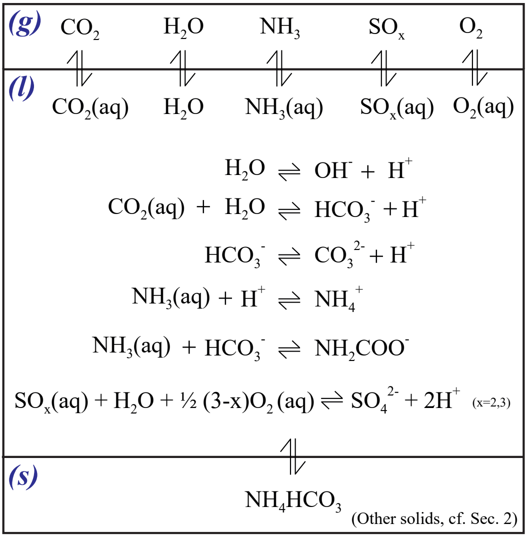

FIGURE 4.2: Schematic representation of the phase equilibria in the $CO_2{-}NH_3{-}H_2O{-}SO_x$ system. Many solid compounds could precipitate under the relevant process conditions (cf. Section 4.2), however ammonium bicarbonate is the only stable salt that could be formed under the process conditions investigated in this work.

$$NH_3(aq) + HCO_3^- \rightleftharpoons NH_2COO^- + H_2O \tag{4.11}$$

$$SO_x(aq) + H_2O + \frac{1}{2}(3-x)O_2(aq) \rightleftharpoons SO_4^{2-} + 2\,H^+ \quad x = 2,3 \tag{4.12}$$

*Solid-Liquid Equilibrium*:

$$NH_4HCO_3(s) \rightleftharpoons NH_4^+ + HCO_3^- \tag{4.13}$$

### 4.2.1 *Modeling of the Liquid Speciation*

The thermodynamic model presented in this section has been used to describe the liquid speciation of the $CO_2-NH_3-H_2O-SO_x$ system accounting for the strong non-idealities of the liquid phase through the extended-UNIQUAC model.[28,76]

The condition for chemical equilibrium of each $r$-th chemical reaction in the system yields the following equation:

$$-\frac{\Delta G_r^\circ(T)}{RT}=\sum_i \nu_{i,r}\ln(m_i\gamma_i)\quad\forall\, r \tag{4.14}$$

where $\Delta G_r^\circ(T)$ is the change in standard Gibbs free energy of the $r$-th reaction at the temperature $T$, $m_i$ and $\gamma_i$ are the concentration (molality-based with respect to water, assumed as the solvent in the system) and the activity coefficient of the $i$-th component, respectively, and $\nu_{i,r}$ is the stoichiometric coefficient of component $i$ in the $r$-th reaction.[28]

The following conservation equations for the overall amounts of nitrogen, of carbon, and sulfur atoms present in the liquid phase have been applied:

$$m_C^\circ-m_{CO_2}-m_{HCO_3^-}-m_{CO_3^{2-}}-m_{NH_2COO^-}=0 \tag{4.15a}$$

$$m_N^\circ-m_{NH_3}-m_{NH_4^+}-m_{NH_2COO^-}=0 \tag{4.15b}$$

$$m_S^\circ-m_{SO_4^{2-}}=0 \tag{4.15c}$$

where the quantities $m_C^\circ$, $m_N^\circ$, and $m_S^\circ$ in eq 4.15 are the overall concentration of carbon, nitrogen, and sulfur in the system.

The condition for electroneutrality in the liquid phase yields:

$$m_{NH_4^+}+m_{H^+}-m_{OH^-}-m_{HCO_3^-}-2m_{CO_3^{2-}}-m_{NH_2COO^-}-2m_{SO_4^{2-}}=0 \tag{4.16}$$

As described in detail in Section 4.3, this work uses ammonium sulfate (also referred to as AS in the following) in the experiments in place of $SO_2$(g) and $SO_3$(g) to avoid the presence of hazardous compounds in the laboratory. The solid-liquid equilibrium of the ammonium sulfate, described by the following equation, has been therefore considered:

$$(NH_4)_2SO_4(s) \rightleftharpoons 2\,NH_4{}^+ + SO_4{}^{2-} \tag{4.17}$$

It must be noted that in the range of AS concentration used in this work, the solutions investigated were *undersaturated* with respect to ammonium sulfate and the dissolution of AS, which is mildly acidic, did not lead to a significantly change in the pH of the solutions, nor to a significant increase of the total pressure above the ammonium sulfate containing solutions, as reported by Kurz et al.[74] Therefore, the overall carbon, nitrogen and sulfur concentrations of aqueous ammonia solutions containing BC and AS have been computed based on the nominal concentrations of dissolved salts, i.e. $m^{\circ}_{\mathrm{BC}}$, and $m^{\circ}_{\mathrm{AS}}$, and on the nominal aqueous ammonia concentration, $m^{\circ}_{\mathrm{NH_3}}$:

$$m^{\circ}_{\mathrm{C}} = m^{\circ}_{\mathrm{BC}} \tag{4.18a}$$

$$m^{\circ}_{\mathrm{N}} = m^{\circ}_{\mathrm{NH_3}} + m^{\circ}_{\mathrm{BC}} + 2m^{\circ}_{\mathrm{AS}} \tag{4.18b}$$

$$m^{\circ}_{\mathrm{S}} = m^{\circ}_{\mathrm{AS}} \tag{4.18c}$$

The molality-based concentrations appearing in eq 4.18 have been computed based on the nominal amount of water (solvent), $M^{\circ}_{\mathrm{s}}$, initially added to the reactor.

In line with the experimental procedure that minimizes the head space (consisting mainly of air) of the sealed reactor used in this work (cf. Section 4.3), the vapor-liquid equilibria of the system have been neglected in the model due to their minor contribution to the overall mass balances.

The computation of the liquid speciation has therefore been performed by solving the equations that describe the liquid phase equilibrium reactions (in the form of eq 4.14) together with eq 4.15 and eq 4.16, also accounting for the BC solid-liquid equilibrium described by eq 4.13 whenever the formation of a solid phase was thermodynamically favorable.

It must be noted that the operating conditions adopted in this work

allowed to assume the equilibrium of the reaction of sulfate ions formation (eq 4.12) to be completely shifted towards the products of the reaction, i.e. the sulfate ion and the proton species. Furthermore, the BC and AS salts have been considered to be fully dissociated in solution. The formation of ion complexes, which to the best of our knowledge does not occur in the system, has not been included in the model (the interested reader is referred to Appendix C for further details).
The activity coefficients of both the neutral and the ionic species have been calculated by using the extended-UNIQUAC model with the parameters proposed earlier.[76] This activity coefficient model has been updated by including the sulfate ion's model parameters, which account for the interactions between the sulfate ions and the other species in solution. These parameters have been estimated by fitting the solubility data of BC in aqueous ammonia solutions containing dissolved ammonium sulfate with a procedure discussed in Section 4.5.2.

## 4.3 EXPERIMENTAL

### 4.3.1 *Materials*

The electrolyte solutions have been prepared by dissolving analytical grade chemicals purchased from Sigma-Aldrich (Buchs, Switzerland) in Milli-Q water (18.2 MΩ cm at 25 °C).
Ammonium bicarbonate (Sigma-Aldrich, $NH_4HCO_3$, BioUltra, $\geq 99.5\,\%$ pure) has been used without further purification, while ammonium sulfate ($(NH_4)_2SO_4$ with purity level greater than 99.0 %) has been degassed and dried under vacuum before use.
Aqueous ammonia solutions at a nominal ammonia concentration, $\omega^{\circ}_{NH_3}$, of 2 % wt have been prepared by diluting a commercial ammonium hydroxide solution (Sigma-Aldrich, puriss. p.a., reag. ISO, reag. Ph. Eur. 25 % wt) with Milli-Q water. The ammonia concentration of the purchased solutions has been determined via acid-base titration performed with a 702 SM Titrino (METROHM, Switzerland) and a 1M HCl titrant solution.
The preparation of the mixtures has been carried out with a PG8001

analytical balance (Mettler-Toled, Switzerland) with a readability and maximum capacity of 0.1 g and 8.1 kg, respectively. The estimated accuracy of the static measurement is ± 0.23 g.
$BaCl_2 \cdot 2\,H_2O$ (Sigma-Aldrich, $\geq$ 99 % pure) has been used to prepare a saturated aqueous solution of $BaCl_2$ at room temperature then used for the $SO_4{}^{2-}$ assay described in Section 4.3.

### 4.3.2 *Methods*

#### *Characterization of the Continuous Phase*

*ATR-FTIR Measurements*. Attenuated total reflection-Fourier transform infrared (ATR-FTIR) spectroscopy has been used to monitor the overall BC liquid concentration (cf. Section 4.5.1). Measurements have been performed with a ReactIR 45m (Mettler-Toledo, Switzerland) equipped with a 1.6 cm DiComp immersion probe and a 6 internal reflections diamond ATR crystal that allows to probe the liquid phase only, regardless of the presence of solids. Spectra have been collected in the 800-3000 $cm^{-1}$ region with a wavenumber resolution of 4 $cm^{-1}$ and averaged over 256 scans using an exposure time of 1 min. The ATR-FTIR background signal has been collected in air at ambient conditions before every experiment.

#### *Characterization of the Suspended Phase*

*FBRM Measurements*. A laboratory-scale device (Lasentec, WA) has been used to perform focused beam reflectance measurements (FBRM). This device has been used for the detection of the onset of primary nucleation during the ATR-FTIR calibration procedure (cf. Section 4.5.1) and for the monitoring of the steady-state reached at the end of the crystallization process. A 1 min measurement duration has been set for all the FBRM measurements at a laser speed of 2 $m\,s^{-1}$.
*μ-DISCO Measurements*. An opto-mechanical stereoscopic device, known as the μ-DISCO, and described elsewhere[38] has been used to perform an off-line characterization of the crystal size distribution (CSD) of the

seeds as well as of the solid products obtained from the crystallization experiments. During the analysis, a representative sample of the crystal population has been suspended in an ethanol solution saturated with BC and continuously recirculated through the μ-DISCO's cell. Measurements have been performed every 2 min acquiring 1600 images per measurement until the cumulative number of sampled particles reached a value above 30,000. Based on an approximation of the volume of each sampled particles, the device allows to reconstruct the 1-D CSD of the population of crystals.

*Powder X-Ray Diffraction*. Powder X-ray diffraction patterns (PXRD) were recorded after samples were spread uniformly over the sample holder using a diffractometer from Bruker (D2 Phaser, 30 kV, 10 mA, Cu KR; Karlsruhe, Germany). Patterns were recorded at $2\theta$ between $10°$ and $80°$ with resolution of $0.02°$ and a scan speed of $5.8\,°\,\mathrm{min}^{-1}$.

*Sulfate Assay*. The presence of sulfate ions in the BC crystals obtained after each crystallization experiment has been assayed gravimetrically as $BaSO_4$, which is sparingly soluble in water.[106] The interested reader is referred to Appendix C for the detailed assay procedure.

An AX205 analytical balance (Mettler-Toled, Switzerland) with a readability and maximum capacity of 0.01 mg and 220 g, respectively, has been used to weigh the amount of $BaSO_4$ precipitated.

### *Seed Crystals Preparation*

Two different batches of BC seed crystals have been used in this work, namely seeds type A and type B. They have been obtained by temperature cycles performed on ammonium bicarbonate crystals recrystallized from a supersaturated aqueous solution of BC. The size ranges obtained were between $100-250\,\mu\mathrm{m}$ for seeds A, and between $150-350\,\mu\mathrm{m}$ for seeds B. The two populations of seeds have been stored under nitrogen atmosphere to prevent contact with moisture in the air prior to use in the growth experiments described in Section 4.3.3. Figure 4.3 shows the normalized volume-weighted CSD of the seeds used in this work (the interested reader is referred to Appendix C for the corresponding micrographs of the seed populations).

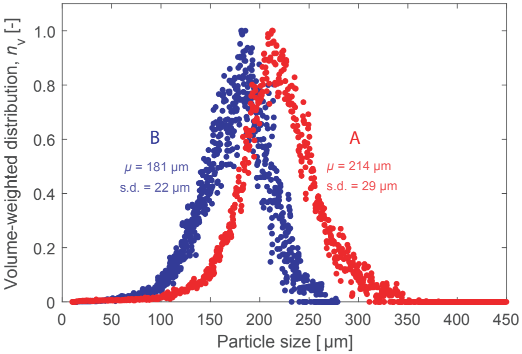

FIGURE 4.3: Number-based crystal size distribution of the populations of BC seed crystals used in this work. The red circular markers define the CSD of the type A seeds, while the blue circular markers irefert to the type B seeds. The most relevant statistical properties of the distribution, such as mean, $\mu$, and standard deviation, $\sigma$, are reported in the plot for each type of seeds. Each distribution has been reconstructed using roughly 30000 particles.

### 4.3.3 *Experimental Setup and Protocol for the Seeded Desupersaturation Experiments*

The presence of highly volatile neutral species in solution such as $NH_3$(aq) and $CO_2$(aq) makes it necessary to operate the system under its own vapor pressure to avoid material loss due to solute evaporation. This has been achieved by performing the experiments in a stainless steel sealed reactor whose technical details have been reported elsewhere.[37] In our experimental setup, the presence of a vapor phase, consisting mainly of inert air (saturated with water, ammonia and carbon dioxide) has been minimized by filling almost entirely the reactor's volume with liquid, thus allowing to neglect the contribution of the gas phase to the material balance of the reactor.

Prior to sealing the vessel, the nominal amounts of water, aqueous ammonia, BC, and AS ($m^{\circ}_{\mathrm{AS}}$) have been fed into the 1.4 L reactor. The maximum operating pressure of the vessel has been set to 5 barg, and a speed of 400 rpm of the 4-bladed stirrer with 45° pitched paddles has ensured adequate mixing of the liquid in the turbulent regime while minimizing attrition and breakage of the dispersed phase. The process temperature has been controlled by means of a CC230 thermostat (Huber, Germany) connected to a Pt-100 probe immersed in the liquid phase of the reactor acquiring data at a frequency of $30\,\mathrm{s}^{-1}$.

On-line monitoring tools such as FBRM and ATR-FTIR have been connected to the reactor by means of custom-made pressure connectors installed on the lid of the vessel, while a solid dosing system described elsewhere[103] has been used for the injection of seed crystals directly into the liquid phase.

The BC crystallization from aqueous ammonia solutions containing sulfate ions has been carried out in the temperature range 10 °C to 18 °C by varying the initial supersaturation, the nominal concentration of ammonia $m^{\circ}_{\mathrm{NH_3}}$, the type of seeds, and the concentration of ammonium sulfate in solution, $m^{\circ}_{\mathrm{AS}}$. It must be noted that the higher solubility of AS compared that of BC allows to crystallize ammonium bicarbonate without precipitating also ammonium sulfate, thus maintaining a constant concentration of sulfate ion throughout the BC crystallization process.

Polythermal seeded desupersaturation experiments[103] have been performed to estimate the growth rate constant of ammonium bicarbonate, and the crystallization procedure has been carried out as follows: during an initial equilibration period a clear undersaturated solution has been stirred at isothermal conditions. Then, a linear cooling ramp of $-20\,^{\circ}\mathrm{C\,h}^{-1}$ has been applied to induce supersaturation. Subsequently, seeding has been performed by injecting seeds (of one type) in the supersaturated solution while monitoring the depletion of the overall BC concentration in the liquid phase via ATR-FTIR measurements. A sudden increase of the total chord length counts measured using the FBRM has been used to identify the occurrence of secondary nucleation during the experiments. In the final phase of the experiment in which the temperature has been kept constant, the crystallization process has been considered concluded whenever a steady value of the mean size of the chord length distribution recorded using the FBRM was reached. The slurry obtained after the growth experiment has been collected and filtered to recover the solid product whose CSD has been further analyzed via μ-DISCO measurements. All the experiments have been performed using a total mass of solution of 1340 g and a seed loading equal to 8−12 % wt of the final solid yield so as to minimize the extent of secondary nucleation.[83] The maximum initial supersaturation explored has been carefully kept below the primary nucleation threshold determined via *ad-hoc* experiments performed at the operating conditions adopted in this work.

## 4.4 MODELING OF THE CRYSTALLIZATION PROCESS

### 4.4.1 *Population Balance Equation*

The modeling framework adopted for the description of the evolution of the population of crystals in the domains of time $t$ and of the particle-size coordinate $L$ is based on the following population balance equation (PBE) in which agglomeration and breakage have been neglected:

$$\frac{\partial n}{\partial t} + G\frac{\partial n}{\partial L} = 0 \tag{4.19}$$

where $n(t, L)$ is the number-based distribution of the crystal population about the particle-size coordinate defined as the number of particles per unit length per unit mass of solvent (water), $M_\mathrm{s}$, and $G$ is the overall size-independent crystal growth rate along the particles' internal coordinate. eq 4.19 has been coupled with the following initial and boundary conditions:

$$n(0, L) = n_\mathrm{s}(L) \tag{4.20a}$$

$$n(t, 0) = 0 \tag{4.20b}$$

where $n_\mathrm{s}(L)$ is the number-based CSD of the seeds population rescaled to the actual mass of seeds, $m_\mathrm{s}$, used in the growth experiment.

Particle nucleation has been neglected during the process, thus the boundary condition of eq 4.20b. Moreover, the *regularity* condition imposes that $G(t, \infty)n(t, \infty) = 0$, thus implying that for sizes that tend toward infinity, if the growth rate $G$ does not vanish, $n(t,L)$ must be zero.[85]

eq 4.19 has therefore been coupled with the continuous phase equation, which accounts for the depletion of solute due to crystal growth, thus:[36]

$$\frac{\mathrm{d}m_{\mathrm{BC}}}{\mathrm{d}t} = -3\rho_{\mathrm{s}} k_{\mathrm{v}} \mu_2 G \tag{4.21}$$

where $m_{\mathrm{BC}}$ is the overall molality of ammonium bicarbonate in solution (regardless of the speciation), $\rho_{\mathrm{s}}$ is the density of the crystalline phase, $k_{\mathrm{v}}$ is the volumetric shape factor, and $\mu_2$ is the second moment of the crystal distribution $n(L,t)$ defined as:

$$\mu_p(t) = \int_0^\infty n(t,L) L^p dL \tag{4.22}$$

with $p = 2$.

In this work, a value of 1 has been assumed for the volumetric shape factor, $k_{\mathrm{v}}$, thus approximating the shape of the particles to that of a cube. The reconstruction of the CSD obtained from the μ-DISCO has been performed consistently with this shape assumption.

The initial condition of eq 4.21 is:

$$m_{\mathrm{BC}}(0) = m_{\mathrm{BC,o}} \tag{4.23}$$

where $m_{\mathrm{BC,o}}$ is the initial overall concentration of ammonium bicarbonate in the liquid phase.

The PBE model given by eqs 4.19-4.23 was solved numerically using a high resolution finite volume method (HRM) with the van Leer flux limiter.[90] Hence, the particle-size domain has been discretized into $N_{\mathrm{b}}$ (250) uniformly distributed grid points, and the time-resolved solution of the PBE has been computed through the second-order accurate scheme proposed by LeVeque.[34] Note that the initial distribution $n_{\mathrm{s}}(L)$ has been discretized accordingly. The stability of the numerical solution has been guaranteed by adapting the time step $\Delta t$ such that the Courant Friedrichs Lewy (CLF) condition is satisfied.[34]

### *Constitutive Equations for Crystal Growth and Solution Supersaturation*

Two crystal growth models have been considered in this study, and both of them are used to estimate size-independent growth rates of ammonium bicarbonate from solution.

The first model, proposed in our previous work,[103] is based on the following empirical expression:

$$G_1 = k_{g,1} S \tag{4.24}$$

where $G_1$ is the crystal growth rate, $k_{g,1}$ is the pre-exponential growth kinetic parameter, and $S$ is the supersaturation defined by eq 1.18.

It is worth noting that the value of the parameter $k_{g,1}$ (eq 4.24), previously fitted in the same temperature range of the experiments carried out in this work, is $4.99 \cdot 10^{-6}\,\mathrm{m\,s^{-1}}$.[103] Moreover, the temperature dependence of the growth rate is implicitly accounted for in the supersaturation.

The second growth model, originally proposed by Kubota and Mullin,[107] assumes crystal growth in the presence of an impurity to be a competitive adsorption process between the crystallizing solute and the foreign species for the active sites of the crystals. Furthermore, equilibrium adsorption conditions are assumed. In detail, the growth rate model is based on the Langmuir-type adsorption isotherm to describe the coverage of $\mathrm{SO_4}^{2-}$ ions (assumed to be the impurity in the system) on the crystal surface as follows:

$$\frac{G_2}{G^\circ} = 1 - \alpha \frac{\kappa m_{\mathrm{SO_4}^{2-}}}{1 + \kappa m_{\mathrm{SO_4}^{2-}}} \tag{4.25}$$

where $G_2$ is the inhibited crystal growth rate, $G^\circ$ is the reference crystal growth rate, $\alpha$ is the *impurities effectiveness factor*, $\kappa$ is an adjustable parameter of the Langmuir isotherm (adsorption equilibrium constant), and $m_{\mathrm{SO_4}^{2-}}$ is the sulfate ion concentration. In this work, the growth rate expressed by eq 4.24, i.e. that describing the growth of ammonium bicarbonate in the absence of the sulfate impurity in the system, has been considered as the reference growth rate, $G^\circ$, in eq 4.25. In the following, we will call this model the *adsorption-growth model*.

According to eq 4.25, the asymptotic behavior of the relative velocity $G_2/G^\circ$ is governed by the *impurity effectiveness factor*, $\alpha$; different asymptotic behaviors have been confirmed experimentally for a variety of inorganic and organic compounds in the literature.[33,108–110]

### 4.4.2 *Fitting Procedure*

A maximum likelihood estimation (MLE) approach has been used to estimate the parameters of the adsorption-growth model (eq 4.25). Under the assumptions of this method, discussed in detail elsewhere,[63] the optimal values of the parameters are such that the probability of observing the experimental data set, i.e. the measured BC concentration data points, is maximized through the following minimization problem:

$$\underset{\mathbf{p}}{\text{minimize}}\ \frac{N_\mathrm{t}}{2} \ln \left[ \sum_{j=1}^{N_\mathrm{t}} \left( \frac{m_{\mathrm{BC},j} - \hat{m}_{\mathrm{BC},j}(\mathbf{p})}{m^\mathrm{ref}} \right)^2 \right] \tag{4.26}$$

where $\mathbf{p} = [\alpha, \kappa]$ is the parameter vector to be estimated, $N_\mathrm{t}$ is the number of experimental data points, $m_{\mathrm{BC},j}$ and $\hat{m}_{\mathrm{BC},j}$ are the $j$-th experimental data point and its model's prediction, respectively. In order to make the objective function dimensionless, the solute concentration has been divided by a reference concentration $m_\mathrm{ref}$ equal to $1\,\mathrm{mol_{BC}/kg_W}$. The optimization problem of eq 4.26 is, in general, nonlinear and nonconvex, and the search for a global minimizer can instead lead to local minima. To rate the quality of any local minimizer found, a visual inspection of the fit between the experimentally measured quantities and the model predictions has been carried out (cf. Section 4.5.4). In this work, the local minimizer $\hat{\mathbf{p}}$ of eq 4.26 has been computed using the gradient-based optimizer LSQNONLIN (in which a trust-region-reflective algorithm is implemented) available in the MATLAB optimization toolbox.[69] After performing the optimization, the confidence regions of the minimizer $\hat{\mathbf{p}}$ can be calculated according to the procedure described in.[103]

It must be underlined that due to the statistical correlation among the parameters of eq 4.25, the optimal values of $\alpha$ and $\kappa$ cannot be uniquely

determined given the set of experimental data available (the interested reader is referred to Appendix C for further details).
The identification of the parameter $\alpha$ requires the estimation of the asymptotic value of the relative growth rate of ammonium bicarbonate for higher and higher concentration of sulfate ions in the solvent. In this work, we refrained from performing such type of experiments due to the substantial effort in terms of experimental activity and modeling (including both the ATR-FTIR calibration and the re-estimation of the parameters of the speciation model) that would be required to investigate the system at higher sulfate ions concentration compared to those explored in this work. Instead, we assigned a value of 1 to the parameter $\alpha$, thus reducing the number of empirical parameters in the adsorption-growth model to one, i.e. the Langmuir constant, $\kappa$, in eq 4.25. It must be noted that, although the choice of the parameter $\alpha$ might not be representive of the behavior of the system, imposing an arbitrary value for this parameter avoids the overparametrization of the adsorption-growth model.

## 4.5 RESULTS AND DISCUSSION

### 4.5.1 *ATR-FTIR Calibration*

The overall concentration of ammonium bicarbonate in aqueous ammonia solutions containing dissolved ammonium sulfate has been estimated by means of ATR-FTIR measurements. Furthermore, the validity of the Beer-Lambert's law in the range of BC concentrations investigatigated[43,76] allows to express the total absorption $y_{\tilde{\nu}}$ of a solution, at a specific wavenumber $\tilde{\nu}$, as the linear combination of the contributions of the $i$-th absorbing species to the spectrum of the mixture. Thus,

$$y_{\tilde{\nu}}(\tilde{\nu}) = \sum_{i=1}^{N_{\mathrm{s}}} m_i \epsilon_i(\tilde{\nu}) \tag{4.27}$$

where $N_{\mathrm{s}}$ is the number of species in the system (including water), and $\epsilon_i$ is the molar absorptivity of the $i$-th component.

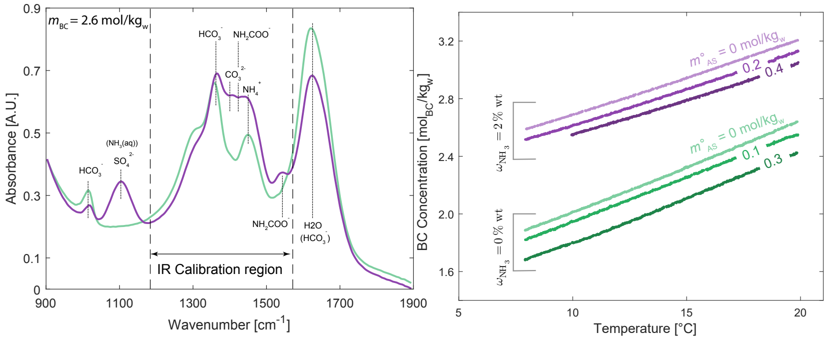

(a) (b)

Figure 4.4: (a) Overlapped IR spectra of a saturated aqueous solution of ammonium bicarbonate (highlighted in green), and of an aqueous ammonia solution (2 % wt $NH_3$) saturated w.r.t. ammonium bicarbonate (highlighted in purple) and containing ammonium sulfate ($m^{\circ}_{SO_4^{2-}}$ =0.2 mol/kg$_W$) . The overall BC concentration of both the solutions is 2.6 mol/kg$_W$. The range of wavenumber, $\tilde{\nu}$, selected for the regression of the PLS models is indicated by the dashed vertical lines. (b) ATR-FTIR based solubility of ammonium bicarbonate in aqueous solution and in an aqueous ammonia solution (2 % wt $NH_3$) at different concentrations of dissolved ammonium sulfate as a function of temperature (8-20 °C). The nominal ammonia concentration of the solution, $\omega^{\circ}_{NH_3}$, is indicated by the color code in the figure, while the color intensity increases as the nominal concentration of dissolved ammonium sulfate, $m^{\circ}_{SO_4^{2-}}$ increases.

In this work, the overall ammonium bicarbonate concentration in solution (regardless of the speciation) has been correlated to the IR spectrum of the mixture by applying a partial least squares (PLS) calibration approach to the IR spectral data[45] (the interested reader is referred to Appendix C for a detailed description of the ATR-FTIR calibration procedure followed in this work).

As it can be seen in Figure 4.4a though, the IR spectra of mixtures characterized by the same concentration of ammonium bicarbonate but by different values of nominal ammonia and dissolved ammonium sulfate, differ a lot, thus making it infeasible to establish a single calibration model that, in a wide range of nominal ammonia and ammonium sulfate concentrations, correlates the IR spectrum of a mixture to the overall BC concentration. To cope with this issue, we have limited our analysis to a set of 6 types of aqueous ammonia solutions containing AS and BC, each of them at a different combination of fixed nominal ammonia and ammonium sulfate concentrations, and for each of these cases we have regressed a dedicated PLS model (which accounts for the speciation of the specific systems considered) in the range of overall BC concentration reported in Table 4.1. The nominal ammonia concentrations covered in this set are 0 % wt (i.e. aqueous solutions) and 2 % wt, while the ammonium sulfate concentrations spans values from $0.1\,\mathrm{mol/kg_W}$ to $0.4\,\mathrm{mol/kg_W}$.

It is worth noting that the selection of the appropriate PLS model for the estimation of the ammonium bicarbonate concentration has to be

| **PLS Model** | **Solvent composition** | | **LV** | **RMSE-CV$_{10}$** | **BC Concentration** |
|---|---|---|---|---|---|
| | $\omega^{\circ}_{NH_3}$ | $m^{\circ}_{AS}$ | | | |
| | [%] | $[\mathrm{mol_{AS}/kg_W}]$ | [-] | $[\mathrm{mol_{BC}/kg_W}]$ | $[\mathrm{mol_{BC}/kg_W}]$ |
| 1 | 0 | 0 | 2 | $7.97 \cdot 10^{-5}$ | $1.89 - 2.64$ |
| 2 | 0 | 0.1 | 2 | $2.26 \cdot 10^{-3}$ | $1.82 - 2.55$ |
| 3 | 0 | 0.3 | 2 | $2.54 \cdot 10^{-3}$ | $1.69 - 2.42$ |
| 4 | 2 | 0 | 3 | $7.00 \cdot 10^{-3}$ | $2.56 - 3.20$ |
| 5 | 2 | 0.2 | 3 | $2.55 \cdot 10^{-3}$ | $2.52 - 3.13$ |
| 6 | 2 | 0.4 | 5 | $3.41 \cdot 10^{-4}$ | $2.54 - 3.04$ |

Table 4.1: Overview of the PLS models used for the estimation of the BC concentration using ATR-FTIR measurements. All the models are applied in the wavenumber range $1200\,\mathrm{cm}^{-1} \leq \tilde{\nu} \leq 1600\,\mathrm{cm}^{-1}$ as indicated in Figure 4.4a. The number of PLS latent variables (LV) varies between 2 and 5 according to the model. Each model is capable of predicting the overall ammonium bicarbonate concentration in the relevant concentration range, while the prediction capability of each model has been assessed by computing the root mean square error of 10-fold cross validation (RMSECV$_{10}$).[45]

made based on the prior knowledge of the solvent composition, i.e. the nominal ammonia content, $\omega^{\circ}_{\mathrm{NH_3}}$, and the nominal ammonium sulfate concentration, $m^{\circ}_{\mathrm{AS}}$, of the sample to be analyzed.

As shown in Figure 4.4a, the range of wavenumber values used by the PLS models is $1200\,\mathrm{cm}^{-1} \leq \tilde{\nu} \leq 1600\,\mathrm{cm}^{-1}$; this region of the IR spectrum, characterized by a marked absorbance of most of the species in solution, contains the relevant *spectral information* used to estimate the overall BC concentration in solution. The sulfate ion IR peak located at $\sim 1100\ \mathrm{cm}^{-1}$[111] has not been included in the calibration set because uncorrelated to the carbon concentration. Moreover, the overlap between the IR peak of the aqueous ammonia species and that of the sulfate ion, both located at approximately $1100\ \mathrm{cm}^{-1}$, makes the estimation of the sulfate concentration in solution rather challenging. Therefore, in this work the sulfate ions concentration has not been directly measured, but instead assumed to be the analytical value resulting from the preparation of the mixture (cf. Section 4.3). The validity of this assumption has been further discussed in Section 4.5.3.

### 4.5.2 *Solid-Liquid Equilibrium of Ammonium Bicarbonate in Aqueous Ammonia Solutions of Ammonium Sulfate*

Figure 4.4b shows the ATR-FTIR based solubility of ammonium bicarbonate in aqueous ammonia solutions at different concentrations of dissolved ammonium sulfate. The solubility of BC has been estimated by applying the PLS calibration models reported in Table 4.1 to the IR spectra of saturated solutions of BC.

The solubility data, measured by applying a methodology described in detail in Appendix C, describes the solid-liquid equilibrium of ammonium bicarbonate as a function of temperature, nominal ammonia, and ammonium sulfate concentration.

As it can be seen in Figure 4.4b, the presence of aqueous ammonia and of ammonium sulfate in solution has a major effect on the BC solubility. On the one hand, an increase of the nominal ammonia concentration leads to an increase of the solubility of ammonium bicarbonate. As a consequence of the increase of the pH, the carbon distribution shifts towards the carbonate species and a higher amount of BC salt can therefore be dissolved in the system prior to reaching saturation. On the other hand, the presence of dissolved ammonium sulfate leads to a lower ammonium bicarbonate solubility due to the surplus of ammonium ions present in solution, which affects the equilibrium described by eq 4.13. This phenomenon is often referred to as the *common-ion effect*.[59]

Prior to the estimation of the growth kinetics of the ammonium bicarbonate from solution, we have investigated the effect of the presence of ammonium sulfate on the liquid speciation of the system. For this purpose, the extended-UNIQUAC model, originally used to account for the non-ideality of the liquid phase in the $CO_2-NH_3-H_2O$ system,[28,76] has been modified to account for the additional presence of the sulfate species in the system. As discussed in Section 4.2.1, the sulfate ion model parameters have been estimated by fitting the measured solubility data of ammonium bicarbonate shown in Figure 4.4b. Assuming saturation conditions, the pertinent equations describing the chemical equilibria of the system (eq 4.14) have been solved together with the mass and the charge balances (eqs 4.15-4.16) while minimizing the following objective function by varying the extended-UNIQUAC volume and surface area parameters of the sulfate ion, $r_{\mathrm{SO_4}^{2-}}$ and $q_{\mathrm{SO_4}^{2-}}$, as well as the sulfate ion's energy interaction parameter vectors, $\mathbf{u}^0$ and, $\mathbf{u}^\mathrm{T}$, appearing in the expression for each species' activity coefficient, $\gamma_i$:

$$\underset{r,q,\mathbf{u}^0,\mathbf{u}^\mathrm{T}}{\text{minimize}} \sum_{s=1}^{N_\omega} \sum_{k=1}^{N_\mathrm{AS}} \sum_{z=1}^{N_\mathrm{obv}} \left[ \ln K_\mathrm{SP}(T) - \ln K_\mathrm{IP}(T, \mathbf{m}^*)|_{s,k,z} \right]^2 \tag{4.28}$$

where

$$K_\mathrm{SP}(T) = \exp\left[ -\frac{\Delta G_\mathrm{BC}(T)}{RT} \right] \tag{4.29}$$

$$K_\mathrm{IP} = (\gamma_{\mathrm{NH_4}^+} m_{\mathrm{NH_4}^+})(\gamma_{\mathrm{HCO_3}^-} m_{\mathrm{HCO_3}^-}) \tag{4.30}$$

In eq 4.28, the vector $\mathbf{m}^*$ indicates the composition of the system at saturation (i. e. at solid-liquid equilibrium with ammonium bicarbonate), the variables $N_\omega$, $N_\mathrm{AS}$, and $N_\mathrm{obv}$ are the number of nominal ammonia concentrations investigated, in this work equal to 2 (i.e. 0 % wt, and 2 % wt), the number of non-zero ammonium sulfate concentrations investigated for each value of $\omega^{\circ}_{\mathrm{NH_3}}$, equal to 2, and the number of concentration measurements (observations) at the relevant experimental conditions, respectively.

The variable $\Delta G_{\mathrm{BC}}(T)$ in eq 4.29 is the standard Gibbs free energy of formation of BC in aqueous solution[30] at temperature $T$; $R$ is the ideal gas constant. The parameter $K_{\mathrm{IP}}$ in eq 4.30 is the ionic product of ammonium bicarbonate, i.e. a function of the temperature and composition of the system. The minimization of eq 4.28 implies therefore that, at saturation, the ionic product and the solubility product, $K_{\mathrm{SP}}$, coincide.

The data set used for the parameter estimation consists of a pool of 20 equally distributed solubility data points ($N_{\mathrm{obv}}$) collected along each of the 4 solubility curves shown in Figure 4.4b (excluding the ones measured in absence of dissolved ammonium sulfate).

The parameter regression has been performed using the optimizer *fmincon* in the Matlab Optimization Toolbox.[69] The values of the sulfate ion's parameters proposed by Thomsen et al.[28] have been used as an initial guess for the optimization, while the remaining model parameters have been taken from our previous work.[103]

As it can be seen in Figure 4.5, the resulting set of optimal parameters, as given in Tables 4.2-4.4, allows to describe the solid-liquid equilibrium of BC accurately in the entire range of operating conditions investigated. In fact, the BC solubility curves of Figure 4.4b collapse into a single curve, i.e. the solubility product of BC, $K_{\mathrm{SP}}(T)$, when plotted in the activity-based phase diagram shown in Figure 4.5.

| **Parameter** | **Value** |
|---|---|
| $r_{\mathrm{SO_4}^{2-}}$ [-] | 10.18 |
| $q_{\mathrm{SO_4}^{2-}}$ [-] | 18.55 |

Table 4.2: Optimal extended-UNIQUAC parameters relative to the volume and surface area of the sulfate ion (cf. Section 4.5.2).

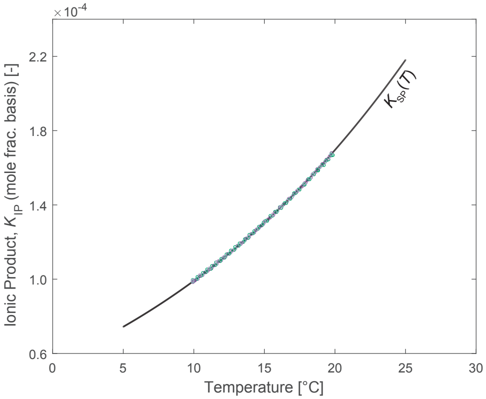

FIGURE 4.5: Activity-based solubility data of ammonium bicarbonate in aqueous ammonia solutions containing ammonium sulfate as a function of temperature. The overlapping circular markers correspond to the measured solubility data shown in Figure 4.4b (cf. the relevant color code), while the solid curve is the solubility product of ammonium bicarbonate $K_{SP}(T)$ taken from Darde et al..[30] The data at different nominal ammonia and ammonium sulfate concentrations overlap nicely and fit the BC solubility product rather well, thus indicating that the speciation model is able to describe the BC solid-liquid equilibrium accurately. The extended-UNIQUAC parameters for the $SO_4{}^{2-}$ ion has been estimated based on the methodology described in Section 4.5.2.

### *Mean Ionic Activity Coefficient of Ammonium Bicarbonate*

In this section, the impact of the solvent composition on the mean ionic activity coefficient of ammonium bicarbonate, $\gamma_\pm$, defined as

$$\gamma_\pm = (\gamma_{NH_4{}^+}\gamma_{HCO_3{}^-})^{\frac{1}{2}} \tag{4.31}$$

has been assessed using the extended-UNIQUAC model previously estimated (cf. Section 4.5.2). Eq 4.31 has therefore been used to perform a parametric analysis of the effect of the presence of free ammonia and ammonium sulfate in aqueous solutions of BC.

| $u_{ij}^0$ | $H_2O$ | $NH_3$(aq) | $CO_2$(aq) | $NH_4^+$ | $H^+$ | $OH^-$ | $CO_3^{2-}$ | $HCO_3^-$ | $NH_2COO^-$ | $SO_4^{2-}$ |
|---|---|---|---|---|---|---|---|---|---|---|
| $H_2O$ | 0 | | | | | | | | | |
| $NH_3$(aq) | 774.41 | 1140.20 | | | | | | | | |
| $CO_2$(aq) | 205.32 | 2500.00 | 40.52 | | | | | | | |
| $NH_4^+$ | 142.58 | 1010.60 | -5.05 | 0 | | | | | | |
| $H^+$ | $10^5$ | $10^{10}$ | $10^{10}$ | $10^{10}$ | 0 | | | | | |
| $OH^-$ | 600.50 | 2046.80 | 2500.00 | 1877.90 | $10^{10}$ | 1562.90 | | | | |
| $CO_3^{2-}$ | 232.71 | 1662.40 | 2500.00 | 226.60 | $10^{10}$ | 1588.00 | 1458.30 | | | |
| $HCO_3^-$ | 625.93 | 3641.90 | 767.81 | 643.24 | $10^{10}$ | 2500.00 | 800.01 | 771.04 | | |
| $NH_2COO^-$ | 1.27 | 1006.40 | 2500.00 | 85.21 | $10^{10}$ | 2500.00 | 2500.00 | 612.95 | 1405.20 | |
| $SO_4^{2-}$ | **341.07** | **3577.36** | **1775.77** | **57.56** | $\mathbf{10^{10}}$ | **1791.47** | **1785.86** | **819.50** | **300.66** | **1223.73** |

Table 4.3: Extended-UNIQUAC interaction energy parameters $\mathbf{u}_{ij}^0$ ($\mathbf{u}_{ij} = \mathbf{u}_{ij}^0 + \mathbf{u}_{ij}^T(T - 298.15)$ and $\mathbf{u}_{ij}^0 = \mathbf{u}_{ji}^0$). The values of the parameters in bold have been added to the model proposed in Chapter 2.

| $u_{ij}^T$ | $H_2O$ | $NH_3$(aq) | $CO_2$(aq) | $NH_4^+$ | $H^+$ | $OH^-$ | $CO_3^{2-}$ | $HCO_3^-$ | $NH_2COO^-$ | $SO_4^{2-}$ |
|---|---|---|---|---|---|---|---|---|---|---|
| $H_2O$ | 0 | | | | | | | | | |
| $NH_3$(aq) | 0.0996 | 4.0165 | | | | | | | | |
| $CO_2$(aq) | 11.8880 | 0 | 13.6290 | | | | | | | |
| $NH_4^+$ | 0.0052 | 19.6218 | 14.8936 | 0 | | | | | | |
| $H^+$ | 0 | 0 | 0 | 0 | 0 | | | | | |
| $OH^-$ | 8.5455 | 0.0904 | 0 | 0.3492 | 0 | 5.6169 | | | | |
| $CO_3^{2-}$ | 2.6495 | -0.1314 | 0 | 4.0556 | 0 | 2.5176 | -1.3448 | | | |
| $HCO_3^-$ | -1.9399 | 0.2249 | 0.0437 | -0.0002 | 0 | 0 | 1.7241 | -0.0198 | | |
| $NH_2COO^-$ | 6.8968 | 6.1568 | 0 | 5.6035 | 0 | 0 | 0 | 3.4233 | 0 | |
| $SO_4^{2-}$ | **18.57** | **-3.40** | **0.72** | **12.76** | **0** | **7.37** | **1.06** | **2.15** | **-0.47** | **4.52** |

Table 4.4: Extended-UNIQUAC interaction energy parameters $\mathbf{u}_{ij}^T$ ($\mathbf{u}_{ij} = \mathbf{u}_{ij}^0 + \mathbf{u}_{ij}^T(T - 298.15)$ and $\mathbf{u}_{ij}^T = \mathbf{u}_{ji}^T$). The values of the parameters in bold have been added to the model proposed in Chapter 2.

Figure 4.6 shows $\ln \gamma_\pm$ of ammonium bicarbonate, plotted against the BC salt molality, parametrized with respect to the ammonium sulfate concentration (purple curves), and the nominal ammonia concentration (pink curves). The black curve, shown as reference, is $\ln \gamma_\pm$ of BC in aqueous solution. For this case, $\ln \gamma_\pm$ exhibits an infinite negative gradient as the salt concentration approaches zero. This is a consequence of the long-range forces acting between the molecules in solution pro-

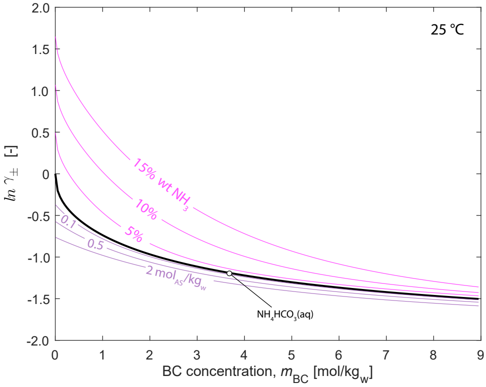

Figure 4.6: Logarithm of the mean ionic activity coefficient of ammonium bicarbonate, $\gamma_\pm$, as a function of BC molality at 25 °C. The black solid curve refers to the reference case of pure BC in aqueous solution, while the purple and pink curves represent the cases of aqueous solutions of BC containing ammonium sulfate, and aqueous solutions of BC containing ammonia, respectively.

gressively vanishing.[112] At higher salt concentration however, the curve flattens out, and in this concentration range, not investigated experimentally in this work, the effects of short-range interactions become important and dominate the behavior.

In the case of aqueous solution of BC, $\gamma_\pm$ approaches unity as the solution approaches ideality (i.e. infinite dilution). However, this does not happen in all the other cases investigated due to the residual non-vanishing concentration of nominal ammonia or ammonium sulfate in the solvent.

As it can be seen in Figure 4.6, ammonium sulfate and aqueous ammonia show counter-acting effects on the mean ionic activity coefficient of BC. On the one hand, the presence of ammonium sulfate reduces the activity of BC in solution, on the other hand, the presence of aqueous ammonia tends to increase it. Based on these findings, the effects of ammonia and ammonium sulfate on the BC mean ionic activity coefficient are most likely to counter balance each other in the range of aqueous ammonia and ammonium sulfate concentrations explored in this work.

### *Speciation of Ammonium Bicarbonate in Aqueous Ammonia Solutions of Ammonium Sulfate*

Figure 4.7 shows the modeled equilibrium speciation of saturated aqueous ammonia solutions of BC containing dissolved ammonium sulfate in the temperature range 10 °C to 20 °C. As it can be seen in Figure 4.7, the dominant species in the solutions investigated are the ammonium and the bicarbonate ions represented by the red and by the blue curves, respectively.

In an aqueous solution (cf. Figure 4.7a) ammonium bicarbonate dissociates *congruently*, without a significant extent of speciation[40] (note that the vertical axes in Figures 4.7a-c span the same range of values but are scaled differently), thus leading to a ratio between the ammonium and the bicarbonate ions in solution, $\varrho$, close to unity.

Compared to the previous case, the pH variation resulting from an increase in nominal ammonia concentration to 2 % wt (cf. Figure 4.7d) is responsible for the shift of the carbon and nitrogen species towards the carbonate ($CO_3{}^{2-}$) and the carbamate ($NH_2COO^-$) ions, respectively, whereas the presence of dissolved $CO_2$(aq) can be neglected under these conditions. Eventually, the change in the stoichiometry of the system leads to values of the ratio $\varrho$ of about 1.7.

The behavior of the quaternary system, in the range of ammonium sulfate concentration explored in this work is very similar to that observed for the AS-free system. According to the results of the speciation model, the dissolution of higher and higher amounts of ammonium sulfate leads to an increase of the ammonium and sulfate ion concentrations (cf. Figures 4.7b-c and Figures 4.7e-f), which do not modify significantly either the equilibrium concentration of the carbonate and carbamate ions or the concentration of the free aqueous ammonia in solution. As a general trend, the concentration of the bicarbonate ion decreases as the ammonium sulfate concentration increases because of the *common-ion effect* discussed in Section 4.5.2. This leads to an increase of the ratio

$\varrho$ to values between 2 and 2.5 for the case of the aqueous ammonia solutions of BC containing AS shown in Figures 4.7e-f.

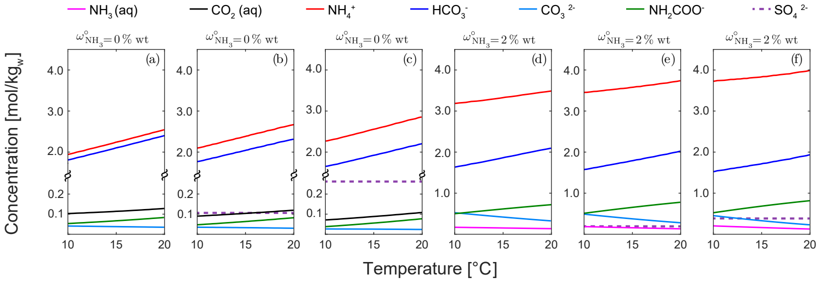

FIGURE 4.7: Equilibrium speciation of aqueous ammonia solutions saturated w.r.t. ammonium bicarbonate, containing ammonium sulfate in the temperature range 10-20 °C. The sulfate ion concentration is indicated with a dashed purple line. (a-c) Species distribution in an aqueous solution of BC at the nominal ammonium sulfate concentration of 0 mol/$kg_W$, 0.1 mol/$kg_W$, and 0.3 mol/$kg_W$, respectively (note that the vertical axes span the same range of values but are scaled differently). (d-f) Species distribution in an aqueous ammonia solution of BC at the nominal ammonium sulfate concentration of 0 mol/$kg_W$, 0.2 mol/$kg_W$, and 0.4 mol/$kg_W$, respectively.

### 4.5.3 *Validation of the Adsorption-growth Model's Assumptions*

In this section, the main adsorption-growth model assumptions are discussed prior to the fitting of the model parameters.

The first assumption relates to the ammonium sulfate concentration, $m^{\circ}_{AS}$, which is assumed to remain constant during the course of each growth experiment. As a consequence of the *common-ion effect* (cf. Section 4.5.2), the solubility of BC hence the supersaturation are affected by the AS concentration in solution. Though not being a species directly involved in the crystallization of ammonium bicarbonate, the $SO_4^{2-}$ ions could be incorporated in the solid phase as solvent inclusions or permanently adsorbed on the crystal surface depending on the crystal-

| Solvent Composition | Run | $T_{\text{initial}}$ [°C] | $T_{\text{final}}$ [°C] | $S_0$ [-] | $m_s$ [g] | Seeds | Product Impurity $[\text{mol}_{\text{SO}_4^{2-}}/\text{mol}_{\text{BC}}]\cdot 10^6$ |
|---|---|---|---|---|---|---|---|
| $\omega^\circ_{\text{NH}_3} = 0\,\%$ wt<br>$m^\circ_{\text{AS}} = 0.1$ mol/kg$_\text{w}$ | G01 | 18.1 | 15.7 | 0.06 | 3.78 | A | 438 |
| | G02 | 17.4 | 14.3 | 0.07 | 3.44 | A | 598 |
| | G03 | 15.5 | 10.1 | 0.06 | 7.64 | A | 825 |
| $\omega^\circ_{\text{NH}_3} = 0\,\%$ wt<br>$m^\circ_{\text{AS}} = 0.3$ mol/kg$_\text{w}$ | G04 | 16.1 | 13.4 | 0.09 | 3.61 | B | 1157 |
| | G05 | 16.5 | 14.0 | 0.10 | 3.61 | B | 474 |
| | G06 | 16.5 | 14.4 | 0.15 | 7.03 | B | 508 |
| $\omega^\circ_{\text{NH}_3} = 2\,\%$ wt<br>$m^\circ_{\text{AS}} = 0.2$ mol/kg$_\text{w}$ | G07 | 18.1 | 15.7 | 0.06 | 3.78 | A | 282 |
| | G08 | 17.4 | 14.3 | 0.07 | 3.44 | A | 415 |
| | G09 | 15.5 | 10.1 | 0.06 | 7.64 | A | 656 |
| $\omega^\circ_{\text{NH}_3} = 2\,\%$ wt<br>$m^\circ_{\text{AS}} = 0.4$ mol/kg$_\text{w}$ | G10 | 16.1 | 13.4 | 0.09 | 3.61 | B | 696 |
| | G11 | 16.5 | 14.0 | 0.10 | 3.61 | B | 1650 |
| | G12 | 16.5 | 14.4 | 0.15 | 7.03 | B | 1520 |

TABLE 4.5: Overview of the BC growth experiments discussed in Sec 4.3.3. The variables $T_{\text{initial}}$ and $T_{\text{final}}$ are the initial and final temperature of each experiment, $S_0$ is the initial level of supersaturation exploited, and $m_s$ is the initial mass of BC seeds of the growth experiment. All crystallization runs have been carried out using a cooling rate of $-20\,°\text{C}\,\text{h}^{-1}$ and a stirring rate of 400 rpm. The $SO_4^{2-}$ impurity of the crystals obtained after the growth process has been assessed gravimetrically as discussed in Section 4.3. The level of impurity is reported in ppm (mole-based). The CSD of the product of each growth experiment has been characterized using μ-DISCO measurements and reported in Appendix C for completeness.

lization conditions adopted,[33,113] thus leading to a sulfate concentration depletion in the liquid phase.

As discussed in Section 4.5.1, since ATR-FTIR measurements could not be easily exploited to measure the concentration of $SO_4^{2-}$ ions, we have preferred to quantify the amount of sulfate impurity in the BC crystals by means of a gravimetric assay based on $BaSO_4$ (cf. Section 4.3). The calculated impurity content for each growth experiment performed is summarized in Table 4.5, together with the set of operating conditions adopted; note that the impurity concentration is expressed in part per million (mole basis).

On average, the amount of impurity was found to be ca. 2300 ppm molar, i.e. less than 0.28 % wt of the crystal mass, while no noticeable differences between the PXRD patterns of the crystallized material and those of commercial ammonium bicarbonate could be seen (the interested reader is referred to Appendix C for the PXRD patterns of the samples). Based on these findings, we therefore deemed the sulfate inclusions in the BC crystals to be low enough to neglect the loss of $SO_4^{2-}$ ions from the liquid to the solid phase during the experiments.
The second model assumption relates to the volumetric shape factor of the BC crystals assumed to be constant and equal to that of a cube (cf. Section 4.4.1). We investigated if any change of the shape of BC crystals occurred during the growth process by means of μ-DISCO measurements of the CSD of 4 crystallization runs, namely G03, G06, G09, G12 (cf. Table 4.5). Then, we applied a supervised machine learning algorithm described in detail elsewhere[38] to the data collected in order to classify each sampled particle into one of the following five classes, i.e. cuboid, needle, agglomerate, platelet, and sphere; Figure 4.8 shows the percent fraction of classes for each experiment mentioned above as well as for the distributions of seed crystals. The purple circular markers in Figure 4.8 indicate the total particle count of each measurement. Note that the values of the fraction of spheres and platelets, estimated to be below ca. 1 % and 2 %, respectively, have been lumped into the cuboid class because considered to be negligible compared to that of the other classes.
Based on the observation of the crystal shape classification results shown in Figure 4.8, the majority of the particles have been classified as cuboids, while the overall distribution of classes of the products did not exhibit any significant change compared to that of the seed populations, thus validating the assumption of unchanged volumetric shape factor of the BC crystals upon growth.

### 4.5.4 *Adsorption-growth Model Fit*

The adsorption-growth model has been fitted to the time-resolved BC concentration profiles of seeded growth experiments in which the

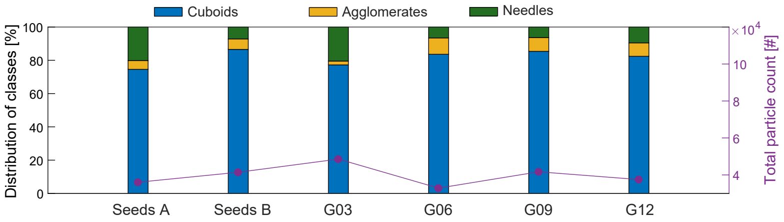

Figure 4.8: Percent fraction of crystal-shape classes of the crystallization products relative to the runs G03, G06, G09, and G12. The fractions of classes relative to the initial seed populations (i.e. seed types A and B) are reported as benchmark. Note that the fractions of spheres and platelets, negligible compared to that of the other classes, have been lumped into the cuboid class. The purple circular markers indicate the number of sampled particles (readable on the right ordinate axis) used to build the statistical analysis.

| **Kinetic Parameter** | **Value** |
|---|---|
| $\hat{k}_{g,1}{}^{103}$ [$\mathrm{m\,s^{-1}}$] | $(4.99 \pm 0.06) \cdot 10^{-6}$ |
| $\alpha$ [-] | $1^{*}$ |
| $\kappa$ [$\mathrm{kg_W/mol_{AS}}$] | $(4.53 \pm 0.05) \cdot 10^{-6}$ |

Table 4.6: Optimal values of the kinetic parameters of the ammonium bicarbonate growth models described in Section 4.4.1 (eq 4.24 and eq 4.25). The asterisk refers to an arbitrarily set model parameter value (not resulting from a fitting procedure). The confidence intervals of the model parameter, $\kappa$, (eq 4.25) have been computed assuming a probability, $\mathcal{P}$, of 95 %, while $k_{g,0}$ has been taken from the ammonium bicarbonate growth model proposed in Chapter 3.

overall solute concentration has been measured using ATR-FTIR spectroscopy (cf. Section 4.5.1). The optimal value of the growth rate parameter $\kappa$ in eq 4.25 has been found to be 4.53 $\mathrm{kg_W/mol_{AS}}$, while Table 4.6 reports the complete set of model parameters used in this work (including their confidence intervals).

The experimental data set for the parameter estimation, reported in

Table 4.5, consists of 12 desupersaturation experiments, 6 of which have been carried out in an aqueous solution, while the remaining ones have been carried out in a 2 % wt aqueous ammonia solution of BC. The concentration of the sulfate impurity has been varied between 0.1 $\mathrm{mol/kg_W}$ and 0.4 $\mathrm{mol/kg_W}$, and it has been assumed constant throughout each experiment (i.e. with negligible loss of $\mathrm{SO_4}^{2-}$ from the solution to the solid phase, cf. Section 4.5.3).

The range of initial supersaturation explored, i.e. $0.06 \leq S \leq 0.15$, allowed to perform growth experiments while minimizing the impact of secondary nucleation. This has also been confirmed by inspecting the volume weighted CSD of the crystallized products, which did not show any significant presence of fines (the interested reader is referred to Appendix C for the CSD of the final product of each growth experiment).

The goodness of the model fit can be visually inspected in Figure 4.9 where the circular markers are the experimental overall BC concentration data points, and the blue solid curves are the output of the adsorption model. The dashed lines in Figure 4.9 indicate the value of the BC solubility at the relevant temperature. Additionally, the red solid curves represent the *predicted* BC concentration profiles computed with a kinetic model (also referred to as the standard growth model in the following) that does not account for the adsorption of sulfate ions. The standard growth model employs eq 4.24 to compute the crystal growth rates and uses a value of the kinetic parameter $k_{g,1}$ of $4.99 \cdot 10^{-6}\ \mathrm{m\,s^{-1}}$, which is taken from our previous work.[103] The supersaturation $S$ has been computed according to eq 1.16 in Chapter 1 using the thermodynamic model exploited in this work.

As it can be seen in Figure 4.9, the standard growth model progressively overestimates the BC concentration profiles as the ammonium sulfate concentration increases, thus overpredicting the growth rates. On the contrary, the adsorption-growth model is capable of reproducing the experimental data rather well. In light of these results, we conclude that we can indeed attribute the inhibition of the BC crystal growth mainly to the presence of sulfate ions in solution.

The thermodynamic framework developed for the computation of the activity of BC, shared by the standard and the adsorption-growth models, allows for an unbiased computation of the BC supersaturation in the system without the sulfate species as well in the cases where sulfate is present. The differences in growth rates predicted by the two models can only be explained in light of a different underlying growth mechanism acting in the system containing $SO_4{}^{2-}$ ions. This conclusion is also supported by the fact that the standard growth model proposed in Chapter 3 is capable of predicting accurately the BC growth rates in the $CO_2-NH_3-H_2O$ system free of sulfate ions under the same conditions of temperature and nominal ammonia concentration adopted in this work, while, as mentioned above, it fails to predict the growth kinetics in the system containing the impurity.

The growth inhibition mechanisms related to the presence of impurities in solution can be thermodynamically or kinetically driven. In electrolytic systems for instance, the supersaturation can be reduced by the formation of ionic complexes of the impurities.[114] For example, the case of the $MgSO_4(aq)$ system is rather striking because an apparently simple higher-valent and largely dissociated electrolyte is in fact a mixture of ionic complexes whose nature and relative concentrations vary considerably as a function of the overall solute concentration.[115]

Growth inhibition can instead be kinetically controlled when a foreign species is temporarily (or permanently) adsorbed on the active sites of the crystals.[107] As an example, Dobberschütz et al. studied the case of growth inhibition of calcite ($CaCO_3$) and were able to associate it to the adsorption of the foreign inorganic species $Mg^{2+}$ and $SO_4{}^{2-}$ on the active steps of the crystals.[116]

We refrain from trying to identify the nature of the BC growth inhibition mechanism in the system under investigation due to the difficulty of probing the solid-liquid interface of the crystals experimentally. Furthermore, we speculate that the process is driven by an underlying impurity adsorption mechanism active at the crystal interface rather than driven by phenomena occurring in the bulk liquid phase, such as ion complexation for instance. This claim is supported by the fact that Hayes et al. were able to rule out the complexation of the $SO_4{}^{2-}$ ions with $NH_4{}^{+}$ ions in solution by using Raman spectroscopy in solution.[117] Furthermore, in our study no evidence of the complexation of the $SO_4{}^{2-}$ ions has been found during a Raman spectroscopic investigation of aqueous ammonia solutions containing AS and BC reported in Appendix C for the sake of brevity.

As shown in Figure 4.10, it can be noted that the values of the relative growth, $G_2/G_{\mathrm{ref}}$, are significantly reduced as the sulfate ion concentration increases. For the case of the highest sulfate impurity concentration investigated in this work, i.e. $0.4\,\mathrm{mol_{AS}/kg_W}$, the overall growth rates decreases by roughly 65 % compared to the case in the absence of the impurity.

As discussed in Section 4.4.2, no further physical interpretation of the asymptotic behavior of the relative growth of ammonium bicarbonate can be proposed by analyzing Figure 4.10 since the parameter $\alpha$ in eq 4.25 has been arbitrarily set equal to 1 to avoid the overparametrization of the adsorption-growth model. We are aware of the fact that an experimental investigation of higher values of sulfate ions concentration compared to those of this work would certainly shed light on the real asymptotic behavior of the relative growth rates of ammonium bicarbonate. At the same time however, the range of sulfate concentration analyzed in this work is representative of the values observed in an industrial process like the CSF-CAP and have been used to develop an empirical adsorption-growth model capable of describing the macroscopic effect of phenomena occurring at the molecular level, i.e. the diffusion and the adsorption of sulfate ions on the surface of ammonium bicarbonate crystals during crystal growth.

## 4.6 CONCLUSIONS

In this article, we have extended the kinetic model for ammonium bicarbonate growth in aqueous ammonia solutions proposed in our previous work[103] to account for the presence of the sulfate species in solution. This has been achieved by using a Langmuir-type adsorption isotherm model capable of describing the effect of the sulfate impurity on the growth process.

Since the presence of the sulfate species has also an impact on the speciation of the system and on the other species' activity in solution,

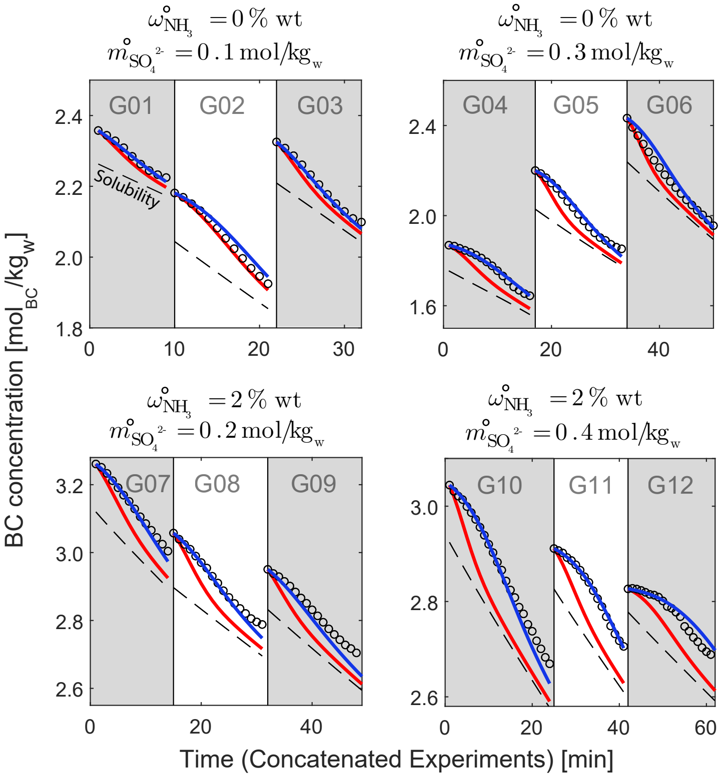

FIGURE 4.9: Concatenated seeded polythermal desupersaturation experiments of ammonium bicarbonate in aqueous ammonia solutions containing ammonium sulfate (cf. Table 4.5). The circular markers are the overall BC concentration data points measured using ATR-FTIR, the red curves are the predictions of the standard growth model (cf. Sec 4.5.4) that does not account for the presence of sulfate ions in solution, while the blue curves represent the predictions of the competitive growth model (accounting for the presence of sulfate ions in solution) whose parameters have been fitted in this work (cf. Table 4.6). The dashed lines indicate the ammonium bicarbonate solubility at the relevant temperature.

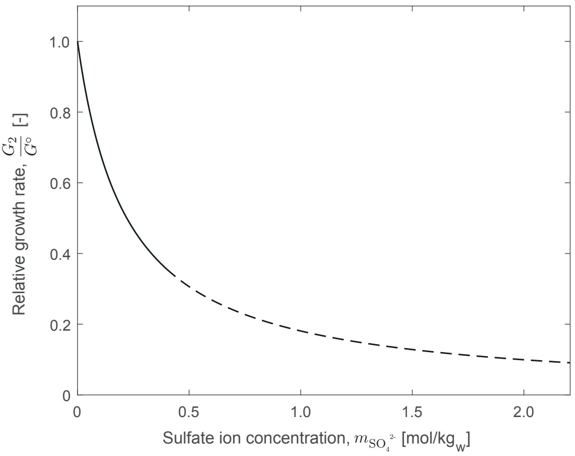

Figure 4.10: Relative growth rate (eq 4.25) as a function of sulfate ion concentration in solution. The parameters of the Langmuir isotherm are reported in Table 4.6. The solid line indicates values of the relative growth rates in the range of ammonium sulfate concentration explored in this work, while the dashed line refers to extrapolated values.

a rigorous thermodynamic model has been used for the computation of the ammonium bicarbonate supersaturation. In this regard, the thermodynamic model employed in this work is an extension of the speciation model for the $CO_2-NH_3-H_2O$ system proposed in our previous work[76] and includes the presence of the sulfate species in a thermodynamically consistent way.

The information on the overall ammonium bicarbonate concentration depletion, measured using ATR-FTIR spectroscopy during desupersaturation experiments, has been used to perform a parameter estimation of the adsorption-growth model.

The study has revealed a significant inhibition of the crystal growth rates of ammonium bicarbonate as the concentration of the sulfate impurity in solution increases, while the kinetic model proposed has been found to describe the experimental data rather well in the range of experimental conditions explored.

The constant morphology of the obtained crystals might indicate that the impurity adsorbs isotropically onto the crystal surfaces, thus hindering both the diffusion of solute molecules on the crystal surface and the integration of solute molecules into the crystal lattice. In turn, this causes a reduction of the overall crystal growth rates. Furthermore, an analysis of the ammonium bicarbonate crystal purity (cf. Table 4.5) revealed that sulfate ions have been sparingly included in the solid phase at the experimental conditions reported. This indicates that the foreign species is only temporary adsorbed on the crystal surface without being included in the crystal lattice.

Ultimately, this study sheds light on the several implications that the purity of the solvent has on the CSF-CAP. In particular, it highlights the existing trade-off between the opportunity of reducing capital costs associated to the emission control system by performing a simultaneous absorption of $CO_2$ and $SO_x$ in the same absorption unit and the drawback of an increase in required crystallization equipment volume as a consequence of the ammonium bicarbonate crystal growth rates inhibition caused by the presence of the sulfate impurity.

## NOMENCLATURE

### *Acronyms*

| | |
|---|---|
| AS | Ammonium sulfate |
| ATR-FTIR | Attenuated total reflection infrared spectroscopy |
| BC | Ammonium bicarbonate |
| CAP | Chilled ammonia process |
| CCS | Carbon capture and storage |
| CLF | Courant Friedrichs Lewy condition |
| CSD | Crystal size distribution |
| CSF-CAP | Controlled solid formation chilled ammonia process |
| DISCO | Dual imaging system for crystallization observation |
| FBRM | Focused beam reflectance measurement |
| FGD | Flue gas desulfurization |
| HRM | High resolution method |
| LV | PLSR latent variable |
| MLE | Maximum likelihood estimation |
| PBE | Population balance equation |
| PLS | Partial least squares |
| PXRD | Powder X-ray diffraction |
| RMSE-CV$_{10}$ | Root mean squared error of 10-fold cross validation [$\mathrm{mol\,kg^{-1}}$] |
| UNIQUAC | Universal quasi-chemical |

### *Greek Symbols*

| | |
|---|---|
| $\alpha$ | Impurity effectiveness factor (eq 4.25) [-] |
| $\epsilon_i$ | Molar absorptivity of the $i$-th component [A.U. $\mathrm{kg_W/mol}$] |
| $\gamma$ | Activity coefficient for an electrolyte species [-] |
| $\gamma_\pm$ | Mean ionic activity coefficient of BC(eq 4.31) [-] |
| $\kappa$ | Langmuir isotherm adjustable parameter (eq 4.25) [$\mathrm{kg_W/mol_{AS}}$] |
| $\mu$ | Mean of the CSD distribution |
| $\mu_p$ | $p$-th moment of the CSD |
| $\nu_{i,r}$ | Stoichiometric coefficient of the $i$-th component in the $r$-th reaction [-] |
| $\omega^\circ_{\mathrm{NH_3}}$ | Nominal ammonia concentration (% wt) in aqueous solution [-] |
| $\rho_\mathrm{s}$ | Density of the crystalline phase [$\mathrm{kg/m^3}$] |
| $\tilde{\nu}$ | IR spectrum wavenumber [$\mathrm{cm^{-1}}$] |
| $\varrho$ | Ratio between the ammonium and the bicarbonate ions in solution [-] |

## *Roman Symbols*

| | |
|---|---|
| $\Delta G_r^\circ$ | Change in standard Gibbs free energy of the $r$-th reaction $[\mathrm{J\,mol^{-1}}]$ |
| $\Delta G_{\mathrm{BC}}$ | Standard Gibbs free energy of formation of BC $[\mathrm{J\,mol^{-1}}]$ |
| $G^{\mathrm{ref}}$ | Reference overall size-independent crystal growth rate $[\mathrm{m\,s^{-1}}]$ |
| $G_1$ | Overall size-independent crystal growth rate in absence of impurities $[\mathrm{m\,s^{-1}}]$ |
| $G_2$ | Overall size-independent crystal growth rate in presence of impurities $[\mathrm{m\,s^{-1}}]$ |
| $k_{\mathrm{g},1}$ | Pre-exponential growth kinetic parameter $[\mathrm{m\,s^{-1}}]$ |
| $K_{\mathrm{SP}}$ | Ammonium Bicarbonate solubility product (mole frac. based) [-] |
| $K_{\mathrm{IP}}$ | Ammonium Bicarbonate ionic product (mole frac. based) [-] |
| $k_{\mathrm{v}}$ | Volumetric shape factor [-] |
| $L$ | Particle-size coordinate [m] |
| $\mathbf{m}$ | Vector of compositions (molality-based) $[\mathrm{mol/kg_w}]$ |
| $m$ | Solute concentration (molality-based) $[\mathrm{mol\,kg^{-1}}]$ |
| $m_{\mathrm{AS}}^\circ$ | Nominal ammonium sulfate concentration in solution $[\mathrm{mol/kg_w}]$ |
| $m_{\mathrm{BC}}$ | Overall ammonium bicarbonate concentration in solution $[\mathrm{mol/kg_w}]$ |
| $M_{\mathrm{s}}$ | Mass of the solvent (water) [kg] |
| $m_{\mathrm{s}}$ | Mass of seed crystals for the growth experiment [kg] |
| $n$ | Crystal size distribution (number-based) $[\mathrm{m^{-1}kg_w{}^{-1}}]$ |
| $N_\omega$ | Number of nominal ammonia concentrations investigated |
| $N_{\mathrm{AS}}$ | Number of non-zero ammonium sulfate concentrations investigated |
| $N_{\mathrm{b}}$ | Number of grid points for the particle-size domain discretization |
| $N_{\mathrm{obv}}$ | Number of observations |
| $N_{\mathrm{s}}$ | Number of species in the system (including water) |
| $n_{\mathrm{s}}$ | Crystal size distribution (number-based) $[\mathrm{m^{-1}kg_w{}^{-1}}]$ |
| $N_{\mathrm{t}}$ | Number of data points in the experimental time series |
| $\mathcal{P}$ | Probability [%] |
| $\mathbf{p}$ | Parameter vector for the growth model (eq 4.25) |
| $q_i$ | Extended-UNIQUAC surface parameter for the $i$-th component [-] |
| $R$ | Ideal gas law constant $[\mathrm{J\,mol^{-1}\,{}^\circ C^{-1}}]$ |
| $r_i$ | Extended-UNIQUAC volume parameter for the $i$-th component [-] |
| $S$ | Thermodynamic supersaturation [-] |
| $T$ | Temperature [°C] |
| $t$ | Time [s] |
| $\mathbf{u}^0$ | Extended-UNIQUAC energy interaction parameter vector $[\mathrm{J\,mol^{-1}}]$ |
| $\mathbf{u}^T$ | Extended-UNIQUAC energy interaction parameter vector $[\mathrm{J\,mol^{-1}}]$ |
| $y_{\tilde{\nu}}$ | IR absorbance of a solution [A.U.] |

### *Subscripts and Superscripts*

| | |
|---|---|
| $\circ$ | Superscript pertaining to a nominal concentration |
| $0$ | Subscript pertaining to an initial condition |
| $i$ | Subscript pertaining to the $i$-th chemical species in solution |
| $*$ | Superscript pertaining to quantity at saturation |
| $\hat{}$ | Superscript pertaining to an estimator |

# 5

# DESIGN OF THE CSF-CAP CRYSTALLIZATION SECTION

## 5.1 INTRODUCTION

This chapter focuses on the development of a rate-based mathematical model for the CSF-CAP crystallization section. This mathematical tool couples mass transfer by crystallization with heat transfer by convection, thus enabling the design and optimization of a continuous crystallization process where energy consumption and productivity are as important as crystal quality.

The proposed design approach focuses therefore on selecting suitable continuous crystallization equipment, e.g. combinations of well-mixed and plug-flow crystallizers,[33,86] and on the identification and comparison of optimized process configurations.

Furthermore, sensitivity analyses for BC secondary nucleation and dissolution kinetic rates have been carried out to account for the variability of the crystallization kinetics. For this purpose, realistic values of the kinetic parameters, based on literature data for similar inorganic salts,[118] have been used with the objective of explaining the effect of crystallization and dissolution kinetics on the process.

As far as the application of the developed optimization framework to

---

The work presented in this chapter has been reproduced with permission from Milella, F.; Gazzani, M.; Sutter, D.; Mazzotti, M. Process Synthesis, Modeling and Optimization of Continuous Cooling Crystallization with Heat Integration – Application to the Chilled Ammonia $CO_2$ Capture Process. *Ind. Eng. Chem. Res.* **2018**, *57*, 11712–11727. DOI: 10.1021/acs.iecr.8b01993. Copyright 2018 American Chemical Society.

It must be noted that, since the research discussed in this chapter has been historically developed before a quantitave estimation of the crystallization kinetics of ammonium bicarbonate, fictitious crystallization and dissolution kinetics have been used in this study instead of the ones presented in the previous Chapters.

the CSF-CAP is concerned, the validity of this work is restricted to the process conditions corresponding to the equilibrium-based optimized simulation presented by Sutter et al.[25] Nonetheless, the results from the model show how the main design variables are coupled and how they can best be tuned in such a challenging engineering process relevant not only for developing more efficient $CO_2$ capture processes, but also for all crystallization processes in which heat recovery, equipment size and energy consumption are of interest.

The chapter is organized as follows: Section 5.2 introduces the thermodynamics of the system and, in particular, discusses the electrolyte species that form during $CO_2$ absorption in aqueous ammonia. In section 5.3, the unit operations of cooling crystallization, solid/liquid separation, and solid dissolution are discussed together with the equipment selected for crystallization and dissolution. Section 5.4 provides a description of the mathematical model used to simulate viable process configurations. This model embeds the key physical phenomena occurring during crystallization and heat transfer, and it also capable of assessing the overall process operation via specific key performance indicators. Eventually, the outcome of this investigation is thoroughly presented in section 5.5.

For the operating conditions of interest of the CSF-CAP,[37] the thermodynamically stable solid form is BC.[26,30,40] In accordance with this, ammonium bicarbonate is assumed to be the only solid compound precipitating during cooling crystallization. The solubility of BC in aqueous ammonia solution has been calculated using the updated extended-UNIQUAC model presented by Darde et al.[30]

## 5.2 PROCESS DESCRIPTION

Figure 5.1 shows the CSF-CAP solid handling section in which three continuous operations, namely cooling crystallization of BC, solid/liquid separation, and complete dissolution of BC, are performed sequentially. A detailed description of the overall CSF-CAP can be found in Sutter et al.[25] while the complete $CO_2$ capture process flow diagram is provided in Appendix D.

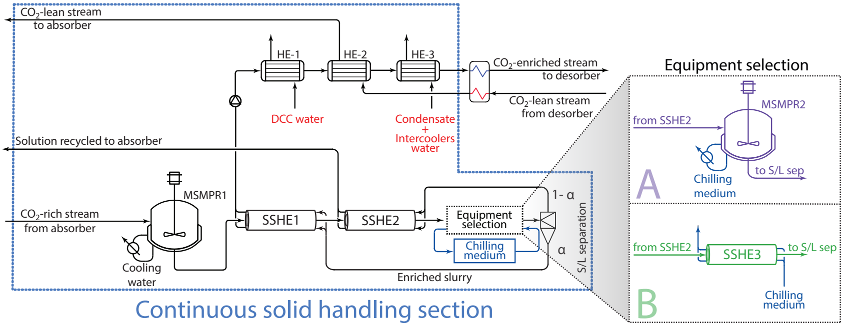

FIGURE 5.1: Flow scheme adopted for the continuous solid handling section of the CSF-CAP. The dashed blue box indicates the battery limit of the section; cf. Appendix D for the complete $CO_2$ capture plant flow diagram. In addition, configurations A (in purple) and B (in green) identify the process alternatives adopted for the continuous cooling crystallization of ammonium bicarbonate. Configuration A exploits an MSMPR for the final crystallization step while configuration B uses an SSHE. The parameter $\alpha$ is the ratio between the mass flow rate of the enriched slurry and that of the stream sent to the solid/liquid separation. The available plant excess heat sources used to achieve complete solid dissolution are listed in Table 5.1.

Supersaturation in the solution is generated using cooling crystallization[119] by exploiting the high dependence of BC solubility on temperature.[26,72] Alternatives are not feasible because of the high volatility of $CO_2$ and $NH_3$ (evaporative crystallization) or not intended here because of the increased complexity in case of using an anti-solvent (e.g. an alcohol). Cooling crystallization has therefore been applied in the form of a continuous multistage process that involves two types of crystallizers which are discussed below.

- *Scraped surface heat exchangers (SSHEs)* are tubular crystallizers/heat exchangers which consist of two coaxial cylinders as shown in Figure D.2. The main shaft is equipped with scraper blades in order to prevent encrustation and blockage due to the uncontrolled growth

| Heat Source | $T_{\mathrm{IN}}$ [°C] | Power [MW] |
|---|---|---|
| $CO_2$-lean from desorber | 61 | 200 |
| Flue gas DCC water | 53 | 90 |
| $CO_2$ intercoolers water | 120 | 55 |
| Reboiler condensate | 130 | 50 |

TABLE 5.1: Excess heat sources available for the plant. Power duties and temperature of the streams from Sutter et al.[25]

of a crystal layer on the inner wall, which is the coldest surface of the crystallizer. Scraped surface heat exchangers are usually used to process viscous liquids or to crystallize from the melt.[120–123] This work assumes that a warm crystallizing suspension flows inside the inner tube. A colder slurry containing dissolving crystals (or a chilling medium, depending on the operating mode) flows countercurrently between the cylinders. The geometry of such equipment is fully defined by the internal diameter, $d_{\mathrm{i}}$, the ratio between the external and the internal diameters, $a = d_{\mathrm{e}}/d_{\mathrm{i}}$, and the tube length, $x_{\mathrm{r}}$.

- *Mixed suspension mixed product removal (MSMPR)* crystallizers are widely used in industrial processes as well as in the lab.[124] A suspension is continuously fed to a stirred tank where crystal nucleation and growth are achieved by cooling the suspension below the saturation temperature of the feed stream. The crystallizer's body is designed to enclose a volume sufficient for retention of the growing crystals and the required thermal duty is provided by external circulation of the crystallizer's magma in dedicated heat exchangers.[33]

With reference to Figure 5.1, the cooling crystallization is performed between the initial temperature, $T_{\mathrm{abs}}$, and the final temperature, $T_{\mathrm{cry}}$, with a crystal throughput that depends on the final crystallization yield,

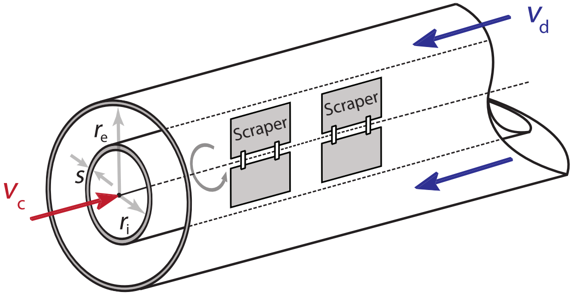

FIGURE 5.2: Schematic representation of a scraped surface heat exchanger (SSHE) consisting of two cylindrical steel tubes with an axial shaft on which the scraped blades are mounted. The cooling crystallization/dissolution process is performed by feeding a crystallizing slurry to the internal tube while a colder slurry containing dissolving crystals flows countercurrently in the outer annular passage. The variables $r_i$, $r_e$, and $s$ are the inner radius of the internal tube, the inner radius of the external tube, and the tube's thickness, respectively.

$Y_{BC}$. Accordingly, a $CO_2$-rich solution coming from the absorber at temperature $T_{abs}$ is fed to the first MSMPR crystallizer, MSMPR1. A steady state crystal size distribution (CSD) is generated through nucleation and growth with characteristics depending on the residence time in the unit. The crystallization process is then carried on in the series of tubular crystallizers, called SSHE1 and SSHE2. Finally, crystallization is completed in the last unit which is cooled using a chilling medium, e.g. R134a or liquefied ammonia, which evaporates at the pressure corresponding to 0 °C.

In this work, two different process configurations for the cooling crystallization have been studied. They differ in the type of equipment exploited for the final phase of the crystallization. Configuration A, highlighted in purple in Figure 5.1, includes a second MSMPR, called MSMPR2. In turn, configuration B, highlighted in green in Figure 5.1, uses a third tubular crystallizer, called SSHE3. In both cases, the final crystallization temperature is $T_{cry}$.

The solid-free mother liquor recovered from the solid/liquid separation is assumed to be heated up by 1 °C, in line with the assumptions made by Sutter et al.,[25] while flowing through the annular passage of the second tubular crystallizer, SSHE2. This heating procedure avoids to recycle a supersaturated solution to the absorber and, at the same time, it allows for heat integration. The slurry obtained after cooling crystallization is concentrated via solid/liquid separation in a dedicated hydro-cyclone. The separation process, assumed to be ideal, splits the inlet stream into a solid-free mother liquor and an enriched slurry. Its suspension density is controlled via the splitting factor parameter, $\alpha$, which is the ratio between the mass flow rate of the enriched slurry and that of the inlet stream of the hydro-cyclone.

Prior to solvent regeneration, solids in the enriched slurry must be completely dissolved in order to prevent clogging of the packed columns of the desorber. To this end, the enriched slurry is first recycled to SSHE1 and then to a dedicated dissolution section. In this configuration, SSHE1 also serves the purpose of reducing the need for chilling by enabling heat integration between the warm crystallization suspension coming from MSMPR1 and the cold enriched slurry that flows countercurrently in the annular passage of SSHE1. The dissolution of the solids in the enriched slurry is limited by the temperature that can be reached at the end of SSHE1. Notably, this temperature is always below the complete dissolution of BC which is given by the BC solubility and varies depending on the slurry density achieved after the solid/liquid separation. Solid dissolution is finalized by processing the slurry exiting SSHE1 in a series of shell and tube heat exchangers, called HE-1, HE-2, and HE-3. They exploit plant excess heat sources that provide heat at temperature levels around 100 °C (cf. Table 5.1). The section is operated at the pressure of 10 bar, as simulated in the work by Sutter et al.,[25] to avoid vapor formation and prevent cavitation of the centrifugal pumps.

| Parameter | Value | Parameter | Value |
|---|---|---|---|
| **Rich $CO_2$ stream from absorber**[25] | | **Physical properties**[30] | |
| Temperature, $T_{\mathrm{abs}}$ [°C] | 21.4 | Density, $\rho$ [kg m$^{-3}$] | 1016 |
| Free $NH_3$ concentration, $\omega_{NH_3}$ [-] | 0.07 | Viscosity, $\mu$ [Pa s] | $10^{-3}$ |
| Solute concentration, $c_{\mathrm{abs}}$ [kg m$^{-3}$] | 193.6 | Conductivity, $k$ [W m$^{-1}$ °C$^{-1}$] | 0.6 |
| **Process**[25] | | Heat capacity, $\hat{c}_p$ [J °C$^{-1}$ kg$^{-1}$] | 3723 |
| Splitting factor, $\alpha$ [-] | 0.25 | Crystal density, $\rho_{\mathrm{s}}$ [kg m$^{-3}$] | 1586[125] |
| Temperatures [°C]: | | Heat of crystallization, $\Delta H_{\mathrm{BC}}$ [kJ kg$^{-1}$] | 481 |
| cooling water inlet temp., $T_{\mathrm{CW}}$ | 15.0 | Ideal gas constant, $R$ [J °C$^{-1}$ mol$^{-1}$] | 8.314 |
| Ambient temperature, $T_{\mathrm{Amb}}$ | 15.0 | | |
| MSMPR operating temp., $T_{\mathrm{MSMPR1}}$ | 18.0 | **Modeling** | |
| final crystallization temp., $T_{\mathrm{cry}}$ | 5.0 | Reference concentration, $c_{\mathrm{r}}$ [kg m$^{-3}$] | 198.9 |
| chilling medium temp., $T_{\mathrm{chill}}$ | 0.0 | Reference temperature, $T_{\mathrm{r}}$ [°C] | 21.4 |
| absorber recycle | 6.0 | Crystal shape factor, $k_{\mathrm{v}}$ [-] | $\pi/6$ |
| Desorption pressure, $p_{\mathrm{des}}$ [bar] | 10 | HRM number of bins, $N_\lambda$ [-] | 30 |
| Minimum $\Delta T$ for heat exchange [°C]: | | BVP convergence tol., $\epsilon_{\mathrm{BVP}}$ [-] | $10^{-4}$ |
| liquid to liquid | 3 | Tearing convergence tol., $\epsilon$ [-] | $10^{-6}$ |
| evaporator of chilling duty | 5 | Pipe roughness [-] | $10^{-3}$ |
| condenser of chilling duty | 10 | SSHEs blades rot. speed [Hz] | 1 |
| COP for refrigeration unit [-] | 5.4 | SSHE tubes conductivity, $k_{\mathrm{t}}$ [W m$^{-1}$ °C$^{-1}$] | 24 |

TABLE 5.2: Process parameters for the simulations. The $CO_2$-rich stream properties and operating parameters, unless explicitly mentioned, have been adapted from Sutter et al.[25] The mass fraction-based free $NH_3$ concentration, $\omega_{NH_3}$, in the rich-$CO_2$ stream refers to the ammonia content of the solvent on a carbon-free basis.

## 5.3 MODELING

### 5.3.1 *Model Equations*

A detailed rate-based model has been developed in order to simulate the continuous crystallization-dissolution process shown in Figure 5.1, under realistic operating conditions. The following assumptions are made in developing the model: (1) incompressible fluid flow with physical properties assumed to be temperature independent (cf. Table 5.2); (2) mono-dimensional description of the fluid flow through the SSHEs; (3) negligible axial and radial dispersion due to the turbulent flow regimes investigated; (4) steady state (SS) for the crystallization and dissolution processes; (5) perfect mixing in the MSMPR crystallizers; (6) negligible crystal agglomeration and breakage in all the equipment.

The set of equations used in the mathematical model consists of the population balance equations (PBEs), the solute mass balance equation, and the energy balance. The PBEs describe the evolution of the crystal size distribution throughout the crystallization process. Furthermore, the appropriate constitutive equations for crystallization kinetics and heat transfer also form part of the model. Due to the dissociation equilibria and the non-ideality of the liquid phase,[26] the solution supersaturation is computed based on activities.

The model equations have been cast in dimensionless form in order to reduce the number of model parameters while also reducing numerical hurdles. The following dimensionless variables for solute concentrations, $c$, suspension temperature, $T$, crystal size, $L$, and spatial coordinate of the crystallizer, $x$, are used in this work:

$$\gamma = \frac{c}{c_\mathrm{r}}, \quad \vartheta = \frac{T}{T_\mathrm{r}}, \quad \lambda = \frac{L}{L_\mathrm{r}}, \quad \xi = \frac{x}{x_\mathrm{r}}, \tag{5.1}$$

where $\gamma$ is the dimensionless concentration of BC, $\vartheta$ is the dimensionless temperature of the suspension, $\lambda$ is the dimensionless particle size, and $\xi$ is the dimensionless spatial coordinate of the crystallizer. The parameters $c_\mathrm{r}$, $L_\mathrm{r}$, $T_\mathrm{r}$, and $x_\mathrm{r}$ are used to scale the problem. The values assumed for $c_\mathrm{r}$ and $T_\mathrm{r}$ are reported in Table 5.2 while $L_\mathrm{r}$ and $x_\mathrm{r}$ vary according to the specific process simulation.

Furthermore, the crystal size distribution, $\tilde{n}$, (based on a unit volume of solution) is defined as a function of the dimensionless particle size, $\lambda$, through the differential relationship $\tilde{n} d\lambda = n dL$, where $n(L)$ is the dimensional particle size distribution. The evolution of the dimensionless CSD, $\tilde{n}$, is described by a dimensionless continuity equation in the particle phase space, adapted from Randolph et al.:[124]

$$\frac{\partial \tilde{n}}{\partial \tau} + \mathrm{Da}\frac{\partial (\tilde{G}\tilde{n})}{\partial \lambda} + \nabla_\xi \cdot (\tilde{\mathbf{v}}\tilde{n}) - \widetilde{B} + \widetilde{E} = 0 \tag{5.2}$$

where $\tau$ is the dimensionless residence time, $\widetilde{B}$ and $\widetilde{E}$ are the birth and death functions accounting for nucleation, agglomeration, and breakage. The Damköhler number, Da, defined as

$$\mathrm{Da} = \frac{t_{\mathrm{res}}}{L_{\mathrm{r}}/k_{\mathrm{g,0}}} \tag{5.3}$$

represents the ratio between the residence time, $t_{\mathrm{res}}$, and the characteristic crystallization time calculated as $L_{\mathrm{r}}/k_{\mathrm{g,1}}$, with $k_{\mathrm{g,0}}$ being the growth rate constant. The dimensionless quantity $\nabla_{\xi} \cdot (\tilde{\mathbf{v}}\tilde{n})$ in eq 5.2 is the divergence of the CSD flux in the space domain and for a one-dimensional model, it corresponds to the partial derivative $\partial(\tilde{v}\tilde{n})/\partial\xi$.

*MSMPR Crystallizer Balance Equations*

The modeling of a well-mixed isothermal crystallizer at steady state assumes negligible crystal breakage and agglomeration, negligible change in suspension volume, as well as a negligible impact of the external circulation loop for heat transfer on the crystallization kinetics. Eventually, integrating eq 5.2 over the entire crystallizer volume and applying Gauss's theorem (the unit vector normal to the control volume's surface is defined positive when pointing outwards from the surface) to the spatial divergence of the dimensionless CSD flux leads to the following equation:[124]

$$\frac{d\tilde{n}}{d\lambda} = \frac{\tilde{n}_{\mathrm{in}} - \tilde{n}}{\mathrm{Da}\tilde{G}} \tag{5.4}$$

with the boundary condition given as

$$\tilde{n}(\lambda = 0) = \frac{L_{\mathrm{r}}J}{k_{\mathrm{g,0}}\tilde{G}} \tag{5.5}$$

where $\tilde{n}_{\mathrm{in}}$ is the inlet CSD, and $J$ and $\tilde{G}$ are the secondary nucleation and dimensionless crystal growth rates at the MSMPR operating temperature and supersaturation, respectively.
eq 5.4 is coupled with the solute mass balance

$$c_{\mathrm{r}}(\gamma_{\mathrm{in}} - \gamma) = k_{\mathrm{v}}\rho_{\mathrm{s}}L_{\mathrm{r}}^{3}(\tilde{\mu}_{3} - \tilde{\mu}_{3,\mathrm{in}}) \tag{5.6}$$

where the parameters $\gamma_{\text{in}}$ and $\tilde{\mu}_{3,\text{in}}$ are the dimensionless inlet solute concentration and dimensionless third moment of the inlet distribution, $k_{\text{v}}$ is the volume shape factor of the crystals, and $\rho_{\text{s}}$ is the crystal density. The dimensionless $i$-th moment, $\tilde{\mu}_i$, of the dimensionless CSD is calculated as follows:

$$\tilde{\mu}_i = \int_0^\infty \tilde{n}\lambda^i d\lambda = \frac{1}{L_{\text{r}}^i}\int_0^\infty nL^i dL = \frac{\mu_i}{L_{\text{r}}^i} \quad i = 0, \ldots, n \tag{5.7}$$

where $\mu_i$ is the corresponding $i$-th moment of the original distribution $n(L)$.
eq 5.4-5.6 have analytical solutions for the case of an MSMPR processing a clear solution as inlet stream, i.e. $\tilde{n}_{\text{in}}(\lambda) = 0$. Conversely, numerical integration is required in general when $\tilde{n}_{\text{in}}(\lambda) \neq 0$.

### *SSHE Crystallizer Balance Equations*

Three types of SSHE are present in the process, namely:

1. SSHE1, where crystallization and dissolution simultaneously occur in the inner tube and in the annular passage, respectively;

2. SSHE2, where crystallization exclusively occurs in the inner tube of the crystallizer while in the outer passage a solution is heated up (i.e. the recycle to the absorber);

3. SSHE3 (only for the case of configuration B), where crystallization occurs in the tube side while a saturated boiling medium used for chilling purposes flows in the annular passage.

As in the case of MSMPR crystallizers, breakage and agglomeration phenomena have been neglected in the SSHEs, too. Secondary nucleation has also been included in the model of the tubular crystallizers as a boundary condition on the PBE. The following equations are obtained where the subscripts c and d indicate crystallization and dissolution, respectively:

**Population Balances**

$$\mathrm{Da_c}\tilde{G}\frac{\partial \tilde{n}_\mathrm{c}}{\partial \lambda}+\frac{\partial \tilde{n}_\mathrm{c}}{\partial \xi}=0 \tag{5.8a}$$

$$\mathrm{Da_d}\tilde{D}\frac{\partial \tilde{n}_\mathrm{d}}{\partial \lambda}+\frac{\partial \tilde{n}_\mathrm{d}}{\partial \xi}=0 \tag{5.8b}$$

**Solute Mass Balances**

$$c_\mathrm{r}\frac{\mathrm{d}\gamma_\mathrm{c}}{\mathrm{d}\xi}+k_\mathrm{v}\rho_\mathrm{s}L_\mathrm{r}^3\frac{\mathrm{d}\tilde{\mu}_{3,\mathrm{c}}}{\mathrm{d}\xi}=0 \tag{5.8c}$$

$$c_\mathrm{r}\frac{\mathrm{d}\gamma_\mathrm{d}}{\mathrm{d}\xi}+k_\mathrm{v}\rho_\mathrm{s}L_\mathrm{r}^3\frac{\mathrm{d}\tilde{\mu}_{3,\mathrm{d}}}{\mathrm{d}\xi}=0 \tag{5.8d}$$

**Energy Balances**

$$\frac{\mathrm{d}\vartheta_\mathrm{c}}{\mathrm{d}\xi}+4\mathrm{St_c}\phi(\vartheta_\mathrm{c}-\vartheta_\mathrm{d})-\Psi_\mathrm{c}k_\mathrm{v}L_\mathrm{r}^3\frac{\mathrm{d}\tilde{\mu}_{3,\mathrm{c}}}{\mathrm{d}\xi}=0 \tag{5.8e}$$

$$\frac{\mathrm{d}\vartheta_\mathrm{d}}{\mathrm{d}\xi}+\frac{4}{\alpha}\frac{\hat{c}_{p,\mathrm{c}}}{\hat{c}_{p,\mathrm{d}}}\mathrm{St_c}\phi(\vartheta_\mathrm{c}-\vartheta_\mathrm{d})-\Psi_\mathrm{d}k_\mathrm{v}L_\mathrm{r}^3\frac{\mathrm{d}\tilde{\mu}_{3,\mathrm{d}}}{\mathrm{d}\xi}=0 \tag{5.8f}$$

The mathematical model of the tubular crystallizer describes the coupling of heat transfer and crystallization. This is accomplished through eq 5.8a-f where the population and solute mass balances, eq 5.8a-b (obtained recasting eq 5.2 for a scraped surface crystallizer at steady state) and eq 5.8c-d respectively, are coupled with the energy balances on both sides of the heat exchanger, eq 5.8e-f (the non-dimensional energy balance is derived in Appendix D). The dimensionless number that arises from the algebraic manipulation of the energy balance is the Stanton number, St, defined as

$$\mathrm{St}=\frac{U^{(\mathrm{i})}}{\rho v\hat{c}_p} \tag{5.9}$$

where $\rho v$ is the suspension's mass flux, $\hat{c}_p$ is the specific heat capacity of the fluid, and $U^{(\mathrm{i})}$ is the overall convective heat transfer coefficient referred to the surface on the internal tube of the SSHE. This dimensionless number represents the ratio of the thermal energy transferred

into/from a fluid to the thermal capacity of that fluid.
Both sensible and latent heat transfer have been taken into account since the crystallization and dissolution phenomena, especially in the case of inorganic compounds, imply a substantial amount of latent heat being released/gained during the process.[119] Such heat source/sink terms are described through the dimensionless heat of crystallization/dissolution intensity parameter, $\Psi$, defined as

$$\Psi = \frac{\Delta H_{\mathrm{BC}} \rho_{\mathrm{s}}}{\rho \hat{c}_p T_{\mathrm{r}}} \tag{5.10}$$

where the specific latent heat of crystallization of BC in aqueous ammonia solution, $\Delta H_{\mathrm{BC}}$, has been estimated as 481 kJ/kg by applying the updated extended-UNIQUAC model presented by Darde et al.[30] at infinite dilution conditions. The heat of reaction associated to the speciation in the liquid phase has been neglected, considering it minor compared to the latent heat contribution.
The parameter $\phi$ in eq 5.8e-f is the slenderness ratio of an SSHE, defined as

$$\phi = \frac{x_{\mathrm{r}}}{d_{\mathrm{i}}} \tag{5.11}$$

where $x_{\mathrm{r}}$ is the length of the SSHE and $d_{\mathrm{i}}$ is the inner diameter of the internal tube. The range of values of the SSHE slenderness ratio for configuration B has been reported in Appendix D for completeness. Table 5.3 lists the sets of boundary conditions that apply to the process, depending on the type of crystallizer and process configuration.

### *Complete Solid Dissolution Section*

The model adopted for simulating the complete solid dissolution section sequentially solves the energy balances for each shell and tube heat exchanger under the assumption that equilibrium between the solid and liquid phase is reached. The sizing of the equipment is therefore not performed since this task is outside the scope of the work. The imposed

| Equipment | CSD | Temperature | Concentration |
|---|---|---|---|
| MSMPR1 | $\tilde{n}_{\mathrm{M1}}(\lambda=0)=L_{\mathrm{r}}J/G$ | $\vartheta_{\mathrm{M1}}$ | $\gamma_{\mathrm{M1,in}}=\gamma_{\mathrm{abs}}$ |
| SSHE1 | $\tilde{n}_{\mathrm{c,1}}(\lambda,\xi=0)=\tilde{n}_{\mathrm{M1}}(\lambda)$<br>$\tilde{n}_{\mathrm{c,1}}(\lambda=0,\xi)=L_{\mathrm{r}}J/G$<br>$\tilde{n}_{\mathrm{d,1}}(\lambda,\xi=1)=\tilde{n}_{\mathrm{M2}}(\lambda)/\alpha$<br>$\tilde{n}_{\mathrm{d,1}}(\lambda,\xi=1)=\tilde{n}_{\mathrm{c,3}}(\lambda,\xi=1)/\alpha$ | $\vartheta_{\mathrm{c,1}}(\xi=0)=\vartheta_{\mathrm{M1}}$<br>$\vartheta_{\mathrm{d}}(\xi=1)=\vartheta_{\mathrm{cry}}$<br>$\vartheta_{\mathrm{d}}(\xi=0)=\vartheta_{\mathrm{M1}}-\Delta\vartheta_{\mathrm{p}}$ | $\gamma_{\mathrm{c}}(\xi=0)=\gamma_{\mathrm{M1,out}}$<br>$\gamma_{\mathrm{d}}(\xi=1)=\gamma_{\mathrm{M2,out}}$<br>$\gamma_{\mathrm{d}}(\xi=1)=\gamma_{\mathrm{c,3}}(\xi=1)$ |
| SSHE2 | $\tilde{n}_{\mathrm{c,2}}(\lambda,\xi=0)=\tilde{n}_{\mathrm{c,1}}(\lambda,\xi=1)$<br>$\tilde{n}_{\mathrm{c,2}}(\lambda=0,\xi)=L_{\mathrm{r}}J/G$ | $\vartheta_{\mathrm{c,2}}(\xi=0)=\vartheta_{\mathrm{c,1}}(\xi=1)$<br>$\vartheta_{\mathrm{d,2}}(\xi=1)=\vartheta_{\mathrm{cry}}$<br>$\vartheta_{\mathrm{d,2}}(\xi=0)=\vartheta_{\mathrm{cry}}+\Delta\vartheta_{\mathrm{abs}}$ | $\gamma_{\mathrm{c,2}}(\xi=0)=\gamma_{\mathrm{c,1}}(\xi=1)$<br>$\gamma_{\mathrm{d,2}}(\xi=1)=\gamma_{\mathrm{M2,out}}$<br>$\gamma_{\mathrm{d,2}}(\xi=1)=\gamma_{\mathrm{c,3}}(\xi=1)$ |
| SSHE3 | $\tilde{n}_{\mathrm{c,3}}(\lambda,\xi=0)=\tilde{n}_{\mathrm{c,2}}(\lambda,\xi=1)$<br>$\tilde{n}_{\mathrm{c,3}}(\lambda=0,\xi)=L_{\mathrm{r}}J/G$ | $\vartheta_{\mathrm{c,3}}(\xi=0)=\vartheta_{\mathrm{c,2}}(\xi=1)$<br>$\vartheta_{\mathrm{c,3}}(\xi=1)=\vartheta_{\mathrm{cry}}$<br>$\vartheta_{\mathrm{d,3}}(\xi)=\vartheta_{\mathrm{chill}}$ | $\gamma_{\mathrm{c,3}}(\xi=0)=\gamma_{\mathrm{c,2}}(\xi=1)$ |
| MSMPR2 | $\tilde{n}_{\mathrm{M2,in}}(\lambda)=\tilde{n}_{\mathrm{c,2}}(\lambda,\xi=1)$ | $\vartheta_{\mathrm{M2}}=\vartheta_{\mathrm{cry}}$ | $\gamma_{\mathrm{M2,in}}=\gamma_{\mathrm{c,2}}(\xi=1)$ |

Table 5.3: Boundary conditions used in the mathematical model. Purple color applies to configuration A, green color applies to configuration B. Black color applies to all configurations. The parameters $\Delta\vartheta_{\mathrm{p}}$, $\vartheta_{\mathrm{cry}}$, $\vartheta_{\mathrm{chill}}$, and $\alpha$ refer to the dimensionless pinch point temperature between the stream coming from MSMPR1 and the stream exiting SSHE1 (dissolution side), the final dimensionless crystallization temperature, the chilling medium dimensionless temperature, and the splitting factor (cf. Section 5.2), respectively. The parameter $\Delta\vartheta_{\mathrm{abs}}$ represents the dimensionless temperature increase of the solid-free stream recycled to the absorber.

energy balances account for the sensible and latent heat transferred during the process as follows:

$$Q_i-\frac{c_{\mathrm{r}}\Delta\gamma_i\Delta H_{\mathrm{BC}}}{\rho}-T_{\mathrm{r}}(\vartheta_i-\vartheta_{i-1})\hat{c}_{p,\mathrm{c}}=0\quad i=1,\ldots,3 \tag{5.12a}$$

$$\vartheta_0=\vartheta_{\mathrm{SSHE1,d}}(\xi=0) \tag{5.12b}$$

where the subscript $i$ refers to the $i$-th heat exchanger, and accordingly $Q_i$ is the specific excess plant heat processed, $\Delta\gamma_i$ is the variation of solute concentration due to dissolution, and $\vartheta_{\mathrm{SSHE1,d}}$ is the dimensionless temperature of the suspension that undergoes dissolution at the inlet of the SSHE1. Table 5.1 summarizes the specification of the plant excess heat sources used in this work.

### 5.3.2 *Crystallization Kinetics*

This study employs empirical kinetic equations for secondary nucleation, growth, and dissolution of BC in aqueous ammonia solution. Secondary nucleation, i.e. the formation of nuclei as a result of the presence of solute crystals in a supersaturated solution, has been considered the most relevant nucleation mechanism in the crystallizers. Note that this process includes crystallizers that operate in a regime of low supersaturation, thus fulfilling the requirements for the mechanism of secondary nucleation to be operative.[126]

According to Mersmann,[119] the solution supersaturation, $S^*$, which represents the driving force for crystallization, is defined as

$$S^* = \left[ \frac{a_\pm^2(\vartheta, \gamma)}{K_{\mathrm{SP}}(\vartheta)} \right]^{\frac{1}{2}} \tag{5.13}$$

where the ammonium bicarbonate mean molal activity in solution, $a_\pm$, is computed using the updated extended-UNIQUAC model presented by Darde et al.,[30] accounting for equilibrium speciation in the liquid phase. The temperature dependence of the BC solubility product, $K_{\mathrm{SP}}$, reported in Darde et al.,[30] is used in this work.

The constitutive equations adopted for the crystallization kinetics are:

$$J = k_{\mathrm{n},1} \exp\left(-\frac{k_{\mathrm{n},2}}{R\vartheta}\right) G^{k_{\mathrm{n},3}} \mu_3 \tag{5.14}$$

$$G = k_{\mathrm{g},0}\tilde{G} = k_{\mathrm{g},0} \exp\left(-\frac{E_{\mathrm{a,g}}}{R\vartheta}\right) (\ln S^*)^{k_{\mathrm{g},2}} \tag{5.15}$$

$$D = k_{\mathrm{d},1}\tilde{D} = k_{\mathrm{d},1} \exp\left(-\frac{k_{\mathrm{d},2}}{R\vartheta}\right) (1 - S^{*2})^{k_{\mathrm{d},3}} \tag{5.16}$$

where $J$ is the secondary nucleation rate, $\tilde{G}$ is the dimensionless growth rate scaled by the pre-exponential factor $k_{\mathrm{g},0}$, and $\tilde{D}$ is the dimensionless dissolution rate, scaled by the pre-exponential factor $k_{\mathrm{d},1}$. Secondary nucleation has been assumed to depend on supersaturation through the growth rate, $G$, the temperature, and the third moment, $\mu_3$, of the CSD. Size-independent growth kinetic parameters for BC in aqueous solution as reported by Sutter et al.[37] have been used. This work applies these growth kinetics to the CSF-CAP solvent that, besides water, contains an excess of ammonia, due to the lack of alternative literature data. Therefore, any kinetic effect due to the different solvent composition has been neglected.

Due to the lack of experimental data for this system, kinetic parameters for secondary nucleation and dissolution rates have been estimated based on available crystallization data for inorganic salts.[118] Table 5.4 summarizes the kinetic parameters used in this work, unless explicitly mentioned otherwise.

### *Heat Transfer Correlation*

This work uses the heat transfer correlation for scraped surface heat exchangers proposed by Goede et al.[121] It combines a regular model for turbulent pipe flow with heat penetration theory to account for the disturbance of the thermal boundary layer by the scraper action. The Gnielinski correlation has been used to evaluate the heat transfer coefficient in concentric ducts.[127] The overall heat transfer coefficient referenced to be surface area of the inner wall of the internal tube of the SSHE, $U^{(\mathrm{i})}$, has therefore been calculated for crystallizing systems characterized by Reynolds numbers, $\mathrm{Re}_\mathrm{c}$, which are between $10^4$ to $10^5$. Furthermore, the additional Reynolds number, $\mathrm{Re}_\mathrm{d}$, that characterizes the flow regime in the annular passage of the SSHE is computed as

$$\mathrm{Re}_\mathrm{d} = \frac{\alpha}{a+1}\mathrm{Re}_\mathrm{c} \tag{5.17}$$

The mathematical derivation of eq 5.17 is provided in Appendix D.

| **Kinetic Parameter** | **Value** | |
|---|---|---|
| **Nucleation** | | |
| $k_{n,1}$ | $5.00 \cdot 10^{27}$ | $[m^{-4}]$ |
| $k_{n,2}$ | $7.67 \cdot 10^{4}$ | $[J\,mol^{-1}]$ |
| $k_{n,3}$ | 1.00 | [-] |
| **Growth**[37] | | |
| $k_{g,0}$ | 0.10 | $[m\,s^{-1}]$ |
| $E_{a,g}$ | $2.58 \cdot 10^{4}$ | $[J\,mol^{-1}]$ |
| $k_{g,2}$ | 2.52 | [-] |
| **Dissolution** | | |
| $k_{d,1}$ | 0.10 | $[m\,s^{-1}]$ |
| $k_{d,2}$ | $2.58 \cdot 10^{4}$ | $[J\,mol^{-1}]$ |
| $k_{d,3}$ | 1.00 | [-] |

TABLE 5.4: Kinetic parameters used as reference values for all simulations, unless explicitly mentioned otherwise. Growth rate parameters of ammonium bicarbonate in aqueous solution have been adapted from Sutter et al.;[37] all the remaining parameters have been estimated based on available crystallization data for inorganic salts.[118]

### 5.3.3 *Numerical Methods*

The numerical solution of the model equations presented in Section 5.3.1 has to cope first with the presence of a recycled stream (enriched cold slurry recycled to SSHE1), which requires an iterative algorithm to solve the problem, and then with the type of boundary conditions that apply to the system (cf. Table 5.3), which requires a numerical algorithm capable of handling boundary value problems (BVPs). Therefore, the most relevant issue is represented by the numerical solution of systems of partial differential equations (PDEs) that requires an efficient numerical method embedded into a BVP algorithm.

A *high resolution* method (HRM) with a van-Leer flux limiter which controls the flux of particles across cell boundaries of the crystal size domain has been chosen to solve the PBE accounting for crystal nucleation and growth.[34,35] This method guarantees high accuracy while allowing for a relatively low computational time and reduced numerical oscillations.[90] Eq 5.8a has been transformed into a system of ordinary differential equations (ODEs) in which the dimensionless crystal size domain is discretized into 30 volume bins, $N_\lambda$. This choice satisfies the need of achieving a good degree of accuracy in solving the balance equations without excessive utilization of computational time or memory resources. Eq 5.8b, which represents the case of size-independent crystal dissolution, has been transformed into a single ODE by use of the moving pivot method.[128] Based on the values of the dissolution rate, the whole CSD rigidly migrates towards smaller crystal sizes while fulfilling the mass and energy balances.

Eventually, the resulting set of ODEs consisting of the transformed PBEs, coupled with solute mass balances and energy balances, has been solved simultaneously in the dimensionless crystal size and space domains of the crystallizers. Furthermore, the counter-current flow arrangement adopted for the scraped surface heat exchangers requires the fulfillment of boundary conditions located at both ends of the finite space domain, $\xi \in [0, 1]$. The solution of a two-point BVP which satisfies the Dirichlet boundary conditions is therefore required. Although there is no guarantee of the existence and uniqueness of the solution for BVPs, in contrast to initial value problems (IVPs), it is standard practice to exploit numerical methods such as the shooting method, the finite-difference method, or the collocation method to obtain a solution for the problem. In this work, the steady state solution for SSHEs has been computed using a built-in MATLAB (R2015a) solver, *bvp5c*, developed by Kierzenka et al.,[129] which implements a collocation method based on a four-point Lobatto IIIA formula. The relative error tolerance, $\epsilon_{\mathrm{BVP}}$, for the BVP solver has been set to a value of $10^{-4}$. This algorithm produces a solution that is continuous and has a continuous first derivative in the entire domain. The solver is also able to handle vectors of unknown parameters that are computed along with the solution. This feature has been exploited for the computation of the required length of the tubular crystallizer by treating the spatial scaling parameter, $x_\mathrm{r}$, as an unknown parameter. Its converged value represents the required heat exchanger length for assigned process specifications.

The collocation method, coupled with a high resolution scheme, generates a linearized system of equations to be numerically solved. The number of unknowns is $(3N_\xi - 2)N_\mathrm{e}$,[129] $N_\mathrm{e}$ being the number of equations and $N_\xi$ the number of mesh points for the space domain discretization required by the collocation method. The number of required spatial mesh grid points is highly dependent on the problem's complexity and is internally computed by the collocation method. Typically, convergence is reached with less than 100 discretization points for the space domain for the kind of BVPs solved in this study. On the contrary, $N_\mathrm{e}$ is known and given by the total number of ODEs to be solved, which is strongly influenced by the number of bins used for the crystal size domain discretization. In light of these considerations, $N_\lambda$ appears to be constrained by an upper bound value that limits the size of the inverse matrix used for computing the BVP solution below the maximum standard size allowed by Matlab. Ultimately, the value of $N_\lambda$ equal to 30 allows for relative error for solute mass balance below 2% without incurring computational problems. The balance equations for the MSMPR2 (eq 5.4-5.6), whose feed is a suspension, were integrated numerically using the *ode23s* Matlab solver.

### *Convergence of the Process Flow Scheme Simulation*

The simulated flow schemes are solved through a sequential modular approach[130] that decomposes the process into sub-units based on the number of pieces of equipment. Each unit is then solved sequentially so that the balance equations are fulfilled. The convergence of the recycle, i.e. the enriched cold slurry recycled to SSHE1, is achieved by using an iterative algorithm that updates the entire flow scheme simulation until the Euclidean norm between two consecutive CSDs of the enriched slurry stream obtained after solid/liquid separation, $\tilde{n}_\mathrm{S/L}$, is less than the tolerance value, $\epsilon$, i.e.:

$$||\tilde{n}_\mathrm{S/L}^{(i+1)} - \tilde{n}_\mathrm{S/L}^{(i)}|| \leq \epsilon \tag{5.18}$$

where the superscript $i$ denotes the $i$-th iteration of the algorithm. Typically, convergence is reached after three to four iterations and the $i$-th updated enriched slurry's CSD, $\tilde{n}_{\mathrm{S/L}}^{(i)}$, is used as a guess distribution to solve eq 5.8 in an iterative way.

### 5.3.4 *Process Optimization*

A multi-objective optimization problem constrained by the final BC crystallization yield has been solved by minimizing a set of two objective functions. Those are represented by key performance indicators (KPIs) defined as follows. The first is the crystal productivity, $P$, defined as the mass rate of precipitated solid after cooling crystallization, $\dot{m}_{\mathrm{BC}}$, per unit of crystallization volume, i.e.

$$P = \frac{\dot{m}_{\mathrm{BC}}}{\sum_{i=1}^{N} V_i} \quad \left[\mathrm{kg_{BC}/(m^3h)}\right] \tag{5.19}$$

where the summation in eq 5.19 is extended to the whole set of crystallizers of the adopted configuration. The volume of the auxiliary equipment, e.g. ancillaries connected to MSMPR crystallizers, has not been included in the computation. Eventually, this leads to an overestimation of the optimal productivity. Nevertheless, this is the condition of maximum theoretical attainable productivity for the process configurations studied in this work.

The second indicator, $e_{\mathrm{tot}}$, is the specific energy penalty strictly associated to the novel crystallization section in the CSF-CAP. It represents the required equivalent amount of electric energy per unit mass of solid crystallized and it is defined as

$$e_{\mathrm{tot}} = \frac{Q_{\mathrm{chill}}}{\mathrm{COP}} + \frac{1}{\eta_{\mathrm{p}}}\left(\sum_{i=1}^{N} \frac{\Delta p_i}{k_{\mathrm{v}}\rho_{\mathrm{s}}\mu_3} + e_{\mathrm{p}}\right) \quad \left[\mathrm{MJ_{el}/kg_{BC}}\right] \tag{5.20}$$

The energy penalty contributions of eq 5.20 are the specific thermal energy for chilling needed for crystallization, $Q_{\mathrm{chill}}$, the friction losses, $\Delta p_i$, summed over the entire number of SSHEs, and the specific pumping energy, $e_\mathrm{p}$, required to operate the desorption section under pressure. The Fanning friction factor, $f$, is computed through the Colebrook equation, and the pump efficiency, $\eta_\mathrm{P}$, is assumed to be 0.76. The electric duty associated with the thermal energy for chilling has been computed using the Coefficient of Performance (COP) for a refrigeration unit. The COP has been calculated considering the ideal COP and a second-law efficiency of 0.6, as proposed by Valenti et al.[131] This work neglects the electric energy penalty associated with the scraping action of the SSHEs, since it is assumed to be a minor contribution compared to the the chilling duty.

Although not considered as an objective function in the optimization, the heat integration efficiency, $\eta_\mathrm{th}$, represents the third key performance indicator used to quantify the degree of heat integration of the entire process. It is defined as

$$\eta_\mathrm{th} = 1 - \frac{Q_\mathrm{chill}}{\Delta H_\mathrm{cry}} \tag{5.21}$$

where $\Delta H_\mathrm{cry}$ is the specific enthalpy change of the crystallizing suspension associated to the cooling crystallization process.

Within the framework of process configurations A and B, the energy-productivity constrained optimization is formulated as

$$\begin{aligned} \underset{\boldsymbol{\kappa}}{\text{minimize}} \quad & \left[\frac{1}{P(\boldsymbol{\kappa})},\ e_\mathrm{tot}(\boldsymbol{\kappa})\right] \\ \text{subject to} \quad & Y_\mathrm{BC} \geq 98\% \end{aligned} \tag{5.22}$$

where the vector $\boldsymbol{\kappa} = [t_\mathrm{MSMPR1}, t_\mathrm{MSMPR2}, v_\mathrm{c}, d_\mathrm{i}, a, \Delta T_\mathrm{p}]^\mathrm{T}$ in eq 5.22 represents the set of decision variables.

During the optimization, each MSMPR residence time, $t_\mathrm{MSMPR}$, was varied between 500 and 3600 s; the crystallizing suspension velocity, $v_\mathrm{c}$, was varied between 0.3 and 2.5 m/s in order to cover a range of Reynolds numbers between $10^4$ and $10^5$ for the crystallizing suspension; the SSHEs internal diameter, $d_\mathrm{i}$, and diameter ratio, $a$, assumed to be the same for all the SSHEs, were varied between 0.05 to 0.15 m and 1.1 to 1.5, respectively. The pinch point temperature, $\Delta T_\mathrm{p}$, defined as the temperature difference between the crystallizing suspension entering SSHE1 and the dissolving suspension exiting SSHE1, was varied between 3 and 10 °C.

The first MSMPR's operating temperature as well as the final crystallization temperature have been assumed to be 18 °C and 5 °C, respectively. Cooling water (CW), assumed to be available at 15 °C, is used to keep MSMPR1 at isothermal conditions. The splitting factor, $\alpha$, has been fixed to 0.25, in line with the results presented by Sutter et al.[25] For all simulations, complete dissolution has been achieved using the plant excess heat sources listed in Table 5.1. Table 5.2 summarizes the process parameters adopted for the optimization.

In this work, the genetic algorithm (GA) NSGA-II[132] has been selected for exploring the design space efficiently. It has to be acknowledged that GAs do not guarantee the convergence to a global minimum, but they allow for escaping local minima. NSGA-II also allows for parallel computing with the result of a substantial reduction of the simulation time. All computations reported in this work were carried out on the ETH-EULER cluster using 24 cores and 1 GB RAM for each core. The GA used 60 generations, each of them exploiting a population size of 30 times the number of decision variables considered in the optimization.

## 5.4 RESULTS AND DISCUSSION

### 5.4.1 *Process Assessment*

The constrained optimization performed in this study manages to identify the set of feasible operating conditions that allow for the maximization of the productivity and the minimization of the energy penalty. Moreover, it gives insights into the interplay between decision variables and their effect on the crystallization process, and more generally, on the overall process performance.

Figure 5.3 shows examples of solute concentration trajectories in the phase diagram for two optimized process alternatives. The two configurations differ only in the final crystallization step, which eventually causes the differences in solute concentration paths. In configuration

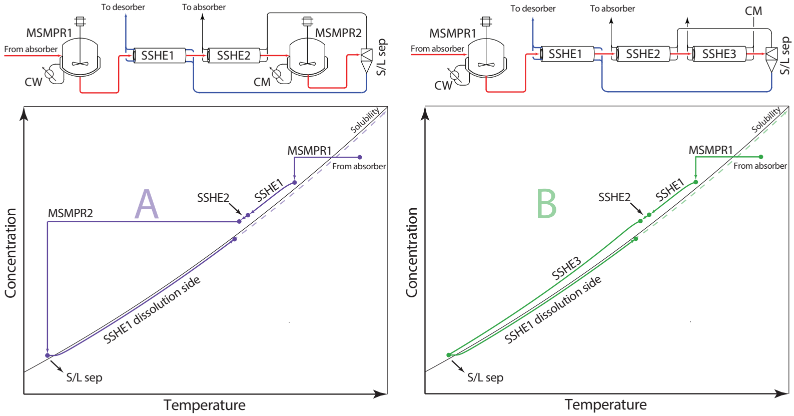

(a) (b)

Figure 5.3: Examples of solute concentration trajectories in the phase diagram for the crystallization and dissolution processes. (a) Configuration A exploits an MSMPR for the final crystallization step. (b) Configuration B exploits an SSHE for the final crystallization step. The dashed lines represent the solute concentration before complete dissolution is reached in a series of shell and tube heat exchangers (cf. Figure 5.1). Red and blue colors in the upper diagrams refer to the suspensions that undergo crystallization and dissolution, respectively.

B, the solute concentration depletion in SSHE3 takes place over the whole range of temperatures of the unit gradually, thus leading to a smooth concentration profile till the final crystallization temperature. In contrast, in configuration A the solute concentration experiences a sudden drop as the process stream is fed to MSMPR2 (cf. Figure 5.3). Figure 5.4 shows the specific energy penalty-productivity Pareto sets for configurations A and B representing all optimal energy penalty/productivity combinations (associated to different operating conditions) while fulfilling the final yield constraint of ammonium bicarbonate, $Y_{\mathrm{BC}}$. All shaded points (dominated points) represent feasible, but sub-optimal ways of operating the process.

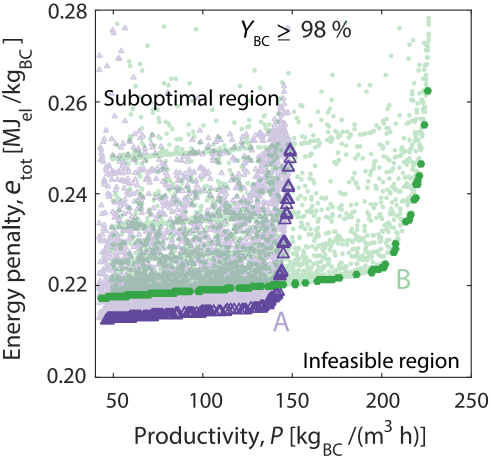

Figure 5.4: Specific energy penalty-productivity Pareto sets (highlighted) for process configurations A (purple △) and B (green •), respectively. Shaded points refer to suboptimal operating conditions.

The flow schemes of the different process configurations can be compared by analyzing the Pareto sets in terms of the corresponding values of the manipulated variables. The productivity of the two configurations is inversely proportional to the overall equipment volume, which is related to the residence time required for crystallization and heat transfer. Configuration B reaches higher values of productivity when compared to configuration A due to the corresponding equipment selection, i.e. a cascade of SSHEs. The intrinsic advantage of tubular crystallizers over MSMPRs is that, on average, they exploit faster crystallization kinetics.[133] Moreover, in the low productivity regime configuration A achieves a higher crystal throughput, $\dot{m}_{BC}$, than configuration B, thus lowering the energy penalty of the process. Ultimately, the energy efficiency is dictated by the effectiveness of latent and sensible heat exchange, the former being determined by the evolution of the CSDs generated during the cooling crystallization and dissolution operations, and the latter being driven by forced convection given the temperature constraints of the process. The choice of crystallization equipment also influences the efficiency of the downstream solid/liquid separation which is a fundamental step of the process. These considerations motivate a systematic assessment of the trends of the operating parameters and a characterization of the CSD obtained at the end of the cooling crystallization process for each of the optimized process configurations.

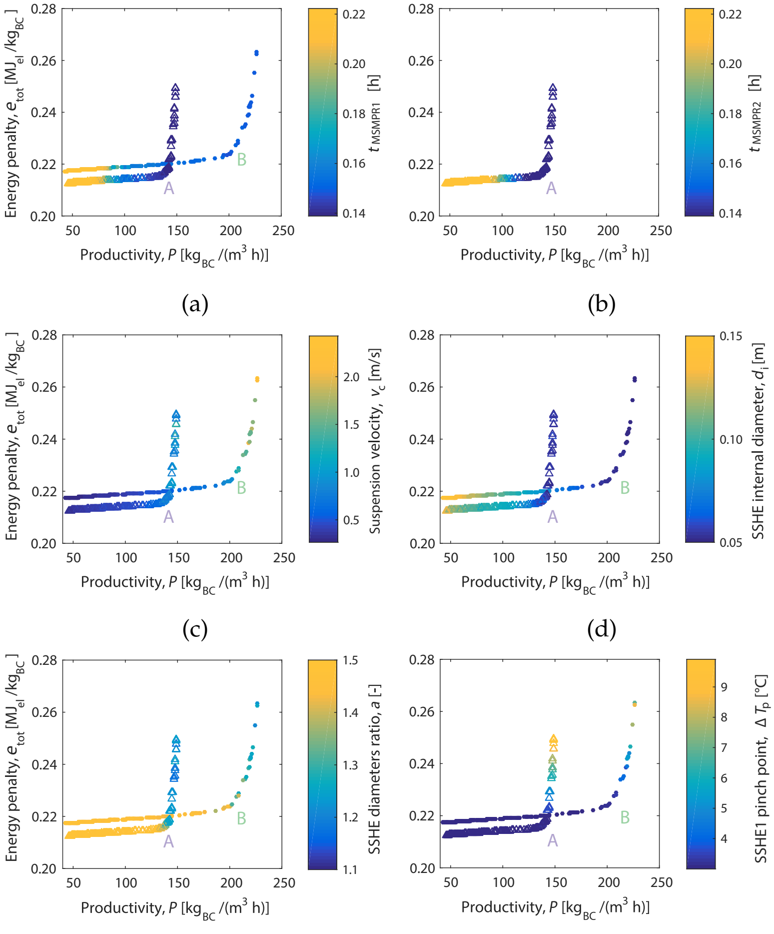

(a) (b) (c) (d) (e) (f)

Figure 5.5: Optimal values of the decision variables along the Pareto sets for process configurations A (△) and B (●). (a) MSMPR1 residence time, $t_{\text{MSMPR1}}$. (b) MSMPR2 residence time, $t_{\text{MSMPR2}}$. (c) Crystallizing suspension velocity, $v_{\text{c}}$. (d) SSHE internal diameter, $d_{\text{i}}$. (e) SSHE diameter ratio, $a$. (f) SSHE1 pinch point, $\Delta T_{\text{p}}$.

### *Optimal Values of the MSMPRs Residence Times*

Figure 5.5a shows the optimal residence time of MSMPR1 along the Pareto sets of the two configurations. The residence time values decrease rapidly towards the lowest level of about 500 s for increasing values of productivity. The equipment volume is therefore minimized, thus maximizing the productivity of the process. Interestingly, the optimization routine converges towards larger and larger residence times as the productivity decreases. According to eqs 5.4-5.6, an increase in residence time yields larger crystallizer volumes, with a negative effect on the productivity, but it also allows for an increase of BC throughput, thus lowering the specific energy penalty.

Compared to the overall residence time in the solid handling section, the residence time in the MSMPR1 is low: the unit acts, above all, as a source of nuclei that then grow in the downstream cascade of crystallizers.

The optimal residence times of the MSMPRs in configuration A follow a similar trend along the Pareto set, as shown in Figure 5.5b. Within the MSMPR2 however, the crystallizer volume is mainly used for crystal growth in order to reach the final crystal yield defined by eq 5.22.

### *Optimal Values of Suspension Velocity and SSHEs' Geometrical Parameters*

Figure 5.5c-e show the optimal values of the suspension velocity, $v_\mathrm{c}$, the inner tube diameter of the SSHEs, $d_\mathrm{i}$, and the ratio between the diameters of the SSHEs, $a$, respectively. The trends are similar for both configurations and are discussed in detail only for configuration B. Figure 5.6a shows the correlation between the values of the suspension velocity, $v_\mathrm{c}$, and of the inner tube diameter of the SSHEs, $d_\mathrm{i}$, along the Pareto set. Productivity can be increased, while minimizing the energy penalty, by simultaneously increasing the suspension velocity and by decreasing the internal diameter of the SSHEs. The optimization algorithm exploits the synergy of these two process variables to minimize the required heat exchange area by increasing the overall heat transfer coefficient of the SSHEs, $U^{(\mathrm{i})}$. The ratio between the diameters of the SSHE, $a$, also affects the heat transfer. In fact, in Figure 5.5e and 5.6b

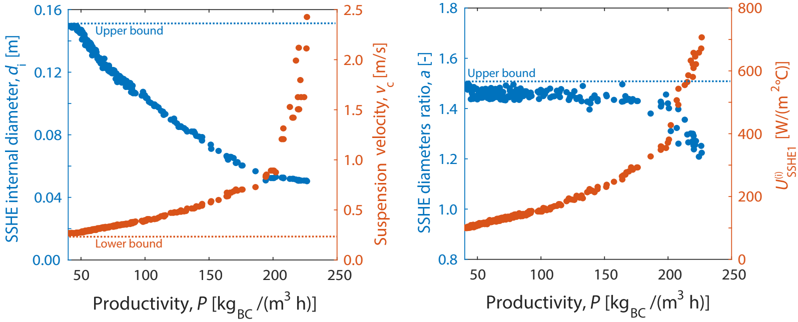

(a) (b)

FIGURE 5.6: Correlations between the process parameters for the optimized configuration B. (a) SSHE internal diameter, $d_{\mathrm{i}}$, and crystallizing suspension velocity, $v_{\mathrm{c}}$ vs. productivity. (b) SSHE diameter ratio, $a$, and SSHE1 overall heat transfer coefficient, $U^{(\mathrm{i})}_{\mathrm{SSHE1}}$, vs. productivity.

two regions can be identified: a first corresponding to low/medium productivity values, where the SSHE diameter ratio approaches the upper bound assigned during the optimization; and a second region towards high productivity values, for which the optimization routine evolves rather sharply in the direction of lower values of the parameter $a$. This behavior can be explained by considering that annular passages with decreasing ratio between diameters exhibit larger and larger values of the convective heat transfer coefficient.[127]

### *Optimal Pinch Point Temperature*

Figure 5.5f shows the optimal values of the temperature pinch point, $\Delta T_{\mathrm{p}}$, which is the operating variable that affects the energy penalty the most. On the one hand, an increase of the pinch point temperature implies a reduction of the heat transfer surface required by SSHE1, thus allowing for a gain in productivity. However, due to the relative magnitudes of heat and mass transfer of this system, this gain appears modest, especially in the high-productivity regime where the steepness of the Pareto set is remarkable. On the other hand, an increase of the pinch point temperature reduces the potential for heat integration due to the inherent temperature constraint imposed to the SSHE1. In general, both configurations exploit low pinch point temperature values (blue points in Figure 5.5f) to minimize the energy penalty of the process. As shown in Figure 5.7, the main contribution to the energy penalty for the case of configuration B is represented by the equivalent electric energy required for chilling, while the energy required for slurry pumping (blue points) and friction losses (green points) represent minor contributions. Only in the high productivity regime the friction losses have a significant impact on the specific energy penalty due to the combined effect of optimal values of the suspension velocity, SSHEs internal diameter, and diameter ratio. Similar results, not reported here for the sake of clarity, can be found for the optimized configuration A.

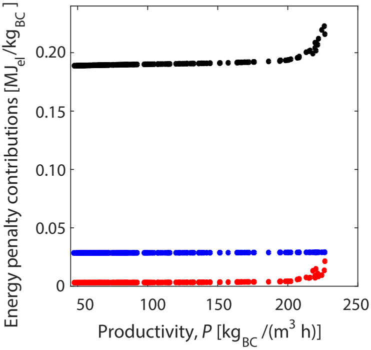

FIGURE 5.7: Contributions to the specific energy penalty, $e_{\mathrm{tot}}$, for the optimized process configuration B. Black dots refer to the equivalent specific electric energy for chilling, red dots refer to the specific energy required to overcome the friction losses of the SSHEs, and blue dots refer to the remaining specific energy for pumping (net of the pressure drops), i.e. pressure increase to regeneration pressure (10 bar).

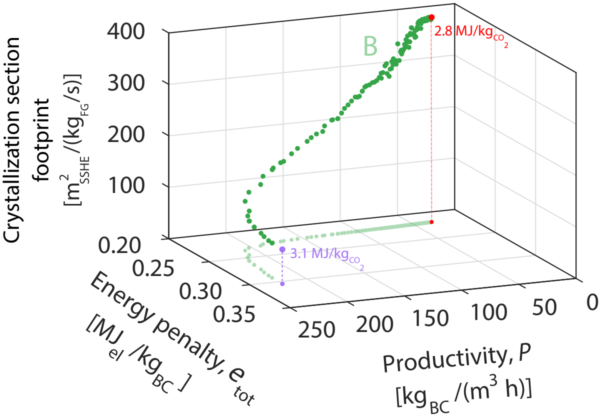

Figure 5.8: Estimate of the crystallization section footprint in the CSF-CAP. The required SSHE heat transfer area per unit mass flow-rate of treated flue gas is expressed as a function of the productivity, P, and specific energy consumption, $e_{tot}$, for the optimized configuration B. The SPECCA index associated with the red and purple points is the lowest and highest achievable value in the process, respectively. The projection of all the points in the productivity-energy penalty plane represents the Pareto set of the optimized configuration B shown in Figure 5.4.

### *Assessment of the Crystallization Section Footprint*

The optimization framework of this study allows to relate optimal productivity and energy penalty to the footprint of the crystallization section in the CSF-CAP and, more in general, to the specific primary energy consumption for $CO_2$ avoided (SPECCA) of the entire capture process. The footprint is defined as the required heat transfer area of the SSHE units per unit flow-rate of treated flue gas, while the SPECCA index is computed according to the definition provided by Sutter et al.[25] For the sake of brevity, the results of the analysis are shown in Figure 5.8 for the optimized configuration B only. Although the absolute values shown in the figure depend on the specific expressions

| Variable | Configuration A | | Configuration B | |
|---|---|---|---|---|
| | Low $P$ | High $P$ | Low $P$ | High $P$ |
| $t_{\mathrm{MSMPR1}}$ [s] | 854 | 501 | 862 | 533 |
| $t_{\mathrm{MSMPR2}}$ [s] | 1746 | 505 | n/a | n/a |
| $v_{\mathrm{c}}$ [$\mathrm{m\,s^{-1}}$] | 0.32 | 1.45 | 0.32 | 2.27 |
| $d_{\mathrm{i}}$ [m] | 0.13 | 0.05 | 0.13 | 0.05 |
| $a$ [-] | 1.49 | 1.23 | 1.45 | 1.22 |
| $\Delta T_{\mathrm{p}}$ [°C] | 3.00 | 9.80 | 3.00 | 9.90 |

Table 5.5: Optimal process parameters relative to the points selected on the Pareto sets shown in Figure 5.9. Orange and light blue colors refer to the low and high productivity cases, respectively.

and values of the transport parameters in the model, the underlying trends are robust. They can be generalized by observing that, in the low energy penalty regime, the footprint of the crystallization section decreases almost linearly with increasing values of productivity, while in the high productivity regime the lowest footprint values are achieved at the expenses of an increased energy penalty. In light of these considerations, the contrast between the reduction of the footprint of the process and the optimization of its heat integration potential reflects the trade-off identified between productivity and energy penalty. In terms of specific energy consumption for $CO_2$ avoided, the computed SPECCA index of the CSF-CAP that features the highest degree of heat integration ($\eta_{\mathrm{th}}$ =25 %) is 2.8 $\mathrm{MJ/kg_{CO_2}}$, while for the case of the least heat integration efficiency of 10 % the SPECCA index increases to about 3.1 $\mathrm{MJ/kg_{CO_2}}$.

### *Properties of the CSD during Cooling Crystallization*

As mentioned in Section 5.4.1, the combined effect of the crystallization phenomena, i.e. nucleation and growth, and the equipment selected for cooling crystallization influence the final properties of the CSD in terms of broadness and presence of fines in the solid product. To show this, the evolution of the CSD for the cases of highest and lowest attainable productivity in configurations A and B (points highlighted in light-blue and orange in Figure 5.9) has been analyzed. Additionally, Table 5.5 summarizes the numerical values of the optimal process variables for each case of interest.

Two statistical parameters are used to characterize the CSD throughout the crystallization process. The first is the number-based mean size of the crystals, $\bar{L}$, used as an estimator of the relative importance of secondary nucleation and growth, and defined as

$$\bar{L} = \frac{\mu_{1,\mathrm{c}}}{\mu_{0,\mathrm{c}}} \tag{5.23}$$

The second statistical parameter is the skewness of the CSD, $\Sigma$, defined as

$$\Sigma = \frac{\mathrm{E}[(L-\mathrm{E}(L))^3]}{(\mathrm{E}[(L-\mathrm{E}(L))^2])^{3/2}} = \frac{\mu_{3,\mathrm{c}}}{{\sigma_{\mathrm{c}}}^3} \tag{5.24}$$

where $\mathrm{E}[\Phi] = \int_0^\infty n(L)\Phi dL$ is the expected value operator, $\mu_{3,\mathrm{c}}$ and $\sigma_{\mathrm{c}}$ are the third moment and the standard deviation (about the mean) of the CSD, respectively. For a symmetric distribution, e.g. a Gaussian distribution, the skewness is zero, while for a distribution with a tail towards large sizes it assumes positive values.

The continuous process configurations A and B exploit the MSMPR1 to generate a population of crystals that, according to eq 5.4, is exponential. Then, the CSD evolves along the downstream crystallizers as shown in Figure 5.9 according to the supersaturation profiles and residence times provided. The formation of new particles is noticeable along the length of the first and second tubular crystallizer and it leads to a reduction of the mean size of the CSD in the high and low productivity regimes in both the configurations. Instead, crystal growth represents the predominant phenomenon in the last step of the cooling crystallization process where the increase of the crystal mean size becomes relevant. From Figure 5.9 it can also be noticed that operating the process in the low productivity region, thus providing more time for crystals to grow, does not produce a significant increase in the CSD mean size when

compared to the high productivity regime. This stems from the fact that supersaturated conditions promote also the occurrence of secondary nucleation.
As a matter of fact, the CSD obtained after cooling crystallization, in both the configurations, preserves roughly the properties and broadness of the initial exponential distribution since its skewness value is close to two, i.e. the theoretical skewness of an exponential distribution. In turn, this can affect the efficiency of the downstream solid/liquid separation whenever a relevant portion of the mass of the solid phase is distributed below the nominal cut-off size of the separator.[124]
In light of these key findings, the process design of a continuous multistage cooling crystallization should also focus on the impact of the type of crystallization equipment and its arrangements on the crystal quality as well as on the optimization of the key process parameters such that favorable crystallization kinetics are obtained.[134]

### 5.4.2 *Sensitivity Analyses of the Crystallization and the Dissolution Kinetics*

The lack of kinetic data for this system motivated a sensitivity analysis on the crystallization kinetics, i.e. secondary nucleation and growth, by means of process simulations carried out using the mathematical model derived in Section 5.3. The general purpose of the analysis is to identify trends of process parameters such as the heat integration efficiency, $\eta_{\mathrm{th}}$ and the attainable final CSD mean size, $\bar{L}$, associated to a variation of the crystallization kinetics. In this regard, configuration B has been optimized according to eq 5.22 using the values of the kinetic parameters reported in Table 5.6.

#### *Effect of Secondary Nucleation Rates*

The nucleation pre-exponential factor, $k_{\mathrm{n},1}$, was varied in order to investigate the effect of different nucleation rates while keeping the growth and dissolution rate-constants unchanged. Figure 5.10a shows an increment of the maximum attainable productivity for increasing values of the secondary nucleation rate-constant. This behavior is explained by

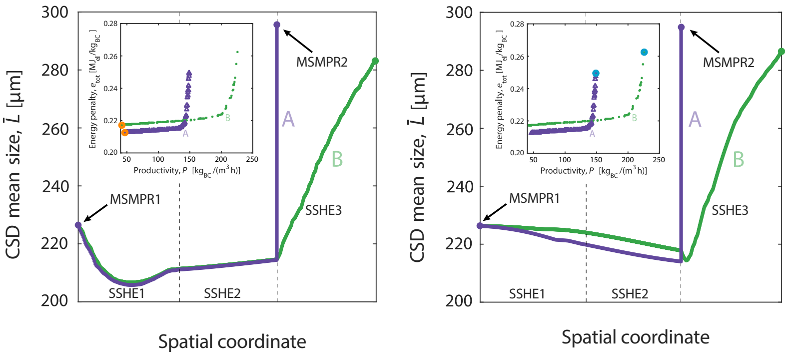

(a) (b)

Figure 5.9: Evolution of the CSD mean size, $\bar{L}$, along the spatial coordinate of the crystallizers for configurations A and B, respectively. Colored dots in the Pareto sets indicate the points interested by the analysis. (a) Spatial evolution of the crystal mean size at low productivity for configuration A (purple line) and configuration B (green line). (b) Spatial evolution of the crystal mean size at high productivity for configuration A (purple line) and configuration B (green line).

| **Kinetic Parameter** | **Value** | | |
|---|---|---|---|
| $k_{n,1}$ [$m^{-4}$] | $5{\cdot}10^{26}$ | $5{\cdot}10^{27}$ | $5{\cdot}10^{28}$ |
| $k_{d,1}$ [$m\,s^{-1}$] | $5{\cdot}10^{-3}$ | $5{\cdot}10^{-2}$ | $5{\cdot}10^{-1}$ |

Table 5.6: Model parameters used for the sensitivity analysis of the crystallization kinetics.

considering that increasing values of the nucleation rate-constant lead to smaller crystallizers, thus higher values of the attainable productivity. As shown in Figure 5.10c, the crystal mean size, $\bar{L}$, remarkably reduces for increasing values of the parameter $k_{n,1}$. In turn, the increment of the total number of particles is responsible for an increase of the crystal surface available for growth, thus leading to a faster depletion of the solute concentration. This is shown in Figure 5.10e where the evolution of the solute concentration profiles (indicated by the red curves) are reported for a selection of points on the Pareto sets in Figure5.10a at the reference productivity of 195 kg/(m$^3$ h). Similarly, the solute concentration in the stream that undergoes dissolution in SSHE1 approaches the solubility curve for increasing values of the secondary nucleation rate constant, the dissolution phenomenon being enhanced by the presence of smaller and smaller particles.

### *Effect of Dissolution Rates*

Process simulations were performed while varying the dissolution pre-exponential factor, $k_{\mathrm{d},1}$, in order to investigate the effect of different dissolution rates while keeping the growth and nucleation rate constants unchanged. Figure 5.10b shows that the rate of dissolution of the crystals in the enriched slurry influences the heat integration efficiency by means of the latent heat exchanged in SSHE1. The amount of latent heat transferred during the process is constrained thermodynamically by the solubility of the compound and kinetically by its dissolution rate. In this regard, Figure 5.10f shows the evolution of the solute concentration profiles for a set of points selected along the Pareto sets of Figure 5.10b at the reference productivity of 172 kg/(m$^3$ h). At the process conditions relative to point 3, the fast dissolution rate leads to a concentration profile that evolves virtually along the solubility curve, thus maximizing the amount of latent heat that can be recovered. For lower dissolution rate constants, e.g. points 2 and 1, the solute concentration is considerably below the achievable equilibrium value at the outlet of the SSHE1. Interestingly, the dissolution rate does not affect remarkably the concentration profile in the crystallizing suspension (red curves in Figure 5.10f) nor the CSD mean size of the final product (cf. Figure 5.10d). This leads to the conclusion that the latent heat released during dissolution has a minor contribution to the energy balance of the SSHE1 (cf. eq 5.8f), thus not affecting significantly the temperature and supersaturation profiles along the crystallizer. In line with these findings, Figure 5.10b shows that in the high productivity regime of the Pareto sets the energy penalty values are not affected by dissolution of crystals regardless of the value of the dissolution rate constant assumed in the simulations. As a matter of fact, the process residence times provided in this operating regime is much lower than the characteristic time required by dissolution, thus rendering the latent heat of dissolution a negligible contribution.

## 5.5 CONCLUSIONS

This study presents a methodology that facilitates the design of multistage continuous crystallization processes that also accommodate for heat integration. The method has been applied to an absorption-based process for post-combustion $CO_2$ capture in which solid formation is exploited to reduce the energy penalty of the entire process.[25] At first, feasible process alternatives have been proposed. Then, a rigorous rate-based model based on mass, energy, and population balances has been used for process simulation. Such a first-principle model is capable to capture robust trends in the process performance in spite of the uncertainty related to the values of the transport parameters of the model. Moreover, the establishment of an optimization framework has allowed for a thorough comparison of the alternative flow schemes highlighting the trade-off between the key performance indicators, i.e. energy penalty and productivity, and the interdependency among individual operating variables. The model shows that process configurations that use primarily tubular crystallizers instead of a cascade of MSMPRs can considerably enhance productivity. This remarkable result emphasizes the sensitivity of productivity and the final product's CSD to the crystallization equipment's specific arrangement. In contrast, the energy penalty appears to be virtually insensitive to changes in the arrangement and type of crystallization equipment (cf. Figure 5.4) being sensible heat the major contribution to the thermal energy integrated during the process, with only a minor contribution coming from latent heat of crystallization. Furthermore, the lack of available kinetic data for this case study motivated a sensitivity analysis on the kinetics of secondary nucleation and dissolution, the output of which is consistent with our understanding of the physical phenomena occurring in the system. Ultimately, an extensive experimental characterization of the mass and heat transfer kinetics in the equipment exploited is required. This activity, outside the scope of this work, would represent a step towards the improvement of the accuracy of the model.

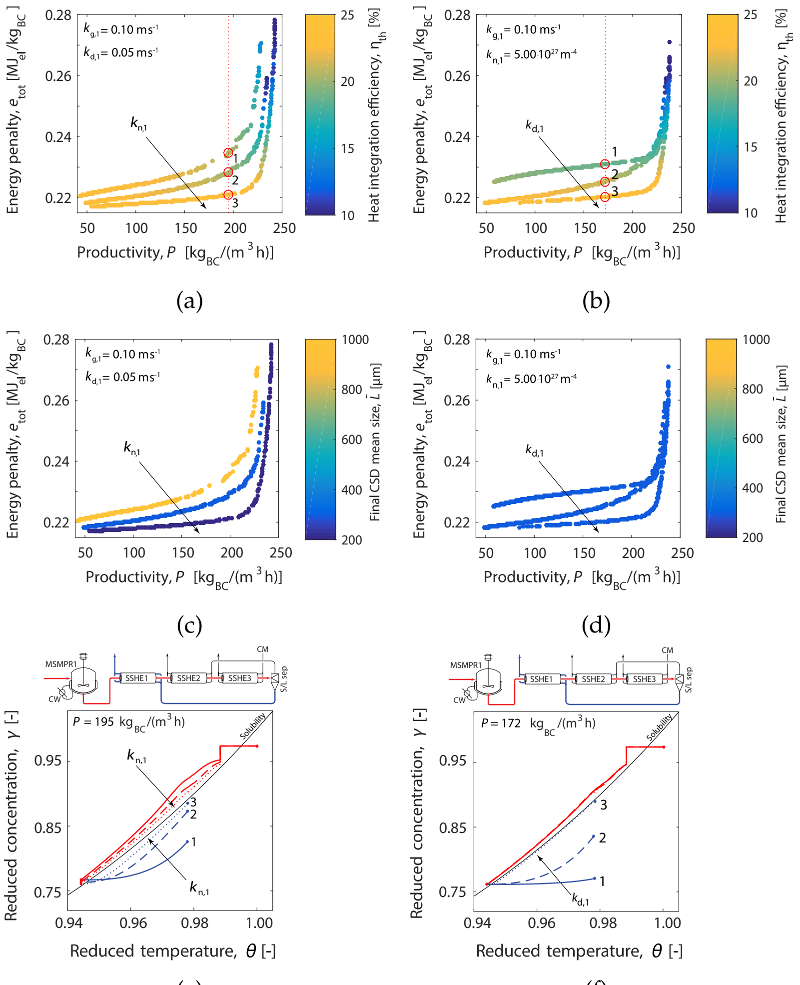

(a)

(b)

(c)

(d)

(e)

(f)

FIGURE 5.10: Sensitivity analysis of the crystallization kinetics. (a-d) Energy penalty-productivity Pareto sets relative to configuration B. (e-f) Trajectory of the dimensionless solute concentration in the phase diagram for the points 1 to 3 in Figures 5.10a-b. Red and blue colors indicate the crystallizing and dissolving suspensions, respectively.

## NOMENCLATURE

### *Acronyms*

| | |
|---|---|
| BC | Ammonium Bicarbonate |
| BVP | Boundary Value Problem |
| CAP | Chilled Ammonia Process |
| CCS | Carbon Capture and Storage |
| COP | Coefficient of Performance |
| CSD | Crystal Size Distribution |
| CSF | Controlled Solid Formation |
| CW | Cooling Water |
| DCC | Direct Contact Cooler |
| E | Expected value operator |
| FG | Flue Gas |
| GA | Genetic Algorithm |
| HE | Heat Exchanger |
| HRM | High Resolution Method |
| IVP | Initial Value Problem |
| KPI | Key Performance Indicator |
| MSMPR | Mixed Suspension Mixed Product Removal |
| PBE | Population Balance Equation |
| PFD | Process Flow Diagram |
| S/L | Solid/liquid separation |
| SS | Steady State |
| SSHE | Scraped Surface Heat Exchanger |
| VLE | Vapor Liquid Equilibrium |

### *Greek Symbols*

| | |
|---|---|
| $\alpha$ | Splitting factor of the solid/liquid separation [-] |
| $\epsilon$ | Tearing convergence tolerance [-] |
| $\epsilon_{\mathrm{BVP}}$ | BVP convergence tolerance [-] |
| $\eta_{\mathrm{p}}$ | Pump efficiency [-] |
| $\eta_{\mathrm{th}}$ | Heat integration efficiency [-] |
| $\gamma$ | Dimensionless solute concentration [-] |
| $\lambda$ | Dimensionless particle size [-] |
| $\mu$ | Viscosity [Pa s] |
| $\mu_i$ | $i$-th moment of the CSD [$\mathrm{m}^i\mathrm{m}^{-3}$] |

| | |
|---|---|
| $\omega$ | Apparent weight fraction [-] |
| $\phi$ | Slenderness ratio of the SSHE [-] |
| $\Psi$ | Heat of crystallization intensity [-] |
| $\rho$ | Solution density [kg m$^{-3}$] |
| $\rho_\mathrm{s}$ | Crystal density [kg m$^{-3}$] |
| $\Sigma$ | Skewness of the CSD [-] |
| $\tau$ | Dimensionless residence time [-] |
| $\vartheta$ | Dimensionless suspension temperature [-] |
| $\xi$ | Dimensionless spatial coordinate [-] |
| $\sigma$ | Standard deviation of the CSD [m] |

*Roman Symbols*

| | |
|---|---|
| $\bar{L}$ | CSD mean size [µm] |
| $\Delta H_\mathrm{BC}$ | Ammonium bicarbonate latent heat of crystallization [kJ kg$^{-1}$] |
| $\Delta H_\mathrm{cry}$ | Specific enthalpy variation during crystallization [kJ kg$^{-1}$] |
| $\Delta p$ | Pressure loss [Pa] |
| $\Delta T_\mathrm{p}$ | Pinch point temperature [°C] |
| $\dot{m}_\mathrm{BC}$ | Ammonium bicarbonate throughput [kg s$^{-1}$] |
| $\mathrm{Da}$ | Damköhler number [-] |
| $\mathrm{Re}$ | Reynolds number [-] |
| $a$ | SSHE diameter ratio [-] |
| $a_\pm$ | Salt mean molal ionic activity [mol$^{2}$ kg$^{-2}$] |
| $c$ | Solute concentration [kg m$^{-3}$] |
| $D$ | Crystal dissolution rate [m s$^{-1}$] |
| $d_\mathrm{i}$ | SSHE internal tube diameter [m] |
| $E$ | Particle death function [m$^{-4}$ s$^{-1}$] |
| $e_\mathrm{p}$ | Specific pumping energy [J kg$^{-1}$] |
| $G$ | Crystal growth rate [m s$^{-1}$] |
| $J$ | Secondary nucleation rate, [m$^{-3}$ s$^{-1}$] |
| $k$ | Thermal conductivity [W m$^{-1}$°C$^{-1}$] |
| $K_\mathrm{SP}$ | Ammonium bicarbonate solubility product [mol$^{2}$ kg$^{-2}$] |
| $k_{\mathrm{d},i}$ | $i$-th dissolution rate parameter |
| $k_{\mathrm{g},i}$ | $i$-th growth rate parameter |
| $k_{\mathrm{n},i}$ | $i$-th nucleation rate parameter |
| $n$ | Crystal size distribution [m$^{-4}$] |
| $\tilde{n}$ | Rescaled crystal size distribution [m$^{-3}$] |
| $\tilde{n}_\mathrm{S/L}$ | Rescaled CSD after solid/liquid separation [m$^{-3}$] |
| $N_\lambda$ | Number of mesh points for the crystal size domain |

| | |
|---|---|
| $N_\mathrm{e}$ | Number of equations solved by the collocation method |
| $N_\xi$ | Number of mesh points used for the space domain discretization |
| $P$ | Productivity $[\mathrm{kg\,m^{-3}\,h^{-1}}]$ |
| $R$ | Ideal gas constant, $[\mathrm{J\,{}^\circ C^{-1}\,mol^{-1}}]$ |
| $r_\mathrm{e}$ | SSHE external tube radius [m] |
| $r_\mathrm{i}$ | SSHE internal tube radius [m] |
| $S^*$ | Solution supersaturation, based on Mersmann[119] [-] |
| $T$ | Temperature [°C] |
| $T_\mathrm{abs}$ | $CO_2$-rich stream temperature (from absorber) [°C] |
| $T_\mathrm{Amb}$ | Ambient Temperature [°C] |
| $T_\mathrm{cry}$ | Final crystallization temperature [°C] |
| $t_\mathrm{MSMPR1}$ | MSMPR1 residence time [s] |
| $t_\mathrm{MSMPR2}$ | MSMPR2 residence time [s] |
| $t_\mathrm{res}$ | Residence time [s] |
| $U$ | Overall heat transfer coefficient $[\mathrm{W\,m^{-2}{}^\circ C^{-1}}]$ |
| $V$ | Crystallizer volume $[\mathrm{m^3}]$ |
| $v$ | Suspension velocity $[\mathrm{m\,s^{-1}}]$ |
| $x$ | Spatial coordinate [m] |
| $Y_\mathrm{BC}$ | Ammonium bicarbonate yield [-] |
| $\hat{c}_p$ | Constant pressure specific heat $[\mathrm{kJ\,{}^\circ C^{-1}\,kg^{-1}}]$ |
| $B$ | Particle birth function $[\mathrm{m^{-4}\,s^{-1}}]$ |
| $e_\mathrm{tot}$ | Specific energy penalty $[\mathrm{MJ_{el}/kg}]$ |
| $f$ | Fanning friction factor [-] |
| $k_\mathrm{v}$ | Crystal shape factor [-] |
| $L$ | Crystal size coordinate [m] |
| $Q$ | Specific excess plant heat $[\mathrm{MW_{th}}]$ |
| $Q_\mathrm{chill}$ | Specific chilling $[\mathrm{MJ_{th}/kg}]$ |

*Subscripts and Superscripts*

| | |
|---|---|
| $\tilde{q}$ | Rescaled instance of the variable $q$ |
| $q_\mathrm{c}$ | Variable $q$ related to the crystallizing slurry |
| $q_\mathrm{d}$ | Variable $q$ related to the dissolving slurry |
| $q_\mathrm{in}$ | Variable $q$ at the crystallizer inlet |
| $q_\mathrm{r}$ | Scaling parameter for the variable $q$ |

# 6

# POSTSCRIPT

It is common that, following several years' devotion to a religion, a student' views about that religion would have matured.
This postscript is intended to communicate the reservations and criticisms I now have about the ammonia-based carbon capture processes that exploit solid formation described in this thesis as well as the open questions that remain.

## 6.1 ON THE LIQUID SPECIATION OF THE $CO_2-NH_3-H_2O$ SYSTEM

Usually, the adjustable parameters of the thermodynamic models for the $CO_2-NH_3-H_2O$ system require experimental speciation data to be tuned accurately. Gathering this type of information is often complicated by the ionic equilibria established in the liquid phase, which also render the interpretation of the measurements obtained from the analytical techniques used, i.e. infrared spectroscopy or nuclear magnetic resonance (NMR), especially complex due to the signal overlap of the single species in the overall IR spectrum or in the NMR shift.
This motivated the design of an IR-based *chemometric methodology* that would allow to estimate the concentration of each single species in solution, thus unveiling the real system composition in a range of overall ammonia and carbon concentrations of industrial relevance (cf. Chapter 2).
It has to be acknowledged that this methodology, although being robust, is limited to systems that obey the Beer-Lamber law. For the case of the $CO_2-NH_3-H_2O$ system, deviations from the *linear behavior* of the IR absorbance of most of the species in solution become noticeable above a concentration of ca. $6\,\mathrm{mol\,kg^{-1}}$, thus posing a practical limit to the mixtures that can be analyzed using this methology. The concentration of aqueous ammonia solutions containing $CO_2$ investigated in this thesis constituted therefore only a fraction of the ones exploitable by the

CSF-CAP process[25] (in which the aqueous ammonia concentration can reach values up to 25 % wt $NH_3$, while in this work the maximum value investigated was 3 % wt $NH_3$).

Further work should be focused on the identification of alternative analytical methods or on the development of experimental techniques for the estimation of the speciation of highly concentrated aqueous ammonia mixtures containing $CO_2$. This would allow to explore a wider range of $NH_3$ and $CO_2$ compositions as well as to improve the accuracy of the available thermodynamic models.

The reaction kinetics of the $CO_2-NH_3-H_2O$ system, which is still a relatively unexplored field,[135,136] plays an important role in the speciation of the liquid phase. In fact, even if the majority of the reactions occurring in the liquid (eqs 1.4-1.8) involves a fast proton exchange, the speciation of the system is kinetically limited by the carbamate formation (eq 1.8) whose equilibrium concentration strongly depends on the ratio between the overall nitrogen and carbon species in the system. As a result, the equilibration time of aqueous mixtures containing $CO_2$ and $NH_3$ in different ratios goes from few seconds to several hours.[64]

Based on these considerations, neglecting the effect of reaction kinetics during the simulation of crystallization, dissolution, or even absorption or desorption processes that involve the $CO_2-NH_3-H_2O$ system may lead to misleading results.

The development of a rate-based approach that takes into consideration the thermodynamic limitations as well as the reaction kinetics in the liquid phase would therefore improve substantially the description of the system, thus allowing for more accurate and reliable process simulations.

## 6.2 ON THE ESTIMATION OF THE CRYSTALLIZATION KINETICS

As discussed in Chapter 2, the computation of the solution supersaturation of aqueous ammonia solutions containing ammonium bicarbonate has been performed neglecting the effect of the reaction kinetics in the liquid phase. For the case of the ammonium bicarbonate crystal growth and dissolution experiments carried out in this thesis, this has been proven to be a reasonable assumption. Kinetic effects would be become however noticeable for values of the aqueous ammonia concentration greater than 10 % wt $NH_3(aq)$.

An optimization routine that combines the information of the solute concentration (measured via the IR-based *chemometric methodology* discussed above) with the mathematical modeling of crystallization/dissolution processes has allowed to estimate the parameters of the kinetic models that describe the ammonium bicarbonate crystal growth and dissolution (cf. Chapters 3-4). It has to be acknowledged that the investigation of this system required to operate the crystallizer under *unusual* operating conditions, i.e. a pressurized enviroment that mitigates the evaporation of solutes.

Although being validated only in a narrow range of experimental conditions, the proposed empirical models provide the foundation of the rate-based modeling framework used for the simulation of continuous crystallization in the CSF-CAP (cf. Chapter 5).

The intensity of primary and secondary nucleation of ammonium bicarbonate, processes known to be important in industrial crystallizers, has not been estimated in this work due to the difficulties associated to modeling stocastich processes and obtaining reproducible experimental data of nucleation events.[33,39] As stated in Chapter 5, this work accounts for ammonium bicarbonate secondary nucleation by using fictitious nucleation rates whose intensity has been varied over a wide range of values, in line with the literature data relative to similar inorganic compounds (cf. Chapter 5).

## 6.3 ON THE IMPACT OF SOLVENT IMPURITIES

Whenever industrial crystallization is of concern, the purity of the solvent has a tremendous impact on the crystallization kinetics as well as on the morphology of the crystals produced.[33]

In the CSF-CAP, the purity level of the solvent may differ based on the gas stream to be processed. Furthermore, the impurities distribution changes accordingly to the composition of the flue gas, of the type of flue gas pre-treatments adopted, and of the operating conditions set for the $CO_2$ capture process.

This thesis focused on the effect that sulfates ions ($SO_4^{2-}$) have on the ammonium bicarbonate crystallization kinetics. In detail, it has been found that sulfates, generated by the chemisorption of $SO_x$ contained in the flue gas directly by aqueous ammonia solutions, have a detrimental effect on the crystallization kinetics of ammonium bicarbonate: concentration values of this species above $0.2\,\mathrm{mol/kg_W}$ reduced the activity of ammonium bicarbonate in solution and caused a substantial inhibition of the overall crystal growth rate of ammonium bicarbonate when compared to the impurity-free system. As discussed extensively in Chapter 4, such inhibition might be caused by the adsorption of sulfate ions on the active sites of the growing crystals.

Ultimately, these findings allow to emphasize the conflict between the benefit of a combined $CO_2$ and $SO_x$ CSF-CAP absorption process (which would lead to a reduction of the capital cost for the emission control system) and the disadvantage of a reduction in crystallization kinetics that leads to an increase in equipment volume required for crystallization.

A good design practice for the CSF-CAP requires therefore to take into account the presence of solvent impurities active towards crystallization, and to limit the concentration of such impurities to a level which does not hinders the crystallization process.

## 6.4 AN INDUSTRY PERSPECTIVE

Since the first patent in 1930 by R. R. Bottoms,[12] $CO_2$ absorption-based processes have become more and more advanced over time, thus allowing for a reduction in the energy demand of the process and outstanding solvent performances. Compared to the established amine-based processes, ammonia-based absorption processes offer the additional theoretical potential of solid formation, which could be used to increase the overall efficiency of the $CO_2$ capture process, as discussed in Chapter 1. One has to consider though that the technology readiness of such hybrid processes is still rather low. In this respect, the CSF-CAP requires lab and pilot-plant scale demonstrations of the operability of the continuous solid handling section of the plant that uses counter-current scraped-surface heat exchangers (crystallizers) and hydro-cyclones for solid-liquid separation (cf. Chapter 5).

Compared to the standard CAP, the CSF-CAP shows increased plant complexity and capital costs (associated to the additional solid handling section) that might hinder the deployment of the technology at large scale (i.e. for gaseous streams of high mass flow-rate). Furthermore, a series of practical issues such as the dynamic response of the continuous crystallization process to an intermittent operation of the power plant, and the stability and control of the interdependent sections of the plant (particularly the ones that involve several energy and material recycles) should be analyzed through dedicated process simulations and experiments.

Currently, the concept proposed in the CSF-CAP appears to be particularly useful for niche industrial applications where the $CO_2$ capture from concentrated point sources is of concern and where the flow-rates to be treated are certainly order of magnitude lower than those of power plants.

Ultimately, the design approach proposed in this thesis aims at providing rough estimates of the crystallization equipment size and of the efficiency of the integrated CSF-CAP process. It also paves the way for future economic analyses of the integrated process such the one proposed by Li et al.[137]

Finally, it must be acknowledged that the fossil fuel challenge is inevitably an energy challenge with certainly no simple solution. In this respect, CCS is most probably an essential part of the portfolio of technologies needed to mitigate climate change. However, the deployment of CCS also embraces a plethora of socio-economical challenges that needs to be addressed in order to employ this technology at large scale and in a sustainable way.

A

# APPENDIX A

## A.1 ATR-FTIR CALIBRATION SETS OF AQUEOUS AMMONIA SOLUTIONS OF AMMONIUM BICARBONATE

The set of standard concentrations of aqueous ammonia solutions of ammonium bicarbonate used for the ATR-FTIR calibration procedure[45] are reported in Table A.1.
Figure A.1 shows the range of ammonium bicarbonate concentrations explored that covers the supersaturated as well as the undersaturated region of the phase diagram. The solid lines in Figure A.1 represent the solubility of ammonium bicarbonate at different nominal ammonia concentration in the solvent, $m^{\circ}_{NH_3}$.

| | **Concentration** [mol/kg$_w$] | | | | **Temperature** [°C] | | | |
|---|---|---|---|---|---|---|---|---|
| *Solute Sample No.* | 1 | 2 | 3 | 4 | 1 | 2 | 3 | 4 |
| $NH_4HCO_3$(aq) ($m^{\circ}_{NH_3}$ = 0 m) | 1.76 | 2.02 | 2.31 | 2.64 | 5 - 25 | $10^{\dagger}$ - 25 | $10^{\dagger}$ - 25 | $16^{\dagger}$ - 25 |
| $NH_4HCO_3$(aq) ($m^{\circ}_{NH_3}$ = 1.2 m) | 2.64 | 2.89 | 3.05 | 3.17 | 5 - 25 | $8^{\dagger}$ - 25 | $12^{\dagger}$ - 25 | $14^{\dagger}$ - 25 |
| $NH_4HCO_3$(aq) ($m^{\circ}_{NH_3}$ = 1.8 m) | 3.06 | 3.27 | 3.42 | 3.53 | 5 - 25 | $6^{\dagger}$ - 25 | $8^{\dagger}$ - 25 | $13^{\dagger}$ - 25 |

TABLE A.1: Set of standard concentrations of aqueous ammonia solutions of ammonium bicarbonate used for the ATR-FTIR calibrations (see Figure A.1); the variable $m^{\circ}_{NH_3}$ refers to the nominal ammonia concentration in the solvent in mol/kg$_w$. The symbol (†) refers to the temperature value corresponding to the onset of primary nucleation.

## A.2 OPTIMAL PARAMETERS OF THE ATR-FTIR CALIBRATIONS

The sets of optimal model parameters for the ATR-FTIR calibration methods based on maximum peak height and on maximum peak area are reported in Table A.2.

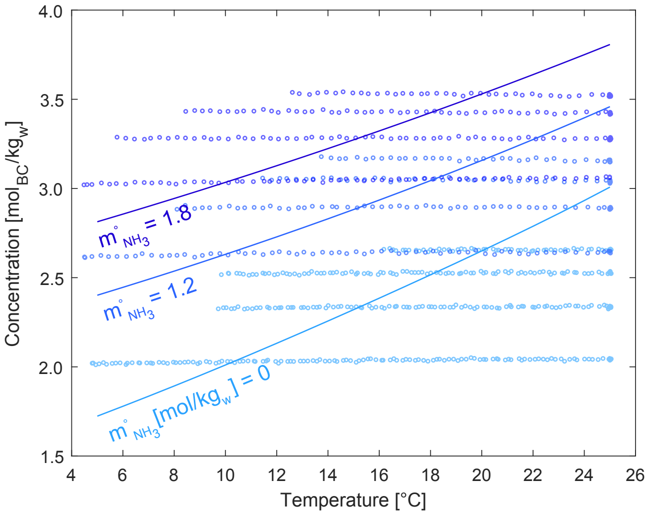

FIGURE A.1: Set of ATR-FTIR calibrations of aqueous ammonia solutions of ammonium bicarbonate in the temperature range 5-25 °C; the variable $m^\circ_{NH_3}$ refers to the nominal ammonia concentration in the solvent in mol/kg$_w$. The IR spectra of the mixtures at constant solute concentration have been collected for calibration purposes (see Table A.1). The concentration data after nucleation has been omitted and excluded from the calibration sets.

## A.3 $^{13}$C NMR SPECTROSCOPIC ANALYSES OF AQUEOUS SOLUTIONS OF $NH_4$CL AND $KHCO_3$ AND OF $NH_4HCO_3$

$^{13}$C NMR Spectroscopic analyses on have been used to qualitatively assess the extent of speciation of aqueous solutions of $NH_4Cl$(aq) and $KHCO_3$(aq) and of $NH_4HCO_3$(aq) used for the validation of the Classical Least Squares (CLS) methodology proposed in this work.
Moving from top to bottom, Figure A.2 shows the $^{13}$C NMR spectra of an equimolar aqueous solution of $NH_4Cl-KHCO_3$ (2.0 m), an aqueous solution of ammonium bicarbonate (2.0 m), and an aqueous solution of ammonium carbamate (1.6 m) at 25 °C respectively. The $^{13}$C NMR peaks

located at 168.24 ppm (indicated with a red dashed line in Figure A.2), 165.62 ppm, and 160.36 ppm refer to the carbonate ion, the carbamate ion, and the bicarbonate ion respectively. Because the equilibration between the carbonate and bicarbonate ions is rapid, the peaks for these two ions appear as a single peak whose position depends on the relative amounts of the two ions.[64]

For the case of the first two solutions, i.e. the solution of $NH_4Cl$(aq) and $KHCO_3$(aq), and the solution of $NH_4HCO_3$(aq), no significant speciation of the $HCO_3^-$ ion can be acknowledged, therefore these mixtures have been used to validate the CLS methodology. On the contrary, for the case of the solution of ammonium carbamate, the significant extent of speciation of the carbon atoms into carbamate and carbonate ions prevented the use of this mixture for validation.

## A.4 FORMATION OF AQUEOUS $CO_2$ IN SOLUTION OF AMMONIUM BICARBONATE

Due to the equilibrium reaction of eqn (1.5) taking place in an aqueous solution of ammonium bicarbonate, $CO_2$(aq) is formed in solution (see Figure A.3).

$$CO_2(aq) + H_2O \rightleftharpoons H^+ + HCO_3^- \tag{A.1}$$

Additionally, the evaporation of $CO_2$(g) leads to a significant pressure increase in the reactor (up to 6 barg depending on the temperature and $CO_2$(aq) concentration).

## A.5 SOLID-LIQUID FLASH CALCULATIONS

A main problem in the calculation of solid-liquid equilibrium is that the number and types of solid phases at equilibrium are not known in advance. This problem is solved by using a stepwise procedure, where the Gibbs function minimization (and stability analysis of the obtained solution) is used compute the number of stable phases in the system. Furthermore, it is assumed that, under the operating conditions investigated, no vapor-liquid or vapor-liquid-solid equilibria is established.

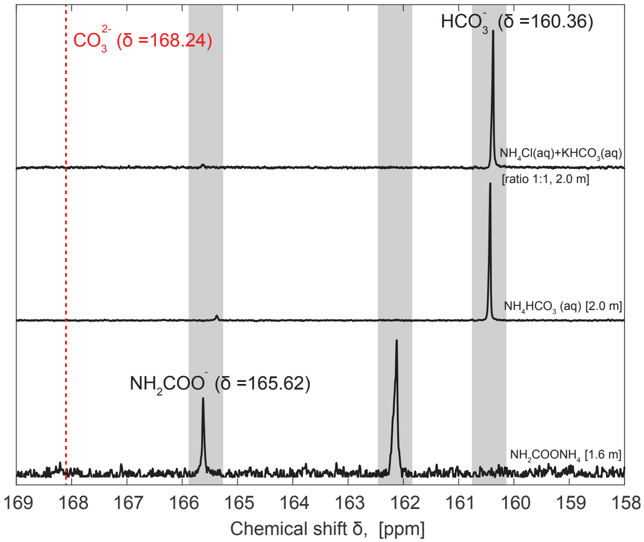

FIGURE A.2: From top to bottom: $^{13}$C NMR spectrum of an equimolar aqueous solution of $NH_4Cl-KHCO_3$ (2.0 m), an aqueous solution of ammonium bicarbonate (2.0 m), and an aqueous solution of ammonium carbamate (1.6 m) at 25 °C respectively. The carbonate, bicarbonate and carbamate ions' peaks are located at 168.24 ppm, at 165.62 ppm, and at 160.36 ppm respectively. For the case of the ammonium carbamate solution, the fast equilibration of the bicarbonate and carbonate ions leads to a single peak whose position depends on the relative amounts of the bicarbonate and carbonate ions.[64]

This leads to the following algorithm, where **S** is the supersaturation vector of the salts in the $CO_2-NH_3-H_2O$ system:

**Algorithm 1** Computation of the Solid-Liquid Equilibria

```
Require: Temperature and total composition of the system (equivalent
  $CO_2$, $NH_3$, and $H_2O$ weight fractions).
  The thermodynamic supersaturations $\mathbf{S}$ of all possible solid phases
  in the system are then calculated.
  if $\mathbf{S}$is less or equal to 1 (for all salts) then
    return  equilibrium liquid speciation of the system
  else
    while $\mathbf{S}$ is greater than 1 do
      identify the salt with the maximum degree of supersaturation
      based on the knowledge of the most unstable salt, compute
      the equilibrium liquid speciation and the solid fraction of the
      compound allowed to precipitate ($\mathbf{S} = 1$).
    end while
    return  equilibrium liquid speciation of the system and the solid
    fraction(s) of the relevant salt(s) precipitated (invariant points, i.e.
    two solid phases in equilibrium with a liquid phase, have also been
    detected).
  end if
```

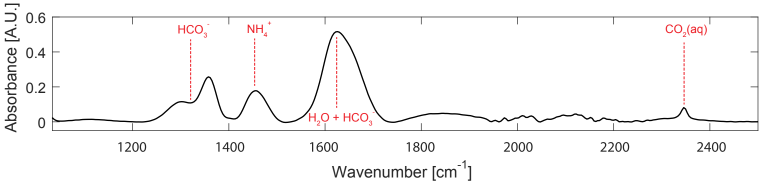

FIGURE A.3: IR spectrum of an aqueous solution of ammonium bicarbonate at 25 °C. The analysis of the spectrum reveals the presence of the $NH_4^+$ (located at 1445 $cm^{-1}$) and $HCO_3^-$ (located at 1355 $cm^{-1}$) ions and the solvent (water, located at 1640 $cm^{-1}$). Additionally, the presence of $CO_2$(aq) can be inferred by the visible asymmetric C=O stretching band of $CO_2$ located at 2343 $cm^{-1}$ in the infrared spectrum of the mixture.

| **Species** | **Method** | **Wavenumber** [$\mathrm{cm}^{-1}$] | $\hat{p}_0$ [$\mathrm{mol/kg_w}$] | $\hat{p}_1$ [$\mathrm{mol/(kg_w\ A.U.)}$] | $\hat{p}_2$ [$\mathrm{mol/(kg_w{}^\circ C)}$] | $\mathbf{R}^2$ [-] |
|---|---|---|---|---|---|---|
| $\mathbf{NH_4^+}$ | Peak Area | $1324 \leq \tilde{\nu} \leq 1522$ | $(-2.506 \pm 0.216) \cdot 10^{-1}$ | $(1.344 \pm 0.011) \cdot 10^{-1}$ | $(1.122 \pm 0.053) \cdot 10^{-2}$ | 0.9985 |
| | Maximum Peak Height | $\tilde{\nu} = 1458$ | $(-5.068 \pm 0.099) \cdot 10^{-1}$ | $10.27 \pm 0.03$ | $(3.638 \pm 0.220) \cdot 10^{-3}$ | 0.9918 |
| $\mathbf{HCO_3^-}$ | Peak Area | $1156 \leq \tilde{\nu} \leq 1466$ | $(4.818 \pm 1.718) \cdot 10^{-2}$ | $(4.856 \pm 0.035) \cdot 10^{-2}$ | $(2.945 \pm 0.480) \cdot 10^{-3}$ | 0.9990 |
| | Maximum Peak Height | $\tilde{\nu} = 1365$ | $(-9.160 \pm 0.092) \cdot 10^{-1}$ | $7.426 \pm 0.020$ | $(3.245 \pm 1.900) \cdot 10^{-4}$ | 0.9937 |
| $\mathbf{CO_3^{2-}}$ | Peak Area | $1208 \leq \tilde{\nu} \leq 1492$ | $(-5.989 \pm 0.337) \cdot 10^{-2}$ | $(1.798 \pm 0.012) \cdot 10^{-2}$ | $(2.331 \pm 0.110) \cdot 10^{-3}$ | 0.9974 |
| | Maximum Peak Height | $\tilde{\nu} = 1395$ | $(-6.850 \pm 0.229) \cdot 10^{-2}$ | $1.827 \pm 0.008$ | $(1.685 \pm 0.070) \cdot 10^{-3}$ | 0.9943 |
| $\mathbf{NH_3}$ | Peak Area | $1033 \leq \tilde{\nu} \leq 1178$ | $(7.230 \pm 0.059) \cdot 10^{-1}$ | $(4.119 \pm 0.020) \cdot 10^{-1}$ | $(3.278 \pm 0.350) \cdot 10^{-3}$ | 0.9988 |
| | Maximum Peak Height | $\tilde{\nu} = 1111$ | $(3.119 \pm 0.049) \cdot 10^{-1}$ | $25.70 \pm 0.09$ | $(3.977 \pm 0.250) \cdot 10^{-3}$ | 0.9976 |

TABLE A.2: Sets of optimal vector parameters $\hat{\mathbf{p}}$ for the ATR-FTIR calibration models based on maximum peak height or on maximum peak area. Coefficients are provided with 95 % confidence bounds.

B

# APPENDIX B

## B.1 STANDARD DEVIATION OF STEADY-STATE ATR-FTIR CONCENTRATION MEASUREMENTS

Figure B.1 shows a series of ammonium bicarbonate steady-state ATR-FTIR concentration measurements in the range $120-240\,\mathrm{g/kg_W}$. The data at each concentration has been mean-centered prior to computing the standard deviation of the measurements (cf. colored clusters in Figure B.1). The obtained value of standard deviation based on the whole experimental data set is $0.35\,\mathrm{g\,kg^{-1}}$.

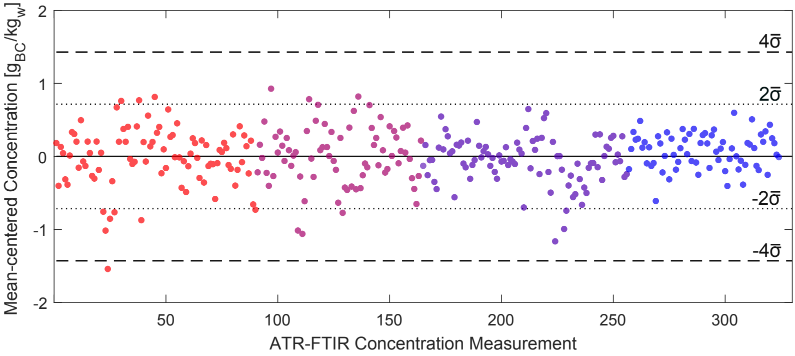

FIGURE B.1: Mean-centered ATR-FTIR concentration measurements of aqueous ammonia solutions of ammonium bicarbonate. The nominal ammonium bicarbonate concentrations of the clusters, moving from the red one to the blue one, are $120\,\mathrm{g\,kg^{-1}}$, $160\,\mathrm{g\,kg^{-1}}$, $200\,\mathrm{g\,kg^{-1}}$, and $240\,\mathrm{g\,kg^{-1}}$, respectively. The standard deviation $\bar{\sigma}$ of the measurements based on the whole experimental data set is $0.35\,\mathrm{g\,kg^{-1}}$. Bands are set to $\pm 2$ and $\pm 4$ standard deviations wrt to the mean-centered concentration.

## B.2 SOLID RAMAN CHARACTERIZATION OF NEEDLE-LIKE AMMONIUM BICARBONATE CRYSTALS

Raman spectroscopy was employed to assess the composition of the needle-like crystals obtained from the experiment discussed in Section 3.4.1.

In this work, a RA 400 Raman spectrometer from Mettler-Toledo (ZH, Switzerland) equipped with a 250 mW frequency-stabilized laser diode at 785 nm and a thermoelectrically cooled CCD detector was used. In situ measurements were recorded using a 5/8 in. ball-type immersion probe (Inphotonics, Norwood, MA) connected via a fiber optic (thicknesses of collection and excitation fibers were 100 and 200 µm, respectively). Solid powder mixtures of the crystallization product as well as of the commercially available ammonium bicarbonate were analyzed, at ambient conditions, using a probe directly immersed in the solid phase. Raman spectra were collected at a laser intensity of 150 mW in the range 190 to 1600 $\mathrm{cm}^{-1}$ with a resolution of 0.5 $\mathrm{cm}^{-1}$ and were averaged over 10 scans using an exposure time of 5 s.

From the similarities between the spectra it can be inferred that the substance crystallized during the experiment is pure ammonium bicarbonate.

## B.3 µ-DISCO CAMERA IMAGES OF THE AMMONIUM BICARBONATE CRYSTALS

Figure B.3 shows the evolution of the crystal habit of ammonium bicarbonate as described in Section 3.4.1. In Figure B.3, from left to right, µ-DISCO camera images of the seed crystal population, of the seed crystals grown at a supersaturation $S \leq 0.05$, and of a subsequent growth phase performed at a higher supersaturation ($S \approx 0.07$) have been reported.

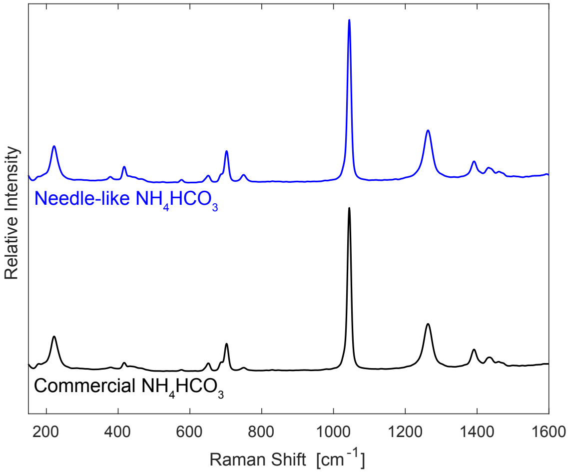

FIGURE B.2: Solid-phase Raman spectra of ammonium bicarbonate collected at ambient conditions. The black curve refers to the commercial ammonium bicarbonate, while the blue curve refers to the product of the cooling crystallization experiment discussed in Section 3.4.1.

## B.4 XRD PATTERNS OF THE CRYSTAL PRODUCTS

The nature of the crystals obtained from the desupersaturation growth experiments reported in Table 3.2 was verified using powder X-ray diffraction, as shown in Figure B.4. Powder X-ray diffraction patterns were recorded after samples were spread uniformly over the sample holder using a diffractometer from Bruker (D2 Phaser, 30 kV, 10 mA, Cu KR; Karlsruhe, Germany). Patterns were recorded at $2\theta$ between $10°$ and $80°$ with resolution of $0.02°$ and a scan speed of $5.83\,°\,\mathrm{min}^{-1}$.
The X-ray pattern of the crystal products matches qualitatively with the one of commercial ammonium bicarbonate (grey pattern in Figure B.4).

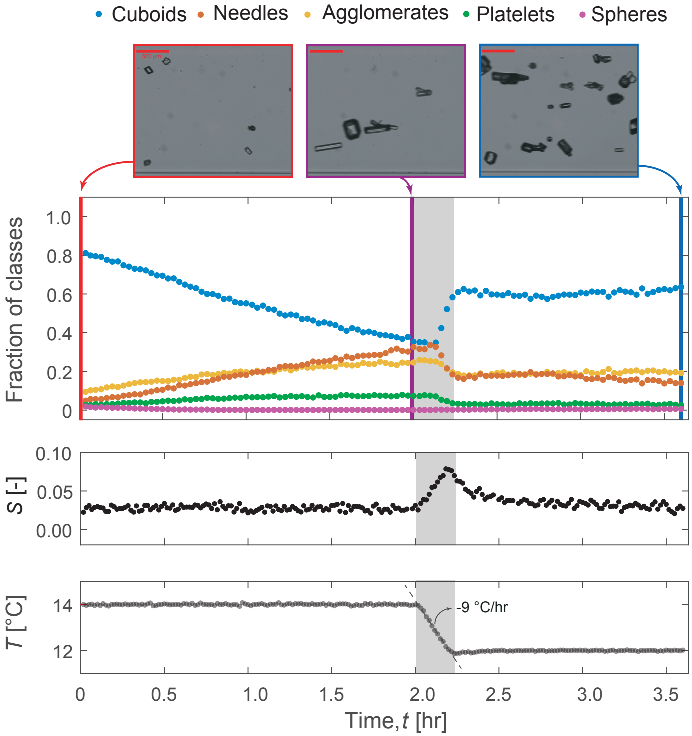

FIGURE B.3: Time-resolved shape change of ammonium bicarbonate crystals during the growth experiment described in Section 5.1. Measurements have been performed every 2 min using the µ-DISCO acquiring 800 images per measurement. The number of sampled particles per measurement is roughly 25,000. The particle shape classification has been performed using an algorithm described elsewhere.[38] The µ-DISCO camera images relative to the different phases of the experiment are highlighted in red, purple, and blue respectively.

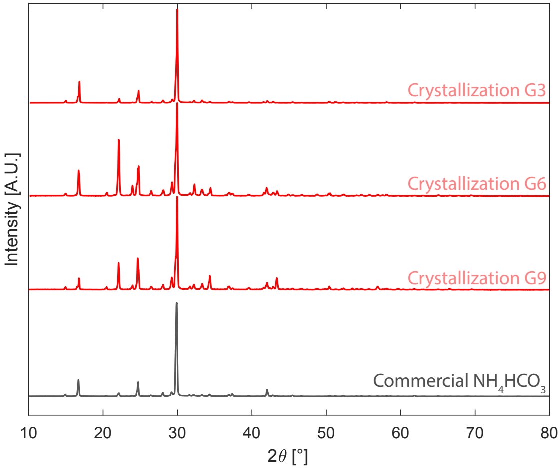

Figure B.4: Powder X-ray diffraction patterns of the crystallization products obtained from the desupersaturation growth experiments reported in Table 3.2. The X-ray diffraction pattern of commercial ammonium bicarbonate is shown as reference.

## B.5 FITTING OF THE GROWTH EXPERIMENTS

Figure B.5 shows the quality of fit of the growth model with respect to the desupersaturation growth experiments reported in Table 3.2. Four independent parameter estimations have been carried out using:

- the whole set of growth experiments at different aqueous ammonia concentrations in the solvent;
- the set of growth experiments at 0 % wt aqueous ammonia solution;
- the set of growth experiments at 2 % wt aqueous ammonia solution;
- the set of growth experiments at 3 % wt aqueous ammonia solution.

The respective values of the optimal growth kinetic parameter $\hat{k}_{g,1}$ are $(4.99 \pm 0.06)\cdot 10^{-6}$, $(6.68 \pm 0.07)\cdot 10^{-6}$, $(5.53 \pm 0.05)\cdot 10^{-6}$, and $(3.55 \pm 0.06)\cdot 10^{-6}$. As it can be noted, the optimal kinetic rate constant of the crystallization process tends to decrease as the nominal aqueous ammonia concentration increases.

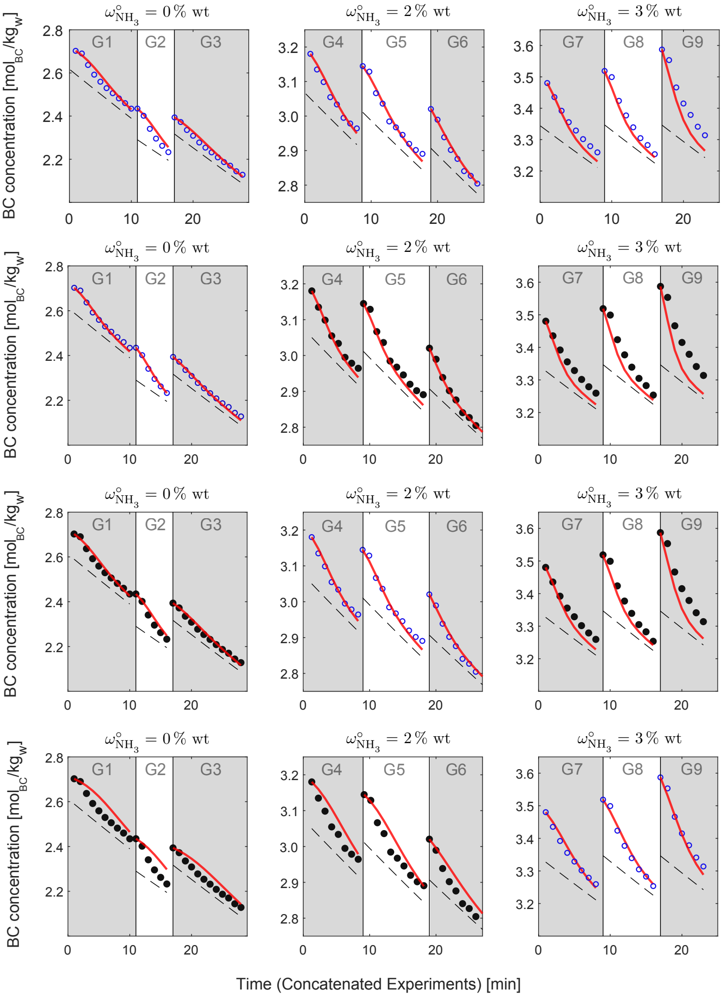

FIGURE B.5: Concatenated seeded polythermal desupersaturation experiments in aqueous ammonia solutions of ammonium bicarbonate (cf. Table 3.2). The hollow circular markers in blue color are the experimental data points used for the regression, while the black circular markers are data not included in the parameter estimation. The red curves are the fitted model's output, while the dashed lines indicate the BC solubility at the relevant temperature.

C

# APPENDIX C

## C.1 ATR-FTIR CALIBRATION STANDARDS

The set of standard ammonium bicarbonate (BC) concentrations used for the ATR-FTIR calibration procedure[45] are reported in Table C.1 together with the solvent composition (i.e. the aqueous ammonia and the ammonium sulfate concentrations).

Figure C.1 shows the ammonium bicarbonate solubility relative to the different solvent compositions investigated as well as the different BC standard concentrations used for the calibrations. The ammonia concentration in the solvent is indicated as a weight percent, while the ammonium bicarbonate and ammonium sulfate concentrations are espressed on a molality basis. It is worth noting that both the supersaturated and the undersaturated regions of the phase diagram have been explored during the ATR-FTIR calibration procedure.

| | **Concentration** [mol/kg$_w$] | | | | **Temperature** [°C] | | | |
|---|---|---|---|---|---|---|---|---|
| *Solute Sample No.* | 1 | 2 | 3 | 4 | 1 | 2 | 3 | 4 |
| NH$_4$HCO$_3$(aq) ($\omega^{\circ}_{NH_3} = 0$ %, $m^{\circ}_{AS} = 0$ m) | 2.01 | 2.32 | 2.52 | 2.65 | 5 - 25 | $10^{\dagger}$ - 25 | $10^{\dagger}$ - 25 | $16^{\dagger}$ - 25 |
| NH$_4$HCO$_3$(aq) ($\omega^{\circ}_{NH_3} = 0$ %, $m^{\circ}_{AS} = 0.1$ m) | 2.01 | 2.56 | 2.72 | n/a | $6^{\dagger}$ - 25 | $10^{\dagger}$ - 22 | $20^{\dagger}$ - 25 | n/a |
| NH$_4$HCO$_3$(aq) ($\omega^{\circ}_{NH_3} = 0$ %, $m^{\circ}_{AS} = 0.3$ m) | 1.89 | 2.13 | 2.72 | n/a | 5 - 27 | $5^{\dagger}$ - 28 | $10^{\dagger}$ - 25 | $20^{\dagger}$ - 29 |
| NH$_4$HCO$_3$(aq) ($\omega^{\circ}_{NH_3} = 2$ %, $m^{\circ}_{AS} = 0$ m) | 2.64 | 2.89 | 3.05 | 3.17 | 5 - 25 | $8^{\dagger}$ - 25 | $12^{\dagger}$ - 25 | $14^{\dagger}$ - 25 |
| NH$_4$HCO$_3$(aq) ($\omega^{\circ}_{NH_3} = 2$ %, $m^{\circ}_{AS} = 0.2$ m) | 2.50 | 2.95 | 3.27 | n/a | 5 - 25 | $7^{\dagger}$ - 25 | $15^{\dagger}$ - 25 | n/a |
| NH$_4$HCO$_3$(aq) ($\omega^{\circ}_{NH_3} = 2$ %, $m^{\circ}_{AS} = 0.4$ m) | 2.50 | 2.85 | 2.95 | 3.28 | $6^{\dagger}$ - 25 | 5 - 25 | $12^{\dagger}$ - 25 | $16^{\dagger}$ - 25 |

TABLE C.1: Set of ammonium bicarbonate standard concentrations in aqueous ammonia solutions containing ammonium sulfate and relative temperature range adopted (see Figure C.1); the variable $\omega^{\circ}_{NH_3}$ refers to the nominal ammonia concentration in the solvent in percent weight, the concentration of ammonium bicarbonate and ammonium sulfate are indicated using a molality basis. The symbol (†) refers to the temperature value corresponding to the onset of primary nucleation.

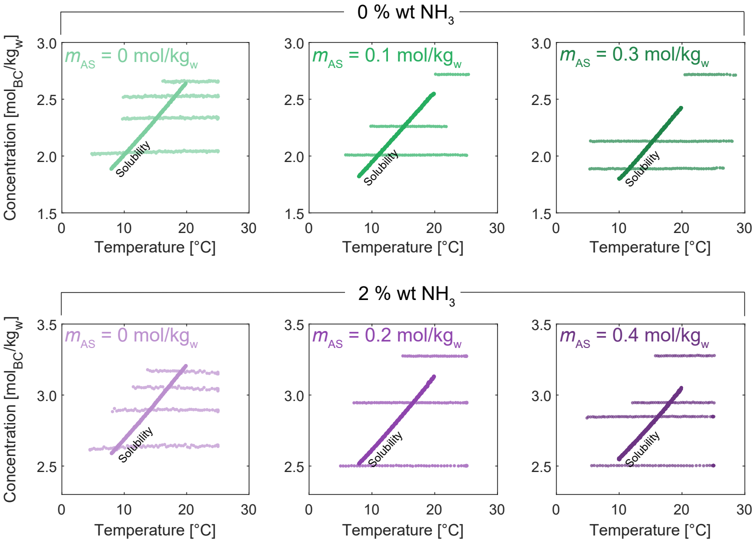

Figure C.1: Graphical representation of the ATR-FTIR calibration sets. The temperature range is 5-29 °C. The solubility curve, highlighted in the graphs, separates the supersaturated region from the undersaturated region of the phase diagram. The nominal ammonia concentration in the solvent is indicated as a weight percent, while $m_{\text{AS}}$ is the nominal concentration of ammonium sulfate is indicated as a molality basis (water being the solvent). Note that the different color codes, green and purple, indicate the different nominal ammonia concentrations in the solvent, i.e. 0 % wt or 2 % wt respectively, while the increasing color intensity indicates increasing concentration of ammonium sulfate in solution.

Two different batches of BC seed crystals have been used in this work, namely seeds type A and type B. They have been obtained by temperature cycles performed on ammonium bicarbonate crystals recrystallized from a supersaturated aqueous solution of BC. The size ranges obtained were between 100−250 µm for seeds A, and between 150−350 µm for seeds B. Figure C.2 shows the corresponding micrographs of the seed populations. Note that the difference in final appearance of the two

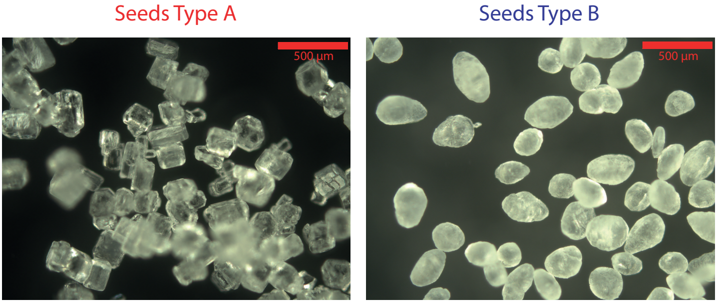

Figure C.2: Micrographs of the populations of seed crystals used in this work.

types of crystals stems from the specific production process of the crystals. In the case of type A seeds the temperature cycles terminated with a cooling step, while in the case of type B seeds the production process ended with a heating step (hence the more rounded shape of the crystals).

## C.2 CRYSTAL SIZE DISTRIBUTION OF THE FINAL CRYSTALLIZATION PRODUCTS

Figure C.3 shows the normalized volume-weighted crystal size distribution (CSD) of the ammonium bicarbonate crystals, $n_{\mathrm{V}}$, obtained after the growth experiments reported in Table 4.5. The CSDs have been sampled using the µ-DISCO[38] and have been compared with the initial seed distributions (shown in gray color). The measurements have been carring out by suspending the crystals in an solution of ethanol (saturated with BC), acquiring 1600 images per measurement every 2 min until the cumulative number of sampled particles reached a value above 30,000.

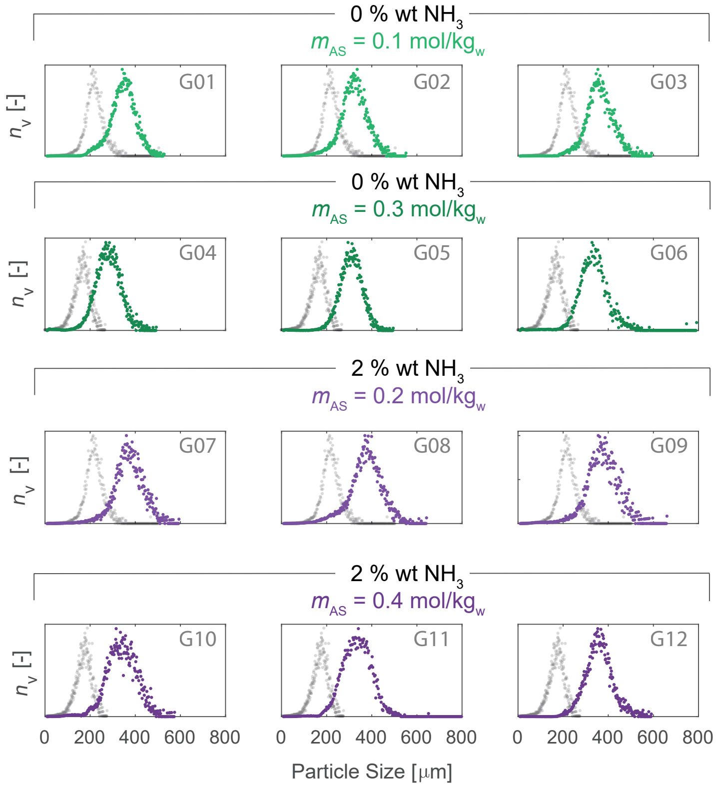

Figure C.3: Normalized volume-weighted crystal size distribution (CSD) of the ammonium bicarbonate crystals, $n_\mathrm{V}$, obtained after the growth experiments reported in Table 4.5. The nominal ammonia concentration in the solvent is indicated as a weight percent, while $m_\mathrm{AS}$ is the nominal concentration of ammonium sulfate indicated as a molality basis (water being the solvent). Note that the different color codes, green and purple, indicate the different nominal ammonia concentrations in the solvent, i.e. 0 % wt or 2 % wt respectively, while the increasing color intensity indicates increasing concentration of ammonium sulfate in solution.

## C.3 IDENTIFIABILITY OF THE PARAMETER SET OF THE ADSORPTION-GROWTH MODEL

In this section, the practical identifiability[88] of the kinetic parameter set of the adsorption-growth model proposed in this work is discussed.
The correlation among the Langmuir constant, $\kappa$, and the impurities effective factor, $\alpha$, which constitute the model parameters, have been studied by analyzing the behavior of the objective function, $\Psi$, defined as

$$\Psi = \frac{N_\mathrm{t}}{2} \ln \left[ \sum_{j=1}^{N_\mathrm{t}} \left( \frac{m_{\mathrm{BC},j} - \hat{m}_{\mathrm{BC},j}(\mathbf{p})}{m^\mathrm{ref}} \right)^2 \right] \tag{C.1}$$

where the index $j$ indicates the $j$-th experimental concentration data points relative to the growth experiments reported in Table 4.5, and $\hat{m}_{\mathrm{BC},j}$ is the model response that depends on the vector parameter $\mathbf{p} = [\kappa, \alpha]$.
The isocontour curves of the objective function $\Psi$, parametrized with respect to the model parameters $\kappa$ and $\alpha$ are shown in Figure C.4. The presence of a locus of points in which the function is minized, rather than a unique point, is representative of the statistical correlation among the parameters. In turn, this means that*only* relative values of the model parameters can be identify, without being able to determine accurately the value of each individual parameter.
As discussed in Chapter 4, the parameters' non-identifiability has been removed by arbitrarily setting the value of $\alpha$ to 1, hence performing a parameter fitting based on the parameter $\kappa$, the only adjustable parameter of the model.

## C.4 XRD PATTERNS OF CRYSTAL PRODUCTS

The nature of the crystals obtained from the desupersaturation growth experiments reported in Table 4.5 was verified by analyzing the powder X-ray diffraction patterns (XRDP) of the solid phase shown in Figure C.5. The XRDP were recorded after samples were spread uniformly over the sample holder using a diffractometer from Bruker (D2 Phaser, 30

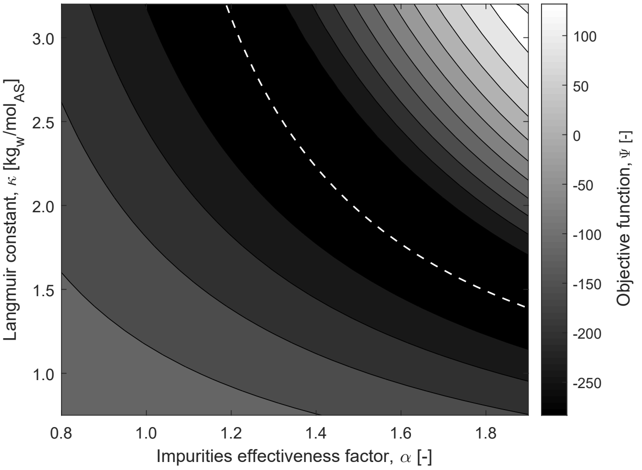

Figure C.4: Indentifiability of the adsorption-growth model parameters. The isocontour lines of the objective function Ψ (eq C.1) have been computed by varying the values of the Langmuir constant, $\kappa$, and of the impurities effective factor, $\alpha$, of the adsorption-growth model. Dashed white line indicates the minimum values of the objective function Ψ.

kV, 10 mA, Cu KR; Karlsruhe, Germany). Patterns were recorded at $2\theta$ between $10^\circ$ and $80^\circ$ with resolution of $0.02^\circ$ and a scan speed of $5.83\,^\circ\,\mathrm{min}^{-1}$.

The X-ray patterns of the crystal products match qualitatively with the one of pure ammonium bicarbonate (black pattern in Figure C.5). The XRPD of pure ammonium sulfate is shown as reference in red.

## C.5 SULFATE ION ASSAY

The procedure involved an extensive washing of the BC crystals with ethanol saturated w.r.t. BC in order to remove any mother liquor adhering to the surface of the crystals. After drying, few grams of BC crystals have been dissolved in an aqueous solution (Milli-Q water). Prior to the

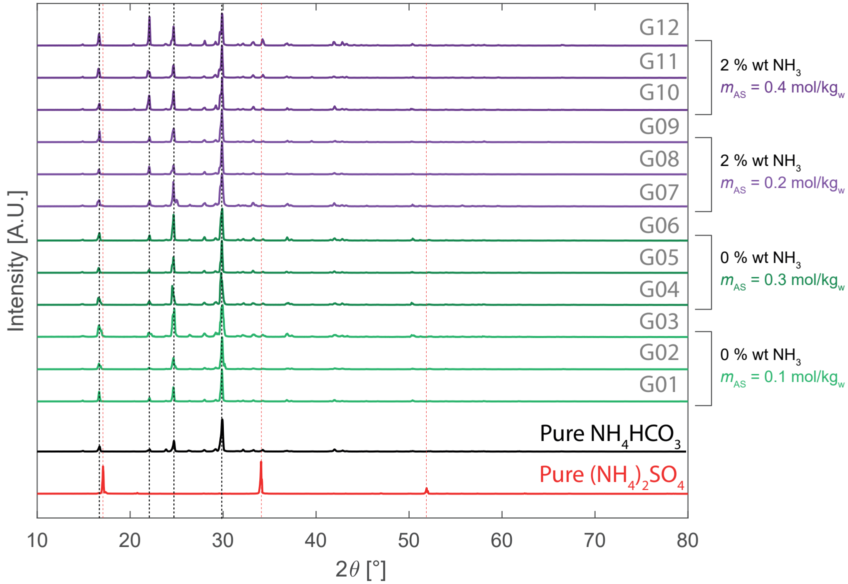

Figure C.5: X-ray diffraction patterns of the crystallization products obtained from the desupersaturation growth experiments reported in Table 4.5. The X-ray diffraction patterns of pure ammonium bicarbonate and pure ammonium sulfate are shown as reference in black and red color, respectively.

addition of BaCl$_2$(aq) to the solution in order to precipitate BaSO$_4$ (that would occur only in presence of SO$_4^{2-}$ ions), all the carbon species have been removed to avoid the concomitant precipitation of BaCO$_3$, which is also sparingly soluble in water. This has been achieved by lowering the pH of the solution by means of an addition of HCl(aq) to the sample. As a consequence of the decrease in pH value, the carbon distribution shifted towards pure CO$_2$(aq) that was easily stripped away from the solution by degassing it in a vacuum oven at 50 °C for about 5 h. Then, the pH of the carbon-free solution has been adjusted to a value of 9 (by adding a NaOH(aq)) so that the sulfur species would be present only as SO$_4^{2-}$ ions.[105]

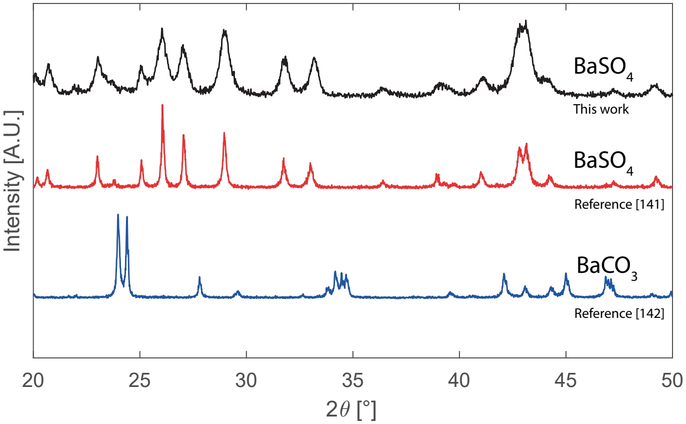

Figure C.6: X-Ray diffraction patterns (XRDP) of the solid phase precipitated during the sulfate assay. The PXRD solid sample has been prepared by collecting all the precipitated solid from the 12 samples (each one from a different crystallization experiment, cf. Table 4.5). The XRDP of barium sulfate[138] (red curve) and of barium carbonate[139] (blue curve) are reported as reference.

After the addition of $BaCl_2$(aq) in stoichiometric eccess, the suspensions were left settling for 24 h. The solids that eventually precipitated were recovered by filtering the suspension (using a 47 mm, 0.45 µm pore size cellulose nitrate filter) and analyzed through PXRD measurements to identify the nature of the crystalline phase. The PXRD solid sample has been prepared by collecting all the precipitated solid from the 12 samples (each one from a different crystallization experiment, cf. Table 4.5) into a single sample that has been ground before the analysis.

An AX205 analytical balance (Mettler-Toled, Switzerland) with a readability and maximum capacity of 0.01 mg and 81 g, respectively has been used to weigh the the amount of precipitated $BaSO_4$.

Figure C.6 shows the PXRD analysis on the solids precipitated during the assays (black curve) and the comparison with the reference XRDP of barium sulfate[138] (red curve) and of barium carbonate[139] (blue curve). As it can be seen from Figure C.6, the compound precipitated during the assay was barium sulfate.

## C.6 RAMAN SPECTROSCOPY CHARACTERIZATION

In this work, the Raman spectrum of an aqueous ammonia solution containing ammonium bicarbonate and ammonium sulfate (nominal concentrations of ammonia, ammonium bicarbonate, and ammonium sulfate, equal to 2 % wt, 2.95 $m_{BC}$, and 0.2 $m_{AS}$, respectively) has been analyzed to investigate the presence of anomalies in the Raman shift modes that could be related to the presence of ion-paring or to the formation of ion complexes in solution. It must be noted that we refrained from generalizing the findings of this cursory analysis, which only serves the purpose of investigating the chemical composition of the mixture.

A RA 400 Raman spectrometer from Mettler-Toledo (Greifensee, Switzerland) equipped with a 250 mW frequency-stabilized laser diode at 785 nm and a thermoelectrically cooled CCD detector was used. In situ measurements were recorded using a 5/8 in. ball-type immersion probe (Inphotonics, Norwood, MA) connected via a fiber optic (thicknesses of collection and excitation fibers were 100 and 200 μm, respectively) in a thermostated reactor at the temperature of 25 °C. The Raman spectra were collected at a laser intensity of 150 mW in the range 190 to 1150 $\mathrm{cm}^{-1}$ with a resolution of 0.5 $\mathrm{cm}^{-1}$ and were averaged over 10 scans using an exposure time of 5 s.

At first, the Raman spectum recorded during the measurement of the aforementioned mixture has been post-processed by applying a *linear baseline* correction in the range 190 to 1150 $\mathrm{cm}^{-1}$. Then, the measured spectrum of the mixture, indicated with purple circular markers in Figure C.7, has been modeled using a least-squares minimization approach. The black solid curve in Figure C.7 represents the result of the fitting procedure and it is obtained by superimposing the contributions of the Raman spectra of the individual species in solution. In detail, the optimization procedure considers the presence of 4 main species,

| **Species** | **Position** [$cm^{-1}$] | **Width** [$cm^{-1}$] | **Height** [A.U.] |
|---|---|---|---|
| Sulfate ion ($SO_4{}^{2-}$) | 981[115] | 10.21 | 480.2 |
| Carbamate ion ($NH_2COO^-$) | 1020[29] | 31.55 | 515.1 |
| Bicarbonate ion ($HCO_3{}^-$) | 1037[29] | 14.33 | 462.3 |
| Carbonate ion ($CO_3{}^{2-}$) | 1066[29] | 13.55 | 300.0 |

Table C.2: Optimal parameter of the Raman peaks of each species present in solution. Note that the peak position of each compound has been taken from literature data.

namely the bicarbonate ion, the carbonate ion, the carbamate ion, and the sulfate ion. Multiple Gaussian/Lorentzian blend functions with independently variable percent Gaussian have been used to model each species' spectrum. The calculations have been performed in MATLAB using the open-source software *Peak Fitter* available on-line.[140] Table C.2 gives an overview of the optimal parameters for each component modeled during the spectrum fitting.

Figure C.7 shows that the measured spectrum of the mixture can be properly reproduced by a linear combination of the spectra of the species in solution. Based on this evidence, which we refrain from generalizing, we neglected the presence of ionic complexes, in the range of ammonium bicarbonate, ammonium sulfate and aqueous ammonia concentrations investigated in this work as well as in the computation of the ionic equilibria for the $CO_2-NH_3-H_2O-SO_x$ system.

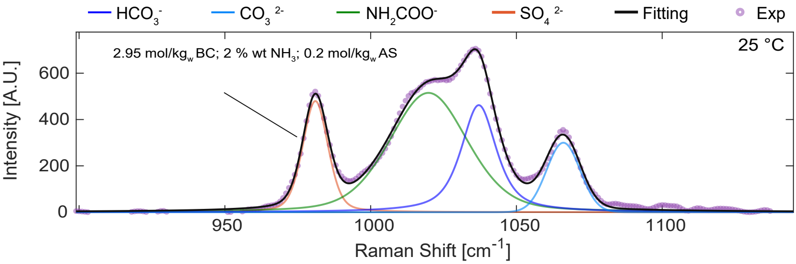

Figure C.7: Raman spectrum of an aqueous ammonia solution containing ammonium bicarbonate and ammonium sulfate at the nominal concentrations of ammonia, ammonium bicarbonate, and ammonium sulfate, equal to 2 % wt, 2.95 $m_{BC}$, and 0.2 $m_{AS}$, respectively. Data has been recorded at 25 °C. The measured intensities of the measured spectrum, reported in arbitrary unit, are represented by purple circular markers, while the black solid line is the fitted spectrum. The remain spectra are the contributions of each species' spectrum to the fitted Raman spectrum of the mixture.

D

# APPENDIX D

## D.1 CSF-CAP PROCESS FLOW DIAGRAM

Figure D.1 shows the process flow diagram of the controlled solid formation Chilled Ammonia Process (CSF-CAP).[25,31] The plant is divided into 6 sections, namely $CO_2$ capture section, continuous solid handling section, $CO_2$ desorption section, $CO_2$ water wash section, $CO_2$ compression section, and flue gas water wash section.

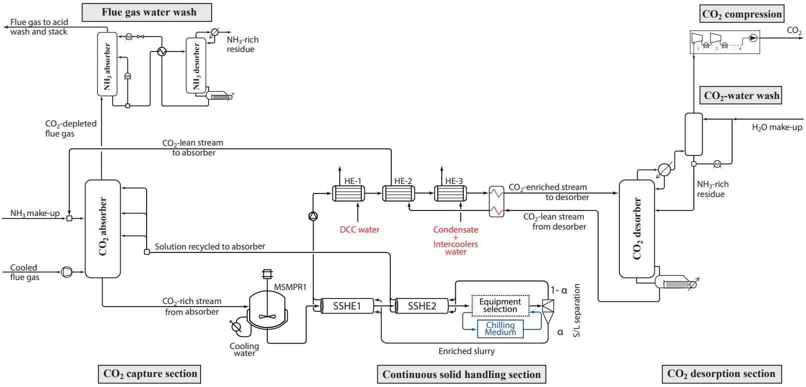

FIGURE D.1: Process flow diagram of the controlled solid formation Chilled Ammonia Process (CSF-CAP) adapted from [25]. The equipment adopted for the final crystallization step, depending on the process configuration (here not shown), can either be an additional MSMPR, or a scraped surface heat exchanger (SSHE), refer to Section 5.2 for further details.

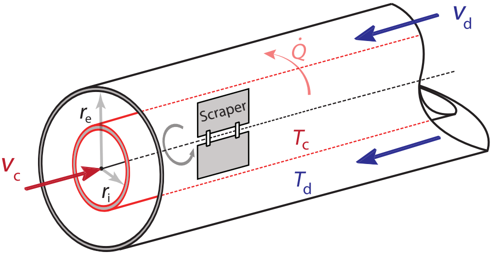

Figure D.2: Schematic representation of a scraped surface heat exchanger (SSHE) consisting of two cylindrical steel tubes with an axial shaft on which the scraped blades are mounted. The cooling crystallization/dissolution process is performed by feeding a crystallizing slurry to the internal tube, while a colder slurry, which contains dissolving crystals, flows countercurrently in the outer annular passage. The thermal flux, $\dot{Q}$, is directed from the crystallizing slurry to the colder suspension that flows in the annular passage. The control volume for the energy balance embeds the internal tube of the SSHE and it is highlighted in red. The variables $r_\mathrm{i}$, $r_\mathrm{e}$, $T_\mathrm{c}$, and $T_\mathrm{d}$ are the inner radius of the internal tube, the inner radius of the external tube, the temperature of the crystallizing suspension and the temperature of the suspension in which crystals undergo dissolution.

## D.2 DIMENSIONLESS SSHE ENERGY BALANCE EQUATION

The energy balance applied over the control volume defined by the internal tube of the scraped surface heat exchanger (see Figure D.2) can be written as:

$$\pi r_i^2 \rho_\mathrm{c} v_\mathrm{c} \hat{c}_{p,\mathrm{c}} \frac{\mathrm{d}T_\mathrm{c}}{\mathrm{d}x} = -2\pi r_i U^{(\mathrm{i})}(T_\mathrm{c} - T_\mathrm{d}) + \Delta H_\mathrm{BC} k_\mathrm{v} \rho_\mathrm{s} \frac{\mathrm{d}\mu_3}{\mathrm{d}x} v_\mathrm{c} \pi r_i^2 \tag{D.1}$$

where the first term of the right-hand side of eq D.1 represents the exchange of thermal energy by convection, while the second term accounts for the release of latent heat of crystallization (source-term). After algebraic manipulation, the dimensionless form of the energy balance is

$$\frac{\mathrm{d}\vartheta_\mathrm{c}}{\mathrm{d}\xi} + 4\mathrm{St}_\mathrm{c}\phi(\vartheta_\mathrm{c} - \vartheta_\mathrm{d}) - \Psi_\mathrm{c} k_\mathrm{v} L_\mathrm{r}^3 \frac{\mathrm{d}\tilde{\mu}_{3,\mathrm{c}}}{\mathrm{d}\xi} = 0 \tag{D.2}$$

where the Stanton number for the crystallizing suspension, $\mathrm{St_c}$, is defined as

$$\mathrm{St_c} = \frac{U^{(\mathrm{i})}}{\rho_\mathrm{c} v_\mathrm{c} \hat{c}_{p,\mathrm{c}}} \tag{D.3}$$

where $\rho_\mathrm{c} v_\mathrm{c}$ is the crystallizing suspension's mass flux, $\hat{c}_{p,\mathrm{c}}$ is the specific heat capacity of the suspension, and $U^{(\mathrm{i})}$ is the overall convective heat transfer coefficient referred to the surface on the internal tube of the SSHE. This dimensionless number represents the ratio of the thermal energy transferred into/from a fluid to the thermal capacity of that fluid.

The parameter $\phi$ is the slenderness ratio of the heat exchanger and it is defined as

$$\phi = \frac{x_r}{d_\mathrm{i}} \tag{D.4}$$

where $x_\mathrm{r}$ is the length of the SSHE and $d_\mathrm{i}$ is the inner diameter of the internal tube. In this work, the value of the slenderness ratio in configuration B ranges between $3.3 \times 10^3$ and $5.4 \times 10^3$ depending on the operating conditions adopted.

Analogously, the dimensionless energy balance for the suspension containing dissolving crystals is

$$\frac{\mathrm{d}\vartheta_\mathrm{d}}{\mathrm{d}\xi} + 4\frac{r_\mathrm{i} x_\mathrm{r}}{r_\mathrm{e}^2 - r_\mathrm{i}^2}\mathrm{St_d}(\vartheta_\mathrm{c} - \vartheta_\mathrm{d}) - \Psi_\mathrm{d} k_\mathrm{v} L_\mathrm{r}^3 \frac{\mathrm{d}\tilde{\mu}_{3,\mathrm{d}}}{\mathrm{d}\xi} = 0 \tag{D.5}$$

where the internal tube thickness, $s$, of the SSHE has been neglected and the Stanton number for the suspension, $\mathrm{St_d}$, is defined as

$$\mathrm{St_d} = \frac{U^{(\mathrm{i})}}{\rho_\mathrm{d} v_\mathrm{d} \hat{c}_{p,\mathrm{d}}} \tag{D.6}$$

The ratio between the Stanton numbers of the suspensions is

$$\frac{\mathrm{St_d}}{\mathrm{St_c}} = \frac{1}{\alpha}\frac{\hat{c}_{p,\mathrm{c}}}{\hat{c}_{p,\mathrm{d}}}\frac{r_\mathrm{e}^2 - r_\mathrm{i}^2}{r_\mathrm{i}^2} \tag{D.7}$$

where the splitting factor $\alpha$ is defined as the ratio between the mass flow rate of the enriched slurry and that of the inlet stream of the

hydro-cyclone (see Figure D.1).
Eventually eq D.5 can be recast as

$$\frac{\mathrm{d}\vartheta_{\mathrm{d}}}{\mathrm{d}\xi} + \frac{4}{\alpha}\frac{\hat{c}_{p,\mathrm{c}}}{\hat{c}_{p,\mathrm{d}}}\mathrm{St}_{\mathrm{c}}\phi(\vartheta_{\mathrm{c}} - \vartheta_{\mathrm{d}}) - \Psi_{\mathrm{d}} k_{\mathrm{v}} L_{\mathrm{r}}^{3}\frac{\mathrm{d}\tilde{\mu}_{3,\mathrm{d}}}{\mathrm{d}\xi} = 0 \tag{D.8}$$

*Stanton Number Computation*

The Stanton number $\mathrm{St}_{\mathrm{c}}$ can be re-written in a more useful form by considering the terms contributing to the overall convective heat transfer coefficient, $h$, based on the inside tube heat transfer area[118,141]

$$\mathrm{St}_{\mathrm{c}} = \frac{U^{(\mathrm{i})}}{\rho_{\mathrm{c}} v_{\mathrm{c}} \hat{c}_{p,\mathrm{c}}} = \frac{\left(\frac{D_{\mathrm{H,c}}}{\mathrm{Nu}_{\mathrm{c}} k_{\mathrm{c}}} + \frac{s}{k_{\mathrm{s}} \ln\left(1+\frac{s}{r_{\mathrm{i}}}\right)} + \frac{D_{\mathrm{H,d}}}{\mathrm{Nu}_{\mathrm{d}} k_{\mathrm{d}}\left(1+\frac{s}{r_i}\right)}\right)^{-1}}{\rho_{\mathrm{c}} v_{\mathrm{c}} \hat{c}_{p,\mathrm{c}}} \tag{D.9}$$

where $D_{\mathrm{H}}$ is the hydraulic diameter for heat transfer.
By neglecting the thermal resistance of the metal wall of the SSHE and considering that $k_{\mathrm{d}} \approx k_{\mathrm{c}}$ eq D.9 reduces to

$$\mathrm{St}_{\mathrm{c}} \approx \frac{\left(\frac{1}{\mathrm{Nu}_{\mathrm{c}} k_{\mathrm{c}}} + \frac{a-1}{\mathrm{Nu}_{\mathrm{d}} k_{\mathrm{d}}\left(1+\frac{s}{r_i}\right)}\right)^{-1}}{\mathrm{Re}_{\mathrm{c}} \mathrm{Pr}_{\mathrm{c}}} \tag{D.10}$$

where $a$ is the ratio between the external and internal diameters of the SSHE, $s$ is the thickness of the wall of the tubes (assumed to be constant for every tube), $k$ is the thermal conductivity, $\mathrm{Re}_{\mathrm{c}}$ and $\mathrm{Pr}_{\mathrm{c}}$ are the crystallizing suspension Reynolds and Prandtl numbers, respectively.

*Reynolds Number for Annular Concentric Passages*

The computation of the Nusselt number for an annular concentric passage involves the computation of the Reynolds number of the system.[141] With regards to the streams processed in SSHE1, the ratio between the mass fluxes of the fluid that flows into the external annular passage and the one that flows in the internal tube (see Figure D.2) is computed as follows

$$\frac{v_\mathrm{d}\rho_\mathrm{d}}{v_\mathrm{c}\rho_\mathrm{c}} = \alpha\left(\frac{d_\mathrm{i}^2}{d_\mathrm{e}^2 - d_\mathrm{i}^2}\right) \tag{D.11}$$

In the same way, the ratio between the Reynolds number is

$$\frac{\mathrm{Re}_\mathrm{d}}{\mathrm{Re}_\mathrm{c}} = \frac{v_\mathrm{d}\rho_\mathrm{d}\mu_\mathrm{c}D_\mathrm{H,d}}{v_\mathrm{c}\rho_\mathrm{c}\mu_\mathrm{d}D_\mathrm{H,c}} \tag{D.12}$$

Substituting eq D.11 in eq D.12, applying the definition of hydraulic diameter, and assuming the ratio $\mu_\mathrm{c}/\mu_\mathrm{d} \approx 1$ leads to

$$\frac{\mathrm{Re}_\mathrm{d}}{\mathrm{Re}_\mathrm{c}} \approx \alpha\frac{d_\mathrm{i}}{d_\mathrm{e} + d_\mathrm{i}} \tag{D.13}$$

Eventually eq D.14 is obtain by introducing the parameter, $a$ in eq D.13

$$\mathrm{Re}_\mathrm{d} \approx \frac{\alpha}{a+1}\mathrm{Re}_\mathrm{c} \tag{D.14}$$

# BIBLIOGRAPHY

1. Lüthi, D.; Le Floch, M.; Bereiter, B.; Blunier, T.; Barnola, J.-M.; Siegenthaler, U.; Raynaud, D.; Jouzel, J.; Fischer, H.; Kawamura, K.; Stocker, T. F. *Nature* **2008**, *453*, 379–382 (cit. on p. 1).
2. Masson-Delmotte, V.; Zhai, P.; Pörtner, H.-O.; Roberts, D.; Skea, J.; Shukla, P. R.; Pirani, A.; Moufouma-Okia, W.; Péan, C.; Pidcock, R.; Connors, S.; Matthews, J. B. R.; Chen, Y.; Zhou, X.; Gomis, M. I.; Lonnoy, E.; Maycock, T.; Tignor, M.; Waterfield, T. *Global warming of 1.5°C: Summary for Policymakers*; tech. rep.; 2018 (cit. on p. 2).
3. Hansen, J. E. *Climatic Change* **2005**, *68*, 269–279 (cit. on p. 1).
4. IEA, *$CO_2$ Emissions from Fuel Combustion, Tech. Rep.* Paris, France: 2018 (cit. on p. 3).
5. IEA, *Key World Energy Statistics, Tech. Rep.* Paris, France: 2019 (cit. on p. 3).
6. IPCC, *Climate Change 2007: Impacts, Adaptation and Vulnerability, Contribution of Working Group II to the IPCC Fourth Assessment Report*; Cambridge University Press: 2007 (cit. on p. 3).
7. IPCC, *Climate Change 2014: Mitigation of Climate Change, Contribution of Working Group III Contribution to the IPCC Fifth Assessment Report*; Cambridge University Press: 2015 (cit. on p. 4).
8. MacKay, D. J., *Sustainable Energy – without the hot air*; UIT Cambridge: 2008 (cit. on pp. 5, 111).
9. IEA, *Energy Technology Perspective – Harnessing Electricity's Potential, Tech. Rep.* Paris, France: 2014 (cit. on p. 5).
10. *Energy Technology Perspectives* 2010*: Scenarios and Strategies to* 2050*, Tech. Rep.* IEA, Paris, France: 2010 (cit. on p. 6).
11. Rochelle, G. T. *Science* **2009**, *325*, 1652–1654 (cit. on p. 6).

12. Bottoms, R. R. Process for separating acidic gases., US 1,783,901 A, 1930 (cit. on pp. 6, 194).
13. Hook, R. J. *Ind. Eng. Chem. Res.* **1997**, *36*, 1779–1790 (cit. on p. 6).
14. Idem, R.; Wilson, M.; Tontiwachwuthikul, P.; Chakma, A.; Veawab, A.; Aroonwilas, A.; Gelowitz, D. *Ind. Eng. Chem. Res.* **2006**, *45*, 2414–2420 (cit. on p. 6).
15. Hu, G.; Nicholas, N. J.; Smith, K. H.; Mumford, K. A.; Kentish, S. E.; Stevens, G. W. *Int. J. Greenh. Gas Control* **2016**, *53*, 28–40 (cit. on p. 6).
16. Budzianowski, W. M. *Int. J. Global Warm.* **2015**, *7*, 184–225 (cit. on p. 7).
17. Bai, H.; Yeh, A. C. *Ind. Eng. Chem. Res.* **1997** (cit. on p. 7).
18. Gal, E. Ultra cleaning of combustion gases including the removal of $CO_2$., WO 2006/022885 A1, 2006 (cit. on p. 7).
19. Gal, E. Multi-stage $CO_2$ Removal System and Method for Processing a Flue Gas Stream., US 8,182,577 B2, 2012 (cit. on p. 7).
20. Yeh, A. C.; Bai, H. *Sci. Total Environ.* **1999**, *228*, 121–133 (cit. on p. 7).
21. Mathias, P. M.; Reddy, S.; O'Connell, J. P. *Int. J. Greenh. Gas Control* **2010**, *4*, 174–179 (cit. on p. 7).
22. Versteeg, P.; Rubin, E. S. *Int. J. Greenh. Gas Control* **2011**, *5*, 1596–1605 (cit. on p. 7).
23. Yu, H.; Morgan, S.; Allport, A.; Cottrell, A.; Do, T.; McGregor, J.; Wardhaugh, L.; Feron, P. *Chem. Eng. Res. Des.* **2011**, *89*, 1204–1215 (cit. on p. 7).
24. Baburau, B. Chilled Ammonia process operation and results from pilot plant at Techology Centre Mongstad., in Trondheim CCS Conference (TCCS-8). SINTEF, Trondheim, Norway, 2015 (cit. on p. 7).
25. Sutter, D.; Gazzani, M.; Mazzotti, M. *Faraday Discuss.* **2016**, *192*, 59–83 (cit. on pp. 7, 8, 25, 57, 60, 67, 106, 112, 152, 154, 156, 157, 171, 179, 185, 192, 225).

26. Jänecke, E. *Z. Elektrochem.* **1929**, *35*, 332–334 (cit. on pp. 9, 25, 54, 57, 67, 86, 152, 153, 158).

27. Jänecke, E.; Rahlfs, E. *Z. Elektrochem.* **1930**, *36*, 645–654 (cit. on pp. 9, 25, 57, 67).

28. Thomsen, K.; Rasmussen, P. *Chem. Eng. Sci.* **1999**, *54*, 1787–1802 (cit. on pp. 9, 25, 54, 59, 61, 62, 64, 67, 114, 116, 131, 132).

29. Wen, N.; Brooker, M. H. *J. Phys. Chem.* **1995**, *99*, 359–368 (cit. on pp. 9, 26, 222).

30. Darde, V.; van Well, W. J. M.; Stenby, E. H.; Thomsen, K. *Ind. Eng. Chem. Res.* **2010**, *49*, 12663–12674 (cit. on pp. 12, 13, 25, 28, 49, 54, 59, 61, 62, 67, 70, 77, 78, 97, 132, 133, 152, 157, 162, 164).

31. Sutter, D.; Gazzani, M.; Mazzotti, M. *Chem. Eng. Sci.* **2015**, *133* (cit. on pp. 12, 28, 67, 70, 225).

32. Kashchiev, D., *Nucleation - basic theory with applications*; Butterworth Heinemann: 2000 (cit. on p. 13).

33. Myerson, A. S., *Handbook of Industrial Crystallization*; Butterworth-Heinemann: 2002 (cit. on pp. 13, 14, 86, 94, 112, 126, 138, 151, 154, 193).

34. LeVeque, R. J., *Finite Volume Methods for Hyperbolic Problems*; Cambridge University Press: 2002 (cit. on pp. 15, 83, 124, 167).

35. Gunawan, R.; Fusman, I.; Braatz, R. D. *AIChE J.* **2004**, *50*, 2738–2749 (cit. on pp. 15, 83, 167).

36. Randolph, A.; Larson, M., *Theory of Particulate Processes, Chapter 3 - The Population Balance*; Elsevier: 1971 (cit. on pp. 15, 79, 80, 87, 124).

37. Sutter, D.; Mazzotti, M. *Cryst. Growth Des.* **2017**, *17*, 3048–3054 (cit. on pp. 16, 25, 29, 51, 68, 102–104, 112, 121, 152, 165, 166).

38. Rajagopalan, A. K.; Schneeberger, J.; Salvatori, F.; Bötschi, S.; Ochsenbein, D. R.; Oswald, M. R.; Pollefeys, M.; Mazzotti, M. *Powder Technol.* **2017**, *321*, 479–493 (cit. on pp. 19, 87, 90, 119, 139, 208, 215).

39. Sutter, D. *Optimizing the Chilled Ammonia Process Technology for Post-Combustion $CO_2$ Capture by Controlling Solid Precipitation.*, Ph.D. Thesis, ETH Zurich, 2017 (cit. on pp. 19, 193).
40. Jänecke, E. *Z. Elektrochem.* **1929**, *35*, 716–728 (cit. on pp. 25, 57, 59, 62, 67, 68, 86, 136, 152).
41. Jänecke, E.; Rahlfs, E. *Z. Elektrochem.* **1932**, *38*, 9–12 (cit. on pp. 25, 67).
42. Milella, F.; Gazzani, M.; Sutter, D.; Mazzotti, M. *Ind. Eng. Chem. Res.* **2018**, *57*, 11712–11727 (cit. on pp. 25, 60, 106, 112).
43. Lichtfers, U.; Rumpf, B. *Chem. Ing. Tech.* **2000**, *72*, 1526–1530 (cit. on pp. 26, 31, 34, 35, 56, 59, 127).
44. Lichtfers, U. *Spektroskopische Untersuchungen zur Ermittlung von Speziesverteilungen im System Ammoniak - Kohlendioxid - Wasser.*, Ph.D. Thesis, Universität Kaiserslautern, 2000 (cit. on pp. 26, 31, 32, 34, 35, 56, 59).
45. Cornel, J.; Lindenberg, C.; Mazzotti, M. *Ind. Eng. Chem. Res.* **2008**, *47*, 4870–4882 (cit. on pp. 26, 33, 43, 44, 46, 76, 128, 129, 197, 213).
46. Nagy, Z. K.; Braatz, R. D. *Annu. Rev. of Chem. Biomol.* **2012** (cit. on pp. 26, 44).
47. Halstensen, M.; Jilvero, H.; Jinadasa, W. N.; Jens, K. J. *J. Chem.* **2017**, *2017* (cit. on p. 26).
48. Rudolph, W. W.; Irmer, G.; Königsberger, E. *Dalton Trans.* **2008**, 900–8 (cit. on pp. 26, 40).
49. Zhao, Q.; Wang, S.; Qin, F.; Chen, C. *Ind. Eng. Chem. Res.* **2011**, *50*, 5316–5325 (cit. on p. 26).
50. Barrett, P.; Glennon, B. *Chem. Eng. Res. Des.* **2002**, *80*, 799–805 (cit. on pp. 31, 50).
51. Nakamoto, K. *Handb. Vib. Spectrosc.* **2006** (cit. on p. 32).
52. Davis, A. R.; Oliver, B. G. *J. Solution Chem.* **1972**, *1*, 329–339 (cit. on p. 32).

53. Pretsch, E.; Bühlmann, P.; Badertscher, M., *Structure Determination of Organic Compounds Tables of Spectral Data*; Springer, Berlin, Heidelberg: 2009 (cit. on p. 32).

54. Hisatsune, C. *Can. J. Chem.* **1984**, *62*, 945–948 (cit. on pp. 32, 34).

55. Frasco, D. L. *J. Chem. Phys.* **1964**, *41*, 2134–2140 (cit. on p. 32).

56. Ekimova, M.; Quevedo, W.; Szyc, Ł.; Iannuzzi, M.; Wernet, P.; Odelius, M.; Nibbering, E. T. *J. Am. Chem. Soc.* **2017**, *139*, 12773–12783 (cit. on p. 31).

57. Schrader, B., *Infrared and Raman Spectroscopy-Methods and Applications*; John Wiley & Sons: 2008 (cit. on pp. 32, 36).

58. Libnau, F. O.; Kvalheim, O. M.; Christy, A. A.; Toft, J. *Vib. Spectrosc.* **1994**, *7*, 243–254 (cit. on p. 32).

59. Skoog, D. A. (cit. on pp. 33, 53, 131).

60. Wolery, T. J., *EQ3/6 A Software Package for Geochemical Modeling, Lawrence Livermore National Laboratory*; Livermore, CA: 2010 (cit. on p. 33).

61. Falk, M.; Miller, A. G. *Vib. Spectrosc.* **1992** (cit. on pp. 34, 49).

62. Haaland, D. M.; Thomas, E. V. *Anal. Chem.* **1988**, *60*, 1193–1202 (cit. on p. 36).

63. Bard, Y., *Nonlinear Parameter Estimation*; Academic Press: 1974 (cit. on pp. 38, 81, 85, 126).

64. Holmes, P. E.; Naaz, M.; Poling, B. E. *Ind. Eng. Chem. Res.* **1998**, *37*, 3281–3287 (cit. on pp. 44, 49, 55, 56, 192, 199, 200).

65. Mani, F.; Peruzzini, M.; Stoppioni, P. *Green Chem.* **2006**, *8*, 995 (cit. on p. 44).

66. Perrin, D. D. *Pure Appl. Chem.* **1969**, *20*, 133–236 (cit. on p. 53).

67. McCann, N.; Phan, D.; Wang, X.; Conway, W.; Burns, R.; Attalla, M.; Puxty, G.; Maeder, M. *J. Phys. Chem. A* **2009**, *113*, 5022–5029 (cit. on p. 55).

68. Darde, V.; Maribo-Mogensen, B.; van Well, W. J.; Stenby, E. H.; Thomsen, K. *Int. J. Greenh. Gas Control* **2012**, *10*, 74–87 (cit. on pp. 57, 67).

69. *MATLAB 9.2 and Optimization Toolbox 7.6*; The MathWorks, Inc.: Natick, MA, 2017 (cit. on pp. 58, 84, 126, 132).

70. Kriesten, E.; Mayer, D.; Alsmeyer, F.; Minnich, C. B.; Greiner, L.; Marquardt, W. *Chemom. Intell. Lab. Syst.* **2008**, *93*, 108–119 (cit. on p. 59).

71. Kriesten, E.; Alsmeyer F. and, A.; Marquardt, W. *Chemom. Intell. Lab. Syst.* **2008**, *91*, 181–193 (cit. on p. 59).

72. Terres, E.; Weiser, H. *Z. Elektrochem.* **1921**, *27*, 177–193 (cit. on pp. 67, 153).

73. Kurz, F.; Rumpf, B.; Maurer, G. *Fluid Phase Equilib.* **1995**, *104*, 261–275 (cit. on p. 67).

74. Kurz, F.; Rumpf, B.; Maurer, G. *J. Chem. Thermodyn.* **1996**, *28*, 497–520 (cit. on pp. 67, 112, 117).

75. Edwards, T. J.; Maurer, G.; Newman, J.; Prausnitz, J. M. *AIChE J.* **1978**, *24*, 966–976 (cit. on p. 67).

76. Milella, F.; Mazzotti, M. *React. Chem. Eng.* **2019**, *4*, 1284–1302 (cit. on pp. 67, 68, 77, 116, 118, 127, 131, 145).

77. Dobberschütz, S.; Nielsen, M. R.; Sand, K. K.; Civioc, R.; Bovet, N.; Stipp, S. L. S.; Andersson, M. P. *Nat. Commun.* **2018**, *9* (cit. on pp. 68, 86, 88, 94).

78. Davis, K. J. *Science* **2000**, *290*, 1134–1137 (cit. on pp. 68, 86, 88, 94).

79. Pertlik, F. *TMPM Tschermaks Mineral. und Petrogr. Mitteilungen*, 67–74 (cit. on p. 71).

80. Han-Qing, Z. *Act. Phy. Sin.* **2005**, *33*, 391–398 (cit. on p. 71).

81. Gmelin, L., *Gmelin Handbuch der Anorganischen Chemie*; Springer-Verlag, Berlin: 1982 (cit. on p. 69).

82. Steinfeld, J. I.; Francisco, J. S.; Hase, W. L., *Chemical Kinetics and Dynamics (2nd Edition)*; Prentice Hall: 1999 (cit. on p. 75).

83. Doki, N.; Kubota, N.; Sato, A.; Yokota, M. *Chem. Eng. J.* **2001**, *81*, 313–316 (cit. on pp. 75, 123).

84. Dei, L.; Baglioni, P.; Sarti, G.; Ferroni, E. *Stud. Conserv.* **1996**, *41*, 9 (cit. on p. 76).

85. Ramkrishna, D., *Population balances : theory and applications to particulate systems in engineering*; Academic Press: 2000, 355 (cit. on pp. 79, 124).

86. Mullin, J., *Crystallization (Fourth Edition)*; Butterworth-Heinemann: 2001, 216 (cit. on pp. 80, 94, 112, 151).

87. Gemperline, P., *Practical Guide To Chemometrics, Second Edition*; CRC Press: 2006 (cit. on p. 81).

88. Brun, R.; Reichert, P.; Künsch, H. R. *Water Resour. Res.* **2001**, *37*, 1015–1030 (cit. on pp. 82, 217).

89. Bötschi, S.; Rajagopalan, A. K.; Morari, M.; Mazzotti, M. *Cryst. Growth Des.* **2019**, *19*, 4029–4043 (cit. on pp. 83, 106).

90. Van Leer, B. *J. Comput. Phys.* **1979**, *32*, 101–136 (cit. on pp. 84, 124, 167).

91. Vetter, T.; Burcham, C. L.; Doherty, M. F. *Ind. Eng. Chem. Res.* **2015**, *54*, 10350–10363 (cit. on p. 85).

92. Fenimore, C. P.; Thrailkill, A. *J. Am. Chem. Soc.* **1949**, *71*, 2714–2717 (cit. on p. 86).

93. Salvalaglio, M.; Vetter, T.; Mazzotti, M.; Parrinello, M. *Angew. Chemie Int. Ed.* **2013**, *52*, 13369–13372 (cit. on pp. 86, 88).

94. Davey, R.; Mullin, J.; Whiting, M. *J. Cryst. Growth* **1982**, *58*, 304–312 (cit. on p. 86).

95. Cody, A.; Cody, R. *J. Cryst. Growth* **1991**, *113*, 508–519 (cit. on p. 86).

96. Eisenschmidt, H.; Voigt, A.; Sundmacher, K. *Cryst. Growth Des.* **2015**, *15*, 219–227 (cit. on p. 86).

97. Fortes, A. D.; Wood, I. G.; Alfè, D.; Hernández, E. R.; Gutmann, M. J.; Sparkes, H. A. *Acta Crystallogr. Sect. B Struct. Sci. Cryst. Eng. Mater.* **2014**, *70*, 948–962 (cit. on p. 86).

98. Weijnen, M.; van Rosmalen, G.; Bennema, P. *J. Cryst. Growth* **1987**, *82*, 528–542 (cit. on p. 88).
99. Hiemstra, T.; Van Riemsdijk, W. *J. Colloid Interface Sci.* **1996**, *179*, 488–508 (cit. on p. 88).
100. De Leeuw, N. H.; Rabone, J. A. *Cryst. Eng. Comm.* **2007**, *9*, 1178–1186 (cit. on pp. 88, 94).
101. Graham, M. D. *J. Assoc. Lab. Autom.* **2003**, *8*, 72–81 (cit. on p. 98).
102. Bozutto, C., *Clean Combustion Technologies*; Alstom Incorporated: 2009 (cit. on pp. 111–113).
103. Milella, F.; Mazzotti, M. *Cryst. Growth & Des.* **2019**, *19*, 5907–5922 (cit. on pp. 112, 122, 125, 126, 132, 140, 141, 143).
104. Rumpf, B.; Maurer, G. *Ind. & End. Chem. Res.* **1993**, *32*, 1780–1789 (cit. on p. 112).
105. Casas, J.; Alvarez, F.; Cifuentes, L. *Chem. Eng. Sci.* **2000**, *55*, 6223–6234 (cit. on pp. 114, 219).
106. Safari, H.; Shokrollahi, A.; Jamialahmadi, M.; Ghazanfari, M. H.; Bahadori, A.; Zendehboudi, S. *Fluid Phase Equilib.* **2014**, *374*, 48–62 (cit. on p. 120).
107. Kubota, N.; Mullin, J. *J. Cryst. Growth* **1995**, *152*, 203–208 (cit. on pp. 125, 142).
108. Davey, R.; Mullin, J. *J. Cryst. Growth* **1974**, *26*, 45–51 (cit. on p. 126).
109. Bliznakov, G.; Kirkova, E. *Krist. Techn.* **1969**, *4*, 331–336 (cit. on p. 126).
110. Black, S.; Davey, R.; Halcrow, M. *J. Cryst. Growth* **1986**, *79*, 765–774 (cit. on p. 126).
111. Zawadowicz, M. A.; Proud, S. R.; Seppalainen, S. S.; Cziczo, D. J. *Atmos. Chem. Phys.* **2015**, *15*, 8975–8986 (cit. on p. 130).
112. Robinson, R. A.; Stokes, R. H., *Electrolyte Solutions: Second Revised Edition*; Dover Publications, Inc., New York: 2002 (cit. on p. 135).
113. De Albuquerque, I.; Mazzotti, M. *Chem. Eng. Tech.* **2017**, *40*, 1339–1346 (cit. on p. 138).

114. Olafson, K. N.; Li, R.; Alamani, B. G.; Rimer, J. D. *Chem. Mater.* **2016**, *28*, 8453–8465 (cit. on p. 142).
115. Buchner, R.; Chen, T.; Hefter, G. *J. Phys. Chem. B* **2004**, *108*, 2365–2375 (cit. on pp. 142, 222).
116. Dobberschütz, S.; Nielsen, M. R.; Sand, K. K.; Civioc, R.; Bovet, N.; Stipp, S. L. S.; Andersson, M. P. *Nat. Commun.* **2018**, *9*, 1578 (cit. on p. 142).
117. Hayes, A. C.; Kruus Peeterand Adams, W. A. *J. Solution Chem.* **1984**, *13*, 61–75 (cit. on p. 142).
118. Perry, R. H., *Perry's Chemical Engineers' Handbook*; McGraw-Hill, New York: 2008 (cit. on pp. 151, 165, 166, 228).
119. Mersmann, A., *Crystallization Technology Handbook Second Edition Revised and Expanded*; Marcel Dekker, Inc., New York: 2001, 1037 (cit. on pp. 153, 162, 164, 190).
120. Garrett, D. E., *Sodium Sulfate: Handbook of Deposits, Processing, Properties, and Use*; Academic Press: 2001, 250 (cit. on p. 154).
121. De Goede, R.; De Jong, E. *Chem. Eng. Sci.* **1993**, *48*, 1393–1404 (cit. on pp. 154, 165).
122. Rao, C. S.; Hartel, R. W. *Crit. Rev. Food Sci. Nutr.* **2006**, *46*, 207–219 (cit. on p. 154).
123. Boccardi, G.; Celata, G. P.; Lazzarini, R.; Saraceno, L.; Trinchieri, R. *Appl. Therm. Eng.* **2010**, *30*, 1101–1106 (cit. on p. 154).
124. Randolph, A. D.; Larson, M. A., *Particulate Processes: Analysis and Techniques of Continuous Crystallization*; Academic Press: 1988 (cit. on pp. 154, 158, 159, 182).
125. Elvers, B.; Bellussi, G., *Ullmann's Encyclopedia of Industrial Chemistry*; Wiley-VCH Verlag GmbH: 2011 (cit. on p. 157).
126. Garside, J.; Davey, R. J. *Chem. Eng. Commun.* **1980**, *4*, 393–424 (cit. on p. 164).
127. Gnielinski, V. *Heat Transf. Eng.* **2009**, *30*, 431–436 (cit. on pp. 165, 177).

128. Kumar, S.; Ramkrishna, D. *Chem. Eng. Sci.* **1996**, *51*, 1333–1342 (cit. on p. 167).

129. Kierzenka, J.; Shampine, L. F. *ACM Trans. Math. Softw.* **2001**, *27*, 299–316 (cit. on pp. 167, 168).

130. Pho, T. K.; Lapidus, L. *AIChE J.* **1973**, *19*, 1170–1181 (cit. on p. 168).

131. Valenti, G.; Bonalumi, D.; Macchi, E. *Fuel* **2012**, *101*, 74–83 (cit. on p. 170).

132. Deb, K.; Pratap, A.; Agarwal, S.; Meyarivan, T. *IEEE Trans. Evol. Comput.* **2002**, *6*, 182–197 (cit. on p. 171).

133. Levenspiel, O.; Wiley, J.; Hepburn, K.; Levenspiel, O., *Chemical Reaction Engineering - third edition*; John Wiley and Sons: 1999 (cit. on p. 173).

134. Vetter, T.; Burcham, C. L.; Doherty, M. F. *Chem. Eng. Sci.* **2014**, *106*, 167–180 (cit. on p. 182).

135. Lillia, S.; Bonalumi, D.; Fosbøl, P. L.; Thomsen, K.; Valenti, G. *Int. J. Greenh. Gas Control* **2018**, *70*, 117–127 (cit. on p. 192).

136. Wang, X.; Conway, W.; Fernandes, D.; Lawrance, G.; Burns, R.; Puxty, G.; Maeder, M. *J. Phys. Chem. A* **2011**, *115*, 6405–6412 (cit. on p. 192).

137. Li, K.; Yu, H.; Yan, S.; Feron, P.; Wardhaugh, L.; Tade, M. *Environ. Sci. Technol.* **2016**, *50*, 10746–10755 (cit. on p. 195).

138. University of Arizona Mineral Museum *rruff.info/R040036* (cit. on pp. 220, 221).

139. University of Arizona Mineral Museum *rruff.info/R040040* (cit. on pp. 220, 221).

140. O'Haver, T. *https://terpconnect.umd.edu/ toh/spectrum/InteractivePeakFitter.htm* **2019** (cit. on p. 222).

141. Gesellschaft, V., *VDI Heat Atlas*; Springer Berlin Heidelberg: 2010 (cit. on p. 228).

# PUBLICATIONS

Articles in peer-reviewed journals (* indicates equal contribution):

6. Milella, F.; Gazzani, M.; Sutter, D.; Mazzotti, M. *Ind. Eng. Chem. Res.* **2018**, *57*, 11712–11727
5. Milella, F.; Mazzotti, M. *React. Chem. Eng.* **2019**, *4*, 1284–1302
4. Milella, F.; Mazzotti, M. *Cryst. Growth & Des.* **2019**, *19*, 5907–5922
3. Milella, F.; Mazzotti, M. *Cryst. Growth & Des.* **2020**, *20*, 948–963
2. Milella, F.; Pérez-Calvo*; Preso, D. B.; Mazzotti, M. *in preparation*
1. Milella, F.; Pérez-Calvo*; Ammann, K.; Mazzotti, M. *in preparation*

Thursday 14th May, 2020
Zurich, Switzerland

# COLOPHON

This document was typeset in LaTeX using the typographical look-and-feel `classicthesis`. The graphics in this thesis were generated using `MATLAB`, and `MS Visio`. Cosmetic editing of the graphics in this thesis were performed using `Adobe Illustrator`. The bibliography was typeset using `biblatex`.